

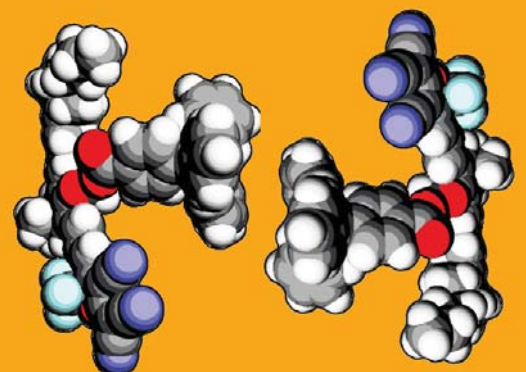
PHOTONICS

CMDITR Review of Undergraduate Research

Contributions from undergraduate research experiences within the
NSF Center on Materials and Devices for Information Technology Research



Volume 6, Number 1



This material is based upon work supported by the STC Program of the National Science Foundation No. DMR 0120967.

All rights reserved. No part of the Review may be reproduced in any form or by any means without written permission.

Any opinions, findings, and conclusions or recommendations expressed in this material are those of the authors and do not necessarily reflect the views of the National Science Foundation.

Printed in the United States at the University of Washington, Seattle, WA

Inquires should be addressed to:

Center on Materials and Devices for Information Technology Research
University of Washington
Department of Chemistry
Box 351700
Seattle, WA 98195-1700

reu@stc-mditr.org

<http://stc-mditr.org>

Volume 6, Number 1

Table of Contents

- 1 Enhancement of Two Photon Absorption in Fabry-Perot Cavity
Robyn Anderson, Loyola Marymount University
- 6 Evaluation of Sealant Materials for Encapsulating Organic Electronic Devices
Gilberto Arreola, California Polytechnic State University, Pomona
- 10 Synthesis of Donor-Acceptor Oligomers for Applications in Organic Field-Effect Transistors
Kristen Brown, Georgia Institute of Technology
- 14 Synthesis of Carbazole and Fluorene Conjugated Copolymers for Use in Organic Solar Cells and Organic Field Effect Transistors
Anesia Burns, University of Florida
- 18 Synthesis of Crosslinkable Hole Transporting Polymers for Organic Light Emitting Diodes (OLEDs)
Igor Coropceanu, Georgia Institute of Technology
- 22 Pyranine Dyed Triglycine Sulfate: A New Dyed Crystal for Single Molecule Microscopy
Andrea M. de la Garza, Heritage University
- 26 Electrostatic Force Microscopy of Photogenerated Charge Carriers in Thin Films of Poly(3-hexylthiophene) / Fullerene Blends
Emilita Diaz, Valencia Community College
- 30 Enabling Robust Object Tracking in Tabletop Augmented Environments
Tarrell Ezell, Alabama Agricultural and Mechanical University
- 34 Sonogashira Coupling of Terminal Acetylenes with Perylene Bisimides
Akil Foluke, Morehouse College
- 38 Use of Spatially Anisotropic Intermolecular Interactions to Define Order in Molecular Films Grown by Physical Vapor Deposition (PVD)
Ryan P. Fraser, Western Washington University
- 42 Use of Ion-Exchange Functionalized DNA as a Host Material for Enhanced Poling Induced Order and Molecular Hyperpolarizability
Derek J. Frei, University of Washington
- 46 Raman Spectroscopy Study of Thermo-Chemical Nanolithography (TCNL) on PPV and Graphene
Ivan Gadjev, Georgia Institute of Technology
- 50 Ab Initio Calculations of the Torsion Potentials of Polyacetylene Oligomers
Matthew Gray, University of Michigan
- 54 Designing and Implementing a Temperature Programmed Desorption Instrument for the Study of Organic Thin Films
Melissa A. Healey, Cornell University
- 58 Passive Wireless Sensors using Reflected Electro-Material Signatures (REMS)
Ryan Hearty, Johns Hopkins University
- 62 Photovoltaic Performance Tracking System
Jason Hightower, University of California San Diego
- 67 The Analysis of Diffuse, Bulk and Bi-Layer Heterojunction Organic Photovoltaic Cells
Dexter Hypolite, University of the Virgin Islands
- 72 Poling and Characterization Methods for Electro-Optic Modulators
Christopher Liu, California Institute of Technology
- 78 Effect of Monomer Chemical Structure on Kumada Catalyst Transfer Polymerization
Elizabeth Merten, University of Washington
- 83 Characterization of Diffraction Gratings Comprised of Core/Shell Nanocrystals
Belinda D. Molina, University of Texas at El Paso
- 87 4-Tritylphenol Bridge Substitution Effects on Dipole-Dipole Interactions of Polymeric Second Order Nonlinear Optical Materials
Rosa Neidhardt, University of California - Irvine
- 91 Effect of Nanoparticle Volume Fraction on Capacitor Properties of a Barium Titanate/Epoxy Nanocomposite
Audrey L. Slutsky, University of West Georgia
- 95 Transmission Sensor of an Advanced Intravital Microscope
Courteny Smith, Norfolk State University
- 99 Light Polarization Changes Passing Crystals of Point Group 42
Steven Steininger, Highline Community College
- 103 New Phthalimide-Based Polymer Semiconductors for Efficient Photovoltaic Cells
Amanda Y. Sun, Duke University
- 109 Electric and Optical Properties of Organic-Inorganic Hybrid Sol-Gel Films
Amy Van Newkirk, Grove City College
- 113 Use of Ion-Exchange Functionalized DNA as a Host Material for Enhanced Poling Induced Order and Molecular Hyperpolarizability
Terry Villarreal, North Seattle Community College & University of Washington
- 117 Plasmon-Resonant Silver Nanoprisms for Performance Enhancement of Organic Photovoltaic Cells
Josiah G. Ward, South Seattle Community College

Welcome to the Sixth Edition of CMDITR's Review of Undergraduate Research

This volume features extended abstracts written by student participants in the National Science Foundation (NSF) Center on Materials and Devices for Information Technology Research (CMDITR) Summer 2009 Research Experiences for Undergraduates (REU) program: Hooked on Photonics.

The REU experience is intended to serve as a catalyst for entry by undergraduates into careers involving science, technology, engineering, and mathematics. Hooked on Photonics provides a rich learning opportunity not only for the undergraduate participants who experience research first-hand prior to committing to graduate study, but also for the student's mentors, be they faculty members, research scientists, post-doctoral fellows or graduate students. While working with REU students, mentors develop teaching and mentoring skills, and benefit from reflecting on the excitement of cutting-edge research upon which their careers have been built.

The CMDITR REU Program placed undergraduate students from across the United States in CMDITR research laboratories at the University of Washington, the University of Arizona, and Georgia Institute of Technology. All of the participants worked on authentic interdisciplinary research projects that contributed to advancements in information technology encompassing activities in chemistry, physics, optics, materials science and engineering. The program emphasized the teamwork nature of scientific research, and was supplemented by a collection of activities including ethics training and workshops in scientific communication.

This publication offers a forum for participants to share their research with their REU peers, future students, CMDITR graduate students and faculty, and others interested in the research activities of CMDITR. To learn more about Hooked on Photonics please visit www.stc-mditr.org/reu.

A special thanks to all of the students for their hard work, to their mentors for their time and patience, and to the REU program coordinators Denise Bale-Mushatt, Olanda Bryant, April Wilkinson, and Kimberly Sierra-Cajas, for their organizational efforts. A final, but important thanks goes to Ly Pham and Suzy Hunter for their work on the production of this volume.

The extended abstracts included here are presented in alphabetical order by the participant's last name.

Philip Reid, CMDITR Director

Enhancement of Two Photon Absorption in Fabry-Perot Cavity

ROBYN ANDERSON, Loyola Marymount University

Dan Owens, Dr. Fuentes-Hernandez, Dr. Kippelen, Georgia Institute of Technology

Introduction

The objective of the planned research is to demonstrate the enhancement of two photon absorption in a Fabry-Perot cavity. Light is quantized in discrete amounts of energy called photons. Photons, like other subatomic particles, exhibit the behaviors of both a wave and a particle.¹ Light's wave properties can be seen through effects such as interference and diffraction. Its particle properties are more evident in light-matter interactions like two photon absorption which will serve as the primary optical limiting agent in the planned research.

It is necessary to fabricate a form of protection for sensitive sensors such as those found in cameras, IR detectors, and the human eye in the event that they are exposed to dangerously high intensities of light. The focus of the research will be directed toward protection from light within the infrared area of the electromagnetic spectrum because of its countless practical applications and encounters in things such as night vision technology, passive missile guidance systems, photography, communications systems, and heating.

Two photon absorption (TPA) is the simultaneous absorption of two photons of identical or different frequencies in order to excite a molecule from one state to a higher energy state.² Since the absorption coefficient is proportional to the intensity, TPA only occurs at higher optical intensities. Because TPA in common materials are typically quite weak, the TPA onset intensity is too high to be of practical value, so it is necessary to find structures in which the TPA can be enhanced.

A Fabry-Perot (FP) interferometer is a resonant cavity that can be used to amplify the properties of the two photon absorbing material that is enclosed within the cavity. Because TPA occurs with high intensity light, FP interferometers filled with TPA materials allow for high transmittance at low intensities and low transmittance at high intensities. FP interferometers consist of two parallel reflective surfaces.¹ The reflective surfaces can be dielectric materials or metals and the characteristics of the two photon absorbing solution vary depending on the material. The material that will be used to fill the cavity is a material which has been proven to have effective TPA at high intensities.⁴

As light enters the cavity, it is repeatedly reflected against the surfaces of the reflective cavity walls. The repetitive reflections continuously expose the TPA material to the light in the cavity which enhanced the TPA process, and prevents a large percentage of it from being transmitted through the cavity and into vulnerable sensors.³

Transmittance, in optics, is the fraction of incident light at a specified wavelength that passes through a sample.¹ The varying transmission function of the cavity is caused by constructive and destructive

interference between the multiple reflections of light between the two reflecting surfaces. Constructive interference occurs when the transmitted beams are in phase and destructive interference occurs when the transmitted beams are out of phase.² Whether the waves are in phase or not depends on numerous factors such as the wavelength of the light, the angle at which the light travels through the cavity, the thickness of the cavity, and the refractive index of the solution between the reflecting surfaces.

It has been shown that the FP interferometer is able to enhance TPA, but the exact specifications of the device have yet to be determined. An optimal FP interferometer will have minimal transmission of high intensity light, maximum transmission of low intensity light, and minimal absorption.

Experimental Methods

Customized MATLAB simulation programs help determine the appropriate layering thickness of the materials deposited on the glass substrates for optimal reflectivity and effectiveness. The thicknesses of the dielectric layers can be adjusted for a specific wavelength using the following method.

1. Specify wavelength
2. Divide wavelength by the index of refraction of dielectric material
3. Divide by four to find optimal thickness

A series of layers with alternating high and low refractive index dielectric materials with these thicknesses is known as a quarter-wave stack, and gives optimal reflectance at the specified wavelength. A series of test mirrors is fabricated in order to calibrate the deposition system and fine-tune the specifications of the quarter-wave stack. The mirrors are then fabricated using either electron beam (E-Beam) or atomic layer deposition (ALD) methods to coat the glass wafers with reflective layers (metals or dielectric quarter-wave stacks). The TPA polymer is then inserted between the two mirrors and the cavity is assembled and secured with a demountable liquid cell.

The dielectric materials used to construct the mirrors are silicon dioxide (SiO_2) and tantalum oxide (Ta_2O_5); SiO_2 has a low refractive index and Ta_2O_5 has a high refractive index.

The TPA polymer material that will be used to fill the Fabry-Perot cavity, lead porphyrin, is most effective at a wavelength of 1064 nm which will serve as the main focal point during this research.

The intensity-dependent two photon absorption will be measured with a high intensity pulsed laser to determine the effectiveness of the cavity and the cavity with the most.

Results and Discussion

Eight double layer dielectric mirrors were simulated in MATLAB and fabricated using E-Beam deposition.

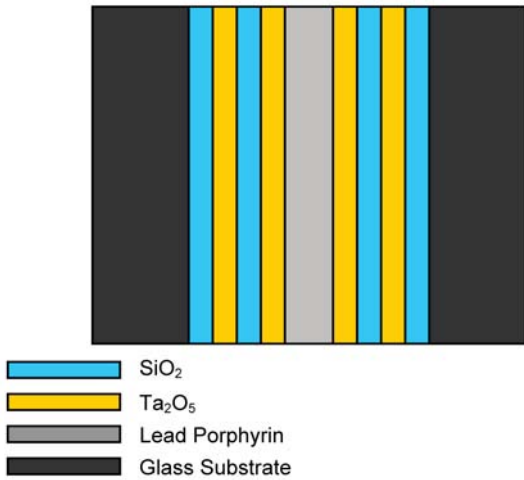


Figure 1. Schematic of double layer dielectric mirror.

The principle measurements that are considered are the transmission and reflection peaks and troughs and the width of the transmission peaks. The narrower the transmission peak, the more sensitive the Fabry-Perot cavity is to adjustments in the refractive index of the TPA material. The transmission peak widths of various mirror designs are compared below.

Figure 2. Simulated transmittance simulations of Fabry-Perot cavities with various layers of SiO₂/Ta₂O₅ dielectric mirrors.

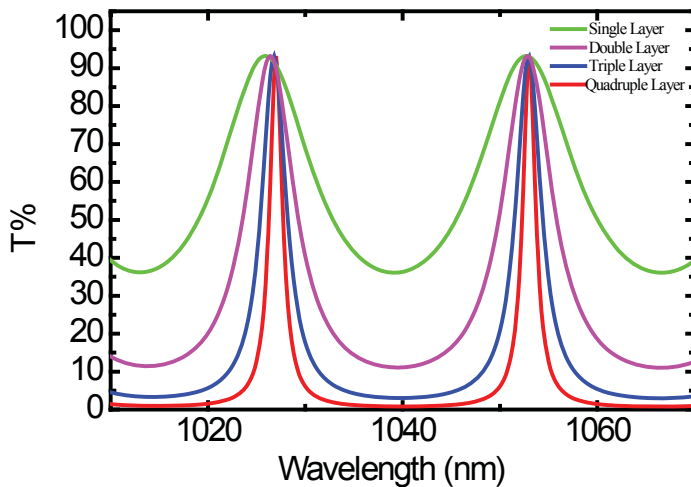


Figure 3. Simulated transmittance and reflectance of a full Fabry-Perot cavity with double layer SiO₂/Ta₂O₅ dielectric mirrors.

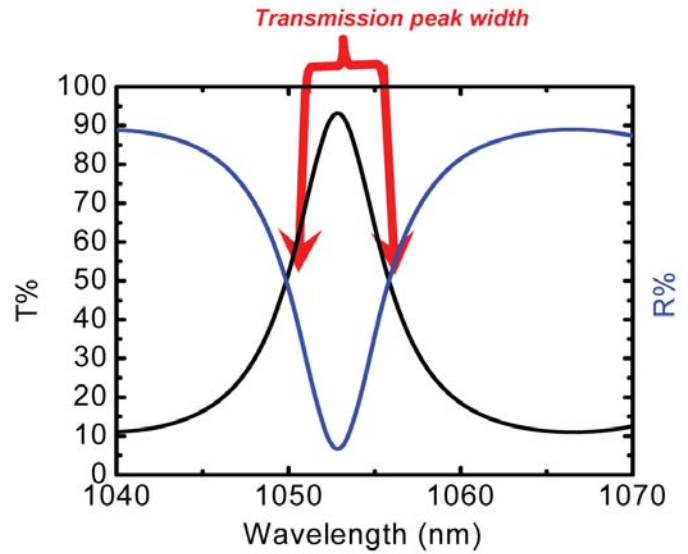


Table 1. Table of transmission peaks of dielectric mirrors with various layers beginning with SiO₂.

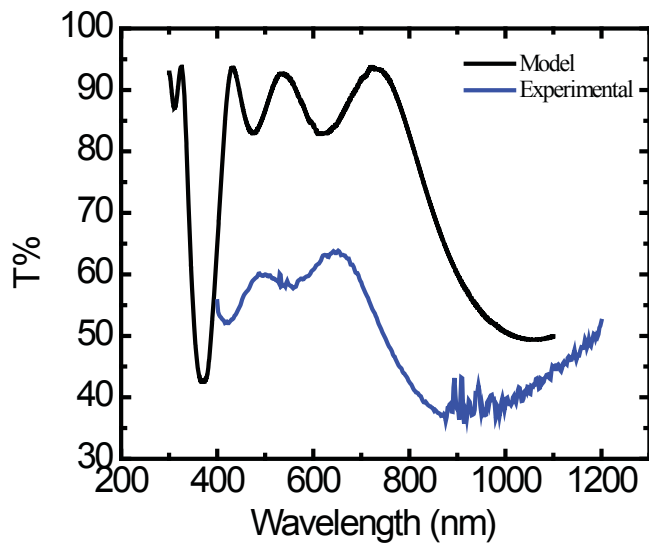
	Transmission Peak Width (nm)
1 Layer	15
2 Layers	6
3 Layers	3
4 Layers	2

Table 2. Table of transmission peaks of dielectric mirrors with various layers beginning with Ta₂O₅.

	Transmission Peak Width (nm)
1 Layer	n/a
2 Layers	15
3 Layers	6
4 Layers	3

From these tables, it can be seen that initializing the deposition with SiO₂ is the best fabrication method. Although a mirror with four layers of dielectric material would yield the narrowest transmission peak, consideration must also be given to factors affecting the fabrication process such as time constraints during the deposition and using a reasonable amount of material. Nonetheless, the best way to observe and document the behavior of experimental dielectric mirrors is to fabricate test mirrors and compare determining measurements like the minimum and maximum values of the transmission and reflectance and the width of the transmission peaks beginning with double layered dielectric mirrors as shown in Figure 1.

Figure 4. Transmission graph of double layer dielectric mirror beginning with SiO₂ layer compared to simulated model data.



Since the glass wafer itself is composed of CaF_2 , the beginning layer of SiO_2 can be omitted and the quarter wavelength dielectric stack can effectively begin and end with a Ta_2O_5 layer (as shown in Fig. 5) which will curtail the amount of material used in the deposition process and the fabrication time. Two substrates were constructed using this method.

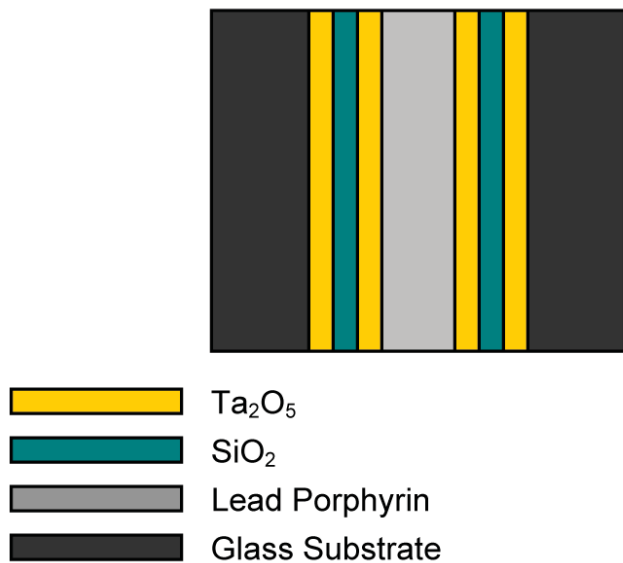


Figure 5. Schematic of Fabry-Perot cavity with dielectric mirrors beginning and ending with Ta_2O_5

Figure 6 shows that this fabrication method yields a much closer transmission to the simulated prediction than the double layer dielectric mirrors and will serve as the production method for the final dielectric Fabry-Perot cavity.

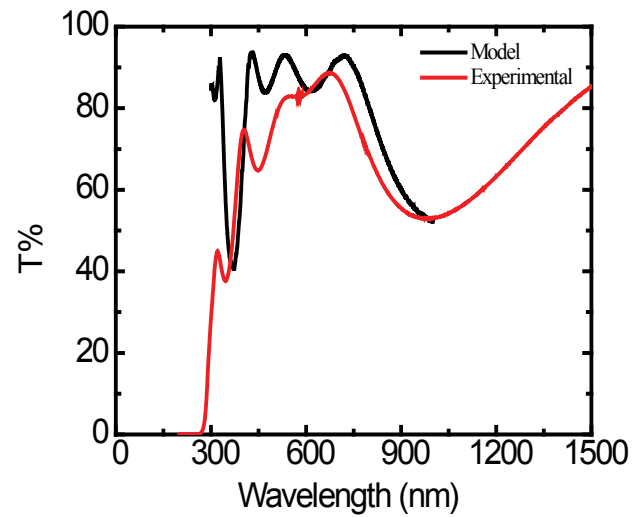


Figure 6. Transmission graph of dielectric mirror beginning and ending with Ta_2O_5 .

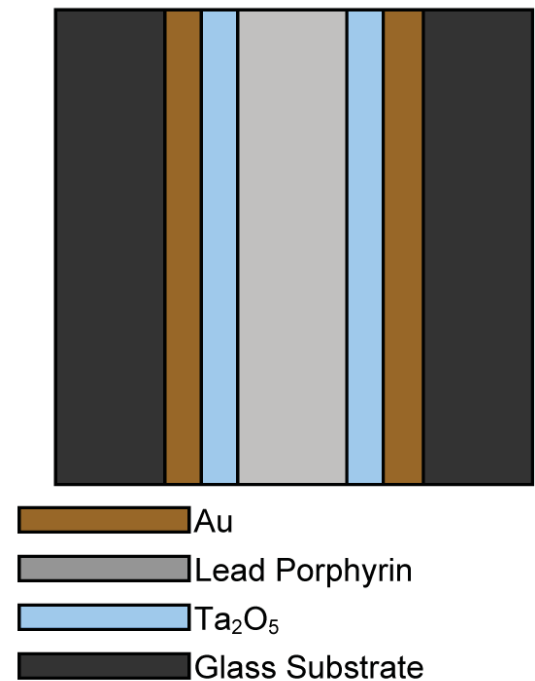


Figure 7. Schematic of metallic mirror.

Metallic mirrors, as shown in Fig. 7, were also fabricated using the E-beam deposition system to deposit 25nm of gold (Au) onto glass disks.

Figure 8 shows various transmittance simulations of metallic mirrors with different thickness of gold. Although the metallic Fabry-Perot cavity with 20 nm thick Au mirrors has the highest transmission peak, the realistic fabrication of a mirror that thin would not yield reasonable transmission data or ellipsometry measurements which makes 25 nm the ideal thickness. Furthermore, since the pulse laser will be testing the cavities at very high intensities, heating will occur within the metallic layer which makes it sensible to insulate the gold layer with a dielectric layer of Ta_2O_5 of thickness 75nm.

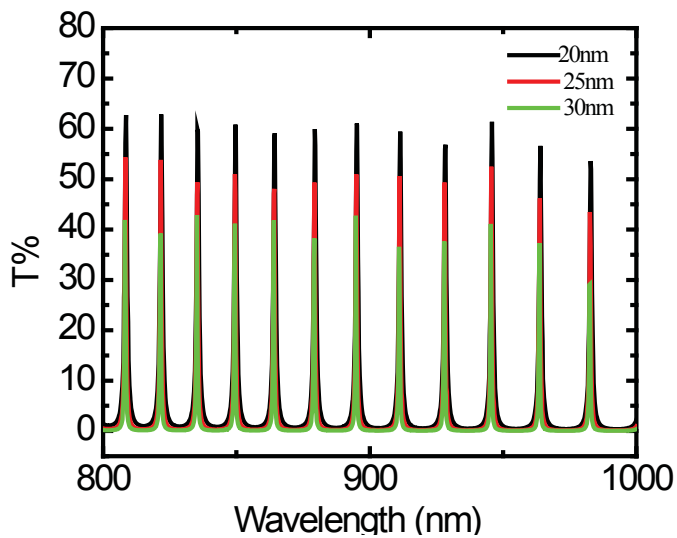


Figure 8. Simulated transmission graph of Fabry-Perot cavity with Au mirrors of varying thicknesses.

Once the full Fabry-Perot cavities were assembled, they were tested with a scanning spectrophotometer and a high intensity pulsed laser. The mirrors and Lead Porphyrin were inserted into the demountable FTIR liquid cell shown in Figure 9 and first tested with a scanning spectrophotometer to yield the transmission results shown in Figure 10.



Figure 9. Demountable liquid cell used to assemble dielectric and metallic Fabry-Perot cavities.

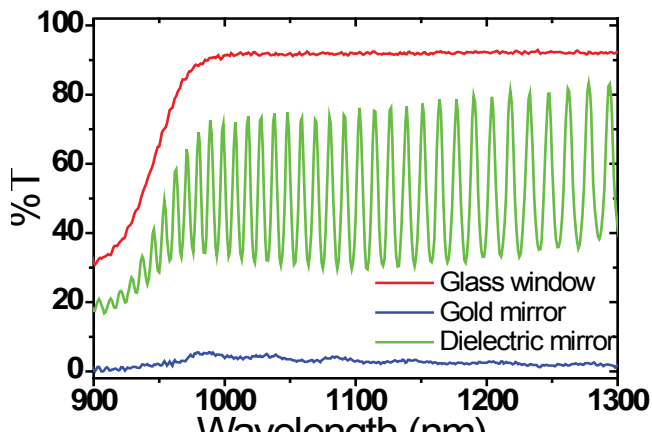


Figure 10. Transmission measurements from scanning spectrophotometer of Fabry-Perot cavity filled with Lead Porphyrin encased by plain glass windows, gold mirrors, and dielectric mirrors.

From this graph, it can be seen that the Fabry-Perot cavity with dielectric mirrors performs the best with transmission peaks in the 70% range. It exhibits healthy peak behavior and has a transmission trough at 1064nm ideal to exploit the TPA in lead porphyrin. The dielectric mirror went on to be tested with the laser to measure its nonlinear transmission data which confirmed that the Fabry-Perot cavity with dielectric mirrors enhances the performance of two photon absorption. Using Beer's law to compare initial and final values of the TPA coefficient β ,

$$I(x) = \frac{I_0}{1 + \beta c x I_0}$$

I_0 - input intensity; $I(x)$ - output intensity; β - TPA coefficient; c - concentration; x - path length

it can be shown that the effectiveness of two photon absorption was increased by more than a factor of eight.

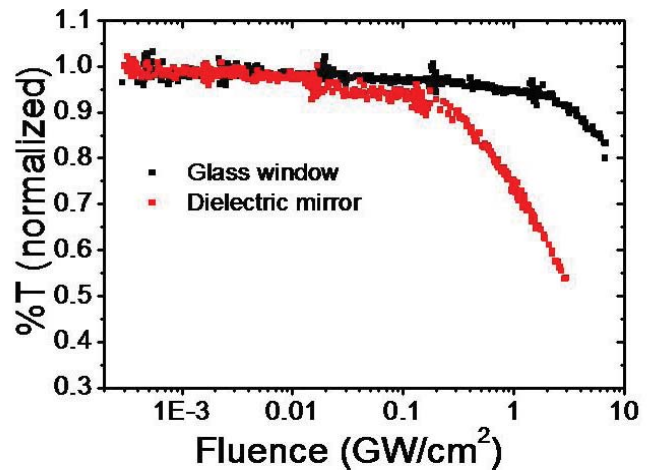


Figure 11. Nonlinear transmission measurement of Fabry-Perot cavity with plain glass windows (black) and dielectric mirrors (gray).

Conclusions

A Fabry-Perot cavity with dielectric mirrors with a design shown in Figure 5 enhances two photon absorption and limits the amount of high intensity light allowed to be transmitted through the cavity. The gold mirror design showed promise during simulations but did not perform satisfactorily during testing. This may be because of poor film quality and the thinness of the gold layers which made the mirrors highly susceptible to scratches.

Future work may include:

- Optimization of fabrication process of dielectric mirrors with annealing and consistent oxidation of deposition materials.
- Experimentation with stronger glass substrates to lessen substrate weakening during testing.
- Troubleshooting gold mirrors and revising configuration.
- Experimentation with different metallic mirror insulators.

References

1. Fowles, R.G.; Introduction to Modern Optics, 2nd ed; Dover Publications Inc.: New York, 1968.
2. Iizuka, K. Fabry-Perot Resonators, Beams, and Radiation Pressure. In Elements of Photonics, Vol. 1; John Wiley and Sons, Inc.: New York, 2002; Vol. 1, 166-236.
3. Monzon, J.J.; Sanchez-Soto, L.L; On the concept of absorption for a Fabry-Perot interferometer. Am. J. Phys., 1996, Vol. 64, 156-163.
4. Perry, J.W; Mansour, K; Marder, S.R; Perry, K.J; Alvarez Jr.,D.A; Choong, I; Enhanced reverse saturable absorption and optical limiting in heavy-atom-substituted phthalocyanines. Optical Letters., 1994, Vol. 19, 625-627.

Acknowledgments

Funds for this research were provided by the Center on Materials and Devices for Information Technology Research (CMDITR), the NSF Science and Technology Center No. DMR 0120967.



ROBYN ANDERSON. After earning a Bachelor of Science in Electrical Engineering at Loyola Marymount University, I plan to continue my education through the completion of a doctoral degree at Cornell University. Conducting research through the Hooked on Photonics program has given me insight into the world of scientific research and the atmosphere of graduate school level research which has inspired me to pursue a research doctoral degree in Electrical Engineering.

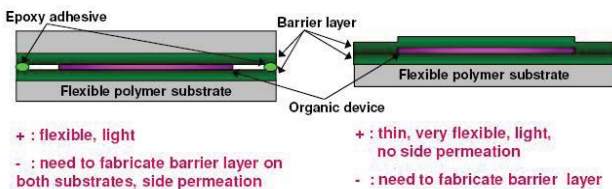
Evaluation of Sealant Materials for Encapsulating Organic Electronic Devices

GILBERTO ARREOLA, California Polytechnic State University, Pomona
Yongjin Kim, Samuel Graham, Georgia Institute of Technology

Introduction

Organic electronics are relatively new types of electronic devices which use conductive polymers or small molecules instead of traditional inorganic semiconductors as the active material. With the potential of solution deposition, it may be possible to create a new flexible large area electronics using organic semiconductors, a feat which is difficult to accomplish with traditional electronic materials. However, because they are very sensitive to oxidation by oxygen and water vapor found in the environment, organic electronics typically have very short life spans. In order to obtain suitable lifetimes for organic electronics, a method to seal the devices and prevent moisture and oxygen from permeating into their package must be implemented. This process is typically referred to as encapsulation.

Current encapsulation techniques include sealing the devices between two glass substrates or other impermeable materials via a UV-curable epoxy sealant. However, such sealants have high permeation rates for water vapor and oxygen, thus becoming the dominant permeation pathway for device degradation. Less permeable encapsulation techniques include the vacuum deposition of inorganic films or inorganic/organic multilayers on top of the device. Such methods have been used to create ultra-low permeation barrier films with water vapor transmission rates (WVTR) as low as 10^{-6} g/m²/day. However, such vacuum deposition techniques require a substantial amount of time and the deposition methods used can themselves cause degradation to the devices. Here we report the evaluation of a new type of barrier sealant for bonding encapsulation layers over the device.



J. S. Lewis, et. al., *IEEE Journal of Selected Topics in Quantum Electronics* 2004, 10, 45-57

To measure the properties of our sealant material, we will use the Ca corrosion test. Because calcium degrades with exposure to water vapor, we can encapsulate thin calcium samples to simulate how an organic electronic would respond to a certain permeation barrier. The effectiveness of this permeation barrier can be analyzed and a reasonable WVTR can be calculated. To isolate the properties of the sealant material, we can package the calcium between two glass substrates. Because the permeation rate through glass substrates is negligible, we can assert that any permeation will be due to the sealant. Implementing this encapsulation method requires a barrier layer with a WVTR as low as 10^{-6} g/m²/day.²

To create our seal, a thin strip of the sealant material was placed near the edge of the substrate and the glass capping substrate was applied. Simply, heat and pressure were applied for a few minutes in order to create an effective seal. Because this process does not require device compatibility with plasma and other vacuum deposition processes, it is potentially applicable to a wider range of organic electronic devices. Here we evaluate the permeation rates through the edge of the devices using the Ca corrosion test to determine the effectiveness of this alternative encapsulation method.

Methods

Calcium samples measuring 4.5 X 7 mm² were encapsulated using two 1 x 1 in² glass substrates and an ordinary two-part epoxy as a sealant. Because the 300 nm thick Ca sample oxidizes with exposure to oxygen and water vapor in the air, the encapsulation process was performed in a nitrogen environment. The samples were then placed in an environmental chamber of 20°C and 50% relative humidity. Microscope images were then taken to observe the changes in the Ca sample (Figure 1).



Figure 1. Microscope image of a calcium sample encapsulated with two-part epoxy after being exposed to 20°C and 50% RH for a week.

The same method was repeated with polyisobutylene filled with a desiccant sealant, and microscope images were also taken (Figure 2). This sealant was applied by raising the temperature to 150°C and applying a relatively small amount of pressure. To reduce the side permeation, the encapsulation method was repeated using the desiccant sealant and a 50 nm layer of Al₂O₃ was applied using atomic layer deposition. Microscope images taken demonstrate a decrease in Ca oxidation (Figure 3).

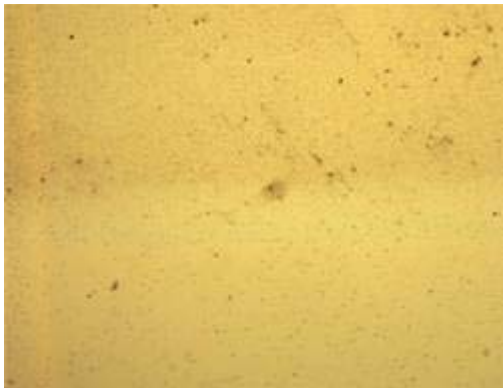


Figure 2. Microscope image of a calcium sample encapsulated with polyisobutylene after being exposed to 20°C and 50% RH for a week.

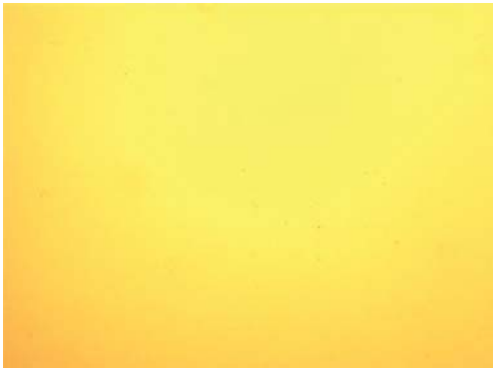


Figure 3. Microscope image of a calcium sample encapsulated with polyisobutylene and a 50 nm layer of Al₂O₃ after being exposed to 20°C and 50% RH for a week.

A calcium test was then used to calculate the WVTR. Aluminum interconnects were attached to allow monitoring of the resistance. The slope of the change in conductance as a function of time, $\frac{dG}{dt}$ can be used to calculate WVTR using

$$WVTR [g^{-1} m^{-2} day^{-1}] = -n d_{Ca} r_{Ca} \frac{d(G)}{dt} \frac{l}{w} \frac{M(H_2O)}{M(Ca)} \quad (1)$$

where n , the molar equivalent of the degradation reaction is assumed to be 2. In Eq. (1), δ_{Ca} is the Ca resistivity ($3.4 \times 10^{-8} \Omega m$), ρ_{Ca} is Ca density ($1.55 \times 10^6 g/m^3$), $M(H_2O)$ is the molar mass of water (18 amu), $M(Ca)$ is the molar mass of Calcium (40.1 amu), and l and w are the length and width of the Ca sensor, respectively.

Results and Discussion

Figure 4 shows images depicting the behavior of the Ca samples sealed with both epoxy and polyisobutylene. The first calcium samples were encapsulated by placing them between two glass substrates and sealing the perimeter with the polyisobutylene sealant. Visual inspection after 2 weeks at 20°C and 50% RH shows that the epoxy sealed samples were totally degraded while the

samples sealed with polyisobutylene were still opaque. Since such testing does not provide WVTR data, new polyisobutylene samples with electrical connections were fabricated to measure Ca corrosion. They were then placed in an environmental chamber of 20°C and 50% relative humidity where resistance measurements were taken every 3 min for approximately 100 hrs. The average WVTR of the samples was $1.5 \pm 0.5 \times 10^{-4} g/m^2 /day$. It should be noted that several samples showed even lower WVTR values as seen in Figure 5, indicating that the process can still be improved.

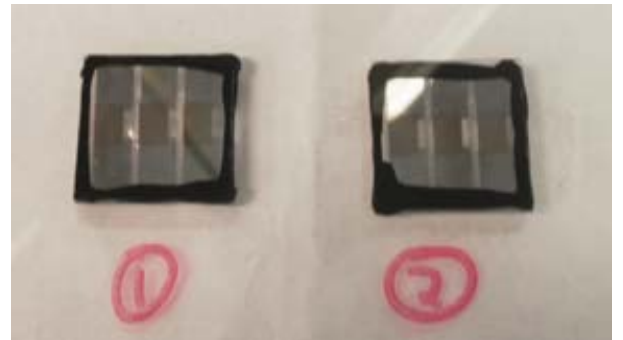
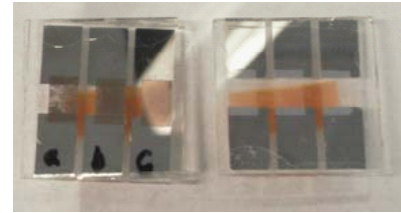


Figure 4. Digital picture of calcium samples encapsulated with two glass substrates. Top: epoxy seal after 3 days of exposure at 20°C/50% RH. Bottom: Polyisobutylene seal after 2 weeks of exposure at 20°C/50% RH followed by 3 days at 50°C/80%RH.

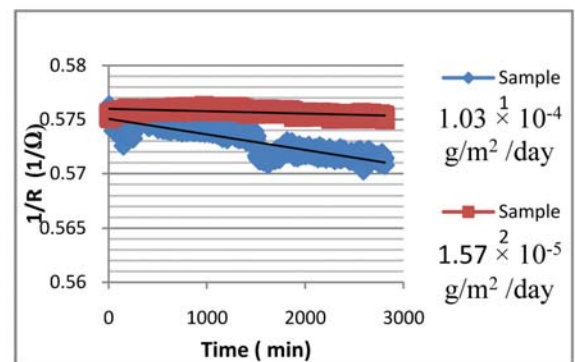


Figure 5. Resistance of calcium sample with polyisobutylene @ 20°C and 50% relative humidity.

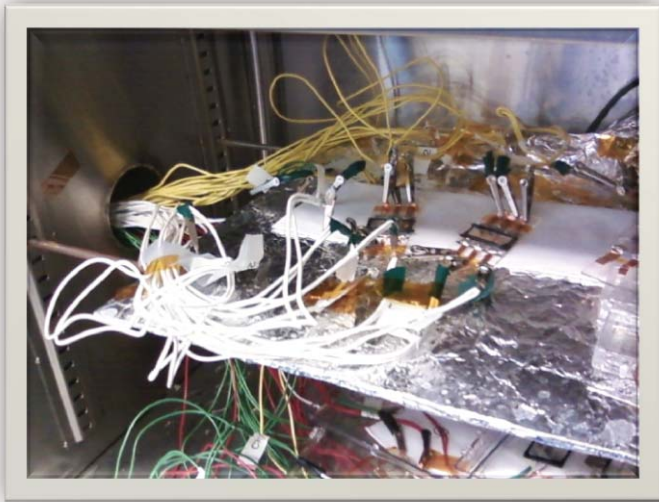


Figure 6. Taking resistance measurements of calcium samples in environmental chamber set to 50°C and 80% RH.



Figure 7. Image of two flexible plastic substrates sealed with a Poly-isobutylene sealant demonstrates the flexibility of this encapsulation method.

To accelerate the degradation effects, the environmental conditions were changed to 50°C and 80% RH in the controlled environmental chamber shown in Figure 6. As expected, the changes in the conditions resulted in a slightly higher WVTR of $2.0 \pm 0.5 \times 10^{-4}$ g/m² day.

The process was repeated once again. However, this time a 100 nm layer of SiN_x was deposited over the seal. This layer was added to observe how it would reduce the permeation. SiN_x was chosen because it can be deposited through Chemical Vapor Deposition (CVD) giving it a faster deposition rate than Al₂O₃, which is deposited through Atomic Layer Deposition (ALD), thus significantly reducing the duration of the deposition process.

The samples were placed in a room environment of 20°C and 60% RH. The calcium degradation test resulted in a WVTR of $3.5 \pm 0.5 \times 10^{-4}$ g/ m² day. The WVTR was higher than expected, showing that the SiN_x has very little positive impact on the WVTR. Uneven application of the sealant may explain the rates obtained. By increasing the environmental conditions to 50°C and 80% RH, the WVTR rose to $5.0 \pm 0.5 \times 10^{-4}$ g/ m² day.

Conclusion and Future Work

We were able to obtain a new sealant material having a WVTR near 10^{-4} g/m² day which is within the WVTR range of some organic electronics. This is the first such sealant which shows such promising behavior. We plan to measure the transmission rate of the sealant with a layer of Al₂O₃ in order to reduce the WVTR.

We plan to utilize different sealing techniques to reduce permeation. We also plan to do further investigation of this sealant to determine if it suitable for encapsulating flexible organic electronics with flexible substrates. This may open the door to a full scale production of flexible organic electronics.

References

1. N. Kim, W.J. Potscavage, Jr., B. Domercq, B. Kippelen, and S. Graham, Appl. Phys. Letts. 94, 163308 (2009)
2. Jay S. Lewis, Michael S. Weaver IEEE Vol. 10 No. 1 (2004)

Acknowledgements

Funds for this research were provided by the Center on Materials and Devices for Information Technology Research (CMDITR) and the NSF Science and Technology Center No. DMR 0120967.

Thanks to Kippelen research group at Georgia Institute of Technology for calcium samples.

Thanks to Tim O'Neil and ADCO Products, Inc. for providing the sealant.



GILBERTO ARREOLA is a mechanical engineering student at Cal-Poly Pomona. A rising sophomore, he has some time to decide what career path to pursue.

Synthesis of Donor-Acceptor Oligomers for Applications in Organic Field-Effect Transistors

KRISTEN BROWN, Georgia Institute of Technology

Lauren Hayden, Dr. Seth Marder, Institute of Technology

Introduction

With the present market for electronics rapidly expanding and changing, there has risen a necessity for new solution processible materials. The current devices used in the electronics industry, based on silicon (Si), are fabricated using complicated and expensive techniques such as vacuum deposition and photolithography. For certain applications, a viable and potentially cheaper alternative to Si transistors is seen in organic field-effect transistors (OFETs) which have potential for solution processibility and low-temperature deposition; this could eliminate the need for the expensive deposition and patterning techniques needed to fabricate the OFET's silicon analogues^{1,2}. Both of these properties of organic materials also allow for deposition on plastic or other flexible substrates, opening up new applications in areas such as electronic paper, sensors, and radio frequency identification cards (RFID)^{3,4}.

Organic transistors typically function using the same physical structure (shown in Figure 1) and basic charge transfer as their Si counterparts. In the current Si transistors, charge transfer occurs by applying a positive or negative voltage to the gate electrode that induces charge at the semiconductor/dielectric layer.⁵ Applying a positive voltage causes an accumulation of electrons in an n-type conducting material; applying a negative voltage causes accumulation of holes in a p-type material. The most commonly used Si transistors (complementary transistors) make use of both p- and n-doped Si as the semiconducting materials in a p- or n-channel transistor.

As the structure and function of OFETs are analogous to inorganic devices, it has become of interest to develop them with both p- and n-type semiconducting materials – the goal being to achieve performance comparable to that of complementary inorganic transistors. However, where traditional Si based transistors require doping by two separate p- and n-type sources, organic semiconductors allow the potential for function both p- and n-type depending on the bias of the gate voltage.⁵ Organic semiconductors of this type are called ambipolar.

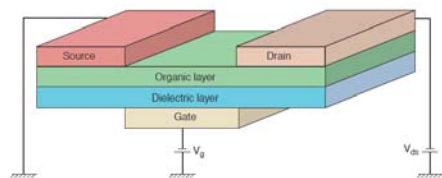


Figure 1. Bottom Gate contact FET

The ambipolar efficacy of organic materials depends on the ease of injection of holes or electrons from the gate electrode. The ease of injection is in part determined by the energy difference between the Fermi level (E_F) of the electrode and the highest occupied molecular orbital (HOMO) or the lowest unoccupied molecular orbital (LUMO) of the organic material. The smaller the difference between the HOMO or LUMO and the E_F , the easier injection becomes.^{5,6,7} Achieving ambipolar transport can be approached through carbon nanotubes, organic bilayers, blends of n- and p-type materials, and by using single-component ambipolar materials.⁵ The end goal of all approaches is to achieve efficient injection of both positive and negative charges into one device.

We are interested in the latter approach to ambipolar character – single component ambipolar materials. In order to achieve ambipolar character in an organic compound it is necessary to have a small band gap (approximately 1.8 eV)⁵ centered around the EF of the electrode. In organic molecules, a small band gap is typically achieved by the presence of conjugated aromatic systems resulting in extensive electron delocalization.^{5,8} However, the bond-length alternation of single and double bonds in conjugated systems results in an increase of the band gap. An additional contribution to an increase in band gap is a result of the energy differences in the resonance structures (aromatic and quinoid) of the aromatic system. Decreasing the band gap in organic materials can be accomplished by minimizing bond length alternation through extended conjugation and by employing the “donor-acceptor (D-A)” approach, among others. Both methods are used in organic polymer chemistry; however, in the case of oligomers (the focus of this project) the donor-acceptor method takes priority as no extended backbone is present.⁷

The consideration of oligomers originated as a result of the problems in synthesis, purification, and solubility associated with polymers. Though polymers exhibit a longer conjugation length than oligomers, which is known to lower the band gap, the necessary addition of alkyl chains to polymers in order to increase solubility frequently results in torsion of the backbone. This torsion leads to a disruption in conjugation and an increase in the band gap.⁹ Using oligomers, solubility can be increased without disruption of conjugation. By applying the D-A approach to oligomers, the problems faced in absence of extended conjugation can potentially be overcome.

The D-A model is typically used to overcome the energy differences between the quinoid and aromatic mesomeric structures. The interaction between a donor and an acceptor helps to accommodate the charges associated with the mesomerism ($D-A \leftrightarrow D^+=A^-$). This stabilizes the resonance energy and helps

decrease the band gap. In oligomers, though such mesomerization is not completely applicable, the D-A approach still has strong relevance. In materials with an alternating D-A pattern, there is a presence of strong intermolecular interactions. These interactions can lead to compact molecular packing, high charge carrier mobility, and high lattice energy.^{10,11} Calculations have also shown that a D-A pattern results in hybridization of the high-lying HOMO of the donor and the low-lying LUMO of the acceptor, resulting in a small band gap (shown in Figure 2)⁸. It is desirable, then, to use this D-A approach to create low band gap semiconductors.

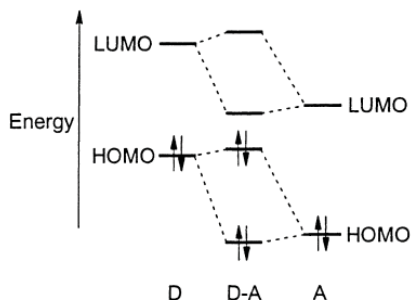


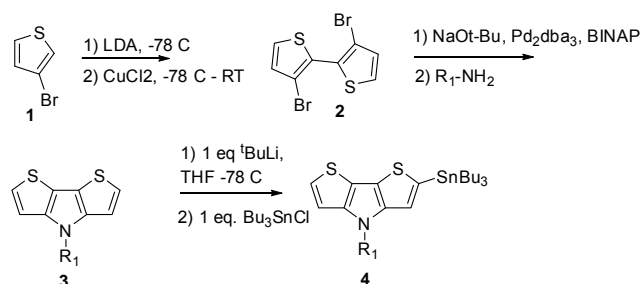
Figure 2. HOMO-LUMO separation from hybridization of the energy levels of a donor and acceptor.⁸

Donors and acceptors of increasing strength can be synthesized to further decrease the band gap by the addition of electron withdrawing groups on the acceptor and electron donating groups on the donor. Cyano (CN), nitro (NO₂), quinoxaline, and thiadiazole are typical electron withdrawing groups for the acceptor, and thiophene and pyrrole groups are used for the donors.⁹ This summer project focused on the use of thiadiazole- and quinoxaline-based acceptors and thiophene- and pyrrole-based donors to create alternating D-A oligomers, working towards low band gap, ambipolar materials for OFET applications.

Experimental

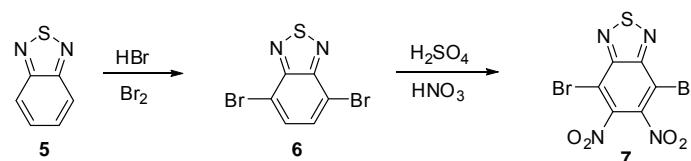
In order to achieve the desired D-A oligomers, the synthesized donor molecules were coupled with the precursor to the desired acceptor molecule using a Stille reaction.

The desired donor was synthesized (Scheme 1) by oxidative coupling of 3-dibromobithiophene to achieve 3,3'-dibromo-2,2'-bithiophene (2). Compound 2 then underwent a Buchwald-Hartwig reaction with the desired amine to give N-alkyl-4H-dithieno[3,2-b:2',3'-d]pyrrole (DTP, 3)¹². The isolated N-alkyl-2-(tributylstannyl)-4H-dithieno[3,2-b:2',3'-d]pyrrole (4) was achieved through a lithiation of 3 followed by addition of tributyltin chloride. Compound 4 was then fully characterized by ¹H NMR, ¹³C NMR, elemental analysis, and high resolution mass spectrometry.



Scheme 1. Donor Synthesis

The acceptor 7 was achieved (Scheme 2) by bromination of benzo[c][1,2,5]thiadiazole (BTD, 5) to yield 4,7-dibromobenzo[c][1,2,5]thiadiazole (Br₂-BTD, 6). The intermediate 7 can be obtained through a nitration reaction with fuming nitric acid and sulfuric acid.



Scheme 2. Acceptor Synthesis

Compound 4 was coupled to a sample of acceptor 7 (provided by Dr. Qing Zhang) using a Stille coupling¹³ to result in a precursor to the desired D-A oligomer.

Results

Following the successful Stille coupling of 7 and 4, the optical properties of the resulting oligomer were examined using UV-vis spectroscopy (Figure 2).

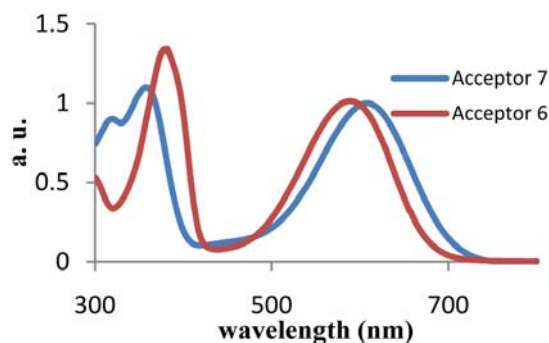


Figure 3. Absorbance spectra of D-A oligomers containing either compound 6 or 7 as the acceptor.

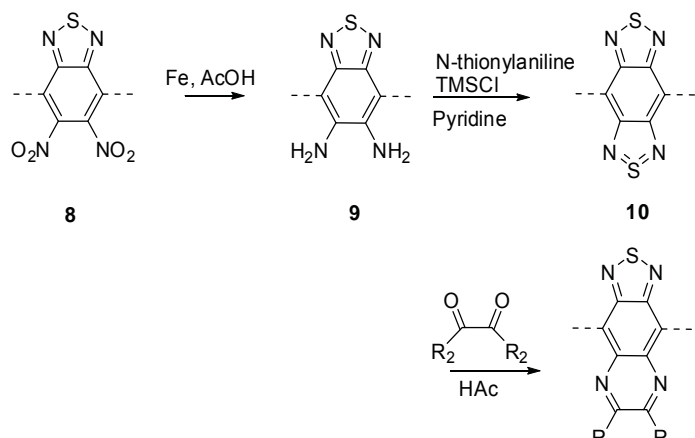
This red shift seen in the absorbance band of the nitrated oligomer is indicative of a smaller band gap. This is a result of the electron withdrawing nitro-groups on the Br₂-BTD that give the acceptor a more electron deficient character.

Conclusion

The precursor to the desired donor-acceptor oligomers was successfully synthesized and is currently under purification. Examining the optical properties using UV-vis has shown a desired decrease in band gap upon addition of electron withdrawing nitro-groups to the acceptor molecule.

Future Work

Two steps are left to achieve the desired D-A oligomer (Scheme 3). The nitrated Br₂-BTD ring 8 will be reduced to 9. The amine groups will then undergo one of two ring closures yielding either benzo[1,2-c:4,5-c']bis[1,2,5]thiadiazole 10 or [1,2,5]thiadiazolo[3,4-g]quinoxaline 11 (Scheme 3).



Scheme 3. Ring Closure

Once the desired oligomers have been synthesized and fully characterized using ¹H NMR, ¹³C NMR, elemental analysis, and high resolution mass spectrometry, their optical properties will be analyzed by a variety of methods including UV-vis and cyclic voltammetry before testing their performance in OFET materials.

References

1. Mas-Torrent Marta, et al. Chem Soc Rev. 2008, 37, 827-838.
2. Facchetti, Antonio, Materials Today, 2007, 10, 28-36.
3. Dimitrakopoulos, Christos D., et al., Adv. Mater. 2002, 14, 99-112.
4. Reese, Colin, et al. Materials Today, 2004, 7, 20-27.
5. Zaumseil, Jana, et al. Chem. Rev., 2007, 107, 1296-1323.
6. Anthopoulos, Thomas D.; et al. Adv Mater. 2004, 16, 2174-2179.
7. Meijer, E.J., et al., Nature. 2003, 2, 678-682.
8. Van Mullekom, H.A.m., et al., Materials Science and Engineering, 2001, 32, 1-40.
9. Bundgaard, E.; Sol. Energy Mater. Sol. Cells 2007, 91, 954-985
10. Sonarm, P., et al., Chem. Mater., 2008, 20, 3184.
11. Park, Y., et al., Org. Lett., 2006, 8, 4699.
12. Koeckelbergs, G., et al., Tetrahedron, 2005, 61, 687.
13. Steckler, Timothy T., et al., Chem. Commun., 2007, 46, 4904-4906.

Acknowledgements

Funds for this research were provided by the Center on Materials and Devices for Information Technology Research (CMDITR) and the NSF Science and Technology Center No. DMR 0120967. Special thanks to Lauren Hayden and Dr. Seth Marder.



KRISTEN BROWN is currently an undergraduate student at the Georgia Institute of Technology. Following the completion of her degree in chemical engineering, she hopes to enter graduate school in Fall 2010 to pursue a Ph.D. in organic chemistry.

Synthesis of Carbazole and Fluorene Conjugated Copolymers for Use in Organic Solar Cells and Organic Field Effect Transistors

ANESIA BURNS, University of Florida

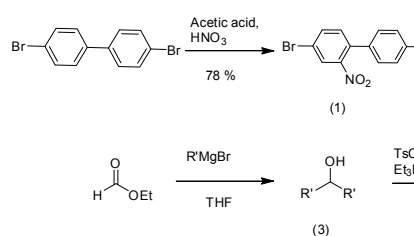
Raghunath R. Dasari, Seth R. Marder, Georgia Institute of Technology

Introduction

Research on conjugated polymers in the field of organic electronics has drawn much interest in recent years due to the potential inexpensive manufacturing processes and large area device applications. Conjugated polymers are polymers with delocalized π -electron systems capable of transporting charge and interacting efficiently with light. They share some electronic properties with inorganic semiconductors yet still retain the mechanical properties of polymers. The degree of overlap between π -orbitals on the polymeric backbone largely determines the electronic and optical properties of conjugated polymers. The advancement in this field has been limited due to the moderately large bandgap and low carrier mobilities of polymeric materials. The band gap, which is the energy gap between the highest occupied molecular orbital (HOMO) and lowest unoccupied molecular orbital (LUMO) is one of the key factors that determine the electronic and optical properties of conjugated polymers. The HOMO-LUMO gap can be controlled, to a degree, by structural modification and this can be used for achieving absorption with a broader range of solar spectrum.¹⁻⁵ The synthesis of new low bandgap conjugated polymers with alternating donor and acceptor groups constitute an attractive option because these may exhibit a low band gap and absorption bands in the visible/near infrared region due to donor-acceptor interaction. To further improve device performance, it is important to create new polymeric structures and analyze and understand their optical, electronic and morphological behavior. Both carbazole and fluorene derivatives shown great promise for use in organic solar cells and organic field-effect transistors (OFETs) since they have the potential to have band gaps of less than 2 eV. The goal of this research is to synthesize new polymeric architectures with carbazole and fluorene derivatives as donor blocks and various electron-deficient compounds as acceptor blocks.

Experimental

The first step in the synthesis of the donor-acceptor co-polymers was the synthesis of the monomers blocks. The scheme for the synthesis of carbazole donor block is shown below.



Scheme 1. Synthesis of 2,7-dibromo-9-alkyl-9H-carbazole.1, 7

4,4'-dibromo-2-nitrobiphenyl (1): Fuming HNO_3 (142.5 mL) was added slowly over a period of 45 minutes to a stirring solution of 4,4'-dibromobiphenyl (30.0 g, 96.15 mmol) and acetic acid (450 mL) at 100 °C. The solution was stirred at 100 °C for 10 hours. Upon cool down to room temperature, water was added to the flask and the resulting yellow paste was collected by filtration. The desired pure compound was obtained after recrystallization from ethanol as a yellow powder (26.91 g, 78.4%).

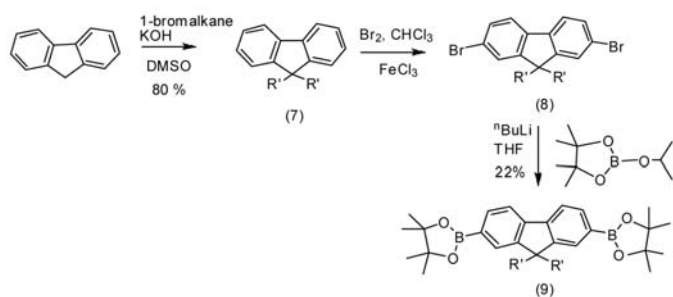
2,7-dibromocarbazole (2): A flame-dried two neck round bottom flask was filled with 25.91 g (72.57 mmol) of 4,4'-dibromo-2-nitrobiphenyl. Triethyl phosphite (93.5 mL) was added to the flask by syringe. The mixture was heated to 160 °C for 22 hours and then left to cool down. The excess triethyl phosphite was removed by distillation and the product was purified by silica gel column chromatography with 5-10% ethyl acetate in hexanes to yield light brown crystals (7.45 g, 31.3%).

Alcohol (3): A three-neck flask was charged with 8.04 mL (100 mmol) of ethyl formate and 146 mL of tetrahydrofuran. The solution was cooled to -77 °C with a dry ice and acetone bath. Alkylmagnesium bromide (300 mL) was added dropwise to the flask in an addition funnel. Upon the completion of addition, the solution was stirred overnight at room temperature. The mixture was poured into a separation funnel, water and diethyl ether was added and the layers were separated. The organic layer was collected and dried over sodium sulfate and the solvent was removed under reduced pressure to yield white crystals (crude product: 28.4 g).

Alkyl p-Toluenesulfonate (4): In a three neck round bottom flask, compound 3 (10.0 g), trimethylamine hydrochloride (3.72 g, 39.0 mmol) and dichloromethane (39 mL) was cooled to 0 °C in an ice bath. A solution of 11.13 g (48.5 mmol) of p-toluenesulfonyl chloride in dichloromethane (39 mL) was added to the flask dropwise by an addition funnel. The mixture was left to stir overnight at room temperature. The mixture was quenched with water and extracted with CH_2Cl_2 . The organic layer was washed with a brine solution and dried over sodium sulfate. The product was purified using a silica gel column eluted with 90% hexanes and 10% ethyl acetate. The solvent was removed under reduced pressure to yield a colorless oil (11.11 g, 69.4%).

N-9'-alkyl-2,7-dibromocarbazole (5): Crushed potassium hydroxide (5.712 g, 102 mmol) was quickly added to a three neck round bottom flask along with 6.67 g (20.4 mmol) of 2,7-dibromo-9H-carbazole. A solution of 10.90 g compound 4 and 32 mL dimethyl sulfoxide (DMSO) was added over 2 hours to the flask at room temperature. The reaction was allowed to stir overnight at room temperature. It was then separated with water and hexane using a separation funnel. The product was in the hexane layer which

underwent rotary evaporation and purified by silica gel column chromatography eluted with hexanes. The pure product was then obtained as a white solid (6.212 g, 93.1%).



Scheme 2. Synthesis of 2,7-Bis(4,4,5,5-tetramethyl-1,3,2-dioxaborolan-2-yl)-9,9-dialkylfluorene.6, 8

2,7-Bis(4',4',5',5'-tetramethyl-1',3',2'-dioxaborolan-2'-yl)-N-9'-alkylcarbazole (6):

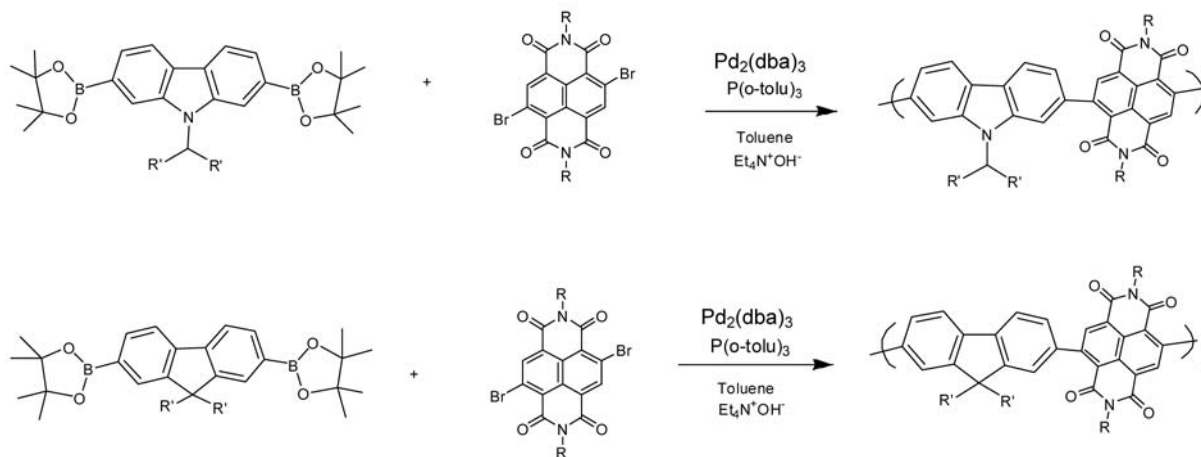
A flame-dried three neck round bottom flask with a thermometer attached was filled with 1.009 g of 5. Tetrahydrofuran (17.80 mL) was added and the flask was placed into a dry ice and acetone bath to cool to -78 °C. Slowly added to the flask was 1.455 mL n-butyl lithium (2.5 M in hexane). The reaction was stirred for approximately 1 hour at -78 °C before 2-isopropoxy-4,4,5,5-tetramethyl-1,3,2-dioxaborolane (0.80 mL, 4.25 mmol) was added. The reaction was then left to stir for an additional hour at -77 °C and then at room temperature overnight. The mixture was poured into a separation funnel where water and diethyl ether was used to wash the product. The diethyl ether layer was collected and dried over magnesium sulfate. The product was recrystallized twice from a 10:1 methanol and acetone solvent mixture to yield a white crystal (0.66 g, 55.2%).

The scheme for the fluorene donor block synthesis is shown below. Synthesis of the fluorene monomer started with a commercially available fluorene compound.

9,9-dialkylfluorene (7): Fluorene (25 g, 150 mmol) and potassium hydroxide (84.25 g, 1504 mmol) were added to a 250 mL three neck round bottom flask. In an inert atmosphere 125 mL DMSO was added by syringe to the flask. The mixture was left to stir for 15 minutes before 58 mL of 1-bromoalkane was added to the rest of the solution. The reaction was left to stir overnight. The reaction was then quenched with water and extracted with ethyl acetate. The product, which was in the ethyl acetate layer, was washed with brine solution and dried over sodium sulfate. The product was purified by silica gel column using hexane as an eluent to yield a pale brown solid (47.11 g, 80.15%).

2,7-dibromo-9,9-dialkylfluorene (8): A three neck round bottom flask was charged with 37.16 g of compound 7. Chloroform (100 mL) was added by syringe and the solution was cooled to 0 °C. After 15 minutes, 0.236 g (1.46 mmol) of ferric chloride was added along with 20 mL chloroform. Bromine (10.25 mL, 79.90 mmol) was added dropwise over 20 minutes. The mixture was taken out of the ice bath and left to warm to room temperature. After 4 hours, the solution was quenched with sodium thiosulfate and washed with water and chloroform. The product was separated in a separatory funnel with chloroform and was purified by silica gel column chromatography with hexanes. The pure product then underwent rotary evaporation. The crude product yield 56.5 g.

2,7-Bis(4,4,5,5-tetramethyl-1,3,2-dioxaborolan-2-yl)-9,9'-dialkylfluorene (9): A flame-dried three neck round bottom flask with a thermometer attached was filled with 2.4 g of compound 8. Tetrahydrofuran (44 mL) was added and the flask was placed into a dry ice and acetone bath to cool down to -78 °C. Slowly added to the flask was 3.69 mL n-butyllithium (2.5 M in hexane). The reaction was stirred for approximately one hour before 2-isopropoxy-4,4,5,5-tetramethyl-1,3,2-dioxaborolane (2.02 mL, 9.908 mmol) was added. The reaction was then left to stir for another hour at -78 °C before it was warmed to room temperature and stirred overnight. The mixture was poured into a separation funnel along with water and diethyl ether the layers were separated. The organic layer was collected and dried over magnesium sulfate. The solvent was then removed under reduced pressure to obtain white solid. The product was purified by recrystallization with hexane to yield white crystals (0.649g, 22%).



Scheme 3. Synthesis of donor-acceptor co-polymers using carbazole and fluorene monomer blocks with naphthalene bisimide acceptors.

Results and Discussion

The synthesis of the desired carbazole donor block was achieved in six steps from the starting material, 4,4'-dibromobiphenyl starting. In the synthesis of carbazole-boronic ester monomer 5 (Scheme 1), the synthesis of compound 2 was repeated several times due to the low yields. The fluorene monomer block synthesis is outlined in Scheme 2. Fluorene (compound 9) was treated with 1-bromo alkane and potassium hydroxide to obtain compound 7. Compound 7 upon further bromination resulted in predominantly in the dibromo fluorene derivative but a tribromo fluorene was also found as a minor compound. These compounds had similar Rf values and isolation by column chromatography was difficult. The pure product of compound 8 was followed by the incorporation of boronic ester groups that was able to produce the desired fluorene monomer 9. Monomers 5 and 9 were then further copolymerized with the naphthalene bisimide acceptor under Suzuki coupling conditions (Scheme 3).

The absorption spectra of the crude polymeric samples in toluene (figures 4 and 5) show high energy absorption bands in the range of 250-400 nm and broad absorption bands between 400 – 600 nm for each copolymer.

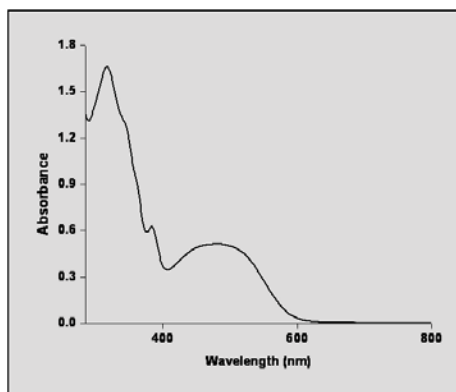


Figure 4. UV-Vis absorption spectrum of a carbazole-based copolymer

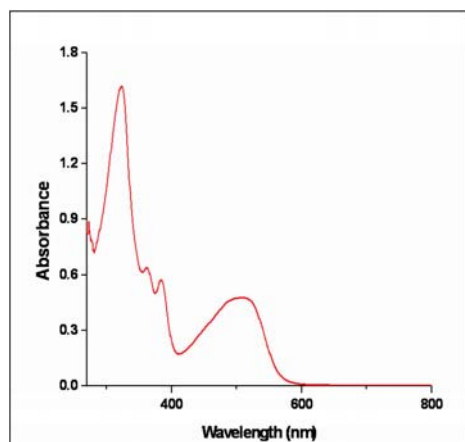


Figure 5. UV-Vis absorption spectrum of a fluorene-based copolymer

Conclusion

The carbazole and fluorene donor monomers were synthesized on a small scale. The donor and acceptor copolymers showed a broad absorption between 400-600 nm. Purification and complete characterization of the copolymers is presently ongoing. Once completed, the newly synthesized polymeric materials' optical and electronic behavior in organic solar cells and OFET devices will be examined.

References

1. Blouin, N.; Michaud, A; Leclerc, M.; Adv. Mater. 2007, 19, 2295-2300
2. Blouin, N.; Michaud, A; Gendron, D. et al, J. Am. Chem. Soc. 2008, 130, 732-742
3. Gunes, S.; Neugebauer, H.; Sariciftci, N. S. Chem. Rev. 2007, 107, 1324-1338
4. Thompson, B. C.; Frechet, J. M. J. Angew. Chem. Int. Ed. 2008, 47, 58
5. Van Mullekom, H.A.M et al. Mater. Sci. and Eng. 2001, 32, 1-40
6. Ranger, M.; Rondeau, D.; Leclerc, M. Macromolecules 1997, 30, 7686-7691
7. Dierksch, F.; Grimsdale, A.; Mullen, K. Synthesis 2003, 16, 2470
8. Liu, S. et al. Chem. Eur. J. 2006, 12, 4351-4361

Acknowledgments

Anesia Burns would like to acknowledge the Chemistry and MDITR Staff, Dr. Seth Marder, Dr. Raghunath R. Dasari, Dr. Cam Tyson, Dr. Keith Oden, Olanda Bryant, Denisha Thomas; The authors would like to acknowledge the support of grants: Center on Materials and Device for Information Technology Research (CMDITR), NSF Science and Technology Center No. DMR 0120967.



ANESIA BURNS' educational goals include earning a bachelor's degree in Materials Science and Engineering with a specialty in polymers, two minors in sales engineering and business administration, and a Ph.D in polymers. She hope this experience will help me reach her goal of becoming a professor.

Synthesis of Crosslinkable Hole Transporting Polymers for Organic Light Emitting Diodes (OLEDs)

IGOR COROPCEANU, Georgia Institute of Technology

Carlos Zuniga, Dr. Seth Marder, Georgia Institute of Technology

Introduction

Light emitting diodes (LEDs) have been one of the most intensively studied fields of materials science during the past half century, as a result of which, great strides have been made in the understanding of the principles underlying their operation and in their implementation into a wide range of devices.¹ While initial research on LEDs focused exclusively on inorganic materials, the discovery of efficient luminescence in organic compounds (originally in anthracene) spawned the new subfield of organic light emitting diodes (OLEDs).² The advantages presented by OLEDs over their inorganic analogs, most notably their significantly lower cost, greater physical flexibility, and high tunability were readily seen and generated much interest in the new field.² Nevertheless initial efforts to develop viable OLEDs were greatly hindered by certain deficiencies characteristic to these devices, most importantly, their low efficiency.

The problem of efficiency was greatly reduced by the introduction of multilayer devices. Whereas the earliest OLEDs consisted of a single emitting layer, new devices containing an emitting layer sandwiched between additional layers with suitable hole and/or electron transporting properties proved to be capable of significantly improving external quantum efficiency (the ratio of the radiative energy to the energy input).³ The basic structure of such multilayer devices usually consists of a transparent anode (usually Indium Tin Oxide (ITO)) deposited on a glass substrate, followed by a hole transport layer (HTL), and emitting layer (EML), an electron transport layer (ETL), and finally the cathode as depicted below⁴:

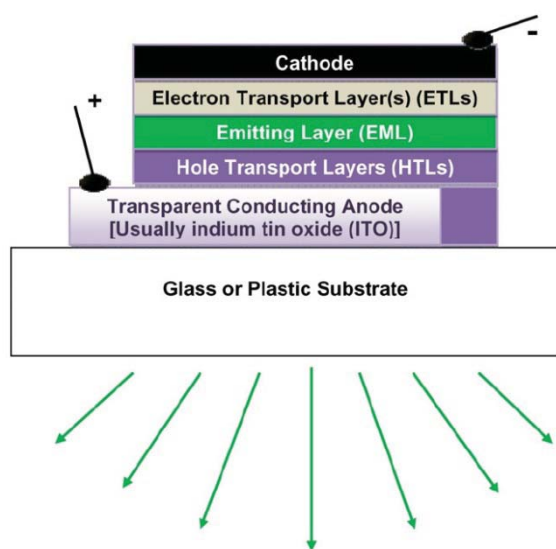


Figure 1

The sequential deposition of the distinct layers is a problematic aspect of OLED construction. Two general methods exist for the addition of the layers: 1) vacuum deposition and 2) solution processing.³ The former method is well-suited towards the fabrication of small devices, however it is difficult to extend to large surface areas and is associated with a high fabrication cost. On the other hand, the latter method can be less expensive and is more amenable to larger surfaces. However, one significant problem encountered in the deposition of solution processed layers is that the previous layer could be dissolved by the solvent in which the new layer is processed.

Three approaches have been developed to address this problem³:

- usage of orthogonal solvents for successive layers,
- change of polarity of a precursor in a certain layer
- usage of crosslinkable polymers.

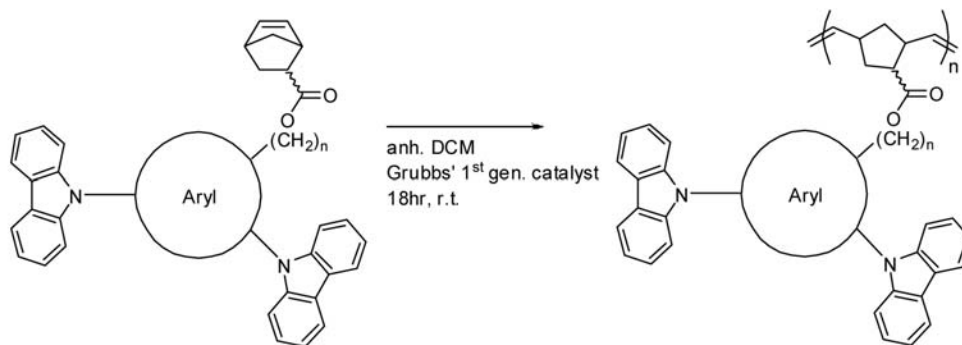
The first method involves choosing the materials making up the layers of a device in such a way that the solvent in which one layer can be processed will not dissolve the layer immediately below it. However, this approach can often be impractical due to the difficulty of finding a set of materials fulfilling this solubility criterion. The second approach has also proven to be of limited applicability.³

The third method involves first depositing a polymer in solution (e.g. by spin coating), then inducing crosslinking (the formation of covalent bonds between polymer chains) by exposing the material to ultraviolet irradiation or to high temperatures. The effect of the crosslinking is to insolubilize the layer affected, thus making it compatible with any solution processed layer deposited above it. As a result, much work is currently being dedicated to the development of crosslinkable materials that display the physical properties requisite of a specific OLED layer.³

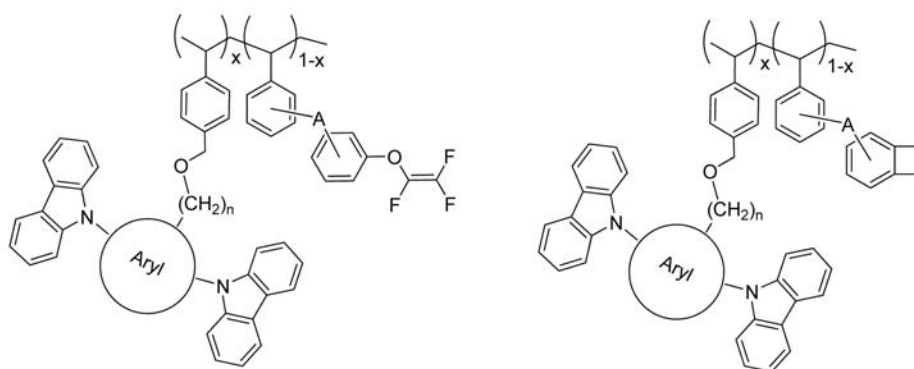
Experimental

The goal of the project was the synthesis of a series of hole-transporting crosslinkable polymers. In the first part of the project, an already known homopolymer was scaled up. The monomer was synthesized through the esterification of a carboxylic acid with the starting alcohol (provided by Carlos Zuniga). This compound was then polymerized in a reaction catalyzed by Grubbs' 1st generation catalyst (see Scheme 1).

In the second part of the project, the goal was to create two new copolymers (see Scheme 2), each containing two side chains, one with a hole transporting (HT) group attached and the other having a thermally crosslinkable group attached. Two types of thermally crosslinkable groups were used: the trifluorovinyl ether (TFVE)



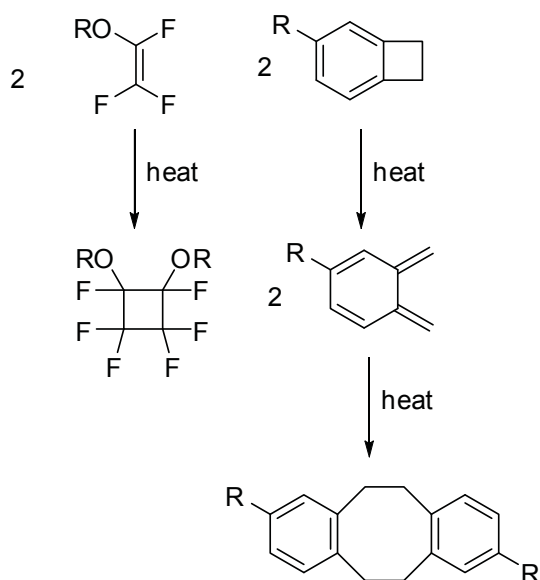
Scheme 1



Scheme 2

Trifluorovinyl Ether:

Benzocyclobutene:



Scheme 3

group and the benzocyclobutene (BCB) group, whose incorporation into crosslinkable OLED materials had been previously described by Jen et al., and Fréchet et al. respectively.^{5,6} The crosslinking reactions for the two groups are displayed in Scheme 3.

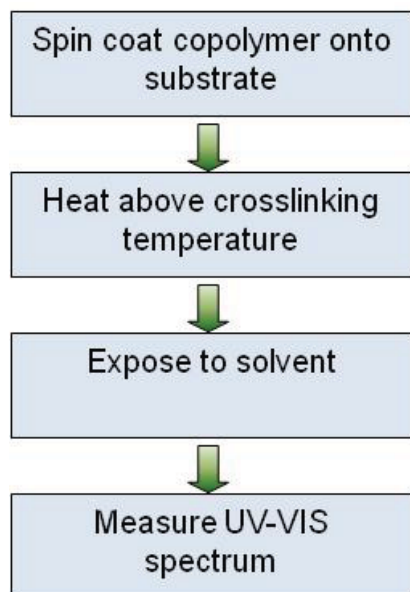
Three monomers were required for the synthesis of the two copolymers:

1. A known hole transporting (HT) styrene-based monomer
2. A new crosslinkable trifluorovinyl ether styrene-based monomer
3. A new benzocyclobutene styrene-based monomer

All three comonomers have been successfully synthesized, purified, and their identity has been verified using ¹H NMR. Furthermore, the ¹³C NMR and mass spectra of the two new monomers have been taken and samples have been sent for elemental analyses.

Future Work

In future work, the copolymers illustrated in Scheme 2 will be synthesized. Once their synthesis is complete, thin films will be produced from the two copolymers. The films will then be subjected to crosslinking evaluation, in a process outlined in Scheme 4 below:



Scheme 4

The concentration of copolymer on a substrate can be determined from its corresponding UV-VIS spectrum. By comparing the reference spectrum (no solvent exposure) to samples exposed to the solvent for various durations, one can determine the level of solvent resistance of the samples, which in turn can be viewed as an indicator of the crosslinking effectiveness.

Finally, depending on the results of the crosslinking evaluation, the materials could be transferred to the Kippelen group where they will be incorporated into OLED devices, which will undergo further studies.

References

1. Schubert, F., E; Gessman, T.; Kim, J. K. In Organic Light-Emitting Devices: Synthesis, Properties, and Application Muellen, K., Scherf, U., Eds.; WILEY-VCH Verlag GmbH & Co.: Weinheim, 2006.
2. Pfeiffer, M.; Forrest, S. In Nanoelectronics and Information Technology: Advanced Electronic Materials and Novel Devices; Waser, R., Ed.; WILEY-VCH Verlag GmbH & Co. KGaA: Weinheim, 2003.
3. Meerholz, K.; Mueller, C.-D.; Nuyken, O. In Organic Light-Emitting Devices: Synthesis, Properties, and Applications Muellen, K., Scherf, U., Eds.; WILEY-VCH Verlag GmbH & Co.: Weinheim, 2006.
4. Shinar, J.; Shinar, R. J. Phys. D: Appl. Phys 2008, 41.
5. Liu, S.; Jiang, X. Z.; Ma, H.; Liu, M. S.; Jen, A. K. Y. Macromolecules 2000, 33, 3514-3517.
6. Ma, B.; Lauterwasser, F.; Deng, L.; Zonte, C. S.; Kim, B. J.; Frechet, J. M. J. Chem. Mat. 2007, 19, 4827-4832.

Acknowledgements

Funds for this project were provided by the Center on Materials & Devices on Information Technology Research (MDITR) the National Foundation of Science (NSF) No.DMR 0120967. I would like to give special thanks to Carlos Zuniga for his help and guidance during the entire program. I also wish to thank Dr. Marder for giving me the opportunity to experience research in his laboratory. Finally, I would like to thank everyone in the Marder group for their support.



IGOR COROPCEANU is a rising junior majoring in chemistry at the Georgia Institute of Technology. He intends to pursue graduate studies in the field of physical chemistry.

Pyranine Dyed Triglycine Sulfate: A New Dyed Crystal for Single Molecule Microscopy

ANDREA M. DE LA GARZA, Heritage University

Erin Riley, Philip Reid, University of Washington

Introduction

Fluorescence intermittency, also known as “blinking,” is the observation that a fluorescent molecule under continuous excitation will undergo emissive and non-emissive periods. Understanding why single molecules (SM) blink is an area of interest in materials science because blinking is believed to be a pathway for photodecomposition, a process that limits the development of chromophore based materials. A firm understanding of the blinking process would lead to the production of more robust chromophore based materials, as well as advances in uses of SM as probes for chemical and biochemical phenomena¹.

Crystals have been used as a host material in the Reid Lab to study the photophysics of SM. During growth, dye molecules are oriented and overgrown within the crystal lattice, creating an environment that is both ordered and oxygen impermeable, thereby reducing photo-oxidation. Photo oxidation is a pathway for irreversible photodecomposition, which reduces the number of fluorescence cycles that can be observed. Both of these qualities make dyed crystals unique from most SM/ host systems where dye molecules are deposited on glass or in a polymer, environments that are highly disordered, and exposed to the atmosphere. Currently the host crystal used is potassium acid phthalate (KAP) due to its flexibility for incorporating dyes of varying size, shape, and chemical affinities^{2,3}. This pioneering work is just beginning to answer questions regarding the nature of interactions between SM and the crystal lattice, such as the role of environmental fluctuations and what excited state reaction pathways lead to SM non-emissive states.

To better address these questions, a new crystal, Triglycine sulfate (TGS) will be studied. TGS has similar characteristics as KAP, in which they are both capable of being produced from aqueous solutions and incorporate a variety of organic luminophores². TGS is a ferroelectric crystal commonly used for Infra-Red (IR) sensing. It can be easily incorporated into a circuit, and its polarization altered by an applied voltage. We will use these properties to investigate the importance of fluctuations in the surrounding dielectric on excited state photophysics by externally driving polarization switches within the crystal. Recently, the lab has dyed TGS with pyranine, a new probe for single-molecule studies for which excited state reactions are well understood, providing a system that is dynamic, but whose chemistry is much more predictable.

This research provided initial characterization of the reaction dynamics of pyranine in TGS. Pyranine is known to undergo excited state proton transfer (ESPT) in solution. We need to determine if pyranine undergoes ESPT in TGS. If so, pyranine will be used to monitor the ESPT between the dye and the crystal by filtering the

fluorescence from its two protonation states, which are spectrally well resolved. This will allow us to monitor an ancillary reaction that doesn't result in a non-emissive state, giving us insight into excited state reactions of SMs. In order to do so, chromophore orientation and characterization of a pyranine dyed TGS crystal must be performed. This is necessary to guide the experimental set up for SM studies, and interpret results.

The solution phase optical titration of pyranine is presented as well as a discussion of the excited state proton transfer properties of pyranine. The crystal growth optimization for obtaining heavily dyed crystals of TGS is discussed, and the orientation of the dye in different sectors of the crystal as determined by fluorescence microscopy is presented.

Experimental Methods

Absorbance spectroscopy was used to determine the molar absorptivity of both the protonated and deprotonated forms of pyranine. Absorbance and fluorescence spectra of pyranine were acquired in aqueous solution as a function of pH with a constant concentration 2.5×10^{-5} M dye. The pH was adjusted by mixing solutions of pyranine in dilute sulfuric acid (0.01M), and in sodium hydroxide (0.01M) solutions. The pH was determined using a Vernier labquest outfitted with a pH electrode.

When developing a process to grow single crystals for SM, quick growth from highly superaturated solution was most successful in obtaining heavily dyed crystals. This was supported by the fact that impurities (dopants) are capable of being added and homogeneously dispersed and large percentages grow in crystals⁴. Pyranine dyed TGS seed crystals were produced in two supersaturated solutions containing the density of (40g/100mL H₂O). Growth was performed by mixing 3 mol glycine: 1 mol H₂SO₄ in an appropriate amount of water. One growth development took place in a controlled environment, a water bath, while the other grew in the uncontrolled lab environment. Approximately six seeds were collected from these solutions and stored. These exact two TGS-pyranine solutions were then re-dissolved and approximately three seed crystals were added to each solution. They were then placed back in their designated environments. The following day the solutions had produced pyranine dyed TGS crystals that were approximately 1.5 cm in their longest dimension.

The orientation of the dye in the crystals were determined by fluorescence microscopy. In this experiment the excitation source is a halogen lamp that was fitted to a microscope. The excitation source was filtered using a 405 nm (10nm FWHM) band pass filter and bounced into the microscope objective (20x) with a 420 long pass dichroic mirror. The back collected fluorescence was filtered

with a 430 emission filter, passed through a rotatable polarizer, and focused onto an optical fiber coupled to an ocean optics spectrometer. The crystals were oriented such that an optical axis was aligned with the pass direction of the polarizer at 0°, this was then rotated every 15°. The approximate orientation of the dye is determined from the maximum angle of the fluorescence intensity.

Results and Discussion

Solution phase characterization of pyranine dye was performed to assess the approximate acidity of the ground and excited states of the dye. First, the molar absorptivities of the dye were determined to be 23,200 M⁻¹ cm⁻¹ and 25,900 M⁻¹ cm⁻¹ at 404 nm (protonated) and 454 nm respectively, using serial dilutions and Beer's law. Optical titration of the dye was performed with both absorbance and fluorescence spectroscopy. From the absorbance and excitation spectra, which report on the ground state electronic structure and populations of the dye, (figure 1) we were able to determine that the pKa of the ground state is approximately 7.3. The emission spectra report on the excited state structure and relative populations of the dye. As can be seen in figure 2, despite the fact that the dye resides in the protonated state in the ground state, and that the protonated species is being selectively excited, the emission spectrum of the excited state is predominately that of the deprotonated species. Since only a small amount of the acidic spectrum is apparent at the lowest pH value, we've approximated the excited state pKa to be close to 1.

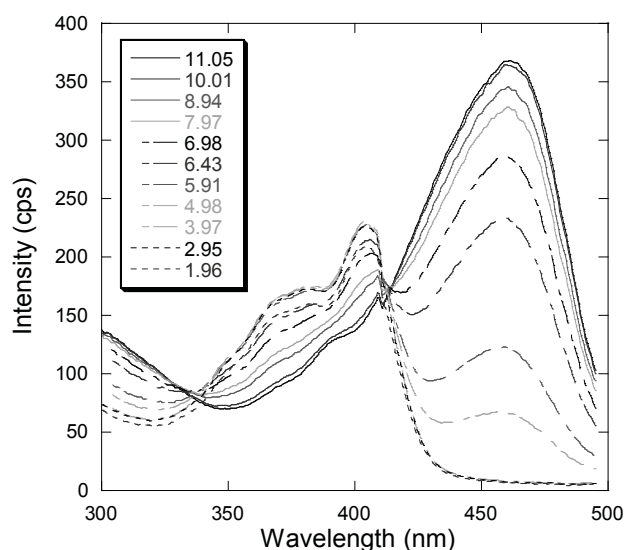


Figure 1: Fluorescence emission spectra of Pyranine dye λ excitation = 404nm.

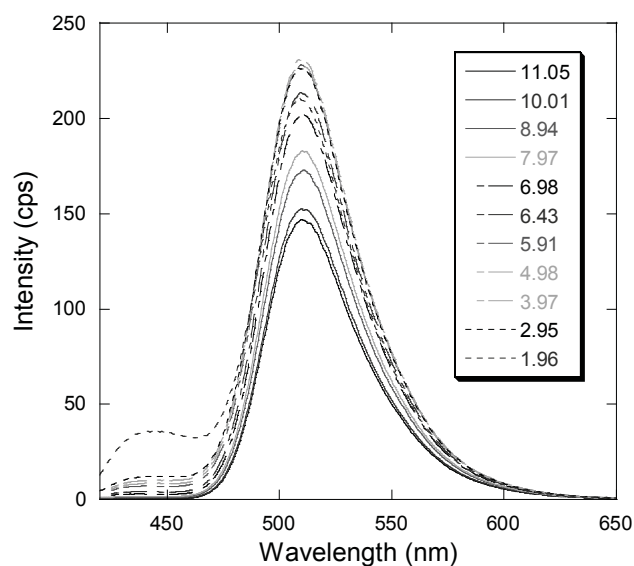


Figure 2: pH dependent fluorescence emission spectra of Pyranine dye λ excitation = 404nm

A schematic for the proton transfer cycle is demonstrated in figure 3. The main characteristic of a photoacid is that the excited state is more acidic than the ground state. The dye loses its proton before the emission of a photon to return to the ground state, whereupon its proton affinity changes and it can regain its proton.

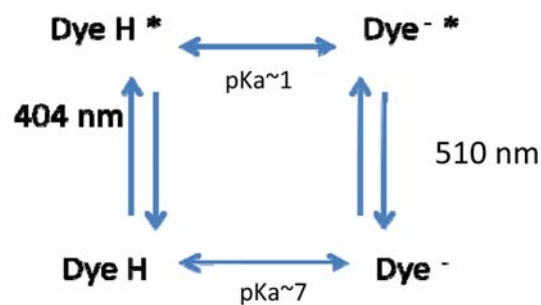


Figure 3: Protonation and deprotonation states of pyranine dye

TGS is grown from an acidic solution of sulfuric acid and glycine. The dye should predominately be in the protonated in the ground state. TGS contains hydrogen bonds that should interact with the exchangeable proton in pyranine. In order to understand the dye incorporation, and its possible substitution into this hydrogen bonding network, we set out to determine the orientation of the dye in the crystal. Figure 4 is a dark field image of a pyranine dyed crystal of TGS. Several colors are apparent in the crystal, as well as dark portions. This indicates that certain sectors of the crystal uptake the dye with chemical specificity, the differing colors indicate that different populations of the dye are present in different sectors.

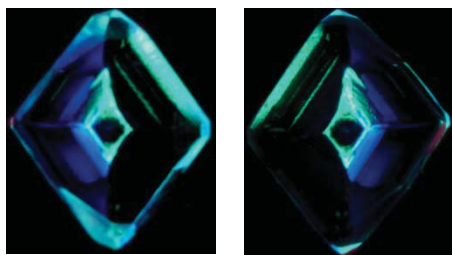


Figure 4: fluorescence dark field image of pyranine dyed TGS crystal as viewed from top and back

The orientation of the dye's fluorescence transition dipole moment was determined in two planes using fluorescence microscopy. TGS possesses a cleavage plane perpendicular to the (010) axis. Once the fluorescence spectra were acquired with the light propagation along the (001) direction, the crystal was cleaved to observe the fluorescence along this other axis. This data will be used later to determine the orientation of the molecule within the lattice. Results are shown in figure 5.

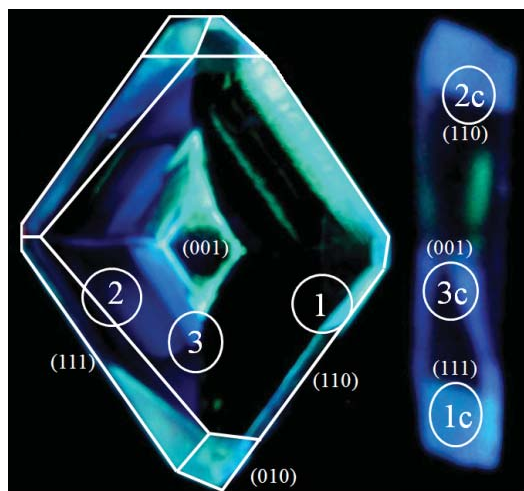


Figure 5: fluorescence dark field image of dyed TGS crystal. Sectors used for data collection. Table 1 portrays angle of highest fluorescence intensity. Orientations are 0° , 90° 0° from (010) for sectors 1, 2 and 3 respectively. And 0° , 15° , and 37.5° from (001) for sectors 1c, 2c, and 3c taken in the cleaved portion.

Conclusion

Solution phase characterization of the optical properties of pyranine dye was performed lending insight into the photoacid properties of the dye. The dye is much more acidic in the excited state, as can be seen by comparing the excitation and emission spectra. The orientation of the dye was determined within TGS crystals using a fluorescence microscope. Future research will be to establish the ESPT of the dye within the crystal, as well as the mechanisms for dye incorporation and the interactions between the dye and the lattice will be deduced from orientation data. Single molecule spectroscopic measurements will be carried out in the near future, leading to better understanding of excited state reactions, and eventually to the engineering and production of more photo-robust materials.

References

1. Cichos, F.; von Borczyskowski, C.; Orrit, M., Power-Law Intermittency of Single Emitters. *Curr. Opin. Coll. Inter. Sci.* 2007, 12, 272–284.
2. Kahr, B.; Gurney, R. W., Dyeing crystals. *Chemical Reviews.* 2001, 101 (4), 893-951.
3. Vetter, W.M.; Totsuka, H.; Dudley, M.; Kahr, B., The perfection and defect structure of organic hourglass inclusion K₂SO₄ crystals. *Journal of Crystal Growth.* 2002, 241 (4), 498-506.
4. Pamplin, B.R. (1980). *Crystal Growth.* Elmsford, New York: Pergamon Press Ltd.

Acknowledgements

I would like to acknowledge the Center on Materials and Devices for Information Technology Research (CMDITR), the NSF Science and Technology Center No. DMR 0120967. I would also like to thank Erin Riley and the Reid group for their support throughout this project.



ANDREA M. DE LA GARZA is currently a Chemistry major at Heritage University. She intends on pursuing her Ph.D. in Pharmaceutical Chemistry after completion of her undergraduate studies.

Electrostatic Force Microscopy of Photogenerated Charge Carriers in Thin Films of Poly(3-hexylthiophene) / Fullerene Blends

EMILITA DIAZ, Valencia Community College

Nasser Peyghambarian, Jayan Thomas, Palash Gangopadhyay, University of Arizona

Introduction

An organic solar cell converts photon flux from the sun into electron/hole electrical current using organic materials as the (photo) active ingredient. The basic structure of a typical organic solar cell includes an active layer where light is absorbed and converted into free charges and a set of contact electrodes to extract the charges. Given the relatively small dielectric constant of organic materials, light absorption in the active layer creates deeply bound excitons (electron/hole pairs) that do not dissociate into free charges. For charge generation, these excitons must diffuse to an interface between materials possessing different electron affinities and be pulled apart. However, these excitons can only travel to a certain distance before recombining back to neutral specie; in effect, the charges need to be extracted before the recombination happens. Generation to recombination, this length is called the exciton diffusion length. Typically, organic materials have *exciton diffusion lengths* in the order of 5-10 nm.

One of the most successful solutions in overcoming the excitonic bottleneck has been to make bulk heterojunction (BHJ) solar cells where the organic donor and acceptor materials are nanoscopically mixed throughout the active layer in an interpenetrating network of donor and acceptor phases. Polymer donor system such as regioregular poly(3-hexyl)thiophene (P3HT) has been studied extensively and has shown power conversion efficiencies up to 6.5% in BHJ configuration.^{1,2} Fullerenes and their derivatives have proven to be the most efficient acceptors, with C60 having a higher acceptor strength than the fullerene derivatives PCBM and BM-C60.³

The goal of this study is to use electric force microscopy (EFM) to investigate the morphology of blend films made from P3HT and C60 under various processing conditions, and the influence of different P3HT/C60 concentrations on photoexcited charge generation.

Experimental Procedures

P3HT and C60 were obtained from Aldrich and MER Corporation respectively and were used without further purification. Anhydrous 1,2-dichlorobenzene (1,2 DCB) from Aldrich was used as solvent to prepare four solutions with overall concentration of 2 wt% and P3HT / C60 ratios of 1:0.5, 1:1, 1:2, and 1:3. 1"×1" glass substrates were cleaned by progressive sonication in acetone, ethanol, and isopropanol, each for 40 minutes, then dried under reduced pressure overnight and were stored inside a desiccator under reduced pressure until used. The Laurell WS-650SZ-6NPP/LITE spin processor was used in fabricating all of the spun coat samples. All solutions were sonicated for 1 hour followed by

warming up in a water bath at 75°C. All samples were spun coat at 1000 rpm spin speed with 500 rpm/s acceleration for 2 minutes followed by a 3000 rpm with 1000 rpm/s acceleration for 2 minutes. For some of the samples a solvent rich environment was created inside the spin processing chamber by placing multiple Kimwipes™ soaked with 1,2 DCB. Solutions were filtered while hot using a 0.2 μm PTFE filter prior to spin coating. ~ 50% of the spun coat samples from each concentration were further annealed at 140°C for 12 minutes in an N₂ atmosphere. The rest of the samples were air dried. A separate set of samples were spun coat under identical conditions but from solutions at room temperature to investigate effect of spin coating at an elevated temperature.

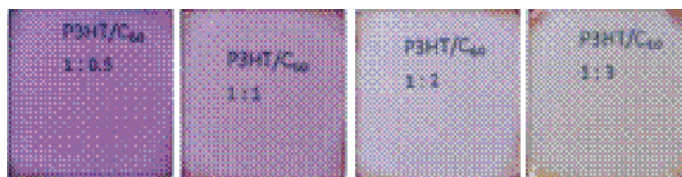


Figure 1: P3HT/C60 samples on glass substrates (labels show the respective concentration of P3HT and C60)

All samples were carefully labeled and kept in a desiccator from which air has been evacuated to prevent the oxidation of the P3HT in the samples. Figure 1 shows photographs of a set of spun coat samples with progressively increasing concentration of C60.

Results and Discussion

Thickness of all films was measured using Dektak 150 profilometer. Films prepared from solutions at room temperature averaged 68 nm, while those spun coat at an elevated temperature averaged at 47 nm. A Varian Carey 5000 UV-Vis-NIR Spectrophotometer was used to record absorption spectra of all samples.

Figure 2 shows that the temperature at which the solutions were spun had a noticeable influence on the optical absorption of the films. 15 nm blue shift of the s_o to t_{2u} transition of C60 in the blend film spun at 75°C indicates a greater interaction between P3HT and C60 molecules, and a possible formation of more polar charge transfer complex. Absence of such a blue shift in the absorption spectra for the film spun at room temperature indicates a physical mixture of the two components. The shoulders present in absorption spectra at higher wavelengths pertain to P3HT and indicates crystalline lamella formation in the thin films.

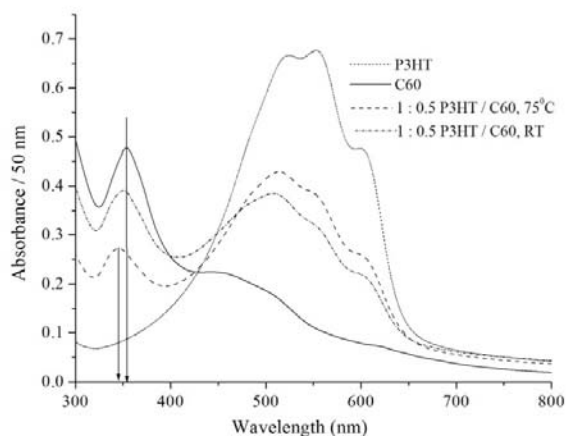


Figure 2: Absorption spectra of annealed films of P3HT, C60, and those of P3HT/C60 1:0.5 mixtures spun from solutions at room temperature and at 75°C (arrows are only to indicate spectral shift).

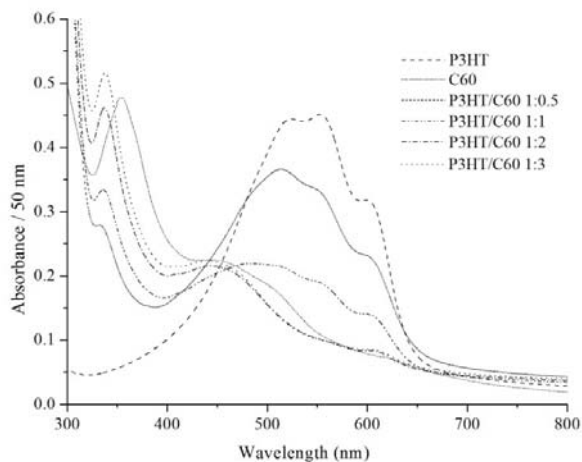


Figure 3: Absorption spectra of blend films spun coat from hot (75°C) solution in solvent-saturated environment and later annealed.

Figure 3 shows that the blend films prepared from different solutions under identical conditions have the same 15 nm blue shift for C60; also there is an apparent blue shift in P3HT absorption, increasing with increasing concentration of C60, another indication of possible charge transfer complex formation.

In Figure 4, the absorption spectra for both annealed and as-casted films show similar behavior, which indicates that for our samples, annealing had little influence on the films' optical absorption properties. Similar behavior was found for films from all concentrations.

A Veeco dilnnova scanning probe microscope (SPM) was used to investigate a possible correlation between the nanoscale morphology of the samples and their ability to produce photoexcited charge carriers. The surface morphology was imaged using Tapping mode™ atomic force microscopy in a forward scan whereas the electric force microscopy was performed in backward scan in synchronization with the photoexcitation pulse for pixel by pixel

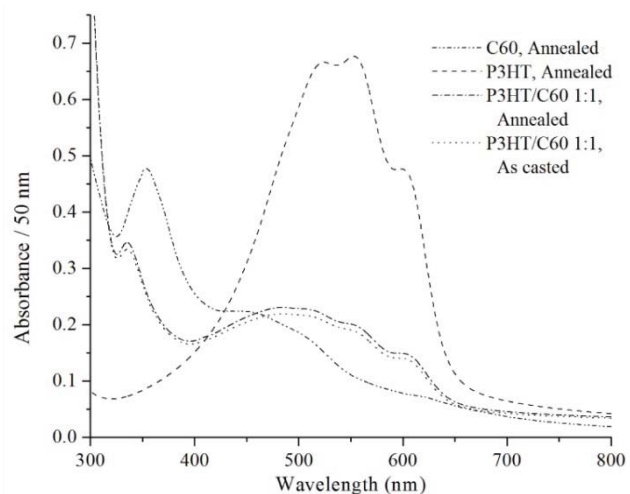


Figure 4: Absorption spectra of as-casted (air dried) and annealed films of 1:1 P3HT/C60 blend.

data collection. Figure 5 shows $4\mu\text{m} \times 4\mu\text{m}$ topographic images of annealed and as casted films of 1:0.5 P3HT/C60 blend. Whereas the annealed film shows substantial presence of phase separated P3HT/C60 composites, the surface morphology of the as casted films is nearly featureless with rms surface roughness of < 10 nm. These images clearly indicate that annealing is a key factor in controlling surface morphology and film structure.

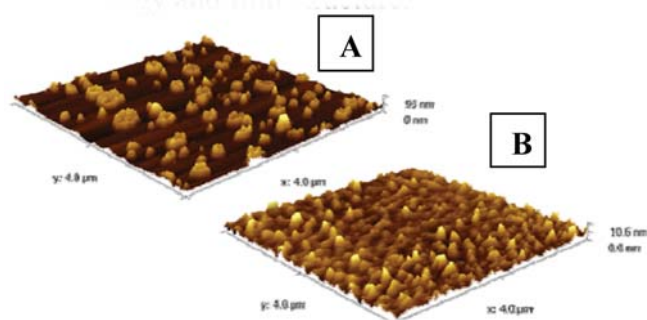
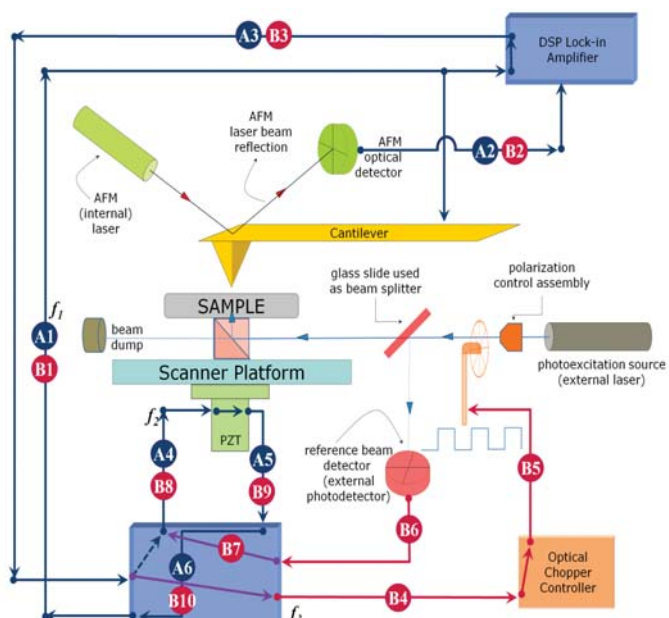


Figure 5: $4\mu\text{m} \times 4\mu\text{m}$ topographic image of (A) annealed and (B) as casted films from 1:0.5 P3HT/C60 blend.

To observe photogenerated surface charge on the samples, an optoelectronic system was designed and built in-lab to augment the capabilities of the dilnnova SPM.4 The optoelectronic add-on has a built-in timing scheme that synchronizes the dilnnova AFM controller and allows a pixel by pixel match of the EFM backward scan with the light pulse from the photoexcitation source (a 473 nm laser). Figure 6 shows the detailed synchronization schemes for photoexcited EFM experiments. Figure 7 shows a photoexcited EFM image along with the topographic image and the correlation between the features clearly indicate the islands formed due to annealing are indeed a composite of P3HT and C60. We did not see any detectable photoexcited charge generation in the as casted films. These observations are key steps in delineating the role of processing conditions, compositions and nanoscale morphology in photoexcited charge generation P3HT/C60 BHJ composites.



- A1** AFM controller sends f_1 (equiv to cantilever's resonance freq) to cantilever and lock-in amp
- A2** optical detector sends lock-in amp info about cantilever's vertical displacement (Δz)
- A3** lock-in amp informs controller that it has collected Δz data from cantilever (handshaking)
- A4** controller then sends f_2 to PZT, which the latter will use to calculate how much to move the scanner platform (Δx)
- A5** PZT tells controller of successful Δx displacement
- A6** controller increments x counter (and y counter if the current row is done) and repeats cycle from step **A1**
- PZT** Piezoelectric actuator that moves the scanner/platform the sample rests on
- $f_1 = f_{\text{resonance, cantilever}}$
- $f_2 = \text{scan rate or scan speed} / \# \text{ of scan lines}$
- $f_3 = \text{TTL modulation synthesized by AFM controller}$
- B1** see **A1**
- B2** see **A2**
- B3** see **A3**
- B4** AFM controller sends f_3 (different from f_1) to chopper controller
- B5** chopper controller tells the chopper to spin at the f_3 frequency
- B6** external photodetector sends reference beam signal to AFM controller
- B7** if a pulse is present, AFM controller collects data from the lock-in amp
- B8** see **A4**
- B9** see **A5**
- B10** see **A6**

Figure 6: Schematic diagram of optoelectronic add-on synchronization that enables photoexcited EFM imaging on the di Innova SPM.

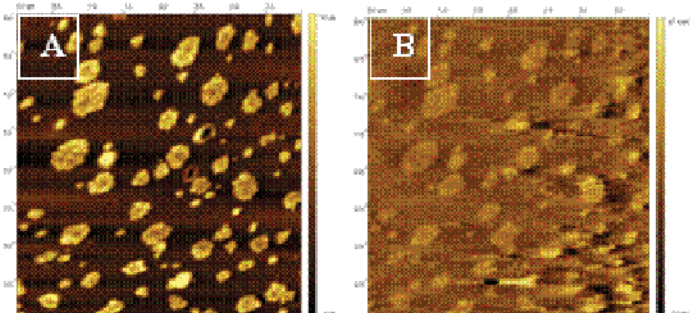


Figure 7: (A) Topography and (B) photoexcited EFM images of annealed films of 1:0.5 P3HT/C60 blend.

Conclusions

We fabricated several spun coat films with different P3HT/C60 blend solutions under different processing conditions, and found that when spun from hot solution, annealing has very little effect on the optical properties of polymer blend films, but alters their nanoscale morphology in a fundamental way by enabling nanoscale phase separation. Initial results indicate that the photoexcited charge generation in our samples is largely from the phase separated domains in the annealed blend films. Work is currently in progress to investigate the correlation of nanoscale morphology and photoexcited charge generation in all the films that were prepared under this study but also on other BHJ type organic material systems.

References

1. Jørgensen, M.; Bundgaard, E.; de Bettignies, R.; Krebs, F. The Polymer Solar Cell. In *Polymer Photovoltaics: A Practical Approach*; Krebs, F., Ed.; SPIE: Bellingham, WA, 2008; pp 12-13.
2. Motaung, D. E. et al. *Sol. Energy Mater. Sol. Cells* 2009, 93, 1674-1680.
3. Sensfuss, S; Al-Ibrahim, M. Optoelectronic Properties of Conjugated Polymer. In *Organic Photovoltaics: Mechanisms, Materials, and Devices*; Sun, S-S, Sariciftci, N. S., Eds.; Taylor & Francis Group: Boca Raton, FL, 2005; p 533.
4. See www.veeco.com for details.

Acknowledgements

This work was made possible by the NSF-sponsored Science and Technology Center on Materials and Devices for Information Technology Research, No. DMR-0120967. The authors would like to thank the NSF, MDITR, and the College of Optical Sciences at the University of Arizona for the invitation to the Hooked on Photonics 2009 program. The authors would like to thank Prof. Robert A Norwood, Olga Kropacheva, Akram Amooali, Ramon Muñoz, Konstantin Yamnitskiy, Alex Kropachev, Dave Cushing, and Elena Temyanko for their generous help in the lab, and Kimberly Sierra-Cajas, LaKeisha McClary, and Trin Riojas for their ever-present support.

EMI DIAZ received her A.S. in Lasers and Photonics from Valencia Community College in Orlando, FL just 4 weeks before she flew to Tucson for Hooked on Photonics 2009. Although unsure about attending graduate school, she hopes that sharing her REU experience with the students at VCC would inspire some of them to apply for next year's REU programs and go on to grad school themselves.

Enabling Robust Object Tracking in Tabletop Augmented Environments

TARRELL EZELL, Alabama Agricultural and Mechanical University
Dr. Hong Hua, Leonard D. Brown, University of Arizona

Introduction

Augmented environments are enhanced workspaces that supplement the real world with computer-generated, virtual imagery. An enduring challenge in the development of augmented environments rests in achieving proper registration between the real and virtual components of the environment to form a cohesive visualization. Our objective is to enable the dynamic tracking of real objects in a tabletop augmented workspace using a camera-based, tetherless tracking system. Our tracking system enables users to interface with virtual data in the workspace using a “magic” lens, which will be explained later, as a handle into the virtual world. Such a system will provide a more natural means of three-dimensional (3D) manipulation which is not possible with more traditional input devices, such as keyboard and mouse. For instance, our proposed tracking system will allow manipulation in six degrees of freedom, rather than restricting to two-dimensional planar manipulation via a traditional mouse. For this project we setup the hardware for a camera-based vision system and extended an existing open-source software package to provide tracking capabilities that are tailored to the needs of an augmented virtual environment called SCAPE. Further exploration in more preliminary user interface ideas based on these new tracking capabilities are needed.



Figure 1: Inside the SCAPE Environment

Background

The SCAPE (Stereoscopic Collaboration in Augmented and Projective Environments) environment is specialized for Augmented Reality (AR) applications¹. SCAPE is a 3D viewing system that consists of a room display and work bench which are further enhanced with



Figure 2: Simulated AR image

many supplemental viewing tools. The system uses HMPDs (Head Mounted Projective Displays) to achieve the visualization capabilities. This environment enables the incorporation of virtual and real objects which is the basis for any AR application.

In Augmented Reality, real world objects and virtual objects are combined as if the viewer was looking at one real scene (figure 2)². Research into AR is an ongoing process that is enhancing many existing real-world applications, from consumer games to highly advanced technologies such as flight simulators.

Enhancing the real world with virtual objects is a non-trivial process that typically involves many hardware and software technologies. ARToolKit is one such software technology that is popular for enabling AR applications. Developed by Kato, ARToolKit is a vision-based system that allows for real-time tracking and identification of bar-code markers³. In addition to SCAPE, extending the ARToolKit will be a focus of this research.

Experimental Methods

I. Marker Identification and Tracking

An objective of this research experience was to break down the coding of ARToolKit so that the markers that we are using can be tracked and implemented into the SCAPE environment using “magic” lenses. This greatly enhances the viewing capabilities of SCAPE, while also incorporating a low-cost more efficient tracking and identification system.

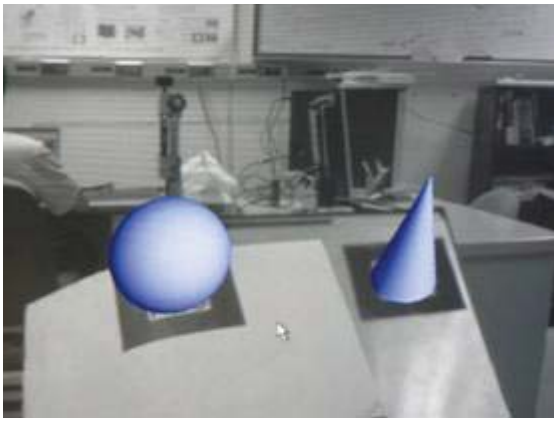


Figure 3: Images being projected with the aid of ARToolKit

The markers are used as the place of projection in the ARToolKit sample applications (figure 3 and 4), but the challenge was to separate the identification and tracking coding so that our own markers can be implemented using ARToolKit. The markers use inner fiducial “barcodes” for the purpose of identification and an outer border for tracking and pose recognition (figure 4), to improve the viewing range of the projected images. The purpose of separating the code is so that we could extend the tracking and pose borders outwards so that the viewing range is extended. (Figure 5)



Figure 4: Marker used by ARToolKit. Refer to figure 3

The purpose for the marker modification is so that we can implement the “magic” lens in SCAPE.¹ A “magic” lens is a viewing tool that currently works with SCAPE as a tool to magnify certain areas of the workbench so that more details can be observed. After the implementation of the “magic” lens with ARToolKit and retro-

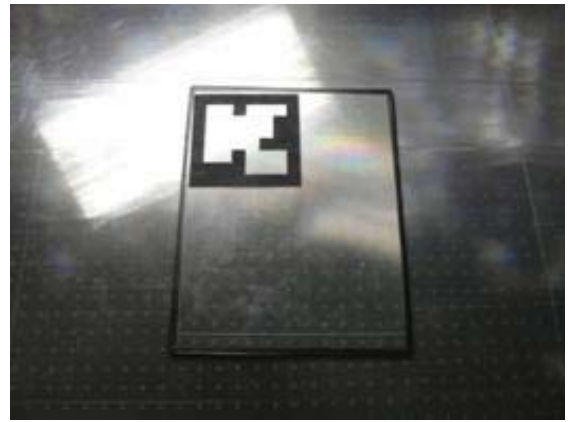


Figure 5: Our proposed marker

reflective material (explained in Section II) we propose to enable more robust viewing capabilities. The sought after output is for it to behave not only as a magnifier, but as a tool to view and manipulate virtual objects in the real world scene. With these capabilities, the “magic” lens will have up to six dimensions of freedom for manipulation and will give the user abilities far beyond that of the current prototype in use. Theoretically, 3D objects will be projected onto the marker to be viewed and manipulated to the needs of the user.



Figure 6: “Magic” Lens

II. Scene Illumination Challenge

To aid in reliability and reduce visible clutter over the observed area, the need to selectively illuminate the scene comes into play. To make this application possible we implemented a Near Infrared (NIR) filter, NIR Light Emitting Diodes (LEDs) and retro-reflective materials in conjunction with the viewing camera.

The Point Grey Research (PGR) Dragonfly² camera was used for scene acquisition. We strategically placed four NIR LEDs around the lens of the camera to illuminate the views space. An NIR filter was used to filter out visible light (figure 7). We then coated the tracking markers with a special retro-reflective material. The selective illumination of the scene is not possible without the aid of retro-reflective materials in the scene.

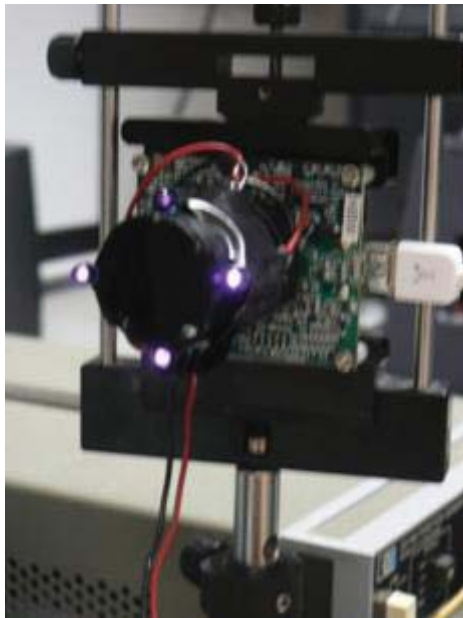


Figure 7: PGR Dragoonfly2 camera with NIR LED's and NIR filter

Retro-reflective material is a special type of material that reflects light back in the direction of the light source; such material is also used on road signs. This material will be coated onto our “magic” lens to help the camera distinguish it from the rest of the scene (figure 5 and 6). The material appears to glow white under the filter and the NIR LEDs (figure 9). Everything in the scene not made of this material will be blackened out and will not show up in the captured image. Used in conjunction with the coaxially mounted NIR LEDs, the retro-reflective material allows us to selectively illuminate only the elements of interest in the scene, thus reducing visual noise and making image segmentation more reliable.

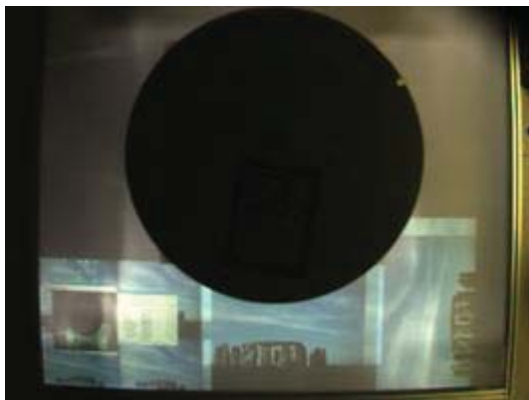


Figure 8: Non-illuminated scene

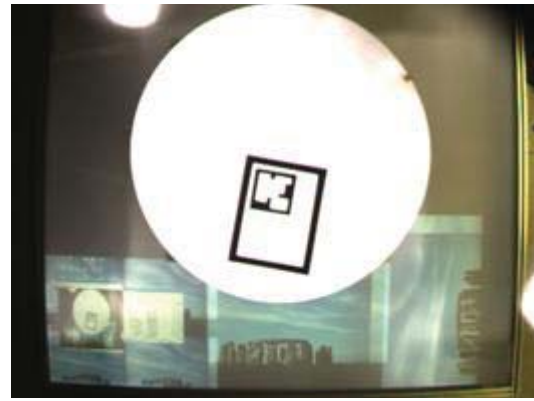


Figure 9: Illuminated Scene

Conclusions and Future Work

The research during this summer was successful for future application to the SCAPE AR environment, though some of summer's findings have not yet been implemented in the environment. The scene illumination phase of the research has been implemented, but a testbed application has not. We were successful in the process of marker tracking and identification and this also will be implemented on the “magic” lens in the future.

In the future more cameras should be strategically placed around the top of SCAPE room to incorporate a wider tracking area. This will enable more robust options for AR object tracking in SCAPE, and thus enhance its capabilities.

References

1. Hong Hua, L. Brown, C. Gao, (2004) "SCAPE: Supporting Stereoscopic Collaboration in Augmented and Projective Environments," IEEE Computer Graphics and Applications, 24(1), 66-75, January/February issue.
2. Introduction to Augmented Reality: <http://www.se.rit.edu/~jrv/research/ar/introduction.html#Section1>.
3. ARTK: <http://www.hitl.washington.edu/artoolkit/>
4. L. Brown and Hong Hua, (2006) "Magic Lenses for augmented virtual environments," IEEE Computer Graphics and Applications, 26(4), pp.64-73, July/August.
5. Kato, H., Billinghurst, M. (1999) Marker Tracking and HMD Calibration for a video-based Augmented Reality Conferencing System. In Proceedings of the 2nd International Workshop on Augmented Reality (IWAR 99). October, San Francisco, USA.

Acknowledgements

This work was made possible by the NSF sponsored Science and Technology Center on Materials and Devices for Information Technology Research, No. DMR-0120967



TARRELL J. EZELL is currently a Senior Electrical Engineering student at the prestigious college of Alabama Agricultural and Mechanical University and plans on completing his baccalaureate degree in the fall of 2009. He plans to one day obtain his PhD in the area of robotics or electro-mechanics.

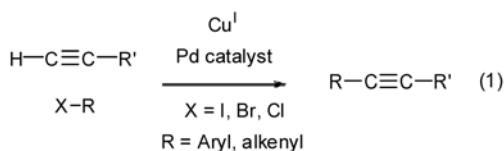
Sonogashira Coupling of Terminal Acetylenes with Perylene Bisimides

AKIL FOLUKE, Morehouse College

Dr. Seth Marder, Dr. Brian Lawrence, Georgia Institute of Technology

Introduction

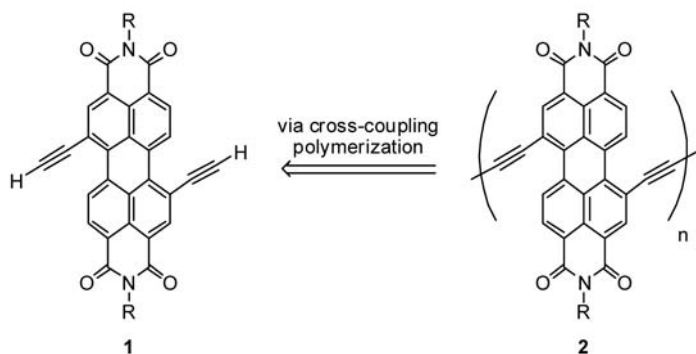
The Sonogashira coupling of terminal alkynes with organohalides has many applications including couplings of acetylene groups with vinyl or aryl halides (see equation 1).¹ Carried out at room temperature, the catalysts required for this reaction are typically a palladium complex and a cuprous halide. Because of this, Sonogashira coupling reactions are both air and light sensitive and must be performed using inert atmosphere techniques.



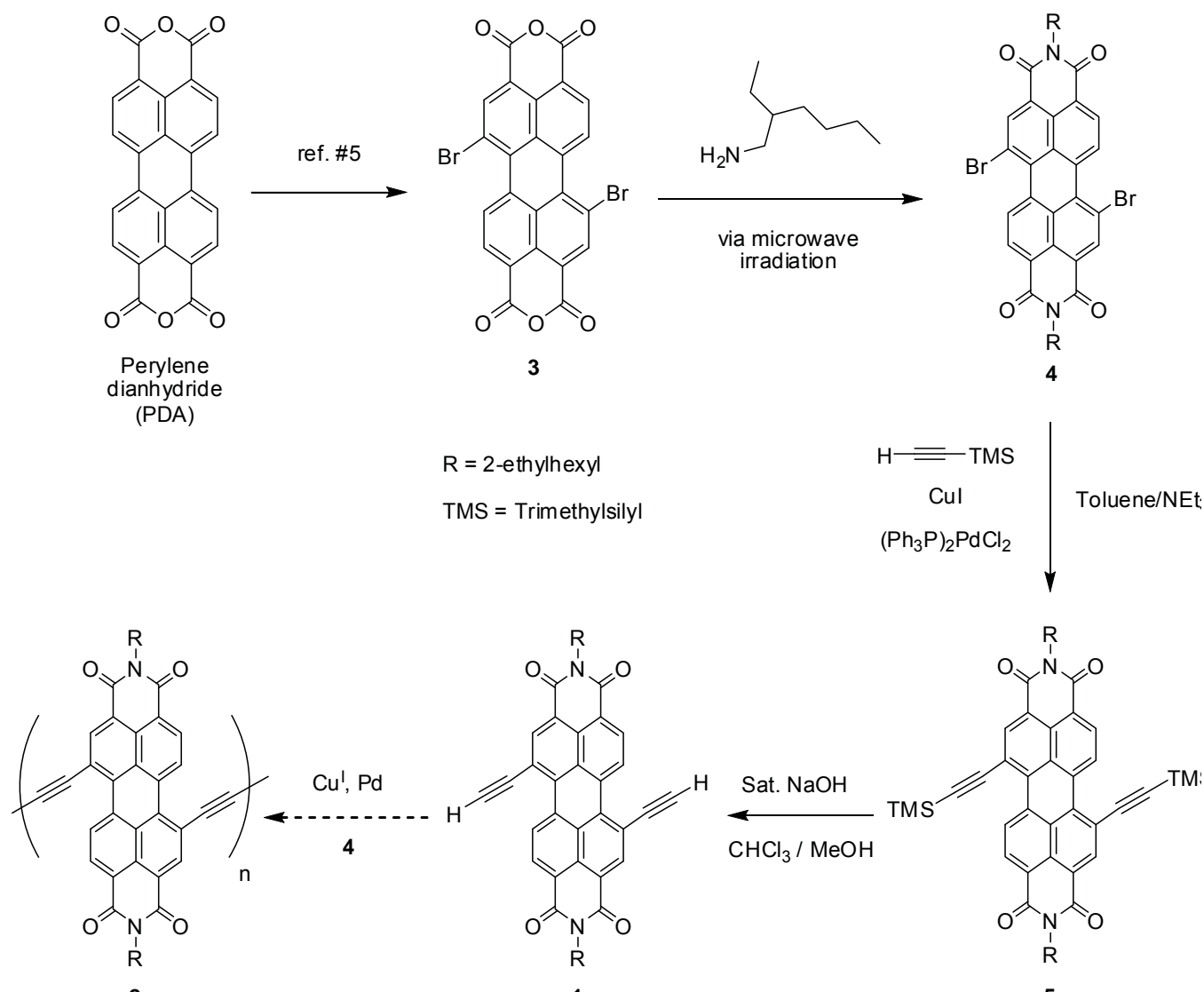
The goal of this project is to employ the Sonogashira coupling to attach terminal acetylene units to the bay position(s) of a perylene bisimide (PDI), an electron deficient polyaromatic

heterocycle (see Scheme 1). It has been established that perylene derivatives absorb light in the visible region of the electromagnetic spectrum.² Using the resultant acetylidyne as a spacer, we envision the preparation of electron deficient oligo- and polymers that contain this core unit. By inserting acetylenes between PDI units, we hope to produce a “bridge” that allows electron transport in such a material (across the PDI groups due to the presence of unsaturation). One advantage that acetylenes provide as linking units is structural: they are both unsaturated and cylindrically symmetrical (alkenes could be considered in place of acetylenes but then isomeric purity becomes a factor).

Ideally, all of these coupling reactions can be executed at room temperature under nitrogen gas.^{2,3} Using standard reaction techniques, it is our intent to explore this reaction chemistry to determine the best acetylidyne for coupling use (trimethylsilyl vs. trisopropylsilyl), the optimal amino group for solubility (ethylhexyl vs. phenyl), and the preferred palladium catalyst (Pd^0 vs. Pd^{II}). While subsequent removal of the silyl groups may cause problems, we anticipate that isolation of the terminal protonated PDI bisacetylene will be achieved.



SCHEME 1: Proposed route to acetylene bridged perylene polymer necessitates preparation of compound 1.



SCHEME 2: Synthesis of bis(2-ethylhexyl)-1,7-bisacetyleneperylene-3,4,9,10-tetracarboxylic acid diimide¹

Methods

All reactions were carried out open to air unless documented otherwise. All commercially available reagents and solvents were used as received with the following exceptions: triethylamine was stored over potassium hydroxide prior to use. A Varian Mercury VX300 NMR spectrometer (operating at 300.225 MHz) was used to acquire all NMR spectra. ¹H NMR spectra are referenced to CHCl₃ (residual solvent peak) at 7.26 ppm. Microwave reactions were carried out in a CEM Discover Lab Mate research scale microwave synthesizer.

Bis(2-ethylhexyl)-1,7-dibromoperylene-3,4,9,10-tetracarboxylic acid diimide (4)

--Thermal

A round bottom flask containing a magnetic stir bar was charged with perylene bisanhydride **3**⁴ (700 mg, 1.27 mmol, 1.00 equiv.; Girindus Solvay Organics, USA) followed by 2-ethylhexylamine (0.78 mL, 7.74 mmol, 6.10 equiv., $\rho = 0.78$) and propionic acid (10 mL)

under positive nitrogen pressure. The flask was fitted with a reflux condenser and heated at 150 °C with stirring overnight. Volatiles were removed in vacuo, and the red solid produced washed with methanol, then filtered. Silica gel chromatography (30 g SiO₂) eluting with toluene (1.5 L) gave the desired product as mixture of 1,6-/1,7-dibromo isomers (326 mg, 33.2%).

--Microwave Irradiation

A 10 mL microwave tube was charged with 2-ethylhexylamine (1.25 mL, 7.65 mmol, 2.00 equiv., $\rho = 0.789$), DMSO (0.625 mL), and magnetic stir bar. Perylene **3** (2.11 g, 3.825 mmol, 1.00 equiv.) was added (reaction begins instantly). The microwave tube was irradiated, with stirring, at 100 W (15 min run time/5 min hold time; $T_{\text{max}} = 150\text{ °C}$, $P_{\text{max}} = 100\text{ psi}$). Purification (as described above) affords the desired as a red solid (2.59 g crude, 43%).

Bis(2-ethylhexyl)-1,7-bis(trimethylsilylacetylene)perylene-3,4:9,10-tetracarboxylic acid diimide (5)

A round bottom flask was charged with perylene **4** (326 mg, 0.422 mmol, 1.00 equiv.), bis(triphenylphosphine) palladium dichloride (29.62 mg, 0.042 mmol, 0.10 equiv.), and cuprous iodide (4.09 mg, 0.021 mmol, 0.05 equiv.). A toluene/triethylamine mixture (1:1; 30 mL) and a magnetic stir bar were added and the mixture was sparged with nitrogen for 30 min. Trimethylsilylacetylene (238.55 μ L, 1.688 mmol, 4.00 equiv., $\rho = 0.695$) was added to the reaction mixture via syringe, and the mixture was heated at 80 °C with stirring overnight. After cooling to room temperature, the now gel-like reaction mixture was diluted with excess chloroform. Volatiles were then removed *in vacuo*. The resultant purple solid was washed with cold methanol/water (9:1; 200 mL) (via ice bath), and vacuum filtered. Silica gel chromatography (55 g SiO₂) eluting with 40% hexanes in chloroform (4 L) gave the desired product as dark purple solid (64 mg, 18.8%).

Bis(2-ethylhexyl)-1,7-bisacetyleneperylene-3,4:9,10-tetracarboxylic acid diimide (1)

A round bottom flask containing magnetic stir bar was charged with perylene **5** (20 mg, 0.025 mmol, 1 equiv.) and chloroform (2.27 mL), then treated with a solution of saturated sodium hydroxide in methanol (0.114 mL).⁵ The mixture was stirred for ten minutes. Water (3.40 mL) was added to the solution and the mixture was extracted with chloroform. The combined organics were washed with water, dried over sodium sulfate, then concentrated *in vacuo* to give a dark purple solid. Silica gel chromatography (20 g SiO₂) eluting with 20% hexanes in chloroform (250 mL) gave the desired product as a dark purple solid: ¹H NMR δ 10.0 (d, 2H), 8.84 (s, 2H), 8.70 (d, 2H), 4.15 (m, 4H), 3.82 (s, 2H), 1.97 (m, 2H), 1.21 – 1.45 (m, 16H), 0.83 – 0.97 (m, 12H).

Results

2-ethylhexylamine was condensed with commercially available perylene bisanhydride **3** using reflux conditions and microwave conditions to yield the corresponding bisimide **4** as a red solid. While no more robust, the microwave irradiations drastically decreased reaction time and increased throughput (**3** \rightarrow **4**). As anticipated, trimethylacetylene was coupled to the bay positions using Sonogashira conditions to yield compound **5** as a purple solid. The best yields and purity were obtained at 80 °C with triethylamine as the base (compared to reactions performed at ambient temperature or with diethylamine as base). Compound **5** was deprotected using mild conditions to yield the target compound **1** as a dark purple solid. Overall, purification of these compounds using silica gel chromatography proved very difficult mostly due to their low solubilities, sometimes producing low isolated yields. It should also be noted that this purification technique was unsuccessful in separating the two regioisomers of any of the compounds formed.

Conclusion

The addition of trimethylacetylene groups to the bay positions of perylene diimides via Sonogashira coupling was successful. Subsequent removal of the silyl groups from these acetylides yielded the desired terminal acetylenes as deep purple solids. Future work will be directed towards preparation of **2**.

References

1. Sonogashira, K.; Tohda, Y.; Hagihara, N. *Tetrahedron Lett.* 1975, No. 50, 4467-4470
2. Shoaee, S.; Eng, E. P.; An, Z.; Zhang, X.; Barlow, S.; Marder, S. R.; Durrant, J. R. *Chem. Comm.* 2008, 4915-4917
3. An, Z.; Odom, S. A.; Kelley, R. F.; Huang, C.; Zhang, X.; Barlow, S.; Padilha, L. A.; Fu, J.; Webster, S.; Hagan, D. J.; Stryland, E. W.; Wasielewski, M. R.; Marder, S. R. *J. Phys. Chem. A* 2009, 113, 5585-5593
4. Wurthner, F.; Stepanenko, V.; Chen, Z.; Saha-Moller, C. R.; Kocher, N.; Stalke, D. *J. Org. Chem.* 2004, 69, 7933-7939
5. Jimenez, A. J.; Spanig, F.; Rodriguez-Morgade, M. S.; Ohkubo, K.; Fukuzumi, S.; Guldi, D. M.; Torres, T. *Org. Lett.* 2007, 9(13), 2481-2484

Acknowledgements

Akil Foluke would like to thank the Georgia Institute of Technology Department of Chemistry and Biochemistry, and the National Science Foundation (through the STC Program under Agreement Number DMR-0120967) for their support of this project.



AKIL FOLUKE is currently a senior at Morehouse College, majoring in chemistry. He plans to pursue his Ph.D. in synthetic organic chemistry after acquiring his Bachelor's degree in Spring 2010. His goal is to one day work in the pharmaceutical and/or biotech industry.

Use of Spatially Anisotropic Intermolecular Interactions to Define Order in Molecular Films Grown by Physical Vapor Deposition (PVD)

RYAN P. FRASER, Western Washington University
Haishan Sun, Phil Sullivan, University of Washington

Introduction

Electro optical (EO) modulators translate an electrical signal into an optical one and vice versa. As the demand to process more information at a faster rate increases and therefore the demand on this technology these devices will need to become smaller and cheaper. In this study we used physical vapor deposition to deposit chromophores onto functionalized glass substrates. We are attempting to use hydrogen bonding to overcome chromophore dipole-dipole interactions to achieve acentric order as shown in figure 1. This will create a material with high electro optic activity.^{1,2}

Background

Currently the preferred method for creating an ordered EO material is to use electric field poling. For this method the chromophore is spin cast onto a substrate. The chromophore is then heated to its glass transition temperature, an electric field is applied across the material, and then the material is allowed to cool with the electric field applied. This method can have inconsistent results and the materials being used can be damaged by the heat. As an alternative we are exploring physical vapor deposition (PVD) with the use of hydrogen bonding to create a highly ordered material (figure 1). A highly ordered material is desirable because it increases the electro-optic coefficient (r_{33}) and therefore the efficiency of the material in EO devices. $r_{33} \propto \beta N \langle \cos^3 \theta \rangle$ where N = number density of molecules (chromophores) β = chromophore hyperpolarizability and $\langle \cos^3 \theta \rangle$ = order parameter. As you increase any of these variables the should increase however each one has its limits and it is difficult to get them all simultaneously to optimal levels. We are concentrating on increasing the order parameter while initialing using a chromophore with a moderate value. The reason for using a moderate value is to minimize problems with dipole-dipole interactions between the chromophores. Figure 1 illustrates the idea of preparing synthetic materials that posses an orientational bias. Here hydrogen bonding interactions are used to stabilize dipolar (head-to-tail) molecular order.

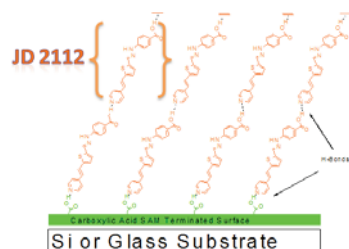


Figure 1. Tobin Marks Chromophore 23 deposited onto a carboxylic acid SAM terminated surface.

Methods

Unfunctionalized Substrates

Glass slides and cover slips were sonicated 10 minutes in acetone and then 10 minutes in IPA. The slides were then O_2 plasma treated for 10 minutes.

Self Assembled Monolayers

Glass cover slips were first sonicated 10 minutes in acetone and then 10 minutes in IPA. The films were then dried and suspended in a $\sim 50 \mu M$ $C_6H_{13}O_5P$ solution in THF. The solution was evaporated until it was no longer touching the cover slips. The cover slips were baked in a vacuum oven overnight at $140^\circ C$. They were then sonicated for 3 minutes 3 times in fresh THF. The slides were then air dried with N_2 .

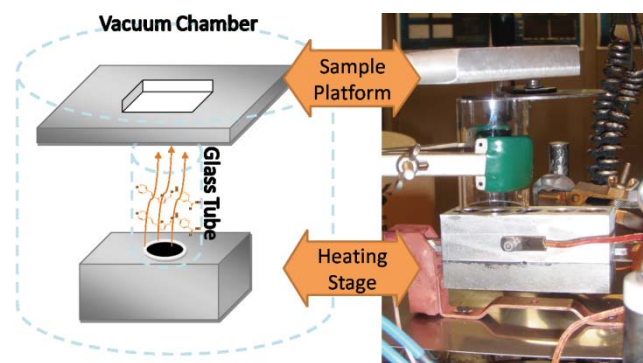


Figure 2. Physical Vapor Deposition Apparatus

Physical Vapor Deposition

A modified Edwards Coating System (figure 2) was used for all PVD. All samples were deposited at $\sim 6.0 \times 10^{-6}$ Torr allowing the chromophores to sublime when heated and then deposit onto the bare substrates or SAM terminated surfaces. The chromophores shown in figure 3 were used for the PVD experiments. They were first deposited onto unfunctionalized glass substrates as controls and later onto carboxylic acid terminated glass substrates. PS 1 started to vaporize at $\sim 180^\circ C$ but deposited optimally at $\sim 210^\circ C$. To achieve a film thickness of ~ 150 nm on glass slides the apparatus was run for two hours at $210^\circ C$. JD 2112 started to vaporize at $\sim 230^\circ C$ but deposited optimally at $\sim 250^\circ C$. To achieve a film thickness of ~ 150 nm on glass slides the apparatus was run for two to three hours at $\sim 250^\circ C$.

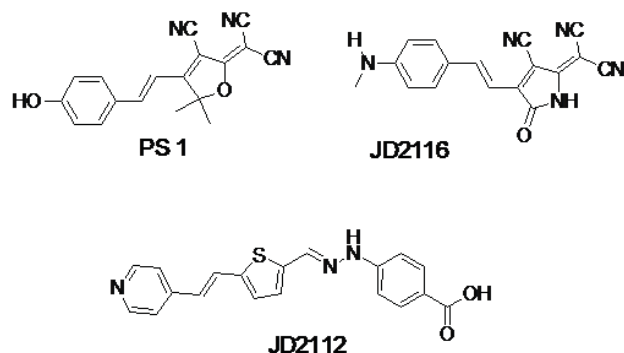


Figure 3. Chromophores used for PVD.

Results/Conclusion

Although not much conclusive data was collected the results look promising. In figure 6 variable angle polarization referenced absorption spectroscopy (VAPRAS) was used to determine the order of the EO chromophores in thin film. For this procedure the film is placed in a modified UV-visible spectrophotometer facing perpendicular to the light beam. It is then rotated at 10 degree intervals up to 40 degrees. This is done with both P and S polarized light. The spectra data from this analysis is then run through calculations that determine a P.2 value. When $0 < P.2 \leq 2$ the molecules are aligned perpendicular to the surface of the substrate, when $-0.5 \leq P.2 < 0$ the molecules are aligned parallel to the surface of the substrate, and when $P.2 \cong 0$ there is little to no order in the material. In figure 6. a), and b) you can see that the results are negative showing that the films have high horizontal order. This was expected since the surface is not functionalized so there is no support for the chromophores to order vertically. On the other hand figure 6. c) shows little to no order. This may be due to the use of a 6 carbon chain rather than a 12 carbon chain carboxylic acid when forming the SAM terminated surface. In figure 5. a), and b) the spectra for the chromophores in solution are similar to those in film. This shows that the chromophores have a relatively low β however they do not absorb in the telecommunication wavelengths therefore they may not have high optical loss. JD 2116, (Figure 6. c)) on the other hand, absorbs near the telecommunication wavelengths allowing the possibility for high optical loss but a higher β value. At this point it is difficult to come to any definite conclusions, because much still needs to be done. This includes more thorough characterization of the current chromophores deposited onto functionalized substrates and eventually test devices. The formation of more reliable SAM's will be necessary to achieve desirable results. Electric poling may also be considered to assist the chromophores in assembling with the desired order. In addition better chromophores will likely be developed with increased β values and a greater capability to deposit with acentric order. With the ability to quickly and easily assemble EO materials onto various devices this method will probably continue to be explored.

Chromophore	ϵ (L mol ⁻¹ cm ⁻¹)	λ_{MAX} (nm) in THF	λ_{MAX} (nm) Thin Film
PS 1	44304	444	459
JD 2112	37496	424	432
JD 2116	28460	660	-

Figure 4. Extinction coefficient and λ_{MAX} data obtained from UV-visible spectra data.

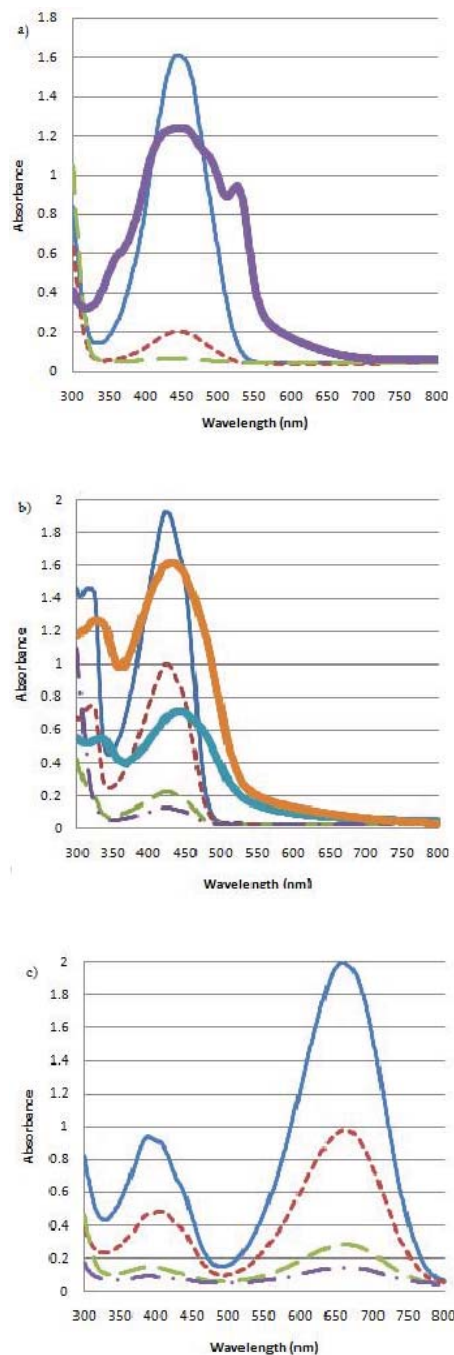


Figure 5. UV-visible spectra for chromophores in solutions and thin films. a) Thin lines PS1 in THF solution, thick line PS1 120 nm film on glass b) thin lines JD 2112 in THF solution, thick lines JD 2112 20 nm film on glass and 120 nm film on carboxylic acid terminated glass, c) thin lines JD 2116 in THF solution.

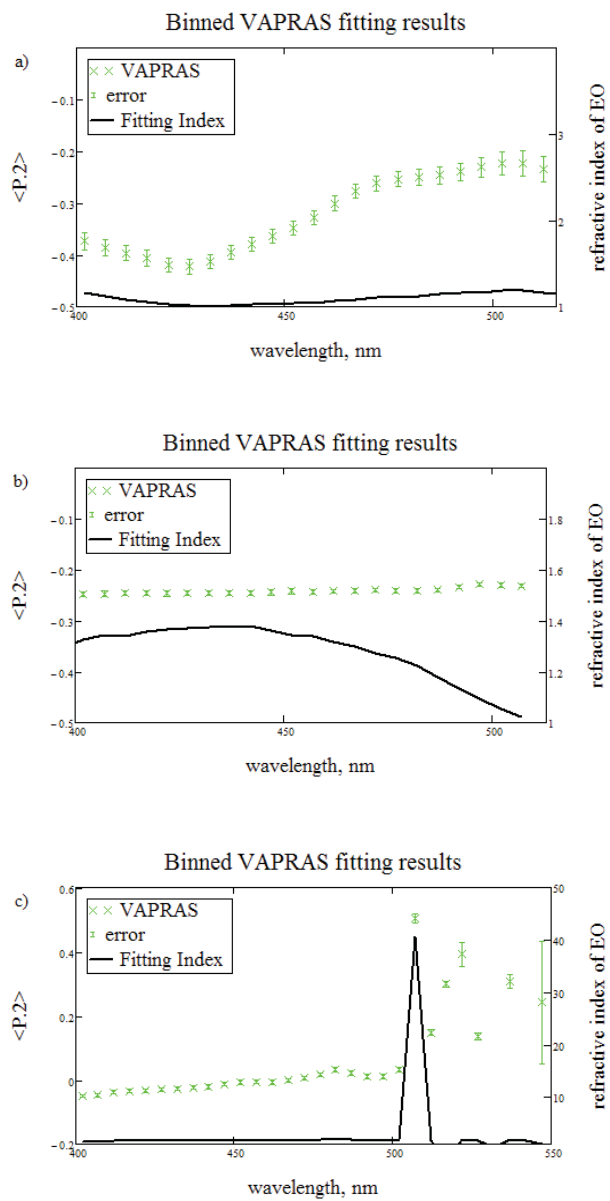


Figure 6. P.2 calculated using the VAPRAS method. a) PS 1 120 nm film on glass P.2 \approx -.4, b) JD 2112 20 nm film on glass P.2 \approx -.24, c) JD 2112 120 nm film on carboxylic acid terminated glass.

References

1. Dalton, L.R. et. al. Optical Materials 2003, 21, 19-28
2. Davies, J. et. al. J. Am. Chem. Soc. 2008, 130, 10565-10575
3. Facchetti, A.; et al. Nature Materials 2004, 3, 910-917
4. Baehr-Jones, T.; et al. Optics Express 2005, 13, 5216-5226
5. Briggs, R. M. et. al. Applied Physics Letters 2009, 94, 021106-1-021106-

Acknowledgments

Funds for this research were provided by Materials and Devices for Information Technology Research (MDITR), an NSF Science and Technology Center No. DMR (0120967).

Prof. Larry Dalton

Dr. Phil Sullivan

Ilya Kosilkin

Meghana Rawal

Ben Olbricht

Dr. Denise Bale

Haishan Sun

Lewis Johnson

Dr. Bruce Eichinger

Prof. Bruce Robinson

Prof. Antao Chen

Dr. Manish Dubey



RYAN FRASER is currently pursuing a degree in Polymer Engineering Technology/ Vehicle Engineering Technology at Western Washington University. He has plans to possibly continue onto graduate school in mechanical engineering with a concentration in alternative energy.

Use of Ion-Exchange Functionalized DNA as a Host Material for Enhanced Poling Induced Order and Molecular Hyperpolarizability

DEREK J. FREI, University of Washington

Lewis E. Johnson, Bruce H. Robinson, University of Washington

Introduction

DNA has the potential to function as a molecular scaffold to align the dipole moments of non-linear optical chromophores for use in photonic devices. This alignment is necessary for a strong electro-optic (EO) response (change of refractive index due to an applied field) in the materials of interest. This strong EO response is, in turn, needed for application of these chromophores in electro-optic modulators, which convert electronic signals into optical signals. These devices depend on materials having high hyperpolarizabilities and low absorbance at telecommunications wavelengths. This high hyperpolarizability on the molecular scale translates into a large nonlinear (field strength-dependent) electric susceptibility on the macroscale, meaning that the refractive index of the material will change when an electric field is applied across the modulator (known as the Pockels effect). This effect contributes to a longer effective path length through the modulator, allowing light to be selectively turned on and off due to interference between waves. Better EO materials are needed in order to reduce the size of devices, leading to quicker capacitor charging, allowing higher switching speeds, as well as less absorbance of the light used to photonically transmit data.

Favorable molecular properties alone, however, are not sufficient to produce an efficient EO modulator. The dipole moments of the chromophores must also be aligned in order to produce a phase shift so that beams of light within a modulator add constructively. However, the alignment of these dipoles is energetically unfavorable because partial charges of polar molecules are in close proximity to partial charges of the same sign on nearby molecules. In addition, random thermal motion places a theoretical limit on the dipole ordering that can be achieved by such chromophores in an applied electric field unless some other mechanism is in place to align the dipoles of the chromophores. One such mechanism is the use of a molecular scaffold such as DNA.

DNA is an attractive molecule to use as a scaffold because of dimensional restrictions that it places on intercalated molecules such as ethidium bromide and the non-linear optical dyes under study. In essence, DNA molecules can be thought of as cylinders with holes where the planar portion of a chromophore can intercalate, thus providing the necessary alignment of the chromophore's dipole moment^{1, 2}.

In order to estimate the efficacy of DNA as a molecular scaffold for chromophores, it is necessary to determine the mode of binding between the chromophores and DNA. The binding mode would determine the maximum chromophore loading for the system and would also affect the design of any photonic device that could be built using DNA as the scaffold for the photonic materials.

Objectives

This project seeks to establish the means by which photonic dyes such as Chromophore 1 shown in Figure 1 bind to DNA in a buffered solution, with the goal of determining the feasibility of using DNA to align the dipoles of these chromophores in actual photonic devices. Ethidium Bromide serves as a convenient, well-studied model that can be used as a baseline against which the behavior of other chromophores can be compared.^{4,6,7} The first objective of the project is to establish an experimental procedure by which the mechanism of ethidium-DNA binding can be verified reliably. This procedure will then be extended to other chromophores whose binding modes are unknown.

Two models in particular are being evaluated for ethidium binding: the independent binding model and nearest neighbor exclusion model. Under the independent binding model, the chromophore binds to each binding site along the DNA segment, while the nearest neighbor exclusion model has the chromophore intercalating at every other binding site. One problem with these models is that they ignore the existence of binding modes other than intercalation. For example, one study indicates that at low ionic strength, ethidium tends to bind to the outside of the DNA double helix instead of intercalating⁴. It is also possible that intercalation for a dye occurs at every third, fourth, fifth, or n th binding site rather than simply every other binding site. In principle, such binding modes could be explored using the techniques discussed in this paper.

Literature sources indicate that ethidium intercalates in DNA via the nearest neighbor exclusion model in TE buffer at mild ionic strength and neutral pH^{4,6,7}. However, the binding modes of other chromophores with possible photonic applications remain unknown; thus, determining the binding modes of the molecules with lesser-known behavior is the goal of these experiments.

In order to examine binding modes, we titrated an ethidium bromide solution with DNA and have begun molecular dynamics studies with ethidium ions and short (approximately sixteen base pair) DNA oligomers. Once the mechanism of ethidium intercalation is verified experimentally and theoretically, the same studies will be extended to Chromophore 1 and 2, shown below in Figures 1 and 2, respectively.

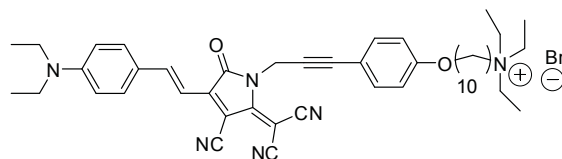


Figure 1. Structure of Chromophore 1.

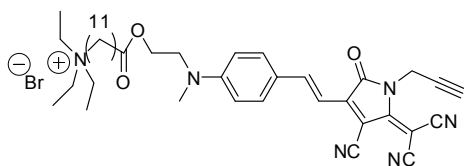


Figure 2. Structure of Chromophore 2.

Experimental Methods

The ethidium bromide-DNA titrations were performed under two sets of experimental conditions. The first set of conditions used deionized water as the solvent, did not control for temperature, and used a Shimadzu UV-1601 spectrophotometer for recording spectra for 400 nm to 600 nm. Samples were stirred for ten minutes using a magnetic stirrer after each addition of DNA. The second set of conditions employed TE buffer (10 mM Tris, 10 mM KCl, and 1 mM EDTA) at pH 7.2 as the solvent and maintained at constant temperature of 25°C. Spectra were recorded with an Ocean Optics diode array spectrophotometer after slightly shorter (3-5 minutes) equilibration intervals. Samples were stirred in-situ and could be monitored at any point during the run. With the second set of conditions, the cuvette containing the ethidium bromide-DNA mixture was held on a 25°C thermal plate with a styrofoam insulating box surrounding the cuvette. The Erlenmeyer flask containing the DNA solution was also immersed in a 25°C water bath to ensure temperature control of the DNA solution prior to mixing with ethidium bromide. Both sets of experimental conditions used 50-100 kDa salmon sperm DNA and electrophoresis grade ethidium bromide. In Figures 3 and 4 below, 2.5 mL of 19.0 µg/mL ethidium bromide was titrated with 20 µL aliquots of 0.995 mg/ml DNA; in Figures 5 and 6, 2.5 mL of 19.0 µg/mL ethidium bromide was titrated with 20 µL aliquots of 1.072 mg/ml DNA. The concentration of DNA was converted into molarity of base pairs using the average base pair molar mass of 660 g/mol.

Figures 4 and 6 show the fraction of ethidium bromide bound to DNA plotted against the molar DNA concentration. The wavelength 480 nm was selected for this analysis because it is near λ_{\max} and thus has good resolution between data points. The fraction of bound ethidium bromide was calculated from the absorption data in Figures 1 and 3 in the following manner:

$$f_b = \frac{Y}{Y+1} \quad (1)$$

In Equation 1, f_b is the fraction of ethidium bromide bound to DNA; and

$$Y = \frac{A - A_f}{A_b - A} \quad (2)$$

where A is the absorbance of the samples of mixed ethidium bromide and DNA, A_f is the absorbance of unbound (free) ethidium bromide in the absence of DNA, and A_b is the absorbance of fully bound ethidium bromide saturated with DNA. The non-linear least squares fits of this data, obtained using a MATLAB

program called MCFit³ (written by L. E. Johnson and N. W. Bigelow), are also shown in Figures 2 and 4 on the same axes, with fits for the independent binding ($n = 1$) and nearest neighbor exclusion ($n = 2$) models shown with the green and red curves, respectively.

It was also determined that stirring the ethidium bromide-DNA solution is crucial in the full equilibration of the system after the addition of each aliquot of DNA. An analysis of the absorption of this solution at 480 nm revealed that the system equilibrates in roughly three minutes when not stirred, whereas stirring the system allows equilibration to be achieved nearly instantaneously.

Results

Figure 3 shows the UV-visible spectra of the ethidium bromide-DNA solutions using the first set of experimental conditions discussed above, and Figure 4 shows the fraction of ethidium bound versus molar DNA base pair concentration. The fraction of ethidium bound was calculated using the equations stated previously. The data in Figure 4 show a strong correlation with the independent binding ($n = 1$) model.

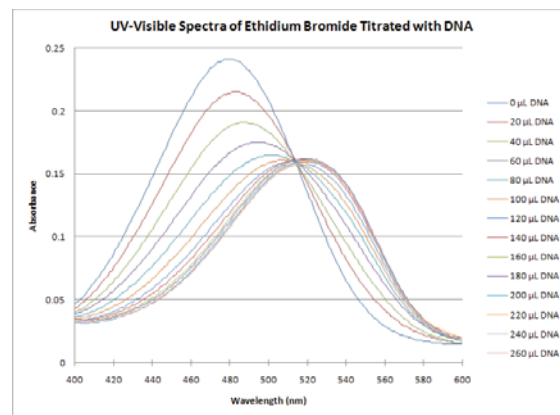


Figure 3. UV-visible spectra of titration of 2.5 mL of ethidium bromide with 20 µL aliquots of DNA without temperature control using deionized water as solvent.

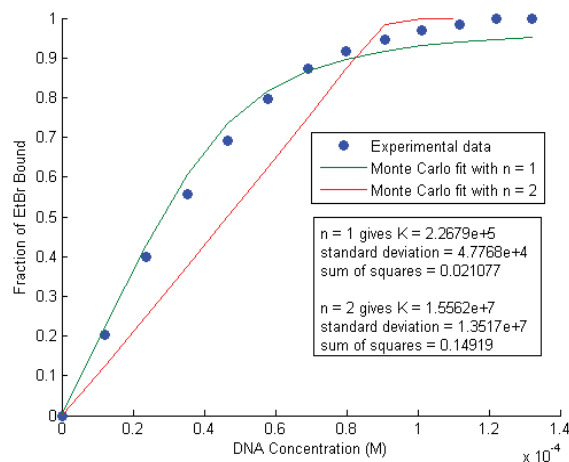


Figure 4. Fraction of ethidium bromide bound to DNA plotted against molar DNA concentration along with Monte Carlo fits of these data using the independent binding ($n = 1$) and nearest neighbor exclusion ($n = 2$) models using deionized water as solvent. (Raw data taken from Figure 3.)

Figure 5 shows the UV-visible spectra of the ethidium bromide-DNA solutions using the second set of experimental conditions mentioned earlier, and Figure 6 shows the fraction of ethidium bound versus molar DNA concentration. The data in Figure 6 show a stronger correlation to the nearest neighbor exclusion ($n = 2$) model than to the independent binding ($n = 1$) model.

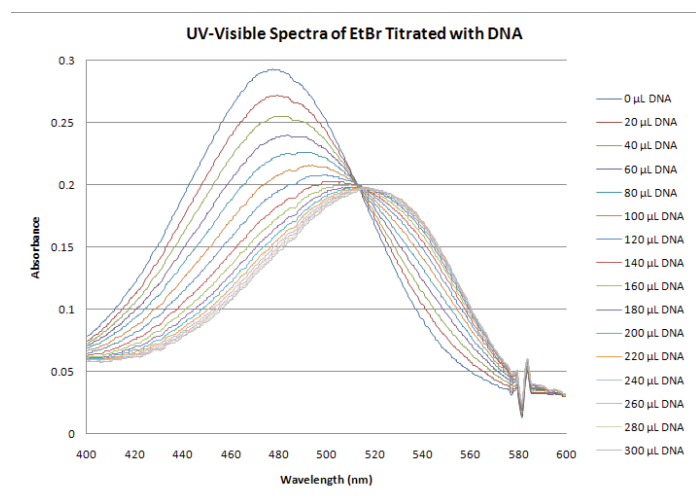


Figure 5. UV-visible spectra of titration of 2.5 mL of ethidium bromide with 20 μL aliquots of DNA using TE buffer as the solvent with temperature control at 25°C.

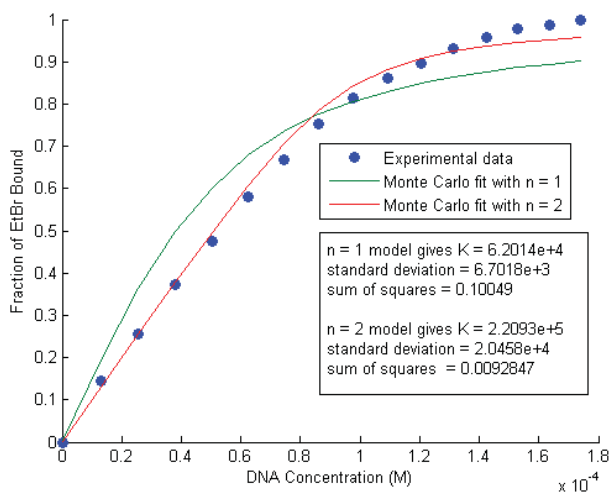


Figure 6. Fraction of ethidium bromide bound to DNA plotted against molar DNA concentration along with Monte Carlo fits of these data using the independent binding ($n = 1$) and nearest neighbor exclusion ($n = 2$) models. (Raw data taken from Figure 5.)

Discussion

The figures above indicate that when deionized water is used as the solvent and the temperature is not controlled, the independent binding ($n = 1$) model dominates, as seen in the smaller sum of squares value for the $n = 1$ model (0.021077) than for the $n = 2$ model (0.14919). Inspection of Figure 4 also shows that the Monte

Carlo fit of the $n = 1$ model clearly follows the experimental data more closely than does the curve for the $n = 2$ model. Nordmeier suggests that this may be due to outside binding rather than intercalation⁴.

On the other hand, the sum of squares values shown in Figure 6 and inspection of the closeness of the models to experimental data indicate that the nearest neighbor exclusion ($n = 2$) model is the dominant mode of ethidium intercalation when the TE buffer mentioned earlier is used as the solvent at 25°C. Since the nearest neighbor exclusion model is the generally-accepted mode of ethidium intercalation^{4,6,7}, the TE buffered, temperature-controlled system seems to be a more appropriate environment for studying the unknown binding modes of photonic dyes.

Conclusions

In order to characterize the binding of photonic dyes to DNA, temperature control, buffering, and stirring are all needed to establish favorable experimental conditions. In particular, TE buffer with 10 mM Tris, 10 mM KCl, and 1 mM EDTA at pH 7.2 and 25°C was used successfully to verify the known binding mode of ethidium bromide. Molecular dynamics studies of ethidium bromide are now underway to examine the sterics and energetics of binding to the DNA. Additionally, the binding of ethidium bromide to CTAB- DNA is being investigated in organic solvents. Once this is accomplished, the modes by which photonic dyes such as Chromophores 1 and 2 bind to DNA can be investigated experimentally and theoretically.

References

1. Miller, Andrew D. *Angew. Chem. Int. Ed.* 1998, 37, 1768-1785.
2. Dalton/Robinson Research Groups. "Use of Ion-exchange functionalized DNA as a host material for enhanced poling induced order and molecular hyperpolarizability." REU summer research project description. University of Washington Department of Chemistry.
3. Bigelow, Nicholas. "Ethidium-DNA Binding Analysis Using Experimental Data and Computer Simulation Methods." Senior thesis. 25 May 2008. University of Washington Department of Chemistry.
4. Nordmeier, Eckhard. *J. Phys. Chem.* 1992, 96, 6045-6055
5. Tinoco, Ignacio Jr.; Sauer, Kenneth; Wang, James C. *Physical Chemistry: Principles and Applications in Biological Sciences*, 2nd ed.; Prentice Hall; Englewood Cliffs, New Jersey, 1985; pp. 562-566
6. Alloisio, M.; Guenza, M.; Cuniberti, C. *Special Publication—Royal Society of Chemistry* 1991, 359-360.
7. Nelson, Jeffrey W.; Tinoco, Ignacio Jr. *Biopolymers* 1984, 23, 213-233.

Acknowledgments

Funds for this research were provided by the Center on Materials and Devices for Information Technology Research (CMDITR), the NSF Science and Technology Center No. DMR 0120967. The Dalton research group is gratefully acknowledged for their valuable insights and laboratory space. The authors would also like to thank Nicholas Bigelow for use of equipment and assistance in re-starting the project, as well as Chris Moss for his assistance with molecular dynamics simulations.

DEREK FREI is currently a junior in the Department of Electrical Engineering at the University of Washington with plans to pursue graduate studies in electrical engineering upon graduation. He feels privileged to take part in the investigation of materials that will revolutionize the field of electrical engineering in the future.

Raman Spectroscopy Study of Thermo-Chemical Nanolithography (TCNL) on PPV and Graphene

IVAN GADJEV, Georgia Institute of Technology

S. Kim, D. Wang, E. Riedo, Georgia Institute of Technology

Introduction

Semiconductors are and have been at the heart of the nano-technological advances in electronics. Developing smaller circuits and faster speeds in microelectronic devices is a vibrant field of research. The current material of choice, silicon, has reached its limits in miniaturization and speed¹.

Two promising materials in microelectronics are graphene and conjugated polymers. Graphene has attracted attention because it has high thermal conductivity while its electrical conductivity properties do not disappear at the nanoscale². Conjugated polymers exhibit many of the valuable properties of silicon yet they are cheaper to produce and more mechanically maneuverable³.

Our goal is to explore the use of atomic force microscopy (AFM) to write electrical nanostructures on graphene oxide and PPV precursor samples using the TCNL technique.

A typical electroluminescence polymer (PPV) has desirable conductive properties and may be used in the production of nanoelectronic devices. PPV is produced by thermal conversion of sulfonium salt precursor poly(p-xylene tetrahydrothiophenium chloride). The process takes place in inert gas conditions or a vacuum where the temperature is maintained at around 300°C. This conversion process burns off thiophenium and hydrochloride from the precursor and the result is PPV⁴.

There are a multitude of routes to produce graphene. Some of these include: reduction of exfoliated graphene oxide (GO) sheets with hydrazine^{5,6,7}, deposition of peeled layers of graphite^{2,8}, reduction of SiC⁹, and thermal reduction of a GO sheet. With the last method, it is possible to use AFM to thermally reduce GO sheets. Thermal reduction burns off oxygen in GO sheets and leaves reduced graphene oxide. The method requires temperatures on the order of 400°C.

AFM is a diverse tool which may be used in a variety of disciplines^{10,11}. By operating in contact mode with a mounted thermal tip, AFM is able to induce local thermo-chemical conversions. This process is referred to as thermo-chemical nanolithography (TCNL).

In order to produce electrical nanostructures, a technique of applying high temperature locally must be used. We hope to achieve the needed local precision by fitting an AFM with a thermal tip cantilever. Such a cantilever has a tip area of high resistivity. The rest of the cantilever is composed of two conductive beams. When a voltage difference is applied to the circuit, the tip reaches high temperatures on the order of a few hundred degrees Celsius¹². In principle, operating the AFM in contact mode will yield a “writing”

technique for electrical nanostructures.

Once the nanostructure patterns are written, it must be verified that the thermo-chemical conversion has indeed produced graphene-like material and PPV from graphene oxide and PPV precursor, respectively. First, the conversion will be verified by Raman spectroscopy and secondly we will study temperature dependence of the pattern using Raman Spectroscopy. This is the first step in nanostructure devising by TCNL.

Experimental Methods

The experimental procedure for graphene and PPV followed the same steps: samples are prepared for TCNL and patterned, then Raman spectroscopy data is gathered from the samples.

To prepare the sulfonium salt precursor poly(p-xylene tetrahydrothiophenium chloride) sample slides, glass slides were sonicated in ethanol and rinsed with piranha solution before the coating. The precursor slides were either left as precursor, heated in a vacuum, or heated in ambient conditions. All samples were from the same batch of glass substrate covered with drop-casted precursor. The vacuum heated PPV slides were prepared by annealing the raw precursor for 4 hours at 280°C in ~20 mTorr vacuum.

The TCNL patterning of the PPV and graphite oxide samples was done on commercially produced AFM machines (Multimode IV, Veeco and PicoPlus, Molecular Imaging). The AFM machines were equipped with thermal tips. The TCNL procedure was developed in previous experiments by the lab and details can be found in the supporting references^{13,14}.

Raman data were obtained from the samples (Jobin Yvon HR800) and compared to those of bulk heat-treated samples.

Results and Discussion

Figure 1 shows an optical image of the TCNL patterns on the sulfonium salt precursor. The patterns are seen as blue squares surrounded by a pink region. The pink color of the surroundings may be due to partial pyrolysis of the precursor substrate caused by the geometry of the thermal AFM tip (see figure 2)¹⁵. Heat is dissipated by not only the end of the tip but by the surrounding heater region. The temperature of the cantilever is highest at the tip and drops off linearly with distance¹³. The heater region is about 70 nm from the precursor when the thermal tip is in contact. Its temperature is high enough to cause changes in the precursor from this distance.

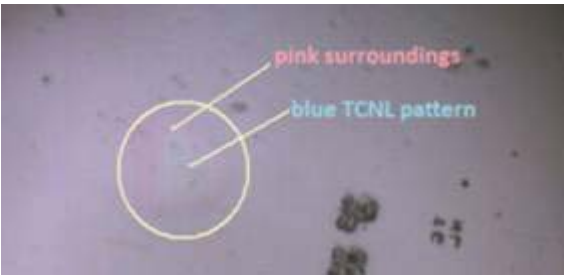


Figure 1. Optical image of TCNL patterns (x10).

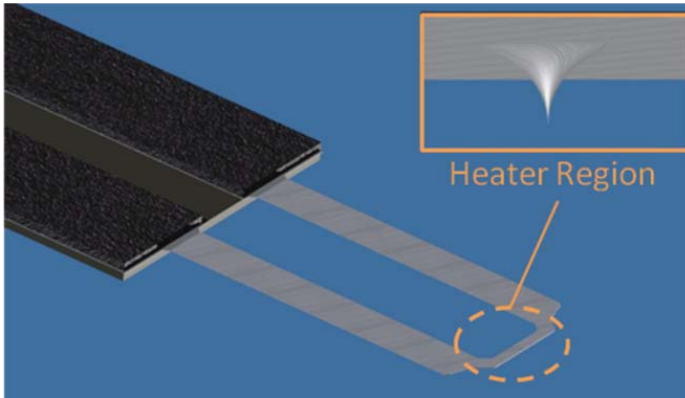


Figure 2. Geometry of thermal tip.

Raman spectroscopic data was gathered from three different PPV samples: raw precursor, vacuum heated PPV, and TCNL patterned PPV. Figure 3 shows the Raman spectroscopy data from a TCNL, vacuum heated PPV, and raw precursor. The dominant peaks in the Raman spectrum of TCNL are found at 1200cm^{-1} , 1340cm^{-1} , and a triple peak at 1550cm^{-1} (not shown). Figure 3 shows the Raman shift in the 1594cm^{-1} peak and the position of the same peak in vacuum heated PPV is 1587cm^{-1} while the raw precursor has a peak at 1593cm^{-1} . The peaks in the Raman spectra of the two TCNL patterns exhibit a shift of about 2cm^{-1} . The pink region has a smaller but still noticeable shift. Also, the TCNL patterns and pink region have narrower, more prominent peaks than the raw precursor. The Raman spectrum of the TCNL area suggests that some of the top portion of the precursor was converted to PPV. TCNL patterning of raw precursor was repeated on a sample with greater thickness. Six patterns were written using the TCNL procedure. The voltage applied to the thermal tip for the patterns was different for each pattern and varied from 8.5V to 14V. Their spectra exhibit the same characteristics as the TCNL patterns performed on the thinner precursor. That is, the peaks are augmented and there is a shift towards vacuum heated PPV.

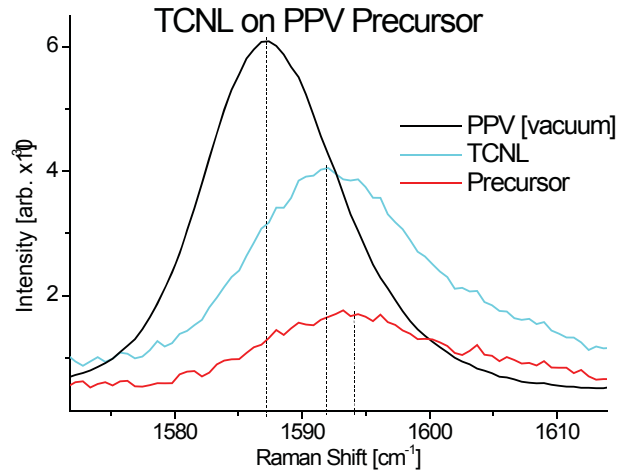


Figure 3. Raman spectra of TCNL patterns, vacuum heated PPV, and raw precursor.

Next, the TCNL technique was applied to graphene oxide samples. As with the samples of PPV, Raman spectroscopy was used to decide whether thermal conversion had occurred in the TCNL patterns. Figure 4 compares the Raman spectrum of a TCNL pattern to that of unaltered graphene oxide. The dominant peaks in the spectrum of graphene oxide are the D band at $\sim 1310\text{cm}^{-1}$ and the G band at $\sim 1600\text{cm}^{-1}$. The D band is due to disorder in the lattice structure of graphite. As more structural disorder is introduced, the ratio of the intensity of the D band to the intensity of the G band (I_D/I_G) will increase^{5,7}. We see such an increase: $I_D/I_G = 1.41$ for the GO sample and $I_D/I_G = 1.66$ for the graphene TCNL pattern. The increase of the intensity ratio indicates that TCNL introduces structural disorder in GO.

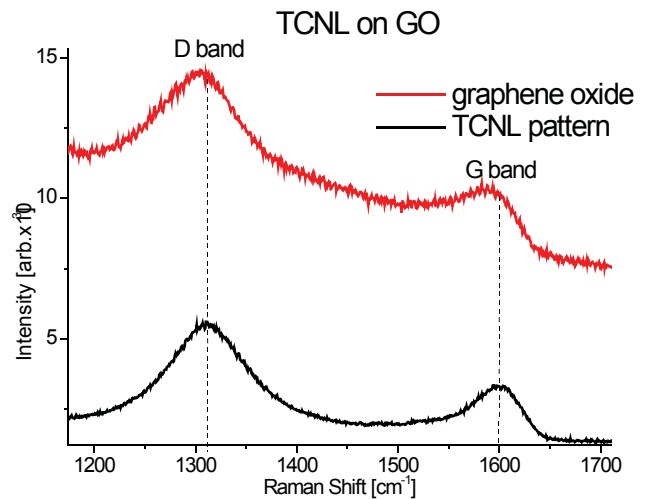


Figure 4. Raman spectrum of graphene oxide (GO) and TCNL pattern on GO.

A shift is seen in the spectrum of the reduced graphene oxide. The D band exhibits a shift of 10cm^{-1} . There is no significant shift in the G band. The literature suggests that the G band should shift towards lower frequency¹⁶. Future work will investigate this discrepancy.

It must be mentioned that GO sheets are not uniform in topography. It is found that the height of a single GO layer may vary as much as 0.6nm ¹⁷. The samples of GO used for TCNL had on average 20 layers. This corresponds to a variation of as much as 10nm . It is possible that the TCNL patterning was done in a region with a deficient number of GO layers. The TCNL technique would then “burn off” enough GO for the layer of graphene underneath to be visible. This in essence does not produce graphene by thermal conversion but exposes the already existing layer of graphene underneath the GO layers. This will also alter the Raman spectrum of the TCNL pattern. Since this graphene layer is so close to the epitaxial graphite (SiC) substrate on which the GO film was deposited, the Raman spectrum will also have contributions from the SiC.

Conclusion

A novel technique, TCNL for writing nanoelectrical patterns has been investigated using Raman Spectroscopy. TCNL was performed on samples of PPV precursor and GO. In both cases, the patterns exhibited structural differences as assessed by Raman spectroscopy. Raman data for the PPV samples suggests that thermal conversion took place at the top portions of the PPV precursor. TCNL also reduced graphene oxide sheets to a graphene-like structure. Further directions will examine the topographic and electric properties of the patterns through friction AFM, Kelvin probe AFM, and proof of concept nanoscale circuits.

References

1. R. W. Keyes. Fundamental Limits of Silicon Technology. Proceedings of the IEEE. 2001;89(3):227-239.
2. A. K. Geim, K. S. Novoselov. The Rise of Graphene. Nature Materials. 2007;6:183-191.
3. J. H. Burroughes, D. D. C. Bradley, A. R. Brown, R. N. Marks, K. Mackay, R. H. Friend, P. L. Burns, A. B. Holmes. Light-emitting diodes based on conjugated polymers. Nature 1990;347:539-541
4. D. C. Bradley, Precursor-route poly(p-phenylenevinylene): polymer characterization and control of electronic properties. J. Phys. D: Appl. Phys. 1987;20:1389.
5. S. Stankovich, D. A. Dikin, R. D. Piner, K. A. Kohlhaas, A. Kleinhammes, Y. Jia, Y. Wu, S. T. Nguyen, R. S. Ruoff. Synthesis of graphene-based nanosheets via chemical reduction of exfoliated graphite oxide. Carbon 2007;45(7):1558-1565.
6. S. Gilje, S. Han, M. Wang, K. L. Wang, R. B. Kaner. A chemical route to graphene for device applications. NanoLetters 2007;7(11):3394-3398
7. J. I. Paredes, S. Villar-Rodil, P. Solis-Fernandez, A. Martinez-Alonso, J. M. D. Tascon. Atomic Force and Scanning Tunneling Microscopy Imaging of Graphene Nanosheets Derived from Graphite Oxide. Am. Chem. Soc. 2009;25(10):5957-5968
8. Geim, A. K.; Novoselov, K. S. The rise of graphene. Nat. Mater 2007;6(3):183-191.
9. Berger, C.; Song, Z.; Li, T.; Li, X.; Ogbazghi, A. Y.; Feng, R.; Dai, Z.; Marchenkov, A. N.; Conrad, E. H.; First, P. N.; de Heer, W. A. Ultrathin Epitaxial Graphite: 2D Electron Gas Properties and a Route toward Graphene-based Nanoelectronics. J. Phys. Chem. B 2004;108(52):9912-19916.
10. E. Meyer, H. J. Hug, R. Bennewitz. Scanning Probe Microscopy The Lab on a Tip. Springer, New York, 2004:45-95.
11. Veeco Metrology Group. Scanning Probe Microscopy Training Notebook. 2000.
12. J. Lee, T. Beechem, T. L. Wright, B. A. Nelson, S. Graham, W. P. King. Electrical, Thermal, and Mechanical Characterization of Silicon Microcantilever Heaters. J. Microelectromech. Syst. 2006;15(6):1644-1655
13. R. Szoszkiewicz, T. Okada, S. C. Jones, Tai-De Li, W. P. King, S. R. Marder, E. Riedo. High-Speed, Sub-15 nm Feature Size Thermochemical Nanolithography. Nano Letters. 2007;7(4):1064-1069
14. D. B. Wang, R. Szoszkiewicz, M. Lucas, E. Riedo, T. Okada, S.C. Jones, S. R. Marder, J. Lee, W. P. King, Local wettability modification by thermochemical nanolithography with write-read-overwrite capability. Appl. Phys. Lett., 2007;91:243104.
15. Jeff Carpenter. Woodruff School of Mechanical Engineering at Georgia Institute of Technology.
16. K. N. Kudin, B. Ozbas, H. C. Schniepp, R. K. Prud'homme, I. A. Aksay, R. Car. Raman Spectra of Graphite Oxide and Functionalized GRaphene Sheets. NanoLetters 2008;8(1):36-41
17. K. A. Mkhoyan, a. W. Contryman, J. Silcox, D. A. Stewart, G. Eda, C. Mattevi, S. Miller, M. Chhowalla. Atomic and Electronic Structure of Graphene-Oxide. Nano Lett. 2009;9(3):1058-1063.

Acknowledgements

Funds for this research were provided by the Center on Materials and Devices for Information Technology Research (CMDITR), NSF Science and Technology Center No. DMR 0120967.

IVAN GADJEV plans to graduate with a B.S. in Physics from Georgia Tech and go into theoretical high energy or theoretical astrophysics research.

Ab Initio Calculations of the Torsion Potentials of Polyacetylene Oligomers

MATTHEW GRAY, University of Michigan

John Sears, Jean-Luc Brédas, Georgia Institute of Technology

Introduction

Conjugated polymers are of interest for their numerous useful properties and applications. These materials offer semi-conducting electrical properties combined with easy, low-cost processing,¹ large non-linear² and linear³ optical response, and facile integration on flexible substrates making them of great interest for applications in electronics and photonics.⁴ Conjugated polymers have thus received a great amount of attention and research.⁵⁻¹⁶ Investigations into the connection between the optical/electronic properties and polymer conformation¹⁰⁻¹⁶ have demonstrated the importance of planarity and conjugation length.¹⁷ Theoretical calculations of the torsion potentials in these compounds allow for a more detailed understanding of conformational disorder and conjugation length in these systems. Investigations¹³⁻¹⁶ into the torsion potentials of polydiacetylene (PDA) chains have been frequently undertaken but with conflicting results. Early calculations¹³ have suggested a torsion barrier potential in PDA of less than 1 kcal mol⁻¹ while recent calculations¹⁴ have suggested a value between 20 and 27 kcal mol⁻¹. These conflicting reports demonstrate the need for a thorough study of PDA using multiple computational techniques. The related compound polyacetylene is of interest for many reasons. Polyacetylene is the simplest possible conjugated polymer: fundamental understanding of polyacetylene improves our ability to understand all conjugated polymers. The similarity to PDA allows for a comparison of how different quantum-chemical techniques handle different systems. The torsion potentials of polyacetylene have not been recently investigated¹⁴ and have received little study since the earlier paper¹³. Given the PDA discrepancy cited previously it is of interest to investigate the previously calculated torsion potentials for polyacetylene. Thus while an investigation into PDA is pursued elsewhere, a parallel study of polyacetylene is undertaken here.

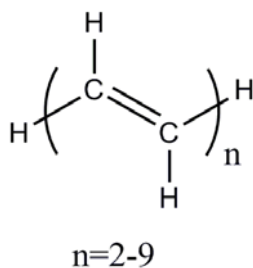


Figure 1. Oligomers of polyacetylene studied here

The torsion barrier energies of numerous polyene oligomers, starting with 1,3-butadiene up to H-(HCCH)₉-H (see Figure 1), will be calculated. The torsion barrier potentials calculated here represent

torsions around the central carbon-carbon single bond of the molecules. The torsion potential of the polymer is approximated by extrapolation to the behavior of an infinitely long oligomer. Multiple basis sets and quantum-chemical methods will be employed and their approximations analyzed to determine both the necessary computational complexity needed for an accurate prediction and the accuracy of different quantum-chemical techniques for modeling these systems.

Results and Discussion

The torsion barrier potentials of the polyacetylene compounds are calculated using the MOLPRO¹⁸ and Q-Chem¹⁹ software packages on Georgia Institute of Technology's Center for Computational Molecular Science and Technology's computer clusters. A series of calculations are run with fixed torsions occurring at the central carbon-carbon single bond. For each molecule the carbon-carbon single bond is set at torsion angles of 0°, 30°, 60°...180°, while all other geometric parameters are allowed to relax. The potentials for polyenes H-(HCCH)_n-H, where n=2,3,4...9, are calculated using second order Møller–Plesset perturbation theory (MP2) with an augmented correlation-consistent polarized valence double-zeta²⁰ (aug-cc-pVDZ) basis set. The torsion barrier potential for the polymer was determined via extrapolation to an infinitely long oligomer using the assumed 1/n oligomer length to torsion potential relation (see Figure 2). The barrier potential at the MP2/aug-cc-pVDZ computational level was calculated here as being 11.46 kcal mol⁻¹.

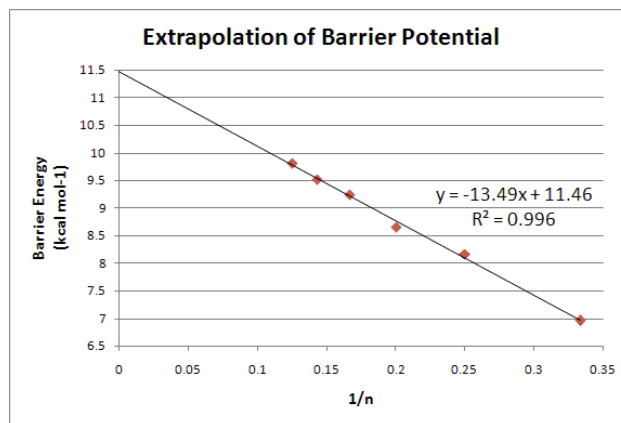


Figure 2. Extrapolation of polyene torsion potential to polymer limit

Quadratic configuration interaction with singles and doubles²¹ (QCISD) and MP2 with a triple-zeta²⁰ (aug-cc-pVTZ) basis set are used on the shortest polyene (1,3-butadiene) in order to benchmark the accuracy of the MP2/aug-cc-pVDZ geometry optimization and determine the relative importance of additional electron correlation effects and basis set effects. The coupled-cluster method with singles, doubles, and perturbative triple excitations (CCSD(T)) is then used as our highest level computation to most accurately determine the energies of these optimized geometries (Figure 3). The near identical torsion barrier energies predicted by the single point CCSD(T) calculations demonstrates that the basis set effects and electron correlation effectively do not improve the geometry optimizations. Likewise an error of only about 0.3 kcal mol⁻¹ is observed between the MP2/aug-cc-pVDZ energy and CCSD(T) energy. Given the computationally prohibitive cost of CCSD(T) at the system sizes of interest in this study, this is an unavoidable error that must be kept in mind. Thus MP2/aug-cc-pVDZ geometries provide excellent approximations in this system, while MP2/aug-cc-pVDZ energies are within a reasonable amount of error, slightly overestimating the torsion barrier energy.

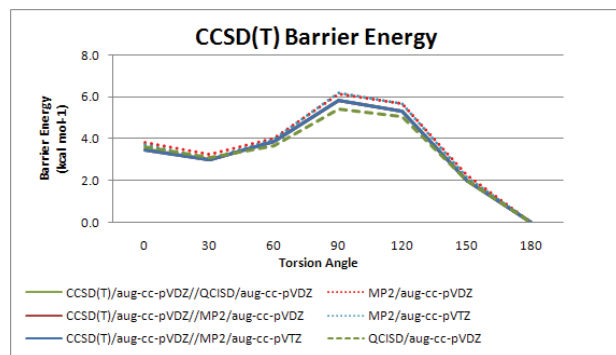


Figure 3. CCSD(T) calculation demonstrating relative accuracy of the MP2/aug-cc-pVDZ method

Density functional theory (DFT) approaches are next analyzed in comparison to the MP2/aug-cc-pVDZ level of theory. The ability of these techniques to properly model this system is of interest because of their popularity and low computational requirements. As expected, the DFT methods increasingly deviate from the higher level computational technique as the size of the system increases (Figure 4).

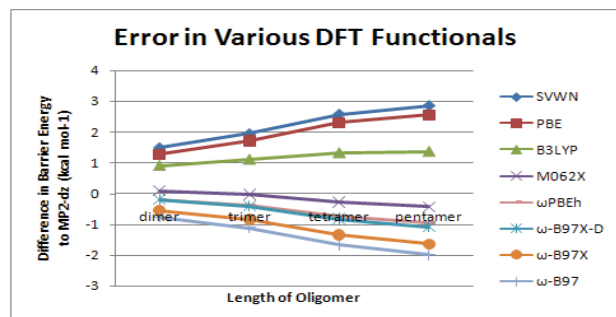


Figure 4. DFT calculations demonstrating relative accuracy of different models against MP2/aug-cc-pVDZ method

The torsion potentials of the first few oligomers are calculated using a variety of different DFT functionals in order to test a spectrum of DFT techniques. Local density approximation (LDA) functionals, such as S²³VWN,²⁴ estimate the properties of the system using only the electron density at a specific point in space. The similar generalized gradient approximation (GGA) functionals, such as PBE,²⁵ use the gradient of the electron density at a specific point in addition. B3LYP²⁶ is an example of a hybrid exchange–correlation functional which simply mixes some Hartree-Fock (HF) exchange with LDA or GGA functionals in order to model some of the longer-range behavior. M06-2X²⁷ is a hybrid meta functional similar to B3LYP but utilizes kinetic energy terms along with the GGA portion of the functional to enact some midrange correlation. Long-range-corrected (LRC) functionals, such as the ω-B97^{28,29,30} series, utilize a similar approach but manipulate the functional so that short range GGA type behavior dominates while at longer ranges the HF contributions dominate.

Conclusions

The torsion barrier potential for polyacetylene (at the polymer limit) is predicted here to be 11.46 kcal mol⁻¹. This extrapolation to the polymer limit marks a sizable increase in the torsion potential from previous calculations.¹⁴ The previous study cited experimental evidence³² that chain end torsions have the smallest torsion barriers and thus are the most likely location of polymer torsions. The study then used the torsion barrier potentials of chain end torsions as the approximation of the polymer behavior instead of extrapolating the behavior of central torsions to the large oligomer limit. Nevertheless, torsion barrier potentials of central torsions were calculated in the past study for two oligomers. The values calculated in this past study for the torsion potential of the tetramer (6.88 vs. 8.16 kcal mol⁻¹ here) and pentamer (7.34 vs. 8.66 kcal mol⁻¹ here) underestimate the torsion potential, though the difference is much less than an order of magnitude. This suggests that the torsion potential of PDA would likely lie closer to the smaller of the previously reported, conflicting values.^{13,14} A parallel study with PDA has been undertaken to investigate this suggestion.

MP2/aug-cc-pVDZ is shown to be an ideal method for these systems well approximating higher-level techniques like QCISD and CCSD(T). MP2/aug-cc-pVDZ also handles increasingly large systems without imposing extreme computational requirements.

As expected, the short range LDA and GGA functionals overestimate the torsion barrier potential and diverge sharply as the system size is increased. This is likely due to the problem of electron self-interaction, which causes the orbitals to be too diffuse and increases the strength of conjugation effects. It is slightly more surprising that the long range LRC functionals diverge nearly as quickly from the MP2/aug-cc-pVDZ estimations as the LDA methods. This could be due to the exclusion of electron correlation effects which would reduce the influence of conjugation properties. Despite a poor approximation to the smallest oligomer, the hybrid method B3LYP suffers slightly less from divergence issues.

While the other DFT methods investigated here diverge quickly as the system size increases, the M06-2X²⁰ method is successful at slowing the divergence problem. This is surprising given that the M06-2X functional takes into account many of the same

considerations as B3LYP and the LRC methods. ω PBEh³¹, another hybrid method much like M06-2X, takes into account full LRC; the increased divergence of ω PBEh compared to M06-2X seems to indicate that increased long-range corrections lead to underestimation of the barrier energy as suggested.

The predicted torsion barrier potential of 11.46 kcal mol⁻¹ should not be easily overcome at room temperature (~0.6 kcal mol⁻¹). Thus conformations in the polymer chain should be stable and conformation transitions infrequent. With the current data we thus conclude that the initial polymerization conformation or any thermally or chemically altered conformation should be stable at room temperature. Therefore perpendicular 'kink' conformations interrupting the conjugation of the system should not be present nor an important consideration in the optical and electronic properties of polyacetylene. On the other hand, cis and trans conformations are both stable and could be present depending on past processes. In order to comprehensively compare to past research, it is suggested that the torsion potentials of rotations around carbon-carbon single bonds next to the end of the oligomer be investigated. Past research³² has suggested that such rotations are the lowest in energy and thus more likely available for torsion at room temperature. Likewise, the effect of conjugation breaking torsions on the barrier potentials of other nearby torsions is of interest for future research. Determining whether the torsion barrier curve of a torsion next to a conjugation breaking torsion more resembles an all trans central torsion or a near-chain-end torsion would be extremely helpful in thinking about these conjugated systems. Though the DFT methods are shown to all diverge in accuracy as the system size increases, it is suggested that they be used in such further investigations due to the computationally prohibitive cost of modeling such large systems with MP2 or other higher level models. It is suggested that the M06-2X and other hybrid methods should be further investigated to pursue these studies.

References

1. Semiconducting Polymers: Chemistry, Physics and Engineering, 2 ed.; Hadziioannou, G.; Malliaras, G. G., Eds.; Wiley-VCH: Weinheim, 2007.
2. Song, J.; Watson, M.; Sekino, H.; Kimihiko, H. *J. Chem. Phys.* 2008, 129, 024117.
3. Carpick, R. W.; Sasaki, D. Y.; Burns, A. R. *Langmuir* 2000, 16, 1270-1278.
4. Shaw, J. M.; Seidler, P. F. *IBM J. Res. Dev.*, 2001, 45, 3-9.
5. Son, S.; Dodabalapur, A. J.; Galvin, M. E. *Science* 1995, 269, 376.
6. Schwartz, B. J. *Annu. Rev. Phys. Chem.* 2003, 54, 141-72.
7. Ma, J.; Li, S.; Jiang, Y. *Macromolecules* 2002, 35, 1109.
8. Salzner, U.; Lagowski, J. B.; Pickup, P. G.; Roirier, R. A. *Synthetic Metals* 1998, 96, 177.
9. Roncali, J. *Chem. Rev.* 1997, 97, 173.
10. Yu, J.; Hu, D.; Barbara, P. F. *Science* 2000, 289, 1327.
11. Almeida, A. M.; Ramos, M. M. D.; Correia, H. G. *Computational Materials Science* 2003, 27, 128-132.
12. Correia, H. G.; Barbosa, H.M.C.; Ramos, M. M. D. *Journal of Non-Crystalline Solids* 2006, 352, 1691-1694.
13. Filhol, J. S.; Deshamps, J.; Dutremez, S. G.; Boury, B.; Barisien, T.; Legrand, L.; Schott, M. J. *Am. Chem. Soc.* 2009, 131, 6976-6988.
14. Brédas, J. L.; Heeger, A. J. *Macromolecules* 1990, 23, 1150.
15. Dykstra, T. E.; Hennebicq, E.; Beljonne, D.; Gierschner, J.; Claudio, G.; Bittner, E. R.; Knoester, J.; Scholes, G. D. *J. Phys. Chem.* 2009, 113, 656.
16. Garavelli, M.; Smith, B. R.; Bearpark, M. J.; Bernardi, F.; Olivucci, M.; Robb, M. A. *J. Am. Chem. Soc.* 2000, 122, 5568-5581.
17. Kohler, B. E.; Woehl, J. C. *Synthetic Metals*, 1997, 84, 851-852.
18. MOLPRO, version 2008.1, a package of ab initio programs, H.-J. Werner, P. J. Knowles, R. Lindh, F. R. Manby, M. Schütz, P. Celani, T. Korona, G. Rauhut, R. D. Amos, A. Bernhardsson, A. Berning, D. L. Cooper, M. J. O. Deegan, A. J. Dobbyn, F. Eckert, C. Hampel and G. Hetzer, A. W. Lloyd, S. J. McNicholas, W. Meyer and M. E. Mura, A. Nicklass, P. Palmieri, R. Pitzer, U. Schumann, H. Stoll, A. J. Stone, R. Tarroni and T. Thorsteinsson, see <http://www.molpro.net>.

19. Q-Chem, version 3.2. Y. Shao, L. Fusti-Molnar, Y. Jung, J. Kussmann, C. Ochsenfeld, S. T. Brown, A. T. B. Gilbert, L. V. Slipchenko, S. V. Levchenko, D. P. O'Neill, R. A. Distasio Jr., R. C. Lochan, T. Wang, G. J. O. Beran, N. A. Besley, J. M., Herbert, C. Y. Lin, T. Van Voorhis, S. H. Chien, A. Sodt, R. P. Steele, V. A. Rassolov, P. E. Maslen, P. P. Korambath, R. D. Adamson, B. Austin, J. Baker, E. F. C. Byrd, H. Dachsel, R. J. Doerksen, A. Dreuw, B. D. Dunietz, A. D. Dutoi, T. R. Furlani, S. R. Gwaltney, A. Heyden, S. Hirata, C.-P. Hsu, G. Kedziora, R. Z. Khalliulin, P. Klunzinger, A. M. Lee, M. S. Lee, W. Liang, I. Lotan, N. Nair, B. Peters, E. I. Proynov, P. A. Pieniazek, Y. M. Rhee, J. Ritchie, E. Rosta, C. D. Sherrill, A. C. Simmonett, J. E. Subotnik, H. L. Woodcock III, W. Zhang, A. T. Bell, A. K. Chakraborty, D. M. Chipman, F. J. Keil, A. Warshel, W. J. Hehre, H. F. Schaefer III, J. Kong, A. I. Krylov, P. M. W. Gill, M. Head-Gordon, *Phys. Chem. Chem. Phys.*, (2006) 8, 3172 - 3191.
20. Kendall, R. A.; Dunning, Jr., T. H.; Harrison, R. J. *J. Chem. Phys.* 1992, 96, 6796-6806.
21. Pople, J. A.; Headgordon, M.; Raghavachari, K. *J. Chem. Phys.* 1987, 87, 5968-5975.
22. Raghavachari, K.; Trucks, G. W.; Pople, J. A.; Head-Gordon, M. *Chem. Phys. Lett.*, 1989, 157, 479.
23. Dirac, P. A. M. *Proc. Cam. Phil. Soc.*, 1930, 26, 376.
24. Vosko, S. H.; Wilk, L.; Nusair, M. *Can. J. Phys.*, 1980, 58, 1200.
25. Perdew, J.P.; Burke, K. ; Ernzerhof, M. *Phys. Rev. Lett.*, 1996, 77, 3865.
26. Stephens, P. J.; Devlin, F. J.; Chabalowski, C. F.; Frisch, M. J. *J. Phys. Chem.*, 1994, 98, 11623-11627.
27. Zhao, Y.; Truhlar, D. G. *Theor. Chem. Account*, 2008, 120, 215-241.
28. Chai, J.-D.; Head-Gordon, M. *J. Chem. Phys.*, 2008, 128, 084106.
29. Chai, J.-D.; Head-Gordon, M. *Phys. Chem. Chem. Phys.*, 2008, 10, 6615.
30. Chai, J.-D.; Head-Gordon, M. *Chem. Phys. Lett.*, 2008, 467, 176.
31. Rohrdanz, M. A.; Martins, K. M.; Herbert, J. M.; *J. Chem. Phys.*, 2009, 130, 054112.
32. Ackerman, K. R.; Kohler, B. E. *J. Chem. Phys.*, 1984, 80, 45.

Acknowledgments

Funds for this research were provided by the Center on Materials and Devices for Information Technology Research (CMDITR), NSF Science and Technology Center No. DMR 0120967.

Computations were supported by the Center for Computational Molecular Science and Technology at the Georgia Institute of Technology.



MATTHEW T. GRAY hopes to obtain a doctorate in either Chemistry or Materials Science and Engineering with which he plans to research in the field of organic electronics.

Designing and Implementing a Temperature Programmed Desorption Instrument for the Study of Organic Thin Films

MELISSA A. HEALEY, Cornell University

Nahid Ilyas, Mary P. Steele, Michael L. Blumenfeld, and Oliver L.A. Monti, University of Arizona

Abstract

A temperature programmed desorption (TPD) instrument was developed to characterize the surface orientation of organic thin films, as well as analyze the energetic properties at the film interface. Preliminary data were collected on sexithiophene (6T) films deposited on highly ordered pyrolytic graphite (HOPG).

Introduction

The goal of this project was to design and implement a temperature-programmed desorption (TPD) instrument so as to aid in achieving a better understanding of interfacial structure of thin organic films in organic solar cells. Highly ordered organic films typically show multiple growth modalities with significant influence on their electronic properties. Yet these modalities are often difficult to observe spectroscopically, requiring alternative approaches. In addition to qualitative film characteristics, temperature programmed desorption can quantitatively determine kinetic parameters of desorption specific to the molecule-substrate combination studied.

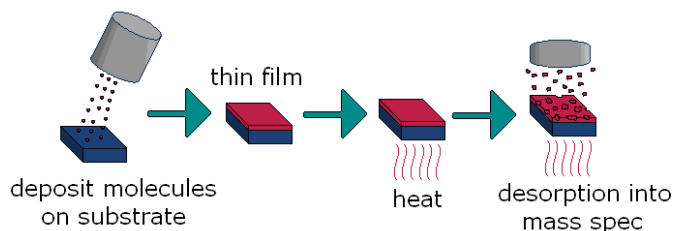


Figure 1

The basic schematic of temperature programmed desorption is as follows:

1. Deposition of a thin film of material on a substrate,
2. Subsequent heating of the thin film, and
3. Analysis of desorbed molecules through a mass spectrometer (see Fig. 1). This formed the basis for the design of the instrument. Many other considerations were taken into account, such as the ability to measure film thickness through use of a quartz crystal microbalance, and a finished, working instrument was successfully achieved (Fig. 2 and 3).

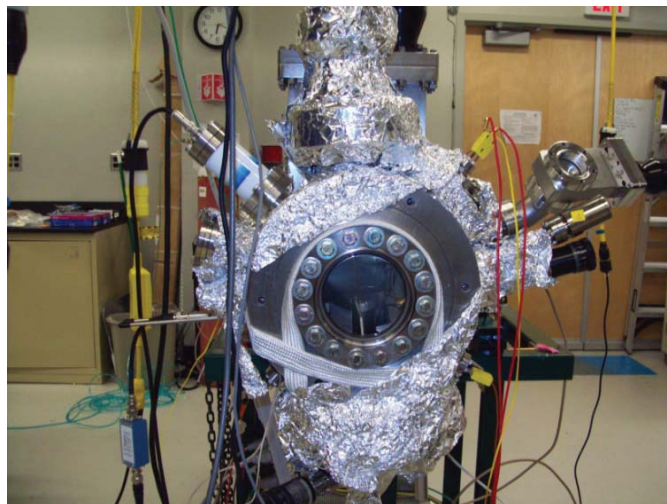


Figure 2

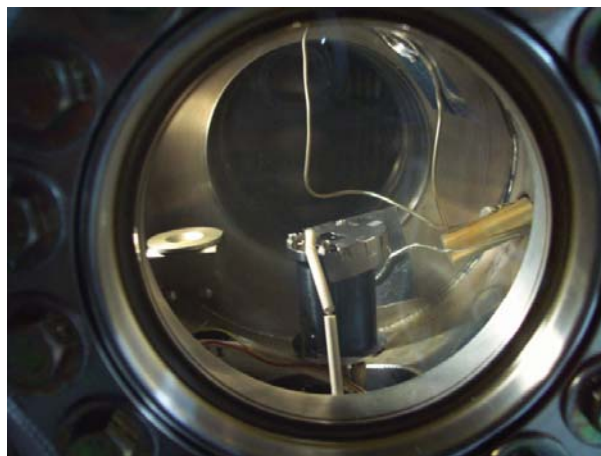


Figure 3

Experimental

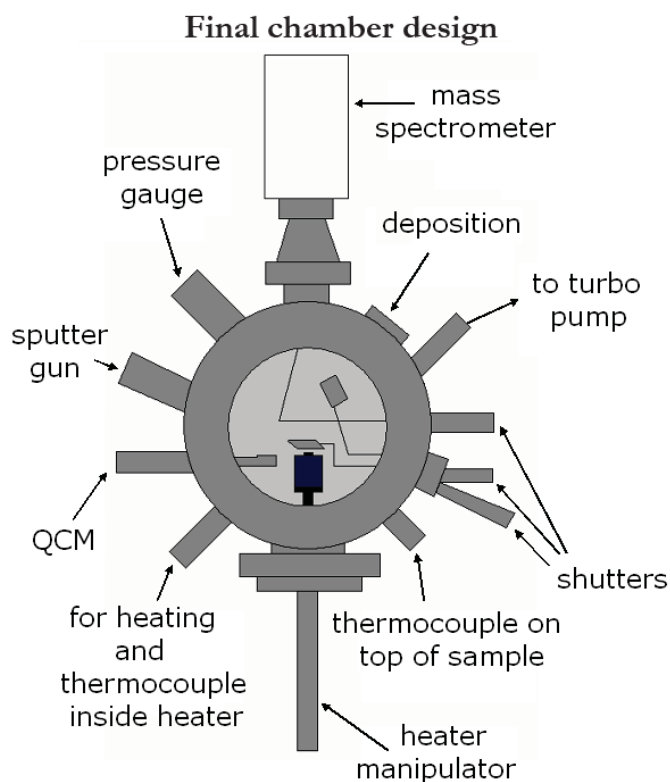
The final chamber design for temperature programmed desorption is shown in figure 4.

A 1 cm square piece of highly ordered pyrolytic graphite (HOPG) was used as the substrate for each experiment. The sample was clipped onto a copper plate, which was mounted on the heater (HeatWave Labs: Model 101491 UHV/O₂ Heater with Sample Clips). This copper plate was to secure the sample to the heater surface (~1 inch diameter) and ensure easy mounting and removal

of the sample. A tantalum cap was fitted over the surface of the heater, with a hole slightly larger than the sample (Fig. 3). This cap was used to prevent excess deposition on the heater surface. A thermocouple was spot welded onto the top of the sample for accurate temperature measurement. This thermocouple was sent to a temperature controller (HeatWave Labs: Model 101303-22A Temperature Controller with Watlow Series 96 1/16 DIN Temperature Controller) as input 1. Two outputs from this temperature controller were used. Output 1 was used for heating, and output 4 was used to send temperature data to the mass spectrometer by means of an analog output voltage from 0-5 V. The entire heater apparatus was attached to a manipulator arm with greater than 30 cm of vertical travel capability.

The main chamber was attached to both a turbo molecular pump, and an ion pump. Through baking at 115°C for about 48 hours, ultra high vacuum (UHV) was achieved (base pressure 10-9 mbar). This was necessary to remove air and water from inside the chamber.

Three shutters were incorporated into the chamber. These were used to: 1. cover the mass spectrometer while deposition occurred, 2. cover the Knudsen cell while out-gassing, and 3. cover the sample while depositing on the quartz crystal microbalance (QCM).



(not shown) back of chamber → ion pump

Figure 4

A homemade Knudsen effusion cell filled with sexithiophene (6T) was heated at 260°C for at least 10 minutes before each experiment. The 6T was then deposited on the QCM until a rate of 1 Å/min was established. Deposition on the HOPG sample occurred at a little above room temperature (~35°C).

After the Knudsen cell was cooled to less than 200°C, the sample was moved vertically until it was a 2-3 mm away from a quadrupole mass spectrometer (QMS 200 Prisma™). An aperture was designed to block unwanted molecules from entering the mass spectrometer. This aperture was slightly smaller than the sample size, in order to neglect edge effects during desorption.

The temperature of the sample was ramped from ~35°C to ~470°C (temperature of annealing HOPG). The temperature ramp was linear, typically 1 K/s. Output from the mass spectrometer was able to record the temperature of the sample and the ion current of desorbing fragments simultaneously through mass spectrometer software Quadstar 422 version 6.0. A background scan before and during deposition was used to identify key fragments of 6T. Plots of ion current vs. temperature were obtained for various initial coverages.

Results

Preliminary data were collected for 6T on HOPG, using a temperature ramp of 1 K/s. Initial film coverages from 5Å-50Å were used. A clear peak at around 133°C was observed for all 6T fragments that were monitored during desorption (Fig. 5). In addition, an initial coverage comparison of a single fragment shows an increase in ion current with increasing coverage (Fig. 6). This indicates that the peak at 133°C is caused by desorption from the multilayer. Kinetic analysis of this data would help us gain insight into the interactions between 6T molecules, and not the desired interface interactions between 6T and HOPG.

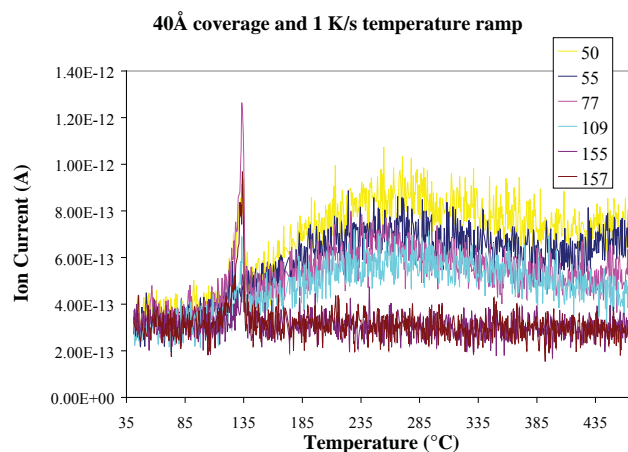


Figure 5

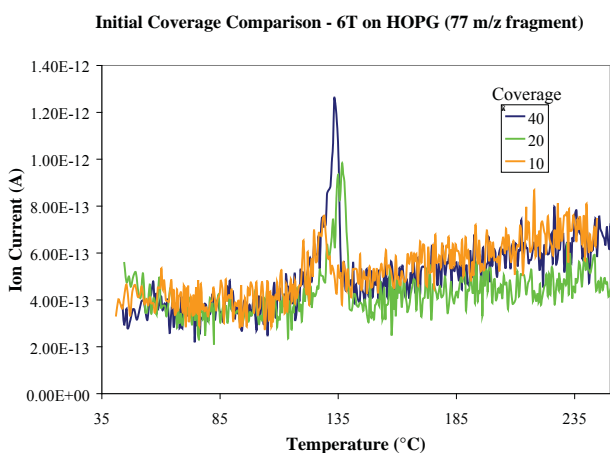


Figure 6

Discussion

Potential reasons that monolayer desorption was not observed could be due to the sensitivity of the instrument, or the crystalline disorder of very thin 6T films on HOPG (Fig. 7). In order to increase sensitivity of the instrument, a new heater will be designed to be smaller than the sample surface. This will eliminate the need for a tantalum cap, which may be causing unwanted molecules to desorb into the mass spectrometer. The thermocouple on top of the sample will then be moved to underneath the sample, eliminating any desorption from the thermocouple wires as well. In addition, 6T will be replaced by vanadyl-naphthalocyanine (VONc), in order to support other research in the lab. HOPG will still be used as a substrate. Additionally, Cu(111) substrates will be used once a sputter gun is incorporated into the chamber. With these changes, more accurate temperature desorption spectra should be achieved, and kinetic analysis of VONc on HOPG and VONc on Cu(111) will be performed.

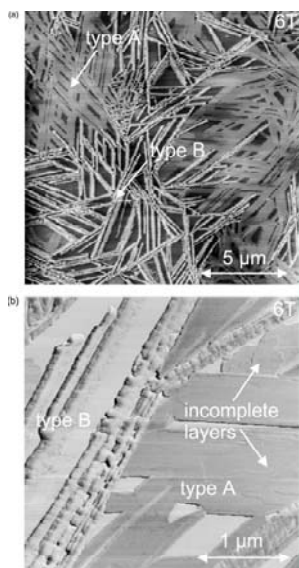


Figure 7 (a) AFM image of a nominal 1nm thick 6T film deposited on HOPG at 300K. (b) an enlarged area is shown. (Ref. 1)

Conclusion

In conjunction with scanning probe microscopy, these TPD data will afford a detailed understanding of specific growth modalities and their potential impacts on thin film device properties. Because HOPG provides a surface of weak attraction, the structural information provided by TPD will be able to model weakly interacting electrode/organic interfaces, or even provide insight into organic/organic interfaces. In contrast, Cu(111) will be able to model strongly interacting electrode/organic interfaces. This will provide critical information to designing organic photovoltaic cells.

In addition, previous research has shown that VONc arranges on the surface in three distinct states. TPD data will help confirm these findings.^{2,3}

References

1. M. Schneider, M. Brinkmann, M. Muccini, F. Biscarini, C. Taliani, W. Gebauer, M. Sokolowski, and E. Umbach, *Chemical Physics* 285 (2002) 345–353.
2. M.L. Blumenfeld, M.P. Steele, O.L.A. Monti, *Appl. Phys. Lett.*, submitted (2009)
3. M.L. Blumenfeld, M.P. Steele, O.L.A. Monti, *J. Appl. Phys.*, submitted (2009)

Acknowledgments

We gratefully acknowledge financial support from the National Science Foundation (CHE-0618477), a National Science Foundation Graduate Research Fellowship for MLB, and the NSF sponsored Science and Technology Center on Materials and Devices for Information Technology Research, No. DMR-0120967. We would also like to thank Ken Nebesny, Paul Lee and the University of Arizona Chemistry Department Machine Shop and Electronics Facility for their valuable contributions.



MELISSA HEALEY is a student at Cornell University and will be completing her degree in chemical engineering in May 2010. She is planning on pursuing a Ph.D. upon graduation.

Passive Wireless Sensors using Reflected Electro-Material Signatures (REMS)

RYAN HEARTY, Johns Hopkins University

Azhar Hasan, Gregory Durgin, Georgia Institute of Technology

Introduction

This research paper discusses passive, wireless data sensors which use reflected electro-material signatures (REMS). REMS technology allows environmental information (i.e. temperature, pH, and changes in the local magnetic field) to be recorded electrodelessly by a sensor and to be read back using passive radiofrequency identification wireless communication. To confirm that a REMS sensor is possible, two models of the REMS material line were constructed: the first, a physical model using a microstrip transmission line embedded with a superparamagnetic substrate; the second, a simulated model of this physical design using Agilent's Advanced Design System software.

RFID Overview

An outline of a standard RFID network is shown in Fig. 1.

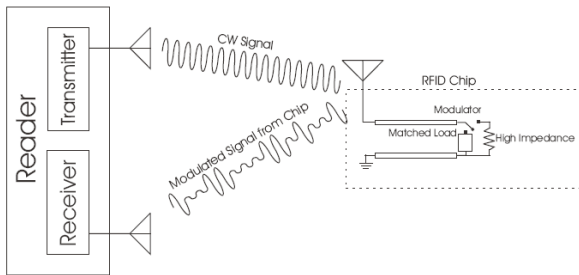


Fig. 1. A model RFID system. CW signal is received at the tag's antenna, travels down the tag's transmission line to the modulation circuitry, where Z_L is either matched or short. This modulates the backscattered wave, encoding identification information.

The conventional purpose of RFID is to obtain identification information from a target RFID tag. An RFID system consists of two main components: the reader (or interrogator) and the RFID tag (or transponder). The reader transmits a continuous-wave (CW) signal which is received by the RFID tag antenna. This signal is used both as a power source for the tag's integrated circuitry (RFIC) and as the carrier signal for the chip's modulated identification code. First, the signal is received by the RFID tag antenna; then it travels down the tag's transmission line, is modulated using an on-board modulator, and reflected back down the transmission line and finally transmitted back by the antenna. This passive technique uses what is called backscattered radiation, because the signal is reflected back to the reader passively by the tag².

Physical Material Line Model

To construct a model of a REMS device, three microstrip transmission lines with different dielectric constants were cascaded together. The objective was to emulate a transmission line with different material properties in different segments of the device, as in Fig. 2. This design introduces discontinuities in the transmission line that will cause reflections at each boundary. The amplitude of the reflected wave at each boundary is proportional to the change in the relative permittivity, ϵ_r . The reflection coefficient, defined as

$$\Gamma = \frac{V_0^-}{V_0^+} = \frac{Z_L - Z_0}{Z_L + Z_0}$$

is related to the relative permittivity of the line through Z_L and Z_0^{-1} , and reduces to

$$\Gamma = \frac{\sqrt{\epsilon_r} - \sqrt{\epsilon_r}}{\sqrt{\epsilon_r} + \sqrt{\epsilon_r}}$$

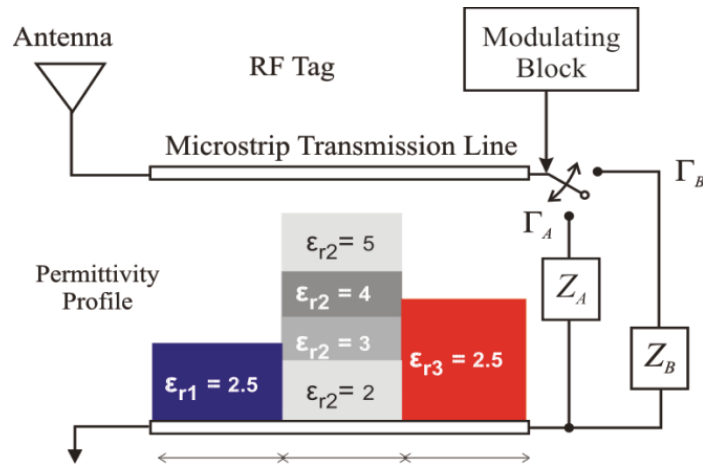


Fig. 2. Model of the REMS concept. Environment-dependent information can be modeled on a microstrip as successive changes in ϵ_r . The figure shows that a different sequence of ϵ_r values on the transmission line results in unique frequency-swept measurements of the reflected signal.

Γ determines the fraction of the incident wave that is reflected and can obtain values between -1 and 1. Overall reflection and transmission through a two-port device such as the microstrip model can be determined by measuring the S-Parameters, or "scattering" parameters, of the device. For a two port device, the

parameter S_{xy} determines the wave traveling through port x via port y . Therefore, S_{11} and S_{22} measure reflections, and S_{12} and S_{21} measure transmissions. They are defined as in Fig. 3.

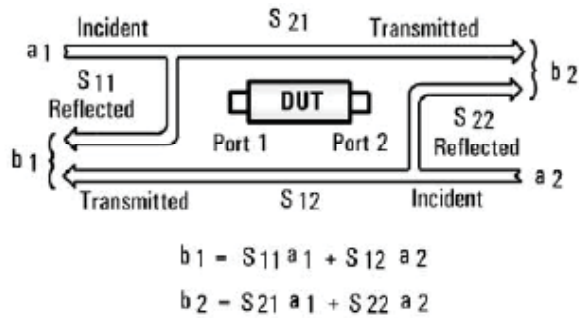


Fig. 3. S-Parameters defined.

The width of the cascaded transmission lines was kept constant so that impedance changes were caused solely by the varying material properties. The two outer materials were the same, with $\epsilon_r = 6.15$; the middle material had $\epsilon_r = 2.2$. Because of the symmetry of this device, it could be safely assumed that $S_{11}=S_{22}$ and $S_{12}=S_{21}$. The S-Parameters of this three-part microstrip were examined using a Network Analyzer.



Fig. 4. Physical REMS model, three-segment microstrip.

To emulate changing material properties, a thin magnetic sheet was placed on top of the microstrip. This material exhibited superparamagnetism, a specially designed paramagnetic material that maintains a high permeability, μ , at frequencies in the range of 5-6 GHz. This was necessary for such RFID modeling because RFID signals are at frequencies well into the MHz range, where ferromagnetic materials exhibit hysteresis and cannot maintain their high μ values. The S-Parameters were measured for this new design in two ways: first, without a nearby magnetic field present, and then with a magnetic field present. The magnetic field induced the magnetic dipoles in the superparamagnetic sheet to align, thus creating a higher μ , and this change in material properties produced a corresponding change in the frequency profile of the backscattered wave (Figs. 5 and 6).

The results of the network analysis revealed that, without the superparamagnetic material attached, the frequency profile of the microstrip in an applied magnetic field showed no deviation

from its profile when there is no magnetic field. As soon as the superparamagnetic material was embedded on the line, there was a shift in the profile; when a magnetic field was then applied, the frequency profile began to shift. This provides evidence for the claim that the changing μ values on the material line imply unique frequency profiles. This trend was observed in both S_{11} and S_{21} measurements.

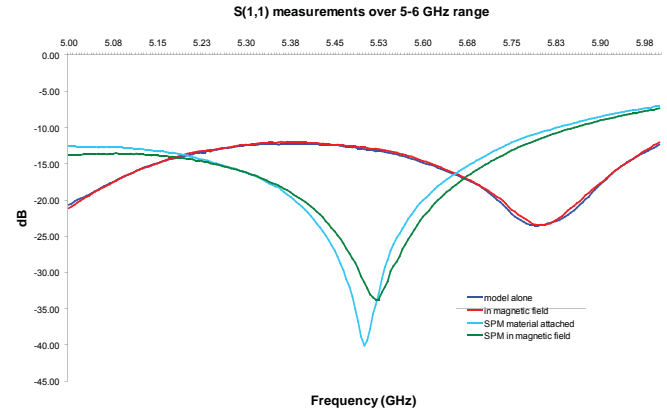


Fig. 5, S11 measurements over 5-6 GHz range.

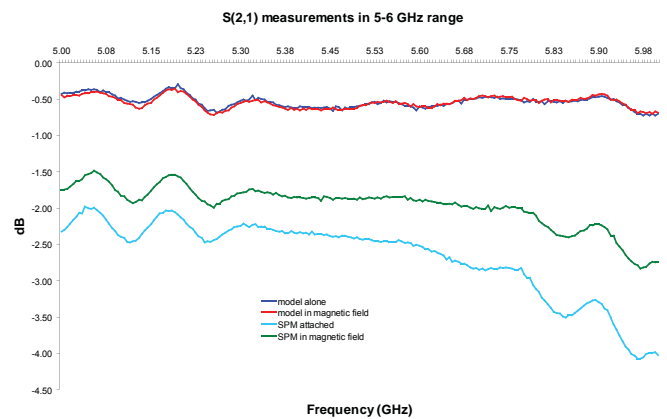


Fig. 6, S21 measurements over 5-6 GHz range.

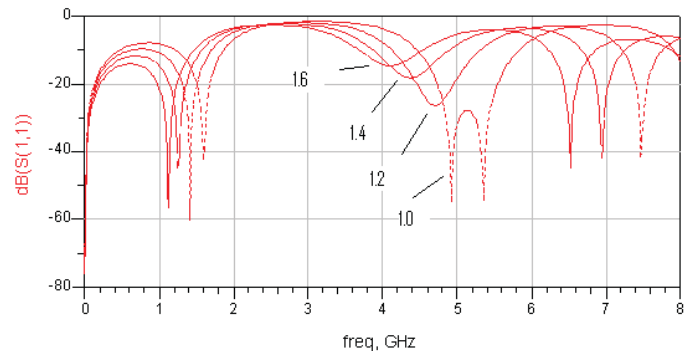


Fig. 7. Uniform magnetic field: $\mu_1=\mu_2=\mu_3=t$

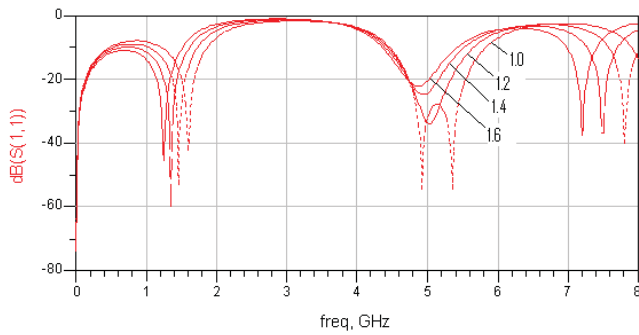


Fig. 8. Magnetic field applied closest to center: $\mu_2=t$ and $\mu_1=\mu_3=(0.9+0.1t)$

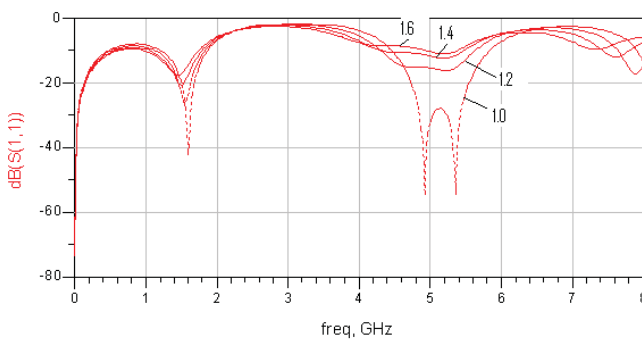


Fig. 9. Magnetic field applied closest to one side: $\mu_1=t$, $\mu_2=(0.9+0.1t)$ and $\mu_3=1$

Simulated Material Line model

To verify the results provided by the physical model of the REMS material line, a simulated replica was designed and frequency-swept measurements were taken using ADS software. The results are shown in Figs. 7 to 9.

I chose to take S_{11} measurements of my simulated material line model. This model consisted of the three substrates, with $\epsilon_1=6.15$, $\epsilon_2=2.20$, and $\epsilon_3=6.15$. The μ_r value of the substrate varied with the parameter t , which took the values 1.0, 1.2, 1.4, and 1.6. To show that a spatial resolution of the applied magnetic field may be possible, three sets of data were collected:

1. Uniform magnetic field with $\mu_1=\mu_2=\mu_3=t$
2. Magnetic field applied closest to center with $\mu_2=t$ and $\mu_1=\mu_3=(0.9+0.1t)$
3. Magnetic field applied closer to one side

$$\mu_1=t, \mu_2=(0.9+0.1t) \text{ and } \mu_3=1$$

The collected data showed that there were unique frequency profiles even for different spatial configurations of the applied magnetic field. This provides more support for the claim that unique frequency profiles are obtainable.

Conclusions

The purpose of this research was to obtain evidence that REMS sensors are feasible. REMS sensors can provide information about the local environment only if, for any given set of properties that are functions of the local environment, there is a unique frequency profile of the backscattered wave. The research met this condition, but only in the case of magnetic materials. The frequency profile of the material line changed for different applied magnetic field strengths, but the exact μ value for each S-parameter measurement was not measured or recorded. Permeability measurements would have to be made alongside the S-parameter measurements to form a correspondence between magnetic field strength, permeability value, and backscattered wave frequency profile.

This leaves open the question of whether it is possible to determine the environmental state from the backscattered wave's unique frequency profile. An algorithm would have to be developed to 'backsolve' for these material properties, which would determine the environmental information that is sought after. Research by other members in Prof. Durgin's lab has indicated that this is possible².

References

1. G. Durgin, "RFID Fundamentals and Applications: Course Notes", Georgia Institute of Technology, 2009.
2. Hasan, Peterson, Durgin. "Feasibility of passive wireless sensors based on reflected electro-material signatures" ACES Journal, "Computational and experimental techniques for RFID systems and applications," 2009.

Acknowledgments

Funds for this research were provided by the Center on Materials and Devices for Information Technology Research (CMDITR), NSF Science and Technology Center No. DMR 0120967.



RYAN HEARTY is a senior at Johns Hopkins University majoring in Electrical Engineering. He hopes to attend graduate school in 2010.

Photovoltaic Performance Tracking System

JASON HIGHTOWER, University of California San Diego

Raymond K. Kostuk, Jose Castro, and Derek Zhang, University of Arizona

Introduction

In order to evaluate PV module performance the energy yield must be measured. The laboratory tests utilize standard test conditions (STC), normally tested under one sun (1000W/m²) at 25°C, these conditions are effective but lack the real conditions of outside installations for performance quality measurements. A customized system capable of evaluating the energy yield of various photovoltaic (PV) modules is necessary for proper efficiency testing. The system should be inexpensive and easy to maintain. This system can be used to evaluate different PV modules and their performance in real installations outside of the lab.

Reasons for Measurements

Each module's material and manufacture will result in different characteristics and features that vary the performance of module throughout the day. This is crucial for understanding which PV materials and manufactures provide the highest efficiency with the best performance under various conditions, such as shading.

The voltage and current characteristics of the module are very important to monitor. A current-voltage (I-V) curve shows the possible combinations of current and voltage output of a photovoltaic device. The power available from a photovoltaic device at any point along the curve is the product of current and voltage at that point. At the short circuit current point, the power output is zero, since the voltage is zero. At the open circuit voltage point, the power output is also zero, this time it is because the current is zero. There is a point on the downward bend of the curve where the maximum power output is located.

The Characteristic Resistance Equation 1:

$R_{ch} = \frac{V_{mp}}{I_{mp}}$, this is the inverse of the characteristic slope line.

The maximum power will give a better quantitative measure of the efficiency of a given module. It is necessary to be able to pull the maximum power at all time throughout the day even as the sun illumination (the irradiance) changes. The characteristic resistance of a solar cell is the output resistance of the solar cell at its maximum power point. If the resistance of the load is equal to the characteristic resistance of the solar cell then the maximum power is transferred to the load and the solar cell operates at its maximum power point.

The output power from a module will change as the sun moves across the sky, increasing or decreasing the irradiance (along with cloud coverage). This indicates that irradiance must also be measured to gain the relationship between maximum power output and the solar illumination. The temperature of the module is also an important measurement, because the open circuit voltage and the resulting I-V curve is a function of the cell operating temperature. Therefore the cell temperature should be monitored as part of the evaluation of the module performance.

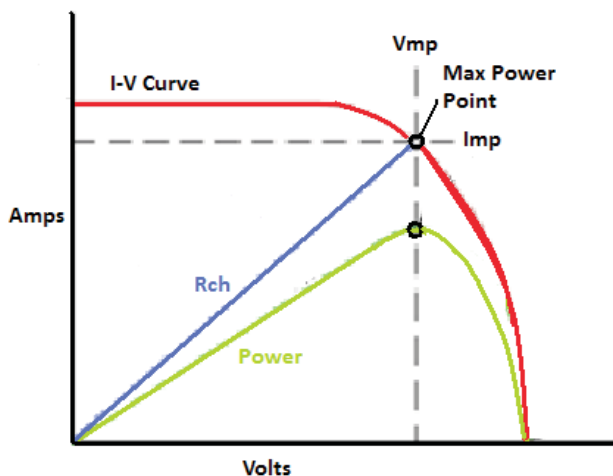


Figure 1: I-V Curve with Resistance and Power.

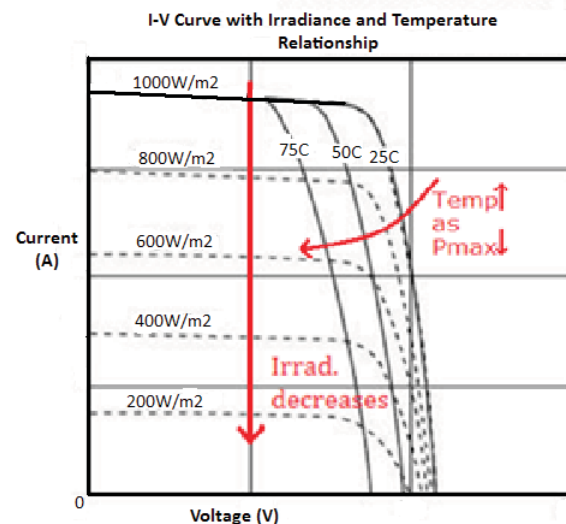


Figure 2: Irradiance and Temperature relationship with the I-V Curve.

Results and Discussion

Off-Grid Maximum Power Tracker

An off-grid (not tied into the power grid) system was ideal for ease of

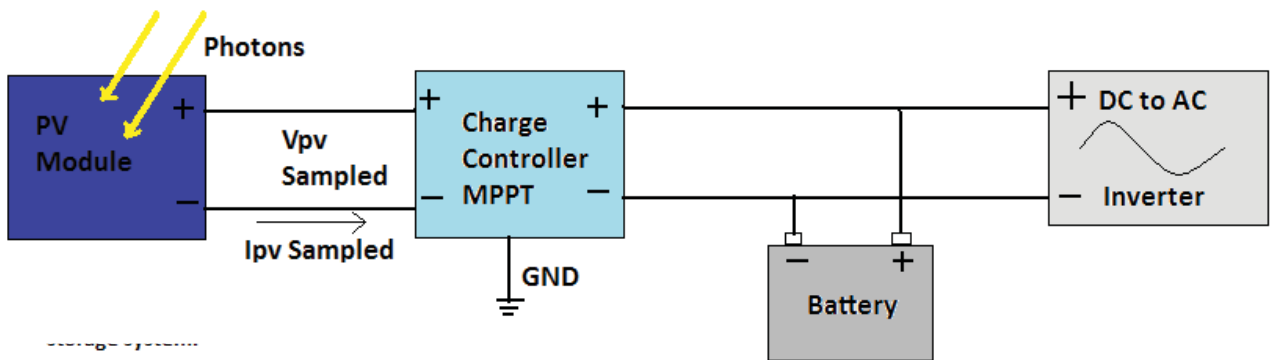


Figure 3: Schematic of a MPPT PV storage system.

operation and portability. Using National Instruments NI-USB-6009 and NI-USB 6008 data acquisition cards worked the most effectively since they are available in Professor Kostuk's lab. The cards can handle a voltage range on its channels between -10 and +10V. The modules voltage can reach values as high as 45V, depending on the module type. So the voltage would have to be dropped before it is collected by the NI-USB-6009. What is an advantage about the NI-USB-6009 is its user friendly interface through LabView 8.5 and its simple type B to type A USB connection. It has 8 analog inputs and has two digital to analog output channels together with 12 digital I/O channels. This device can measure the PV and battery voltage and amps, irradiance, and the temperature.

A Maximum Power Point Tracker (MPPT) is necessary for monitoring the PV yield. A non-MPPT charge controller needs a module at the same nominal voltage as the battery bank. It then connects the module to the battery to charge and disconnect when the battery is in float stage. This is fine for home use where the maximum power is not needed and only the power from the batteries is utilized. But this is impractical for module efficiency testing. An MPPT controller can reach a higher input voltage than the battery to provide an optimum load to the module and is then stepped down to charge the battery. The MPPT charger is more efficient at collecting the same amount of power from the module. The MPPT controller finds the voltage and current that produces the highest module output. What the MPPT controller is doing is adjusting the load on the PV module to find the highest module output available. However, the battery has to be slightly depleted at all times for max power point tracking to take place or else the charge controller will shut off any power from the PV module. To keep the battery depleted a halogen car lamp (3A) was connected directly across the battery's terminals to act as a load. Still, this was not enough to act as an effective voltage drain.

Replacing the Xantrex C-40 non-MPPT charge controller with a new Outback MX60 MPPT Charge Controller is an option to meet the project goals. However, the MPPT charge controller method requires a battery bank and the max power was dependent on the batteries being depleted for the majority of the day. This system is bulky, expensive and complicates the design.

Solid State Variable Load System

After the rejection of the MPPT charge controller system a new off-grid method was suggested. What was desired was an inexpensive and straightforward circuit that could alter the load to pull the max power from the module.

Bipolar Junction Transistors (BJT) were suggested and seemed feasible, but most BJTs are low power and could not handle such high current being pulled from the module. An Insulated Gated Bipolar Transistor (IGBT) was then decided upon after an initial experiment utilizing it in parallel with a power generator. After the success with the power generator it was then powered with a Cadmium Telluride Thin Film module. When it was connected in series with a 5Ω power resistor it behaved as a variable load. This was ideal for resistance matching due to the IGBT's high efficiency and fast switching. Since it is designed to rapidly turn on and off it is ideal to behave like a variable resistor that could match up with the characteristic resistance of the module at any given time.

There was also an issue with overheating. An IGBT rated at 150W was used initially but was soon replaced with a 200W rated IGBT (NTE3323) attached to a large aluminum heat-sink and also a 12Vdc, 0.66A computer fan. This combination kept the new IGBT very cool under the highest PV module power.

The IGBT would be governed by the NI-USB-6009 analogy output. The LabView interface allows the user to use a digital dial that can be varied from 0 to 5V which is then sent to an op amp (NTE941M). The op amp would amplify the input voltage by roughly 6 times and send its output signal to the collector pin of the IGBT.

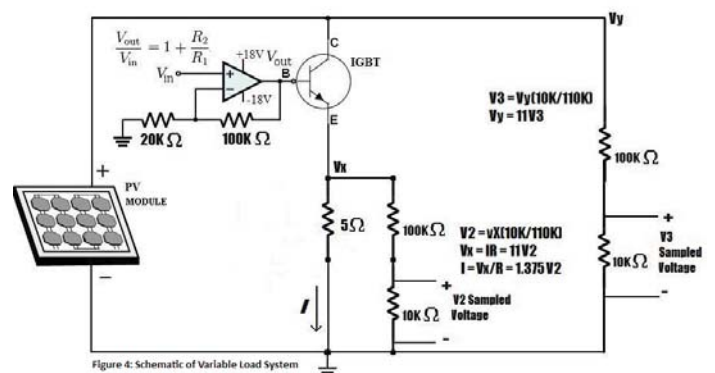


Figure 4: Schematic of Variable Load System

Amplification gain Equation 2:

$$V_{out} = \left[1 + \left(\frac{100K}{20K} \right) \right] V_{in} = 6V_{in}$$

This allows the user to either manually or automatically operate the IGBT with LabView. This does require an additional +/-18V to power the op amp.

To gain the maximum PV voltage a resistance bridge had to be designed. Since voltage is the same in parallel the bridge was placed in parallel, with the IGBT and the 5Ω resistor. A ratio of 1 to 10 was required to gain a voltage in millivolts to be in range of the NI-USB-6008. This voltage and the resistor ratio were then used to find the max voltage (Vy, from figure 4) across the bridge. This same bridge is used in parallel with the 5Ω resistor. After sampling voltage V2 the voltage Vx is calculated. Ohm's Law is used to find the current value with Vx. This current value should be close to the actual current being drawn from the PV module because the resistance in that branch is low resulting in a close value to the PV current.

Ohm's Law Equation 3:

$$V2 = Vx \left(\frac{10k}{110k} \right)$$

$$Vx = IR = 11 * V2$$

$$I = \frac{Vx}{R} = 1.375V2$$

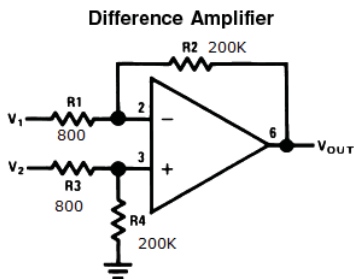
Max Voltage Equation 4:

$$V3 = Vy \left(\frac{10k}{110k} \right)$$

$$Vy = IR = 11 * V3$$

A USB-6009 was employed for all voltage data. Initially the temperature and irradiance were sampled with the USB-6008 along with the voltage samples. However, the voltage channels were inducing a large amount of noise onto the temperature and irradiance signals. The USB-6009 was added to the system to take the temperature and irradiance data, and to send out the IGBT gate signal to reduce the noise on the USB-6008 voltage channels.

There is a thermocouple selection in LabView that can allow any type of thermocouple to be directly attached to the NI-USB-6008. The lab only had two types of thermocouples available, a type J and type K. However, the signals from these two types were too weak for the USB-6009 to detect, which was not in accordance to its specifications. Thermocouple wire, approximately 60ft, was applied as an alternative. It was more accurate than the two thermocouples. The signal was still too weak for the NI-USB-6009 to detect. The solution was to use a differential op amp to amplify the signal of the positive voltage line of the thermocouple wire.



For $R1 = R3$ and $R2 = R4$

$$V_{OUT} = \frac{R2}{R1} (V2 - V1)$$

$$R1//R2 = R3//R4$$

Figure 5: Differential Amplifier for Temperature.

Difference Amplifier Gain Equation 5:

$$V_{out} = \left(\frac{200K}{800} \right) (V2 - V1)$$

$$= 250(V2 - V1)$$

Shading Effects

If the cells of a module are connected in series, the weakest cell will bring the others down to its reduced power level. The shaded cell will act as a power dissipater caused by the remaining cells. The power must be routed around the shaded cells in the string otherwise. The resultant local heating may cause irreversible damage to the module.

Three modules were tested without a load to investigate the performance of the modules under shading conditions. This data is not true power; it was done measuring the open voltage and short current. Though it is not the real power of the modules, the data gives a good idea of their performance.

Conclusion

It is essential to find the max power point of any given PV system for the efficiency testing and characterization experimentation. It is therefore vital to have a testing system that can provide a variable load to pull the max power from the module and take accurate measurements of all the essential data, such as shading. The IGBT solid state variable load system designed in the Photonics Systems Lab at the University of Arizona needs to be improved to operate automatically. It also needs to be programmed in LabView to log its data into data files for record keeping and data analysis.

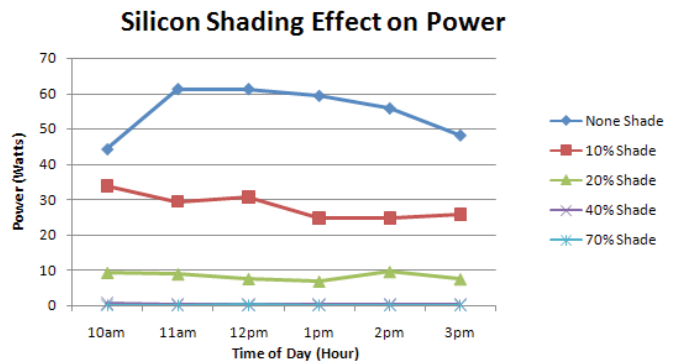


Figure 6: Shading effects on silicon.

Copper Indium Gallium Diselenide Shading Effect on Power

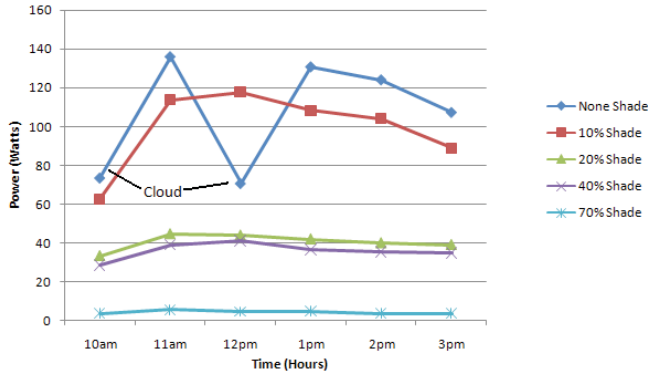


Figure 7: Shading effects on Cadmium Telluride.

Cadmium Telluride Thin Film Shading Effect on Power

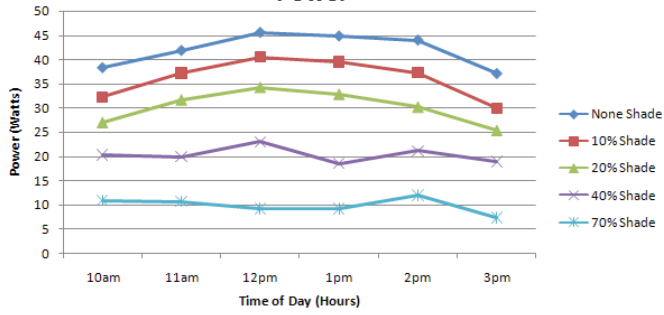


Figure 8: Shading effects on CIGD

References

1. Thomas W. Murphy Jr., July 2008, "Home Photovoltaic systems for physicists" Physics Today.
2. Steve Ransome, June 2008, "Understanding kWh/KWp by comparing measured data with modeling predictions and performance claims", PVSC34 Philadelphia.
3. Antonio Luque and Steven Hegedus, 2003, "Handbook of Photovoltaic Science and Engineering", John Wiley and Sons Ltd.
4. Solar Energy International, September 2004, "Photovoltaics: Design and Installation Manual", New Society Publishers.
5. Christiana Honsberg and Stuart Bowden, "Photovoltaics CDROM", National Science Foundation <http://pvcddrom.pveducation.org/>
6. Stephen Kullmann, May 2009, "Specific energy yield of low-power amorphous silicon and crystalline silicon photovoltaic modules in a simulated off-grid, battery-based system", Humboldt State University.
7. Christian Bendel and Andreas Wagner, May 2003, "Photovoltaic Measurement Relevant to the energy yield" University of Applied Sciences Dortmund.
8. PentaMetric System Instructions, July 1 2008, Bogart Engineering.
9. C-Series Multifunction DC Controller Owner's Manual, November 2003, Xantrex.

Acknowledgements

Dr. Raymond K. Kostuk

Jose Castro

Derek Zhang

University of Arizona

ECE Department

Photonics System Lab

Hooked on Photonics Summer REU 2009

Funding for this research provided by the NSF sponsored Science and Technology Center on Materials and Devices for Information Technology Research, No. DMR-0120967.



JASON HIGHTOWER will be graduating soon from UC San Diego with a BS in electrical engineering and is seeking a Master of Science in EE.

The Analysis of Diffuse, Bulk and Bi-Layer Heterojunction Organic Photovoltaic Cells

DEXTER HYPOLITE, University of the Virgin Islands

William J. Potscavage Jr., Bernard Kippelen, Georgia Institute of Technology

Introduction

Electricity is consumed largely by the world and is often produced by burning fossil fuels and other natural gases. These fossil fuels are non-renewable sources that contribute to global warming. By looking at renewable energies such as solar energy, less pollution can enter the environment, and, hence, the impact that the generation of electricity has on the world can be reduced.

Solar electricity (electricity produced from the sun's light) can be generated by inorganic and organic photovoltaic cells (PV). Although power conversion efficiencies of up to 24% have been obtained in silicon-based PV cells, these devices remain fairly expensive.¹ Organic photovoltaic cells (OPV), on the other hand, have the potential to be less expensive due to the possibility of low-cost production. OPV cells can be a highly flexible unlike most current PV cells. However, OPV cells degrade in moisture and oxygen, and their current life spans are much shorter than Si-based PV cells.

Organic solar cells are usually processed by vacuum deposition or solution processing. In vacuum deposition, small organic molecules in a high vacuum are heated and evaporated to produce a thin film of the molecules. Solution processing can be used for semi-conductive organic-based polymers that are soluble. Spin coating is a common solution processing technique where the film thickness is indirectly proportional to the spin speed. In spin coating, the compound to be deposited is dissolved in a solvent, and a film is formed by spinning a substrate covered in the solution to evaporate the solvent, leaving a thin film of the compound on the substrate.

OPV cells generally consist of organic active layers sandwiched between two electrodes on a substrate. The way that an organic solar cell works can be explained in four consecutive steps. See Figure 1 for a schematic. First, sunlight passes through a transparent electrode and is absorbed by the active layer to generate an excited state known as an electron-hole pair or exciton. Second, the exciton diffuses towards the donor-acceptor interface. Next exciton dissociation occurs at the donor-acceptor interface, with the hole transferring to a donor molecule and the electron to an acceptor molecule. Finally, the electrons move toward the cathode by hopping onto other acceptor molecules and the holes toward the anode by hopping onto donors.²

In previously conducted research, bi-layer and bulk heterojunction OPV devices have been demonstrated. Tang reported power conversion efficiencies of 1% for bi-layer cells.³ In bi-layer devices, p-type and n-type organic semiconductors are deposited on top of each other sequentially with the donor material being placed above the anode. The stacking of the donor and acceptor makes the

interface area planar. Excitons generated within about one exciton diffusion length of the interface can reach the heterojunction and dissociate.⁴ Bulk heterojunction solar cells consist of a blend of p-type and n-type organic materials, and a schematic is shown in Figure 2. While in the bi-layer heterojunction solar cell the donor and acceptor produce a planar surface area, donor and acceptor phases are intermixed in a bulk heterojunction. The surface area of the heterojunction then becomes greater thus creating more area for exciton dissociation. Devices with bi-layer heterojunction and bulk heterojunctions have obtained efficiencies of up to 3.6% and 6%, respectively.²

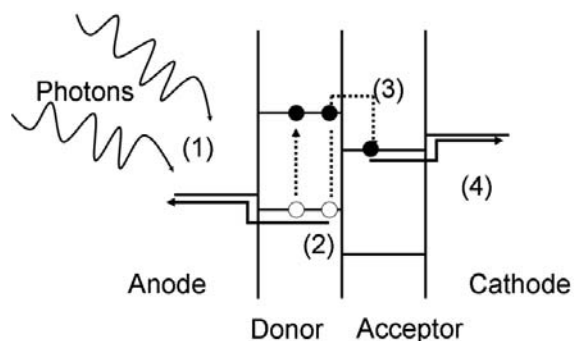


Figure 1. Diagram of how an organic solar works: (1) absorption, (2) exciton diffusion, (3) charge separation, and (4) charge collection.

The goal of this project was to create solar cells with large donor-acceptor interfaces and good charge transport by separately spin coating the donor and acceptor layers since bulk devices are limited by the number of successful material combinations and since bi-layer devices are often limited by short exciton diffusion lengths.

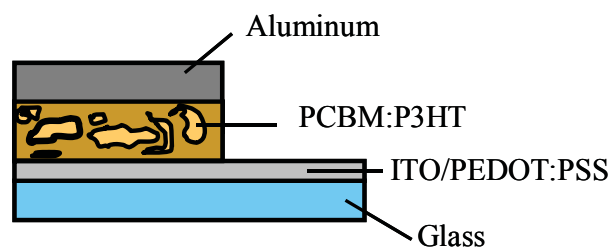


Figure 2. Diagram of the device structure for a P3HT:PCBM bulk heterojunction solar cell. The active layer is found sandwiched between the cathode (aluminum) and anode (ITO).

Spin coating the two active layers may improve the charge transport of the device because more donor molecules will be located near the anode and more acceptors near the cathode for easier transport of charges from the interface to their respective electrode. It may also improve the exciton dissociation by increasing the area of the donor-acceptor interface because of mixing of the sequentially spin-coated layers. This fabrication method may produce a structure in between those of a bi-layer and bulk heterojunctions. The p-type material poly-3-hexylthiophene (P3HT) and the n-type material [6,6]-phenyl C₆₁ butyric acid methyl ester (PCBM) were used for the experiment and are shown in Figure 3. The spin-coated structure was compared to bi-layer and bulk heterojunction devices to understand the impact on device performance.

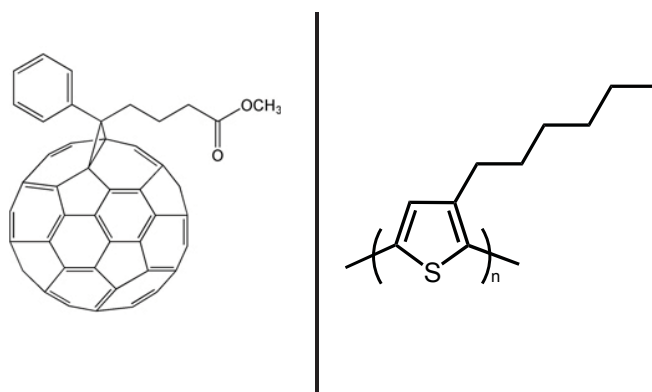


Figure 3. Chemical structure of (1) [6,6]-phenyl C₆₁ butyric acid methyl ester and (2) poly-3-hexylthiophene.

Experimental Method

Glass coated with indium-tin oxide (ITO) was used as the substrate and anode. The glass was cut into 1" × 1" squares. Next, the glass was thoroughly cleaned in ultrasonic baths of soap water, water, acetone and isopropanol. Each bath lasted 20 minutes was done at 40 °C. The ITO was then patterned with SiO_x using electron-beam deposition. Oxygen-plasma treatment was done on the patterned substrates and finally PEDOT:PSS was spin coated onto the ITO.

Bi-layer reference devices were made by spin coating a layer of P3HT from chlorobenzene (10 mg/ml) on the PEDOT:PSS. Thickness was changed with the spin-coating speed. Since PCBM might not be able to be vacuum deposited, a similar acceptor, C₆₀, was vacuum deposited on top of the P3HT. Finally, bathocuproine and aluminum were deposited to finish the sandwich device.

For bulk heterojunction cells, both P3HT and PCBM (1.0:0.7 by weight) were mixed to form a blended solution in chlorobenzene (17 mg/ml). The blended solution was spin coated on top of the PEDOT:PSS, and aluminum was deposited on top to finish the sandwich device.

Finally, the diffuse devices were made by spin coating both donor and acceptor layers. Using the solvent chlorobenzene, a P3HT layer was spin coated onto the PEDOT:PSS followed by a solution of PCBM. The spin speed as well as solvent were varied to see the effect on the device. Aluminum was used as the cathode.

Results and Discussion

The current- voltage characteristics of each solar cell were studied under the dark as well as under illumination. Current density- voltage. (J - V) characteristics were measured to obtain the current density J_{\max} and voltage V_{\max} where the cells produces the maximum power, the open-circuit voltage V_{oc} , and the short circuit current I_{sc} . The fill factor (FF) and power conversion efficiency (η_e) were calculated using Equations 1 and 2.

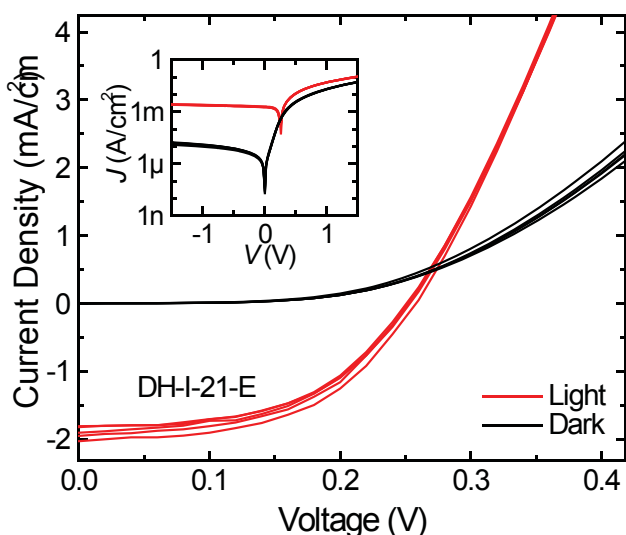
$$\zeta_e = \frac{V_o \cdot J_x \cdot F}{P_{inc}}$$

$$F = \frac{V_{\max} \cdot J_{\max}}{J_x \cdot V_o}$$

Analysis of the Bi-Layer Heterojunction Photovoltaic Cells

Bi-layer OPV cells were fabricated using P3HT and C₆₀. The results yielded power conversion efficiencies of less than 0.50%, probably due to the thin active layers absorbing less light and short exciton diffusion lengths. Figure 4 shows the J - V characteristic for the most efficient bi-layer devices with 70 nm of P3HT and 40 nm of C₆₀. Bi-layer device must also fight the exciton diffusion length as increasing the device thickness (90 nm P3HT and 40 nm C₆₀) led to lower efficiencies (0.18%).

Figure 4. J - V graph of bi-layer device. P3HT was spin coated at 1200 rpm (70 nm) followed



by vacuum deposition of 40 nm of C₆₀. $\eta_e = 0.34\%$, $V_{oc} = 253\text{mV}$, $J_{sc} = 1.90\text{mA/cm}^2$, and $FF = 0.51$.

Analysis of the Bulk-Heterojunction Photovoltaic Cells

Similarly, bulk-heterojunction cells were fabricated with different thicknesses, and the results are summarized in Table 1. Figure 5 shows J - V characteristics for the cells with the highest efficiency,

which were spin coated at 1000 rpm and annealed at 120 °C for 15 minutes.

P3HT:PCBM (1:0.7 ratio)	V_{oc} (mV)	J_{sc} (mA/cm ²)	FF	η_c (%)
500rpm	599	9.9	0.47	3.89
700 rpm	641	11.7	0.58	6.05
1000rpm	589	10.8	0.58	5.12

Table 1. Performance of bulk-heterojunction solar cells made with different spin-coating speeds averaged over 5 devices. Annealing was done for 15 minutes at 150 °C.

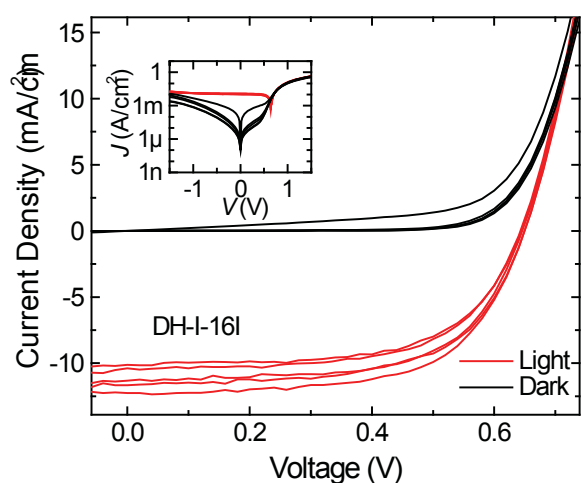


Figure 5. J - V graph of bulk-heterojunction solar cell. P3HT:PCBM solution was spin coated at 1000 rpm followed by annealing at 120 °C for 15 minutes. $\eta_e = 6.20\%$, $V_{oc} = 647$ mV, $J_{sc} = 11.2$ mA/cm², $FF = 0.62$.

Comparing these performance parameters to that of the bi-layer solar cell, the bulk heterojunctions has higher values for all parameters, with efficiencies of up to 6.2% compared to the 0.34% for bi-layer devices. The improved performance is likely related to increased donor-acceptor interface for more efficient exciton dissociation and thicker films for more light absorption.

Analysis of the Diffuse Heterojunction Photovoltaic Cells

Finally, the diffuse heterojunction were fabricated. First, devices were made using chlorobenzene as the solvent for both the PCBM and the P3HT. While thicknesses, as measured by spin coating single layer on glass, of 150 nm, 95 nm, and 55 nm for the P3HT and 90 nm, and 60 nm for the PCBM were used for the devices, the power conversion efficiencies of the devices were all less than 1% with some just approaching that mark. Figure 6 shows the electrical characteristics for the best devices with 55 nm of P3HT and 60 nm of PCBM.

One possible reason for such lower power efficiency is that the

sequential spin coating with the same solvent led to some removal of P3HT. This would then produce a thinner film of the organic material that absorbs less light. However, the open-circuit voltage was the largest off all the geometries tested. Some devices had open-circuit voltages approaching 700 mV.

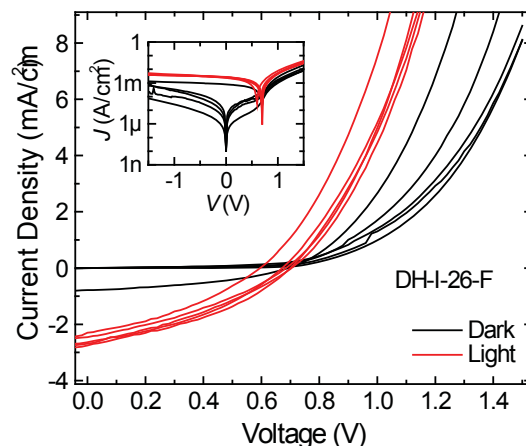


Figure 6. J - V graph of diffuse layer device. P3HT was spin coated at 1200 rpm (55 nm) followed by spin coating PCBM at 1200 rpm (60 nm). $\eta_e = 0.75\%$, $V_{oc} = 673$ mV, $J_{sc} = 2.23$ mA/cm², and $FF = 0.36$.

The performance of the diffuse-heterojunction devices changed significantly when dichloromethane was used as the solvent for PCBM instead of chlorobenzene. Figure 7 shows the J - V curves for the best devices using dichloromethane as the solvent for PCBM with a P3HT layer of 95 nm and a PCBM layer of 60 nm. Efficiencies in the devices are approaching the 2%.

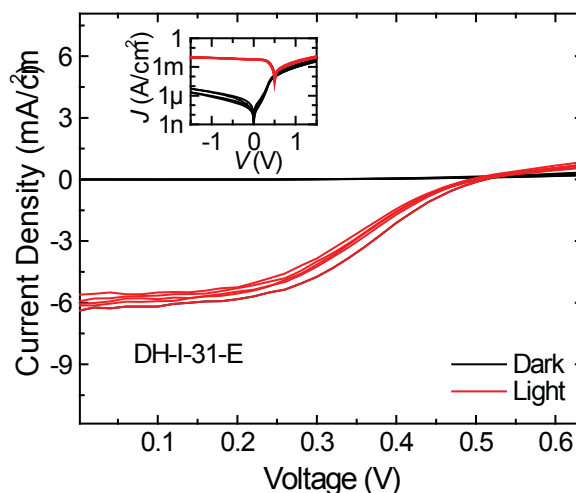


Figure 7. J - V graph of diffuse layer device. P3HT was spin coated at 1000 rpm (95 nm) followed by spin coating PCBM at 1200 rpm (60 nm). $\eta_e = 1.80\%$, $V_{oc} = 502$ mV, $J_{sc} = 6.02$ mA/cm², and $FF = 0.43$.

Measurement of the thickness changed after spin coating chlorobenzene or dichloromethane on top of P3HT layers showed that thickness was less affected by the dichloromethane. Because of the thicker P3HT layers, more light is absorbed and likely leads to the higher J_{sc} . However, there is also a high series resistance in these cells, as indicated by the low current above the V_{oc} , and this may also be related to the thicker P3HT layer.

Conclusions

Bi-layer solar cells were fabricated with PCBM and C_{60} . Thin active layers are required because of the short exciton diffusion lengths. However, the materials had limited light absorption and this led to low power conversion efficiencies. Similarly, the diffuse heterojunction, which was fabricated using the same solvent for both layers, had low performance due to the P3HT layer being washed away after the second spin coating. However, the performance parameters improved significantly when a different solvent was used to spin coat the PCBM. Performance was improved for the diffuse heterojunction compared to bi-layer heterojunction, most likely because of a larger interfacial area between the donor and acceptor in the diffuse structure. The larger interface area would lead to less excitons being lost to recombination.

While the diffuse heterojunction devices were an improvement over the bi-layers, the best performance was still obtained with a bulk-heterojunction of P3HT:PCBM.

References

1. Peumans, P. Yakimov, A. and Forrest S. R. Small molecular organic thin-films photodectors and solar cells. *Journal of Applied Physics* 2003, 93, p.3694.
2. Hoop, H. Organic solar cells: an overview. *Journal. Material Research* 2004, 19, p.1928 and 1932.
3. Tang, C. W. Two layer organic photovoltaic cell *Journal of Applied Physics Letter* 1985, p. 183.
4. Gunes, S. Neugebauer, H. and Sariciftci, N. S., Conjugated polymer-based organic solar cells. *American Chemical Society* 2007, 107, p.1328.

Acknowledgments

I would like to acknowledge William Postcavage for the great technical help in the lab, Dr. Kippelen for inspiration and lab usage, and finally the Kippelen Research Group for support. The authors acknowledge funding for this research provided by the STC Program of the National Science Foundation under Agreement Number DMR-0120967.



DEXTER HYPOLITE'S educational goals include earning a Bachelor of Science and a Master's degree in electrical engineering to then enter industry.

Poling and Characterization Methods for Electro-Optic Modulators

CHRISTOPHER LIU, California Institute of Technology

Adam Jones, Robert Norwood, University of Arizona

Optical data processing and communication hold great potential to allow improved bandwidth and energy efficiency in telecommunications and computing. To enable optical devices to communicate with existing electrical devices, one must be able to modulate a laser source to encode the information from an electrical signal. The devices that perform this function are known as electro-optic modulators. In an electro-optic modulator, the phase and/or amplitude of the light is modulated by the applied voltage.

An electro-optic modulator operates on the principle that the refractive index of the modulator material depends on the applied electric field. In the most commonly applied effect, known as the Pockels effect, the change in refractive index is directly proportional to the applied field. The Pockels effect is exhibited only by materials with inversion-asymmetric structures. In recent devices, the modulating material is generally an electro-optic polymer, whose constituents are known as the chromophores and the host polymer. To maximize the strength of the electro-optic effect, the (polar) chromophore molecules must be oriented as uniformly as possible. This is achieved by a process known as poling, in which an electric field is applied while the temperature is raised above the host polymer's glass transition temperature. This allows the chromophores to move into the desired alignment.

The work was performed in two phases. The first phase focused on the development of a LabVIEW program to control the temperature of the heating system for a new poling apparatus. The new apparatus was designed to replace an old apparatus which was controlled by an old computer and lacked certain desired features. Such features included control of the temperature ramp rate and the ability to save the temperature vs. time data to a text file. The second phase of the project focused on the measurement of the order parameters describing the chromophore orientation distribution. The relationships of the first and second order parameters with poling field and poling temperature were examined.

Experimental Methods

The heated sample stage of the new poling apparatus was constructed of aluminum, with a block for the base, a frame on top of the base, and a screw-in plate to hold in place the heating element and copper tubing for water cooling. A resistance temperature detector was held against the upper surface of the stage with fiberglass tape. The heating element and resistance temperature detector were connected to a Watlow Series SD Profiling PID Controller unit. The Watlow controller was connected to the computer via a USB-to-serial adapter (Fig. 1, 2). The older poling apparatus was of similar physical construction. It handles

low-level temperature reading and control functions within the computer program rather than dedicating them to a separate unit; further information about it is unavailable.



Fig. 1. Main poling oven unit from newer system. Water cooling not connected. Selected parts labeled.

1. Resistance temperature detector under tape
2. Wires connecting heating element and RTD to Watlow controller
3. USB-to-serial adapter



Fig. 2. Watlow temperature controller. In normal operation, upper display shows actual temperature and lower display shows set temperature.

The Watlow controller uses the PID (Proportional-Integral-Derivative) control algorithm in order to control the heating power. In the PID algorithm, the heating power at any given time is a weighted sum of the temperature error (proportional), the error integrated over time (integral), and the rate of change of the error (derivative). The PID algorithm produces a continuous output, but the Watlow controller is limited to switching the heating voltage on and off. Thus it approximates the desired heating power by pulse-width modulation of the output.

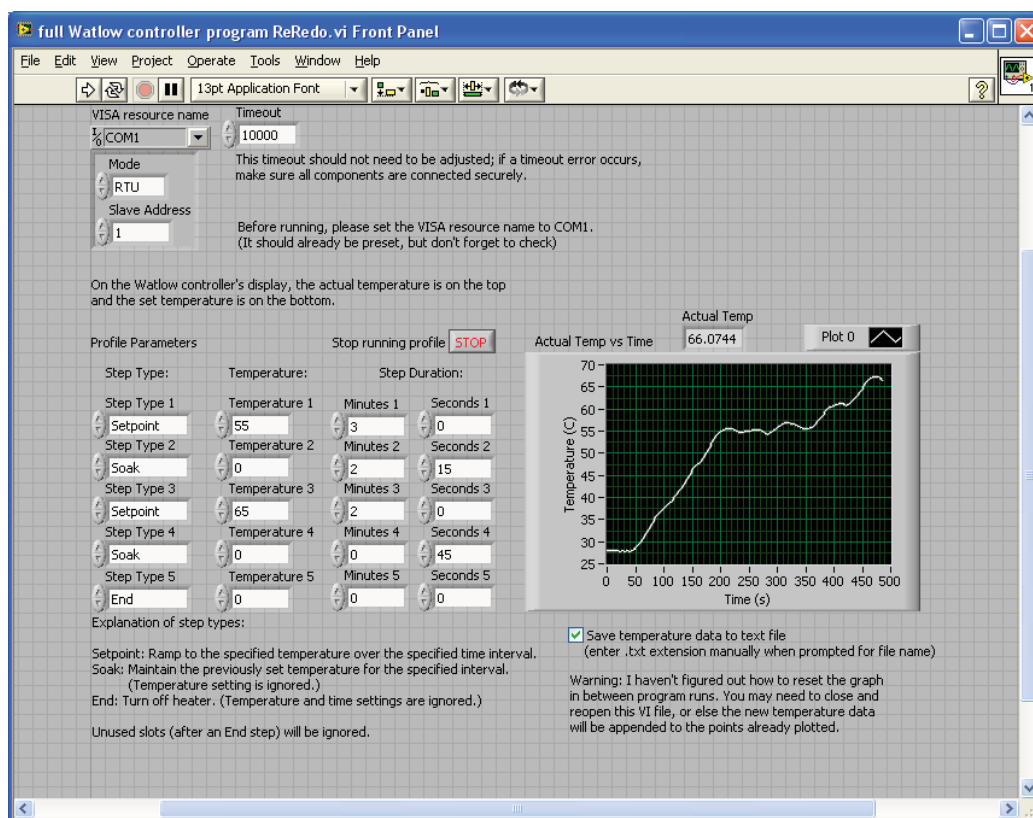


Fig. 3. User interface of LabVIEW program. At lower left are the controls for entering step type, temperature, and time values. At lower right is a plot of actual temperature vs. time. The plot in this screenshot shows suboptimal temperature control performance, specifically instability resulting from the integral coefficient in the PID algorithm being set too high.

The Watlow controller accepts input in the form of a "profile," which consists of commands to adjust the temperature linearly to a specified value over a specified time interval, hold the previously set temperature over a specified time interval, or turn off the heater. The LabVIEW program was designed to configure the Watlow controller for the profile requested by the user, begin executing the profile, read the actual temperature, display a plot of the actual temperature vs. time, and save the temperature vs. time data to a text file (Fig. 3).

Due to practical constraints, the old poling apparatus was used for the samples tested in the second phase of the project. The samples consisted of a glass substrate partly coated with indium tin oxide (ITO), with the electro-optic polymer spin-coated and then a gold electrode layer deposited (Fig. 4). The electro-optic polymer consisted of the SWOHF3ME chromophore (Fig. 5) in PMMA host polymer.

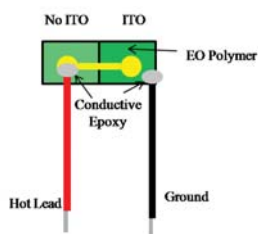


Fig. 4. Diagram of experimental samples.

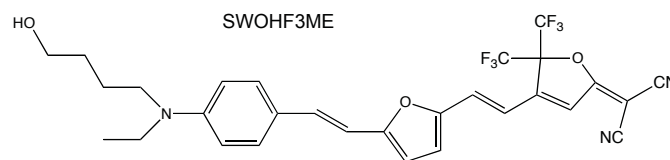


Fig. 5. Structure of SWOHF3ME chromophore molecule.

The distribution of chromophore orientations is generally described by a function $g(\theta, \varphi, t)$ (Fig. 6)¹. We may disregard φ by assuming that the distribution is rotationally symmetric, which is reasonable since the poling field is approximately constant over the space of the polymer layer. Also, we may disregard t if the decay in the orientational parameters is sufficiently slow with respect to the time scale of experimentation. Thus we assume that the distribution is adequately described by $g(\theta)$. The order parameters a_n represent the coefficient of the n th Legendre polynomial $P_n(\cos \theta)$ in the expansion for $g(\theta)$.

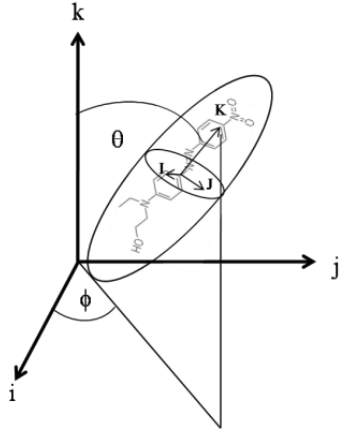


Fig. 6. Definition of ordering angles θ and ϕ . Electric field points along k-axis.

For calculations of the order parameters, an oriented gas model was assumed in which the third and higher order parameters are zero and the Pockels coefficients are related by¹ $r_{33} = 3r_{13}$.

Measurements of the first order parameter were done by the Teng–Man method as described in the reference² (Fig. 6).

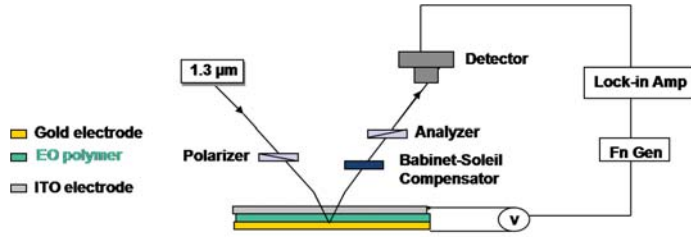


Fig. 7. Diagram of apparatus for first order parameter measurements.

In our setup, the modulating voltage had a DC bias of 3.5 V, a RMS amplitude of 47 V or 58 V depending on the trial, and an oscillation frequency of 1 kHz.

The Pockels coefficient r_{33} was calculated from the modulation amplitude by the following equation:

$$r_{33} = \frac{3\lambda I_m (n^2 - \sin^2 \theta)}{4\pi V_{poly} I_c n^2 \sin^2 \theta}$$

where

- V_{poly} : RMS amplitude of modulating voltage across film
- A modulating voltage of 58 V rms was used for the samples poled at 50, 75, and 100 V/ μm . This was due to an unknown change in the configuration of the equipment. For all other samples 47 V was used.

- I_m : Modulation amplitude measured at lock-in amplifier, average of two trials
- I_c : DC offset of modulating voltage (3.5 V)
- θ : Angle of incidence (45°, i.e. $\pi/4$ rad) (Fig. 7)
- λ : Wavelength of the laser source (1.3 $\mu\text{m} = 1.3 \times 10^6$ pm)
- n : Refractive index of the electro-optic polymer (1.62)

From r_{33} one can calculate the first order coefficient a_1 via the equation

$$a_1 = \frac{1}{fN\beta_{zzz}} \frac{5}{3} r_{33}$$

where

- f : field factor = $(\epsilon_{33} + 2) / 3$
Since $\epsilon_{33} = 3.3$ at 1 kHz for PMMA, $f = 1.77$
- N : Number density of chromophore (information unavailable)
- β_{zzz} : Hyperpolarizability (information unavailable)

Measurements of the second order parameter were performed by means of linear dichroism¹. In this procedure, a laser source at 845 nm was configured such that it could be directed at the sample in one of two possible polarizations, labeled 0° and 90° (respectively perpendicular and parallel to the surface of the optical table). A laser power meter was used to measure the incident and reflected power for each polarization.

The dichroic ratio R is defined as

$$R = \frac{A_{\parallel}}{A_{\perp}}$$

where A_{\parallel} is the absorption for light polarized parallel to the incident plane and A_{\perp} is the absorption for light polarized perpendicular to the incident plane. The second order parameter can be calculated from R as

$$a_2 = \frac{2n^4(R-1)}{2n^4(R-1)+3}$$

assuming that the anisotropy in the refractive index is negligible and that the incidence angle is 45°.

Results and Discussion

The aforementioned functionality was successfully implemented in the LabVIEW program during the time available. The temperature control performance was acceptable but slightly inferior to that of the older apparatus. One problem was that the heater did not switch on until about 30-40 seconds after the start of a typical profile, causing the actual temperature to lag behind the set temperature.

Acceptable linearity in the temperature ramp was achieved up to ramp rates of about 18°C/min. Temperature fluctuations at a steady set temperature varied from ±0.2°C to ±1°C depending on the tuning of the PID parameters. By comparison, the older apparatus had no noticeable lag, a non-configurable ramp rate of about 15°C / min, and about 0.01°C of overshoot and fluctuation.

The probable cause of these symptoms was that the Watlow controller uses a default cycle time of 20 seconds for its pulse-width modulation in order to avoid excessive wear on its mechanical relay. By comparison, the old system uses a solid-state relay with a shorter cycle time, which is permissible since its heating current is lower (about 0.5 A vs. 2 A).

Some samples failed with the electrode wires separating from the conductive epoxy or breakdown of the EO polymer layer. The latter was visible as bubbling under the gold electrode (Fig. 7); it occurred primarily with samples which had been placed in storage for a long time, when poled at 150°C and about 50-60 V/μm.

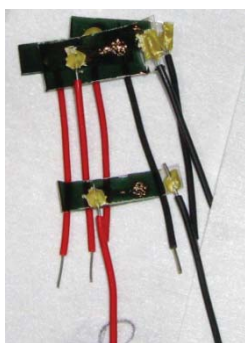


Fig. 8. Samples showing failure by breakdown of polymer layer.

The order parameters obtained for the samples successfully poled were as given in Table 1 below.

Poling Field (V/μm)	Poling Temperature (°C)	a_1 (pm/V)	a_2
56.5	150	0.218	(test not performed)
52.8	150	0.244	0.289
50	120	0.322	0.271
75	115	0.626	0.285
100	115	0.85	0.286
125	115	0.631	0.304
135	115	0.737	0.145
140	115	0.795	0.272
145	115	0.837	0.350
150	115	0.433	0.351

Table 1. Order Parameter Results by Poling Parameters

The maximum value of the first order parameter was arbitrarily estimated at 0.85 due to the unavailability of data on chromophore number density and hyperpolarizability. We attempted unsuccessfully to contact the supplier of the chemicals as well as other lab members.

Plots of the order parameters for the samples poled at 115°C are given below.

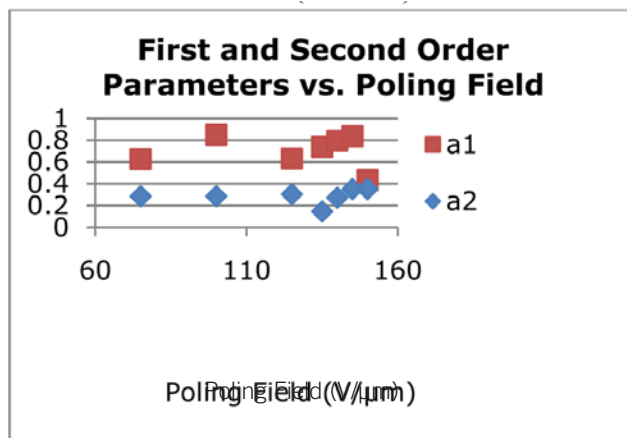


Chart 1. First and Second Order Parameters vs. Poling Field (at 115°C)

Higher poling fields are expected to align the chromophores more accurately. The plotted data as a whole did not show any noticeable trend. The only support for the desired trend appeared in the interval 125 to 145 V/μm and at approx. 50-60 V/μm (not plotted due to different poling temperatures, but had significantly lower a_1 than the points plotted). There are at least two possible sources of error. First of all, the samples were fabricated in several batches which did not correspond in any simple way to the poling parameters used. Also, there were noticeable fluctuations in the lock-in amplifier readings that made it difficult to write down an average value accurately when observing the readings by eye.

The second order parameter did not show a trend with respect to poling field. This is as expected since a uniform poling field should affect the first order parameter only. A second order parameter significantly larger or more significantly correlated with poling parameters than that observed would have been considered an undesirable side effect. The efficiency of a device with a large linear dichroism would be more sensitive to the polarization of the input light.

Conclusions

I successfully developed a LabVIEW program to control the temperature of the new poling oven via the Watlow temperature controller and to record data on actual temperature vs. time. The temperature control accuracy is limited by the design of the Watlow controller and is outside the scope of the LabVIEW program.

Neither the first nor the second order parameter of the poled

samples showed a clear correlation with the poling field. Additionally, time constraints prevented the testing of a sufficiently wide temperature range at any given poling field. It is evident that more samples must be tested in order to thoroughly evaluate the effects of poling field, temperature, and duration. Such testing should include a determination of the temperature and field limits at which the polymer layer breaks down.

Future investigation should consider the effects of the loading density of the chromophore and of different host polymer and chromophore types.

References

1. D. Apitz, R. P. Bertram, N. Benter. Phys Rev E 72, 036610 (2005).
2. G. Khanarian, J. Sounik, D. Allen. J Opt Soc Am B 1996, Vol. 13 No. 9/September 1996, 1927-1934.

Acknowledgments

Funds for this research were provided by the Center on Materials and Devices for Information Technology Research (CMDITR), NSF Science and Technology Center No. DMR 0120967.

Thanks to Ram Voorakaranam for assistance with the physical setup of the new poling system and with some portions of LabVIEW programming.

Thanks to Roland Himmelhuber for assistance with the fabrication of samples.



CHRISTOPHER LIU is an undergraduate in Applied Physics at California Institute of Technology.

Effect of Monomer Chemical Structure on Kumada Catalyst Transfer Polymerization

ELIZABETH MERTEN, University of Washington

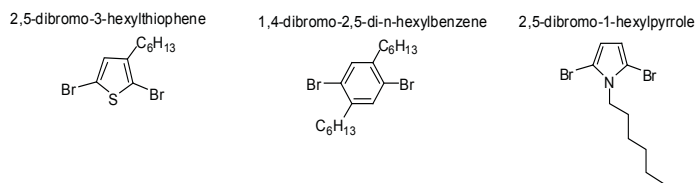
Natalia Doubina, Christine K. Luscombe, University of Washington

Introduction

The ability of chemists to design and synthesize π -conjugated organic polymers remains the key to technological breakthroughs using polymer materials in electronic and photonic devices and the development of nanoscale devices. Traditional approaches to synthesizing these polymers lead to a step growth polymerization, therefore the molecular weight and polydispersity have rarely been controlled. In order to fully utilize the attractive qualities of π -conjugated polymers for the improvement of organic electronic devices, polymerization methods must be developed that allow for greater control over the properties of synthesized polymers.

The recent discovery of Kumada catalyst transfer polymerization (KCTP) of regioregular poly-3-hexylthiophene (rr-P3HT) made by McCullough et al. and Yokozawa et al. has attracted our attention as a gateway to synthesizing more elaborate polymer structures such as block copolymers, star polymers, surface grafted polymers as well as applying this polymerization technique for the synthesis of alternative polymers besides P3HT. In the KCTP mechanism, the polymerization initiator is generated by the transmetalation reaction of two Grignard functionalized monomers with the Ni catalyst. In the next step, the generated Ni(0) species begins the catalytic cycle by inserting into the terminal C-Br bond of the initiator complex and undergoing the transmetalation reaction with another monomer. Thus, based on this unexpected ability of Ni catalyst to migrate intramolecularly to the propagating end of the polymer molecule without diffusion to the reaction mixture, polymerization occurs with addition of one monomer at a time. In the KCTP mechanism, one Ni molecule forms one polymer chain, so the molecular weight of the polymer is proportional to Ni loading and the polydispersity index is very narrow.

The objective of this research is to investigate if KCTP technique could be applied to the synthesis of other polymers besides P3HT. In this study we will take a look at three monomers 2, 5-dibromo-1-hexyl-1H-pyrrole, 2, 5-dibromo-3-hexylthiophene and 1, 4-dibromo-2, 5-di-hexylbenzene and their reactivity to the nickel catalysts, 1, 3-bis(diphenylphosphino)propane nickel(II) chloride and triphenylphosphine nickel(II) chloride. Reactions that have slower reductive elimination and faster oxidative addition states should undergo predominantly chain-growth polymerization and thus successfully display controlled molecular weight and a narrow polydispersity index. Each of the monomers will be synthesized, polymerized and characterized for the potential to create favorable conditions for KCTP polymerization. The concentrations of the nickel catalysts will be varied in the polymerizations of each monomer.



Experimental Section

Synthesis of the Monomers

2-Bromo-3-hexylthiophene (1):

3-Hexylthiophene (4.9485 g, 0.0294 mol, 1 eq), acetic acid (60 ml) and N-Bromosuccinimide (NBS) (5.233 g, 0.294 mol, 1 eq) were placed into a 3 neck round bottom flask covered in aluminum foil and stirred at room temperature for 30 minutes. Water (20 ml) was added and solution was allowed to stir for an additional ten minutes. The mixture was washed with ether and saturated aqueous NaHCO_3 , water then dried with MgSO_4 and filtered. The solvent was removed by rotary evaporation to yield a clear orange liquid (4.6116 g).

2, 5-Dibromo-3-hexylthiophene (2):

2 M NBS (3.5791 g, 20.12 mmol) in a solution of 1:1 mixture of chloroform (60 ml) and acetic acid (60 ml) were added to 2-bromo-3-hexylthiophene (2.4855 g, 10.05 mmol) in a round bottom flask and allowed to reflux for 90 minutes then allowed to cool to room temperature. Solution was washed with chloroform (100 ml) and water (100 ml). The organic layer was extracted then washed with 2.0 M KOH (100 ml, three times) and dried with MgSO_4 and filtered. Solvents were removed by rotary evaporation and column chromatography was performed to yield 2, 5-dibromo-3-hexylthiophene as slightly colored oil. NMR (CDCl_3): δ (ppm) 6.8(s, 1H), 2.5(t, 2H), 1.5(m, 3H), 1.2(m, 8H), 0.9(m, 3H).

1, 4-Di-n-hexylbenzene (3):

1, 4-dichlorobenzene (5 g, 34 mmol), 1,3-bis(triphenylphosphino)propanenickel(II) chloride (18 mg, 33.3 μmol) in a three neck round bottom flask under nitrogen. Dry diethyl ether (40 ml) was added and placed in a cooling bath. Hexylmagnesium bromide (42.5 ml, 85 mmol) was added drop wise to the solution at 0 degrees. Water bath was removed and mixture was allowed to reflux overnight. The mixture was quenched carefully with water (3ml) followed by 2.0 M HCl (30 ml). After phase separation, the aqueous phase was extracted with diethyl ether (25 ml, two times) and the organic phases washed with water (25 ml). Solvent was removed by rotary evaporation after being dried with MgSO_4 and filtered to yield

slightly yellow oil.

1, 4-Dibromo-2, 5-di-n-hexylbenzene (4):

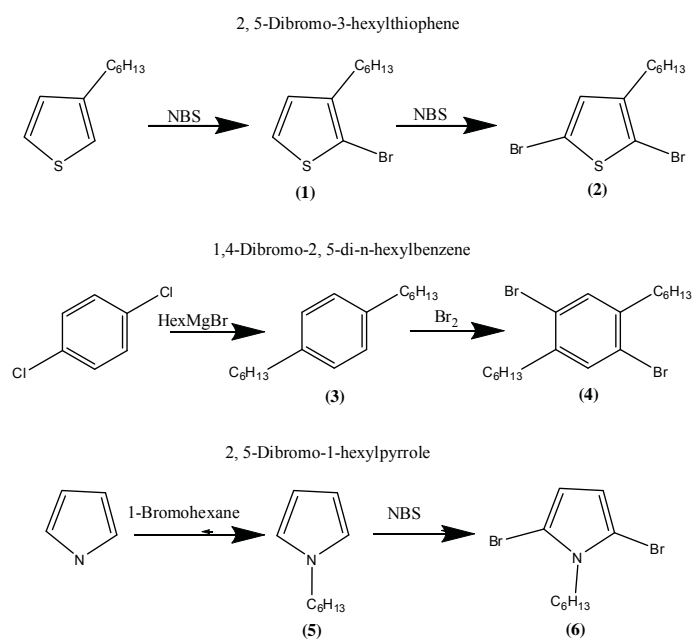
Bromine was added in neat to a solution of 1, 4-dihexylbenzene and iodine in a three neck flask covered in aluminum foil at 0 degrees and stirred. After 1 day at room temperature 20% aqueous potassium hydroxide solution (50 ml) was added and the mixture was shaken under warming conditions until the color disappeared. The mixture was decanted and recrystallized from ethanol to give slightly pink colored crystals. NMR (CDCl₃): δ (ppm) 7.35(s, 2H), 2.64(t, 4H), 1.6-1.49 (m, 4H), 1.41 (m, 12H), 0.8 (t, 6H).

1-Hexyl-1H-pyrrole (5):

Pyrrole (12.87 ml, 185.5 mmol, 1 eq) was added drop wise into a solution of NaH (4.8987 g, 204 mmol, 1.1 eq) and THF (100 ml, 20 ml per gram of NaH) in a three neck round bottom flask under nitrogen at 0 degrees and stirred for one hour at room temperature. Bromohexane (31.25 ml, 222.6 mmol, 1.2 eq) was added drop wise and solution was refluxed overnight. The cloudy yellow solution was cooled to room temperature and quenched carefully with water (25 ml), washed with ether (75 ml, 3 times) then washed once with 1M HCl and dried over anhydrous Magnesium Sulfate. The solution was filtered via gravity filtration and solvents were removed by rotary evaporation to yield a golden colored liquid. Column chromatography was performed to purify the solution.

2, 5-dibromo-1-hexyl-1H-pyrrole (6):

N-Bromosuccinimide (NBS) was added to a solution of 1-Hexyl-1H-pyrrole and dry THF in a round bottom flask covered in aluminum foil. After 3 hours of stirring at -78 C the mixture was allowed to warm slowly to -10C overnight. Triethylamine was added. The solution was then eluted through a short Al₂O₃ plug with hexanes.



Scheme 1: Synthesis routes for monomers.

Preparation of Grignard reagent and polymerization of monomer

Poly -3- hexylthiophene

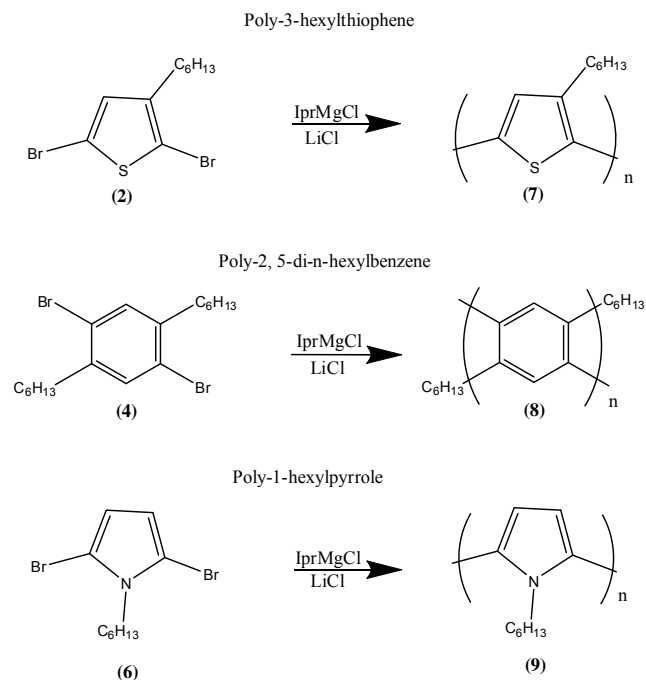
2.0 M Isopropyl magnesium chloride solution in tetrahydrofuran (0.51 ml) and dry THF (5 ml) to four three neck flasks under nitrogen and stirred for five minutes. Lithium Chloride (0.04 g) was added and solution was stirred at RT for 6 hours. 2, 5-Dibromo-3-hexylthiophene (0.3 g) was added drop wise to the solution stirred for 1 hour and nickel catalyst was added. See table 1 for specific amounts.

Poly-2, 5-di-n-hexylbenzene using Ni(dppp)Cl₂

2.0 M Isopropyl magnesium chloride solution in tetrahydrofuran (0.62 ml) and dry THF (5 ml) to four three neck flasks under nitrogen and stirred for five minutes. Lithium Chloride (0.05 g) was added and solutions were stirred at RT for 6 hours. 1, 4-Dibromo-2, 5-di-n-hexylbenzene (0.5 g) dissolved in dry THF was added drop wise to the solution stirred for 1 hour and nickel catalyst was added. See table 1 for specific amounts.

Poly -1- hexylpyrrole

2.0 M Isopropyl magnesium chloride solution in tetrahydrofuran and dry THF to four three neck flasks under nitrogen and stirred for five minutes. Lithium Chloride was added and solution was stirred at RT for 6 hours. 2, 5-dibromo-1-hexyl-1H-pyrrole was added drop wise to the solution stirred for 1 hour and nickel catalyst was added.



Scheme 2: Synthesis routes for polymers.

Table 1: Exact amounts of catalyst used in polymerizations of 2,5-dibromo-3-hexylthiophene and 1,4-Dibromo-2,5-di-n-hexylbenzene		
Poly -3- hexylthiophene		
Flask	Ni(dppp)Cl ₂ (mg)	Ni(PPh ₃) ₂ Cl ₂ (mg)
1	27	
2	9	
3		33
4		11
1,4-Dibromo-2,5-di-n-hexylbenzene		
Flask	Ni(dppp)Cl ₂ (mg)	Ni(PPh ₃) ₂ Cl ₂ (mg)
1	34	
2	11	
3		40
4		13

Results and Discussion

Polymerizations of the monomers were done by using various equivalencies of two nickel catalysts. In the polymerization of 2,5-dibromo-3-hexylthiophene the Ni(dppp)Cl₂ produced promising polymers with molecular weight that was expected from the ratio of catalyst used and a very narrow PDI. Polymerizing the same monomer with the Ni(PPh₃)₂Cl₂ catalyst produced various oligomers as did the 1,4-dibromo-2,5-di-n-hexylbenzene polymerized with the Ni(dppp)Cl₂ catalyst. The polymerization of 1,4-dibromo-2,5-di-n-hexylbenzene with Ni(PPh₃)₂Cl₂ produced a polymer with a narrow PDI and high molecular weight.

Table 1: Results of polymerizations for Poly -3- hexylthiophene and 1,4-Dibromo-2,5-di-n-hexylbenzene				
Poly -3- hexylthiophene				
Flask	Catalyst	Equivalence	Mn	PDI
1	Ni(dppp)Cl ₂ (mg)	20	6900	1.3
2	Ni(dppp)Cl ₂ (mg)	60	10700	1.3
3	Ni(PPh ₃) ₂ Cl ₂ (mg)	20	< 1500	
4	Ni(PPh ₃) ₂ Cl ₂ (mg)	60	2000	5.7
Poly -2,5-di-n-hexylbenzene				
Flask	Catalyst	Equivalence	Mn	PDI
1	Ni(dppp)Cl ₂ (mg)	20	< 2000	
2	Ni(dppp)Cl ₂ (mg)	60	< 2000	
3	Ni(PPh ₃) ₂ Cl ₂ (mg)	20	< 1500	
4	Ni(PPh ₃) ₂ Cl ₂ (mg)	60	10000	1.8

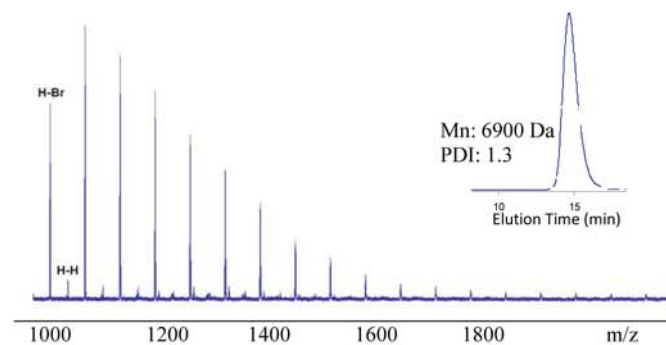


Figure 1: MALDI-TOF and GPC spectrum of P3HT synthesized with Ni(dppp)Cl₂ catalyst, 20 eq

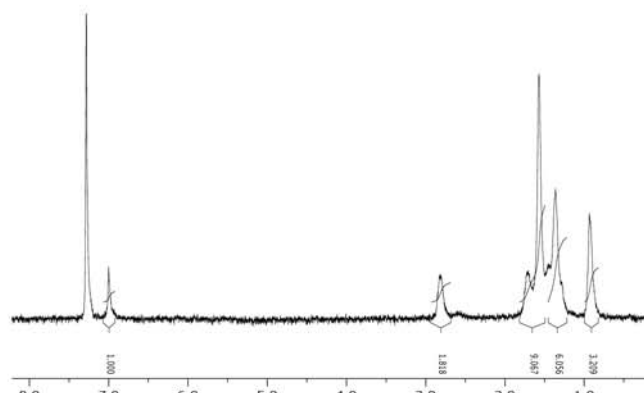


Figure 2: H NMR Spectra of P3HT synthesized with Ni(dppp)Cl₂ catalyst, 20 eq

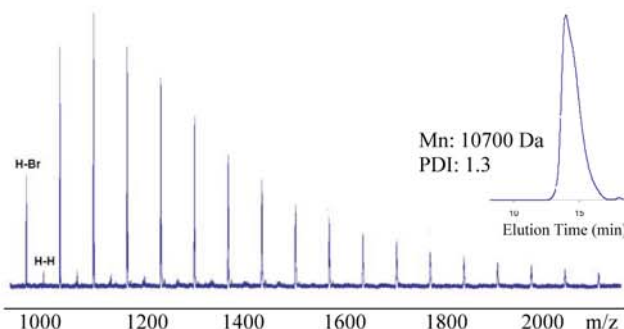


Figure 3: MALDI-TOF and GPC spectrum of P3HT synthesized with Ni(dppp)Cl₂ catalyst, 60 eq

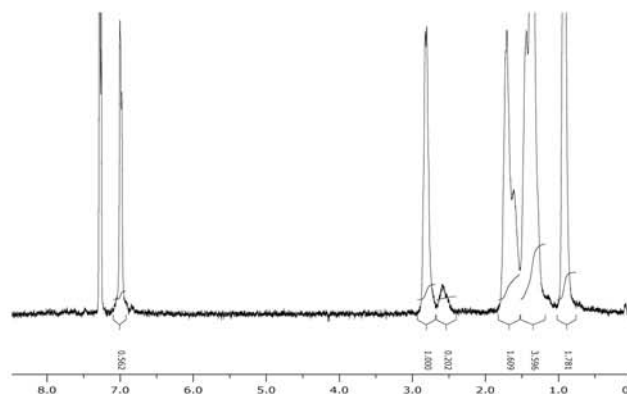


Figure 4: H NMR Spectra of P3HT synthesized with Ni(dppp)Cl₂ catalyst, 60 eq

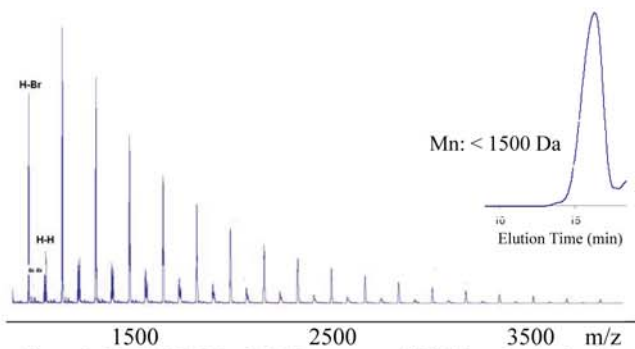


Figure 5: MALDI-TOF and GPC spectrum of P3HT synthesized with $\text{Ni}(\text{PPh}_3)_2\text{Cl}_2$ catalyst, 20 eq

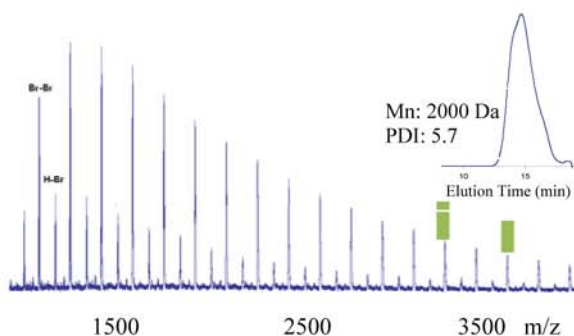


Figure 6: MALDI-TOF and GPC spectrum of P3HT synthesized with $\text{Ni}(\text{PPh}_3)_2\text{Cl}_2$ catalyst, 60 eq

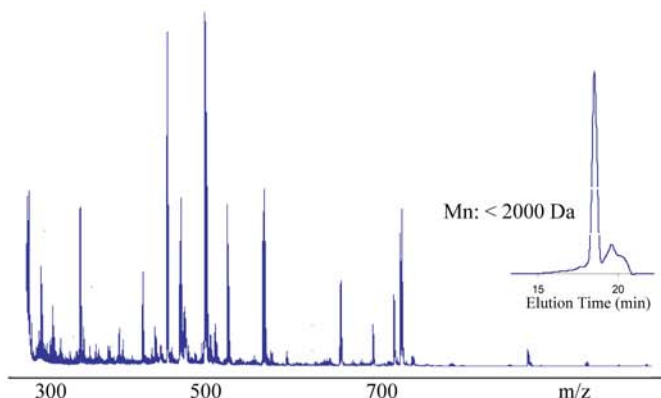


Figure 7: MALDI-TOF and GPC spectrum of Poly-2, 5-di-n-hexylbenzene synthesized with $\text{Ni}(\text{dppp})\text{Cl}_2$ catalyst, 20 eq

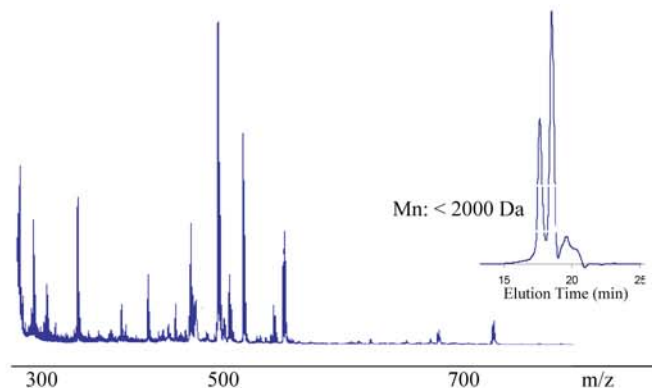


Figure 8: MALDI-TOF and GPC spectrum of Poly-2, 5-di-n-hexylbenzene synthesized with $\text{Ni}(\text{dppp})\text{Cl}_2$ catalyst, 60 eq

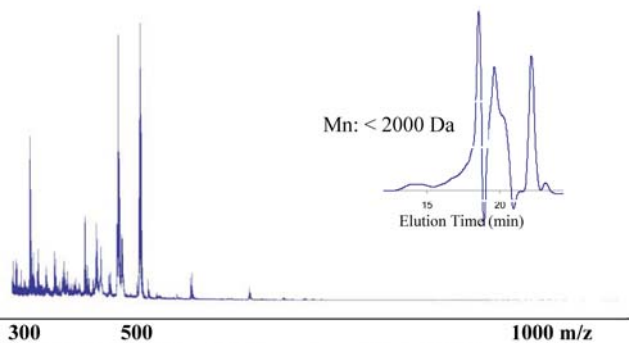


Figure 9: MALDI-TOF and GPC spectrum of Poly-2, 5-di-n-hexylbenzene synthesized with $\text{Ni}(\text{PPh}_3)_2\text{Cl}_2$ catalyst, 20 eq

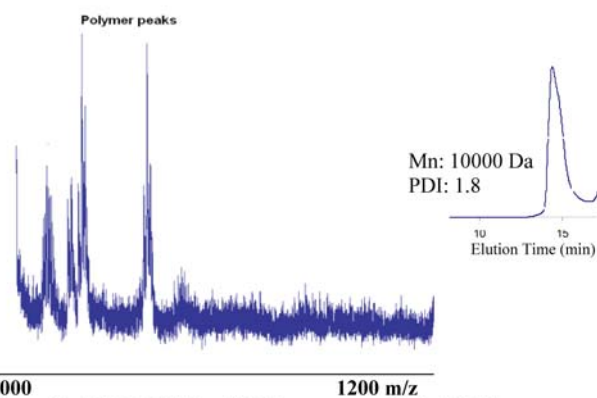


Figure 10: MALDI-TOF and GPC spectrum of Poly-2, 5-di-n-hexylbenzene synthesized with $\text{Ni}(\text{PPh}_3)_2\text{Cl}_2$ catalyst, 60 eq

As seen in figures 1-4 the polymerization of P3HT with the 20 and 60 equivalency of $\text{Ni}(\text{dppp})\text{Cl}_2$ catalyst resulted in a polymer with high molecular weight and narrow PDI. When P3HT was polymerized with the $\text{Ni}(\text{PPh}_3)_2\text{Cl}_2$ catalyst various oligomers formed with low molecular weight as seen in figures 5-6. Similar results are seen in figures 7-8 when poly-2,5-di-hexylbenzene is polymerized with $\text{Ni}(\text{dppp})\text{Cl}_2$. When $\text{Ni}(\text{PPh}_3)_2\text{Cl}_2$ is used at 20 equivalency various oligomers were formed with low molecular weights as seen in figure 9. Changing the concentration of the catalyst to 60 eq produced a polymer with high molecular weight and narrow PDI.

Conclusion

In the process of polymerizing the various monomers with the nickel catalysts we observed that the 2, 5-Dibromo-3-hexylthiophene undergoes chain-growth polymerization with $\text{Ni}(\text{dppp})\text{Cl}_2$ and undergoes step-growth polymerization with $\text{Ni}(\text{PPh}_3)_2\text{Cl}_2$.

1,4-Dibromo-2,5-di-hexylbenzene did not undergo chain growth polymerization with $\text{Ni}(\text{dppp})\text{Cl}_2$. However, 1,4-Dibromo-2,5-di-hexylbenzene monomer polymerized with $\text{Ni}(\text{PPh}_3)_2\text{Cl}_2$ which resulted in polymer with high Mn and low PDI (polymerization mechanism is still under investigation).

Through the data obtained from the experiments we were able to conclude that molecular weights of the polymers can be controlled via Ni(O) loading and the polymers that have an affinity to receive an electron will display characteristics of KCTP.

Acknowledgments

Funds for this research were provided by the Center on Materials and Devices for Information Technology Research (MDITR) National Science Foundation Science and Technology Center No. DMR 0120967. Special thanks to Professor Christine Luscombe, my mentor Natalia Doubina and the members of the Luscombe lab for all of their guidance and support.



ELIZABETH "LIZZY" MERTEN is a current student at the University of Washington working on her bachelor's degree in Materials Science and Engineering as well as Mathematics. She aspires to one day become a research scientist in the field of nanotechnology and its applications in the field of cancer research.

Characterization of Diffraction Gratings Comprised of Core/Shell Nanocrystals

BELINDA D. MOLINA, University of Texas at El Paso

Mario Malfavon, Andrea Munro, Neal R. Armstrong, University of Arizona

Introduction

Currently there is interest to produce "lab-on-a-chip" technologies for applications as sensor platforms. These technologies provide promising applications as inexpensive, low power, and compact devices for portable sensing applications. New sensing platforms are being developed using fully integrated light sources (organic light emitting diodes, OLEDs) and photodetectors (organic solar cells, OPV). The light sources in these platforms suffer from being non-monochromatic (they don't emit at a single wavelength) and they are typically low power devices. We are developing new sensor platform technologies that will take advantage of recently developed nanocrystalline diffraction gratings to in-couple OLED emission into waveguide modes.

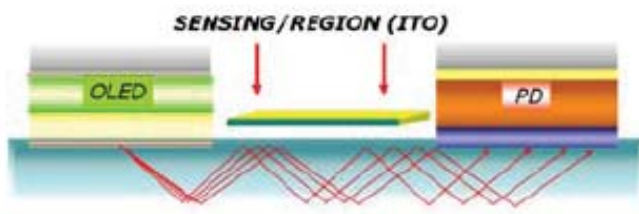


Figure 1: Proposed illustration for a sensor platform.

These more monochromatic light sources will allow these platforms to function as absorbance detectors. Narrow emission from highly fluorescent core/shell semiconductor nanocrystals (NC) can be utilized towards this end if their fluorescence can be coupled into waveguide modes. A favorite semiconductor nanocrystal is CdSe, which is easily size-tunable and emits across Mario Malfavon, Andrea Munro, Neal R. Armstrong, University of Arizona most of the visible wavelength region, depending upon its size (from 2-7 nm diameter particles are possible). Thin CdS "shells" are added to the CdSe NCs core, leading to increased photoluminescence quantum yields afforded by exciton localization on the CdSe core.²

Method

CdSe quantum dots were synthesized using the method developed by Peng.³ A typical synthesis consisted of combining CdO (0.0127g) and stearic acid (0.1140g) in a three neck round bottom flask under argon. The solution was then heated to 150°C until a clear solution formed upon formation of Cd-stearate. When the solution

cooled to room temperature, 1.94g of both trioctylphosphine oxide and hexadecylamine were added and the solution was then heated to 315°C. At this temperature, a Selenium-tributylphosphine (Se-TBP) solution containing Se (0.079 g) dissolved in TBP (0.238g) and dioctylamine (DA) (1.681g) previously prepared and stored in an inert atmosphere glove box was rapidly injected into the Cd-stearate / ligand solution. Crystals nucleated and were grown for two minutes resulting in approximately 3nm diameter nanocrystals. At intervals throughout the growth of the NCs, aliquots were removed to monitor the growth of the crystals by UV-Vis spectroscopy. Growth was terminated by removing the solution from the heating mantle. The NCs were then purified by precipitation with acetone and centrifugation for 3 minutes at 3000 rpm. The resulting pellet was then stored in hexanes for use in the synthesis of CdSe / CdS core /shell nanocrystals.

Nanocrystal Shell growth procedure

Cadmium Sulfide shells were grown using a modification of the SILAR² technique which is based on alternating injections of Cadmium and Sulfur precursors into a solution containing CdSe NC. Here octadecene was minimized for shell synthesis providing more facile and complete purification of nanocrystals for more effective stamping. The amount of cadmium and sulfur precursors required for each layer was determined by calculating the number of surface atoms present in a chosen volume of CdSe core NC solution.² The Cd precursor was prepared by heating CdO (0.0615g), stearic acid (1.083g), and Octadecene (ODE) (10.8mL) to 100°C for 30 minutes until a clear solution formed. The S precursor was prepared by heating Sulfur (0.0128g) and ODE (10mL) at 250°C for 30 minutes. CdSe nanocrystals dissolved in hexanes were added (1.8E-7 mol nanocrystals) to HDA (1.35g) in a three neck round bottom flask under dynamic argon, using Schlenk techniques. Vacuum was then applied while heating to 100°C for 30 minutes to remove hexanes. The system was then placed under dynamic argon and heated to the desired injection temperature of 245°C. The first injection of Cadmium precursor (0.38mL of a 0.04M solution) was rapidly injected to avoid solidification of the Cd precursor solution in the syringe. The S injection (0.38mL of a 0.04M solution) was then added drop-wise, while maintaining the temperature at or above 240°C. The second layer was grown following the same injection method; however increasing precursor volumes to 0.64mL to accommodate the increase in surface atoms resulting from the first shell addition. An aliquot was taken before precursor injection and after growth of each shell to monitor the shell growth via UV-Vis analysis. Once the shells were added the reaction was cooled to room temperature. Purification of the core/shell nanocrystals was done through a series of precipitations. The first precipitation was done via centrifugation in ethanol for 3

minutes at 3000rpm. Two subsequent precipitations were carried out by dissolving the nanocrystal pellet in minimal chloroform and precipitating with acetone, approximately 250% v/v. The recovered nanocrystal pellet was then dissolved in hexanes resulting in a solution with an absorbance of $5.88E-2AU$ at 565 nm, the first wavelength of maximum absorbance. Micro-contact stamping techniques were then used to prepare a diffraction grating using ITO coated glass as a substrate. Two subsequent precipitations were carried out by dissolving the nanocrystal pellet in minimal chloroform and precipitating with acetone, approximately 250% v/v. The recovered nanocrystal pellet was then dissolved in hexanes resulting in a solution with an absorbance of $5.88E-2AU$ at 565 nm, the first wavelength of maximum absorbance. Micro-contact stamping techniques were then used to prepare a diffraction grating using ITO coated glass as a substrate.

Results

CdSe nanocrystal cores with an absorbance maximum at 550 nm, which corresponds to a NC diameter of 3.04 nm, were prepared and dissolved in hexanes until absorbance at this wavelength reached 0.0886 AU (corresponding to an optical density which resulted in a viable NC crystal solution for stamping). Core / Shell nanocrystals prepared as described above, were also dissolved in hexanes, for stamping, to an absorbance of 0.0582 AU at a wavelength maximum of 565 nm. This 15 nm red shift corresponded to approximately 1.5 monolayers of CdS or approximately 1 nm of shell growth, which can also be seen as a visible shift in emission from green to yellow (Figure 4). UV-Vis was taken for absorbance so that diameter calculations could be made. Using UV-Vis we can calculate full width half max. The core nanocrystals had a full width half max of 28nm, the core/shell had a full width half max of 30nm.

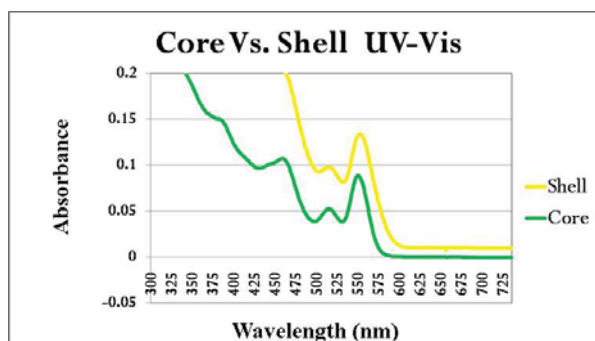


Figure 2: UV-Vis comparing both core and core/shell nanocrystals.

Max Absorbance and Diameter		
	Absorbance(AU)	Diameter(nm)
Core	550 AU	3.04nm
Shell	565 AU	~4.00nm

Table 1: The correlation between max absorbance and diameter.

Nanocrystal cores were stamped using micro-contact stamping techniques to prepare functional diffraction gratings (1200 grooves/mm). Radiation at 488 nm was coupled into the diffraction grating wave guide, not only did the core diffraction grating diffract light but internal reflectance was also observed.

Highly fluorescent diffraction gratings composed of core/shell nanocrystals were also successfully prepared. They not only showed the in-coupling of incident light but also the in-coupling of NC fluorescence. (Fig. 3)

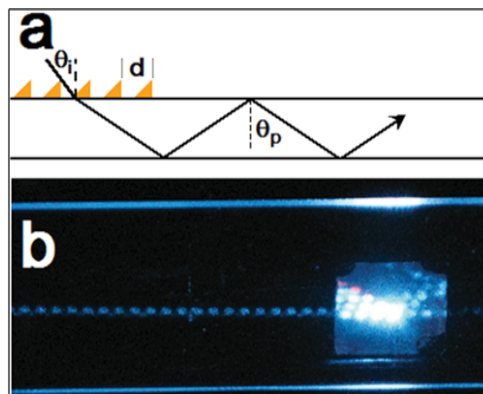


Figure 3: a.) a schematic view of a light being coupled into a wave guide. b.) an actual photograph of a core diffraction grating in-coupling incident light into a waveguide, producing internal reflectance .

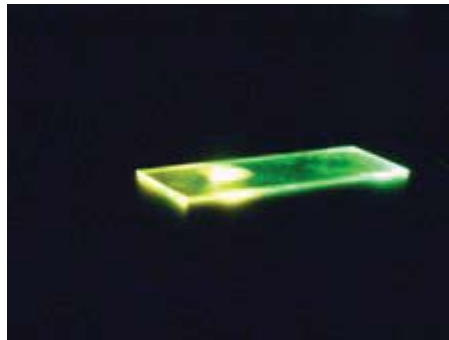


Figure 4: Shows the in-coupling of a green laser (green) and the in-coupling of the fluorescence (orange to the naked eye).

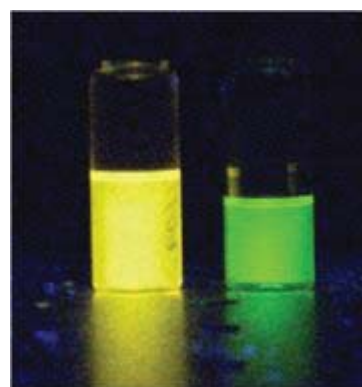


Figure 5: Depicts the shift in emission from green to yellow observing nanocrystal growth

SEM images were obtained to characterize the grating surface. For optimized core diffraction gratings we can see the substrate between the features of the diffraction grating.(Fig. 6) For our core/shell gratings, the lack of observable substrate between features shows that although functional gratings were produced, there is still room for optimizing the microcontact stamping of these materials. (Fig. 7)

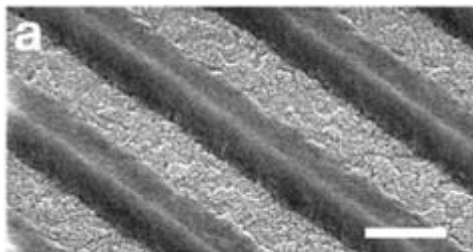


Figure 6: 1200 grooves/mm, the SEM image of our core diffraction grating observes substrates between features

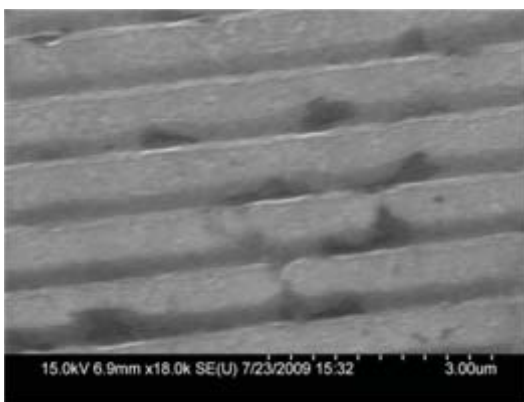


Figure 7: 1200 grooves/mm, the SEM image of our core/shell diffraction grating observes no substrate between features.

Diffraction efficiencies were measured using an argon laser (1.5 mW) for both core and core / shell nanocrystal gratings. Results appear in the table below.

Diffraction Efficiency (%)		
Volume of NC solution (uL)	Cd/Se Core	Cd/S Shell
50	0.53	0.69
75	0.37	0.89
100	0.93	0.04

Table 2: Diffraction efficiencies of both Cd/Se core and Cd/S Shell.



Figure 8: An argon laser (1.5mW) at an angle of 33.5°, showing the diffraction of the core/shell diffraction grating.

Conclusion

Core/shell NCs were synthesized via a SILAR procedure² and diffraction gratings were prepared by a facile micro-contact stamping technique.¹ Gratings composed of microcontact stamped nanocrystals not only diffracted incident laser radiation, but also demonstrated coupling of the NC fluorescence into waveguide modes of the supporting substrate (e.g. commercially available glass microscope slides). These preliminary results indicate that core/shell NC gratings are intriguing for applications where quasi-monochromatic light sources are required (e.g. monodisperse NC samples display a FWHM spectral distribution of ca. 25 nm) for sensor applications.

References

1. Shallcross, R. Clayton; Chawla, Gulraj S.; Marikkar, F. Saneeha; Tolbert, Stephanie; Pyun, Jeffrey; Armstrong, Neal R., Efficient CdSe Nanocrystal Diffraction Gratings Prepared by Microcontact Molding. ACS Nano Submitted
2. Li, J. Jack; Wang, Y. Andrew; Guo, Wenzhuo; Keay, Joel C.; Mishima, Tetsuya D.; Johnson, Matthew B.; Peng, Xiaogang, Large-Scale Synthesis of Nearly Monodisperse CdSe/CdS Core/Shell Nanocrystals Using Air-Stable Reagents via Successive Ion Layer Adsorption and Reaction. Journal of the American Chemical Society 2003, 125 (41), 12567-12575.
3. Qu, L. H.; Peng, X. G., Control of Photoluminescence Properties of CdSe Nanocrystals in Growth. Journal of the American Chemical Society 2002, 124, (9), 2049-2055.
4. Peng, Z. Adam; Peng, Xiaogang; Nearly Monodisperse and Shape-Controlled CdSe Nanocrystals via Alternative Routes: Nucleation and Growth. Journal of the American Chemical Society 2002, 124, 3343-3353.
5. Murray, C. B.; Kagan, C. R.; Bawendi, M. G.; Synthesis and Characterization of Monodisperse Nanocrystals and Close-Packed Nanocrystal Assemblies: Annual Review of Materials Science 2000, Volume 30: 545-610.

Acknowledgements

This work was made possible by the NSF sponsored Science and Technology Center on Materials and Devices for Information Technology Research, No. DMR-0120967.

4-Tritylphenol Bridge Substitution Effects on Dipole-Dipole Interactions of Polymeric Second Order Nonlinear Optical Materials

ROSA NEIDHARDT, University of California - Irvine

Brent Polishak, Alex Jen, University of Washington

Introduction

Nonlinear optical materials are materials that exhibit nonlinear electro-optic effects such as differential frequency mixing and second harmonic generation. These materials have potential uses in various areas such as telecommunications, security and medicine. The telecommunication applications include radio frequency photonics¹, optical switches² and optical data storage². The security applications include land mine detection¹ and the use of Terahertz frequencies for weapons detection. Medical applications include the detection and generation of Terahertz frequencies³ which can be for cellular imaging⁴, label-free genetic analysis⁴, and chemical and biological sensing⁴.

Organic nonlinear materials are a popular area of research because they possess many beneficial characteristics including low dielectric constants, minimal refractive index dispersion, and an ease of fabrication and processing.² With their low dielectric constants and minimal dispersion organic materials produce a large frequency bandwidth and consume less electrical power.⁵ Their ease of fabrication and processing allows for a variety of structures and shapes in various applications.

The nonlinear optical behavior in organic based molecules arises from the perturbation of the electrons in the overlapping pi orbitals by an applied electric field.⁵ In this case, the perturbed electrons respond in a nonlinear fashion under the applied field. Push-pull nonlinear optical materials are made up of chromophores constructed with an electron rich donor, a pi conjugated bridge, and an electron deficient acceptor.⁵ The resulting structure achieves an asymmetric electronic response and leads to an imbalance of the charge distribution yielding a dipole moment. The ease of charge re-distribution in the presence of an externally applied electric field is defined as the hyperpolarizability.⁵ In general, the dipole moment and hyperpolarizability determine the molecular nonlinear optical behavior of a chromophore structure. However, the macroscopic nonlinear optical behavior is more critical to understanding in order to harness the behavior for potential applications.

In order for organic materials to be used for nonlinear optical applications the system at the macroscopic level must be aligned in a noncentrosymmetric ordering⁶. This level of ordering can be attained through a variety of approaches, but is more commonly and efficiently achieved by the process of poling⁷. Poling involves heating a polymeric matrix with chromophore to the glass transition temperature of the composite material thereby allowing the dipoles to move with ease and align with the applied electric field. The polymer is then cooled below the glass transition temperature with the electric field still applied in order to maintain the alignment of the dipoles. One of the key parameters to poling is the strength of

the dipole moment within the dye molecule. A larger dipole moment within the dye molecule will result in a more rapid response to the applied field and an efficient alignment of the molecule to the applied electric field.

However, due to the nature of these dipole moments, the dye molecules energetically favor dipole-dipole electrostatic interactions due to the electron rich and electron deficient parts of the molecules interacting with one another.

These interactions begin at the molecular scale then continue to the macroscopic scale leading to aggregation, phase separation, reduced solubility, and a loss in poling efficiency. Previous research efforts applied bulky functional groups positioned at the acceptor and donor regions of the dye molecule in an attempt to inhibit the dipole-dipole interactions. However, little research has been done on the placement of a rigid, bulky molecule positioned in the middle of a phenyltetraene-based bridge². Substitution in the middle of the bridge, instead of at the acceptor and donor, could potentially reduce the molecular weight of the chromophore and as a result, would allow researchers to dope more chromophore into the polymer for increased electro-optical behavior. The purpose of this study is to determine if dipole-dipole interactions can be inhibited by bulky substitutions in the middle of the bridge.

The objective of this research is to synthesize different structural chromophores with a rigid, bulky and sterically hindering group (4-tritylphenol) attached to the middle of the chromophore bridge to test if this structure can prevent or disrupt dipole-dipole stacking interactions between the chromophores. The three chromophores designed for this research are depicted in Figure 1. The control chromophore with no additional bulky functional groups is AJY-OPh and the two bulky chromophores are AJPR101 and AJPR100. The 3-D image in Figure 2 depicts the tight packing that occurs between two chromophores without bulky bridge substitutions. Figure 3 on the other hand, illustrates the difference in packing when two bulky chromophores, such as AJPR100, attempt to pack. Thus, we set out to determine if such bridge derivation could be used to disrupt, if not weaken the electrostatic interactions between adjacent chromophores.

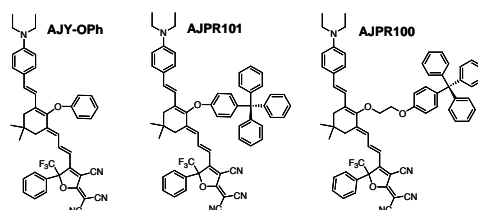


Figure 1. Image of the three chromophores: the non-bulky chromophore (AJY-OPh), the basic bulky chromophore (AJPR101) and the extended bulky chromophore (AJPR100).

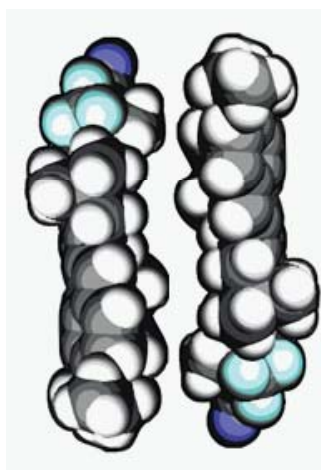


Figure 2. 3-D image of two AJY-Oph chromophores closely packed with acceptors interacting with donors.

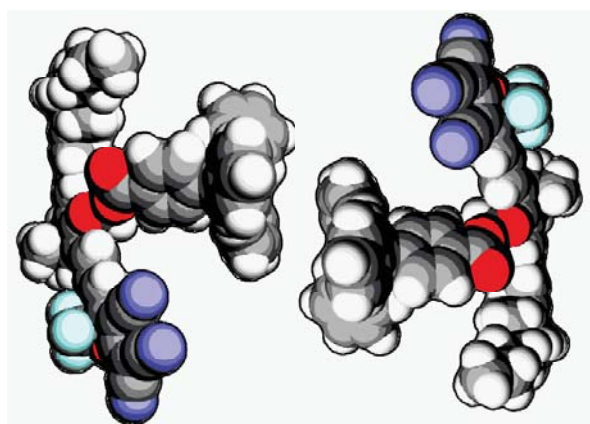


Figure 3. 3-D image of two AJPR100 chromophores packing not as closely as the AJY-Oph chromophores.

Results and Discussion

Synthesis

The experimental module first consists of synthesizing the two bulky dye molecules (AJPR100 and AJPR101). AJY-Oph was previously designed and synthesized by the Jen research group. AJPR101 was designed to contain the 4-tritylphenol moiety directly attached to the pi-conjugated bridge. AJPR100 was designed with an ethylene glycol linkage between the 4-tritylphenol and the pi-conjugated bridge bulky molecule to study the impact of the bulky group if the group were to be distanced from the core bridge. The two molecules were synthesized in a similar fashion following the procedure shown in Figure 4.

However, during the synthesis of AJPR101, the trienenitrile (**2A**) could not be synthesized via the Wittig-Horner reaction using

diethyl(cyanomethyl)phosphonate. We attribute this fact to the steric hindrance of both the reactant and the chromophore around the reactive ketone. The less bulky reagent indicated in Figure 4 was used instead to achieve the trienenitrile (**2A**) for continued synthesis of AJPR101.

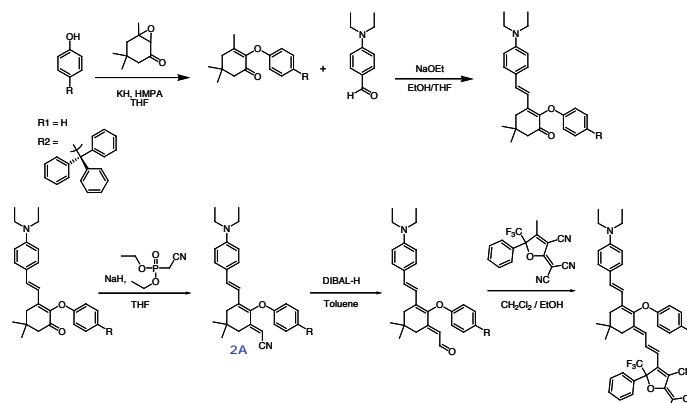


Figure 4. Synthesis of the three chromophores.

Optical Analysis

The optical data was collected via UV vis spectroscopy in order to assess and quantify the energy transitions required to excite the chromophores from the neutral ground state to zwitterionic excited state. The three chromophores were to be placed in three different solvents ranging in polarity to study the solvatochromic behavior of the molecules. In this particular case, the solvatochromic behavior of the three structurally different chromophores could reveal insights into both site-isolation effects and aggregation behavior.

The absorption spectrum in Figure 5 for AJPR100 indicates that the presence of the extended bulky functional group does not distort or twist the conjugation of the chromophore. This observation can be drawn as the comparison chromophore, AJY-Oph contains a similar charge transfer band and is highly planar. The optical data also reveals the band edge of the chromophore absorbance to be ~1150 nm. This information is crucial as it determines the extent of the chromophore's absorption behavior. For application purposes, any overlap between the chromophore's band edge and the potential laser wavelength would result in the absorption of the laser's energy leading to optical losses.

In the extended bulky chromophore, AJPR100, the UV spectra tells that there is no site-isolation going on in the chromophore. In prior research bulky functional groups have been added to the donor and acceptor regions of the chromophore. In these cases, the bulky substitution groups can shield the chromophore from interacting with polar solvent molecules. In non-shielded chromophores with a neutral ground state, the energy required to excite the chromophore decreases as the solvent stabilizes the excited state transition. In a polar solvent, this leads to red shifting (bathochromic) the chromophore charge transfer band. In a chromophore that does exhibit site-isolation, the charge transfer band undergoes minimal shifting behavior, as the chromophore would be shielded from interactions with the solvent molecules. In the UV-spectra shown in Figure 5, the charge transfer bands for both chromophores shift in a similar fashion in the different solvents. Thus, the extended bulky

group does not site-isolate AJPR100 from the solvent molecules.

Thermal Analysis

The thermal analysis data was collected with differential scanning calorimetry (DSC). This analysis revealed the glass transition temperature, the crystallization formation, and the melting temperature. This thermal data aids in the determining whether the chromophores are crystalline or amorphous in nature and the thermal behavior associated with both.

Table 1 shows the collected thermal data of the three chromophores. The T_g represents the glass transition temperature of the chromophore and the T_d represents the decomposition temperature. AJY-OPh is a crystalline material and exhibits a melting point at $\sim 181^\circ\text{C}$. However the extended bulky derivative, AJPR100, exhibits a glass transition at 95°C and decomposition is onset at a temperature of 145°C . As an amorphous solid, AJPR100 cannot re-arrange itself into crystalline ordering and therefore does not pack in a similar fashion as AJY-OPh. Therefore, this data reveals that the presence of the extended, 4-tritylphenol moiety clearly contributes to amorphous behavior of the material and can disrupt dipole-dipole interactions.

Electric Field Poling and E-O Property Measurements

After the synthesis was complete, the next step was to dissolve these dye molecules with amorphous polycarbonate polymer in dibromomethane in order to prepare the polymeric solution for spincoating into thin films. These solutions were then filtered through a $0.2\text{-}\mu\text{m}$ PTFE filter and then spincoated onto indium tin oxide (ITO) coated glass substrates and dried overnight under vacuum at 85°C . After drying, gold contacts were then placed on top of the polymer films to establish an electrical circuit needed to apply an electric field for poling. The films were then poled and characterized using the Teng-Man simple reflection technique with a wavelength of $1.31\mu\text{m}$.⁸

Table 1 shows the collected electro-optic coefficient, r^{33} , values for the chromophores. The r^{33} of the basic, non-bulky chromophore is 122 pm/V at $28\text{ wt}\%$ whereas the extended bulky chromophore it is 110 pm/V at $28\text{ wt}\%$. We hypothesize that the decrease in the electro-optic coefficient is due to two potential possibilities. The first possible reason is that the extended, bulky addition of AJPR100 could be inhibiting the alignment of these chromophores as it may inhibit or complicate the rotation of the chromophore under an applied field. One way to test this hypothesis would be to pole these materials under identical electric fields and in conjunction with second harmonic generation measurements. The rate of alignment could be determined from the second harmonic generation measurements, which could then be compared. If the rates of alignment were clearly different with AJPR100 displaying a lower rate, then we could conclude that the bulky moiety may be inhibiting alignment during poling.

Another possible reason could be that AJPR100 bulky moiety, 4-tritylphenol, adds substantial weight to the chromophore. This in turn reduces the amount of actual chromophore present in a $28\text{ wt}\%$ material. To determine the legitimacy of this explanation, we could match the number density of each chromophore to make sure the same amount of each chromophore is present in both polymeric films. If both sets of polymeric films exhibit similar

electro-optical measurements, then we could conclude that the higher molecular weight of AJPR100 reduces both the amount of chromophore content present in the material, which in turn would result in a lower electro-optical coefficient.

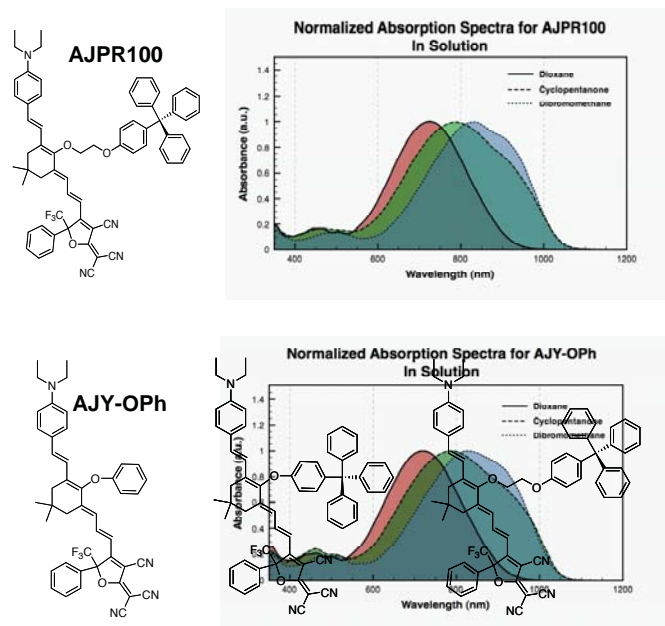


Figure 5. UV spectra for AJPR100 and AJY-Oph.

	T_g ($^\circ\text{C}$)	T_d ($^\circ\text{C}$)	λ_{max}^a (nm)	λ_{max}^b (nm)	λ_{max}^c (nm)	r^{33} (pm/V)
AJY-Oph	--	191	719	791	823	122
AJYPR101	TBA	TBA	TBA	TBA	TBA	TBA
AJYPR100	95	145	725	788	832	110

Table 1. Thermal, optical and poling data for all three chromophores. λ_{max}^a was measured in dioxane. λ_{max}^b was measured in cyclopentanone. λ_{max}^c was measured in dibromomethane. r^{33} values were measured at a wavelength of $1.31\mu\text{m}$. TBA stands for To Be Announced as AJYPR101 is still being synthesized.

Conclusion

The hypothesis of this research appears to be true from the results gathered so far. As shown from the thermal data the bulky substitution does prevent the chromophore from exhibiting crystalline behavior. However, a more thorough collection of data with AJPR101 is needed for a more comprehensive conclusion. Furthermore, more extensive studies will need to be conducted to resolve differences in the electro-optic coefficient values mentioned in the discussion.

References

1. Dalton LR. Nonlinear optical polymeric materials: from chromophore design to commercial applications. *Adv Polym Sci* 2002;158:1–86.
2. Cho, Min Ju; Choi, Dong Hoon; Sullivan, Philip A.; Akelaitis, Andrew J.P.; Dalton, Larry R. *Progress in Polymer Science*. 2008, 33, 1013-1058. See References Within.
3. McLaughlin, C.V.; Hayden, L.M.; Polishak, B.; Huang, S.; Luo, J.; Kim, T.; Jen, A.K. *Appl. Phys. Lett.* 2008, 92, 151107.
4. Ferguson, Bradley; Xi-Cheng Zhang. *Nature Materials*. 2002, 1, 26-33.
5. Gunter, P. *Nonlinear Optical Effects and Materials*. Vol. 72. Berlin: Springer-Verlag, 2000.
6. Würthner, Frank; Sheng Yao; Tony Debaerdemaeker; Rüdiger Wortmann. *J. Am. Chem. Soc. Rev.* 2002, 124, 9431-9447.
7. Kajzar, Francois; Lee, Kwang-Sup; Jen, Alex K-Y. *Advances in Polymer Science*. 2003, 161, 1-80.
8. Teng, C. C.; Man, H. T. *Appl. Phys. Lett.* 1990, 56, 1734.

Acknowledgements

Financial support was provided by the Center on Materials and Devices for Information Technology Research (CMDITR) NSF Science and Technology Center No. DMR 0120967. I want to thank everyone in the Jen lab and especially my mentor Brent for his excellent mentoring and advice for everything. Yo!



ROSA NEIDHARDT is a junior pursuing a degree in chemical engineering at UC Irvine. She is considering pursuing a graduate degree in engineering and plans to study abroad in Japan sometime during her academic career.

Effect of Nanoparticle Volume Fraction on Capacitor Properties of a Barium Titanate/Epoxy Nanocomposite.

AUDREY L. SLUTSKY, University of West Georgia
Ajit Bhaskar, Joseph Perry, Georgia Institute of Technology

Introduction

There is a huge demand for high permittivity and high dielectric strength materials for energy storage¹⁻⁴. Many applications require power and energy to be provided in lightweight and small microelectronic devices^{2,4}. A major impediment to the size reduction of electronic systems falls on discrete passive components, specifically, capacitors^{2,4}. Thus, by reducing the size of capacitors, the size of electronic devices and printed circuit boards (PCBs) can also effectively be reduced^{2,4}. A promising solution to this problem is to embed capacitors in chips or PCBs.

Ceramic thin films can have a high dielectric permittivity and low dielectric loss¹. However, the processability of ceramics is poor and requires high temperature sintering, which is not compatible with many types of substrates¹. Polymers have good processability along with high dielectric strength, but generally possess low permittivity, which negatively affects the storage capacity of the material. Combining polymers and ceramics to form nanocomposites offers the potential to make materials with low cost, low temperature processability, high dielectric strength, high dielectric constant³. As a result, polymer/ceramic nanocomposites are candidate dielectric materials for embedded capacitors³. However, typical polymer/ceramic nanocomposites are not photosensitive, and therefore cannot be patterned with ease into a specific shape on a PCB⁴. Successful development of a polymer/ceramic nanocomposite that included a photosensitive polymer would solve this problem. For this study SU-8, a photosensitive oligomer, is used along with barium titanate (BT) nanoparticles, a ceramic with a high permittivity (around 100). For the polymer/ceramic nanocomposites, the ceramic particles must be surface modified to avoid an agglomeration of nanoparticles¹. Kim et al. have reported that surface modifying BT nanoparticles with phosphonic acids results in high quality nanocomposites with good processability¹.

Experimental Method

BaTiO₃ (BT) nanoparticles were surface modified with phenylbenzylphosphonic acid (PBPA) (Figure 1). For every gram of BT nanoparticles used, 40 mL of ethanol (95:5 (v/v) ethanol/H₂O) was added. The BT and the solvent were ultrasonicated for 35 minutes. After ultrasonication the BT nanoparticles were surface modified with bis-(phenyl)phosphonic acid (PBPA) by adding the PBPA to the ultrasonicated mixture and heating for 15 hours at 70°C. The excess phosphonic acid was removed from the surface modified nanoparticles (PBPA-BT) by centrifugation and rinsing with ethanol (95:5 (v/v) ethanol/H₂O) through ultrasonication for 35 minutes and centrifuging for 40 minutes. After washing the nanoparticles were dried in the vacuum oven for 15 hours at 60°C,

and then were characterized using Fourier transform infrared spectroscopy (Figure 2). Spectra were obtained by using KBr pellets of PBPA-BT, PBPA, and BT.

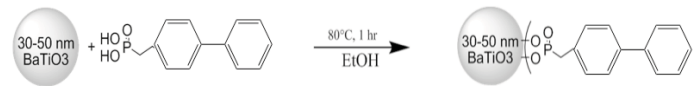


Figure 1. Surface modification reaction of BT with a phosphonic acid.

A process for fabrication of films with a thickness of 2-3 μm was developed. Different ratios of SU-8 and γ -butyrolactone (GBL) were prepared and tested for film formation by spin coating. Solutions were stirred for 12 hours prior to coating and then spin coated at 2300 RPM for 40 seconds. Films were prepared on aluminum-coated glass substrates that had been cleaned using an oxygen plasma. Films were baked on a hot plate at 75°C for 10 minutes, and then at 95°C for 10 minutes. Film thicknesses were measured using a Dektak profilometer. A ratio of 1:1.5 was found to be optimal for film formation. Figure 3 shows the average thickness of each film ratio.

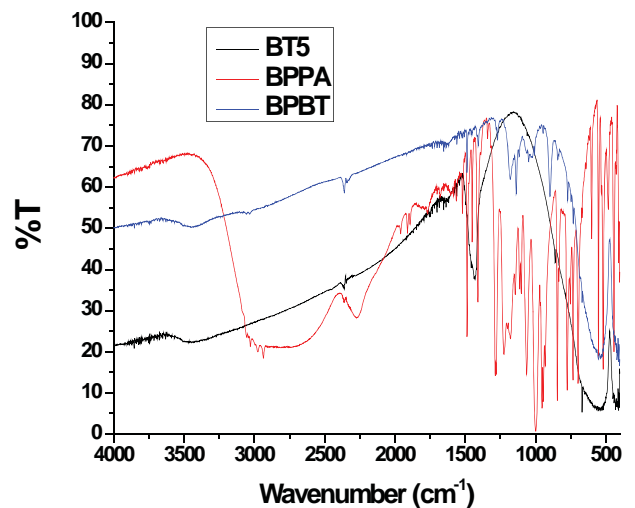


Figure 2. FT-IR spectroscopy of BT, PBPA, and PBPA-BT. Spectra show that surface modification of BT was successful.

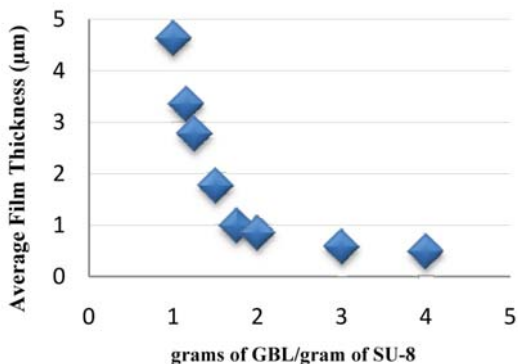


Figure 3. Graph displaying thickness measurements of SU-8 films.

UV-Vis spectroscopy was performed to check the absorbance of the different film components at 365 nm (Figure 4). This was important because the photopatterning experiment used illumination at 365 nm. Spectra of 1:1.5 SU-8:GBL and solutions of BT, PBPA, PBPA-BT, and PBPA-BT with SU-8, all in GBL, were measured. The UV-Vis showed that PBPA-BT absorbed at 365 nm, but SU-8 did not. This indicated that the nanocomposite would not be too strongly absorbing for photopatterning. A cationic initiator, specifically a diaryl iodonium salt, DAI, was chosen for photopolymerization of the epoxide groups of SU-8. However, DAI does not absorb at 365 nm so an ITX sensitizer was chosen to be used in conjunction with DAI.

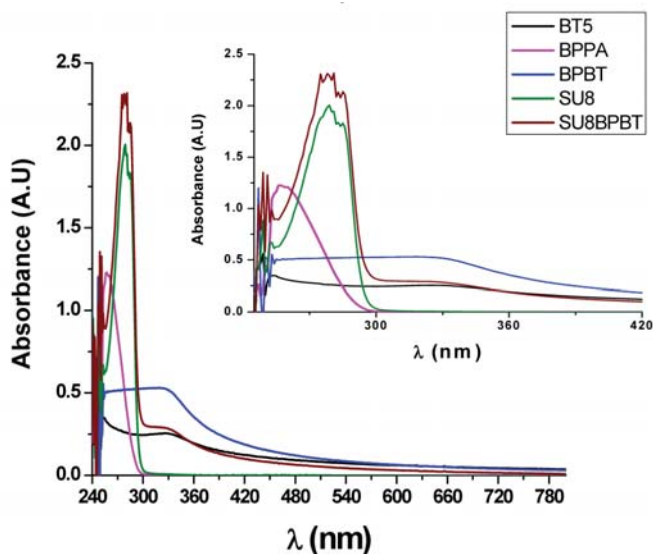


Figure 4. This is the UV vis spectra received for each of the solutions of BT, PBPA, SU-8, PBPA-BT, and SU-8/PBPA-BT all in GBL.

The percent volume loadings used for photopatterning of nanocomposites and capacitor testing were 5%, 10%, and 15% v/v (% PBPA-BT/total volume). The overall process protocol for nanocomposite film formation and photopatterning is shown in Figure 5. The PBPA-BT and GBL for each volume loading was

added to a polypropylene bottle and ball-milled for 48 hours. Then, SU-8 was added to the bottles and the bottles were placed back on the ball mill for four hours. Afterwards, one film of each volume loading was made to check the thickness. Following thickness measurements, solution concentrations were adjusted slightly and ball milled for three days to obtain films 2 - 3 µm thick. After three days the initiator and sensitizer were added, in a dark room, to the solutions. After the initiator and sensitizer were added to the 5% v/v mixture, the bottle was placed back on the ball mill for three hours. During that time, ten Al/glass substrates were cleaned by cold plasma etching. After three hours the mixture was spin coated onto the substrates, and the films were baked as described above. After the pre-exposure bake each film was exposed individually to masked UV radiation. A stop watch was used to time the film exposures. After UV exposure, the films were baked at 95°C and were removed from the hot plate to cool before developing. For developing, the films were immersed in GBL followed by isopropanol, and were rinsed with acetone before being left to dry. The same experimental method was followed for both the 10% v/v and the 15% v/v nanocomposite films.

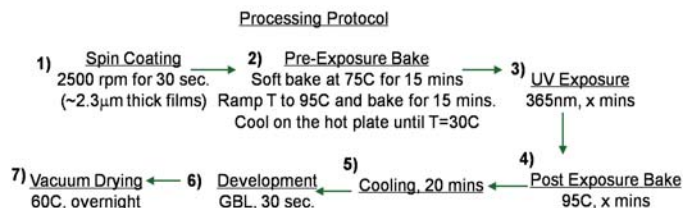


Figure 5. Flow chart of Photopatterning process.

Two samples of nanocomposite on Al/glass from each volume loading (5, 10 and 15%) were used for aluminum (top electrode) deposition, along with one film with a neat SU-8 film. The top electrodes for the devices were deposited via filament evaporation with a shadow mask, in a clean room. This enabled the deposition of circular electrodes, thereby resulting in several devices on a single substrate. One row of large devices was then sliced out with a razor, exposing the bottom electrode. The devices were then characterized for thickness using a Dektak profilometer, and the capacitance and frequency response was measured using a LCR meter with a probe station that was placed inside a glove box. This way, the effects of moisture and oxygen on the capacitance, if any, can be minimized.

Results and Discussion

The results of the photopatterning process showed that we were able to impress a light induced pattern into the nanocomposite. Figure 6 displays the two best examples of photopatterned films for each volume loading tested. Through our studies, it was found that the post exposure bake time needed to be at least 15 minutes, followed by a cooling period of no less than 20 minutes. Also, a UV exposure time of ~1 minute was sufficient to cause a visible change in the film. Exposure times greater than 5 minutes, however, detracted from the quality of the film. A development time of ~15 seconds yielded the best photopattern.

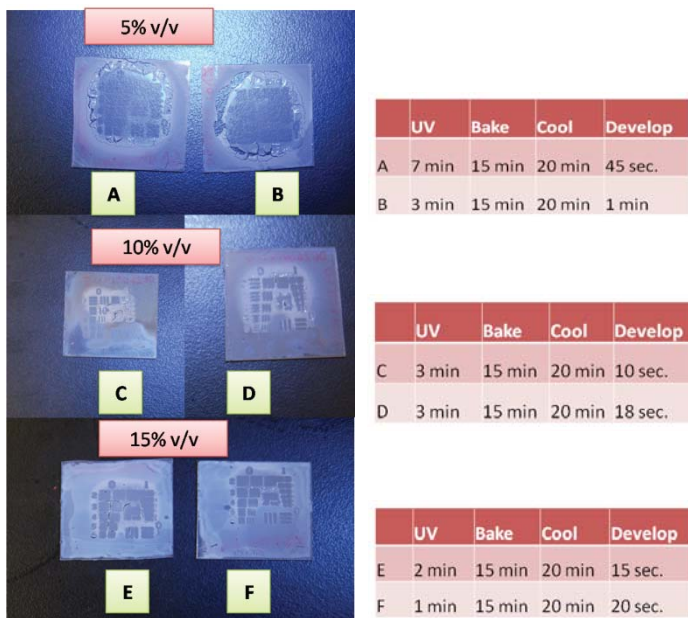


Figure 6. Best two photopatterned films per volume loading. The amount of time each film spent in the critical steps of the photopatterning procedure is also noted.

Upon magnified viewing and probing the surfaces of the film, we observed that the development was incomplete, in that the unexposed areas were not fully removed. If development times were too long, the exposed area of the film peeled away from the substrate. Very interestingly, it was observed that the exposed areas of the films exhibited an increased optical transmission relative to the unexposed areas, as can be seen in Figure 6. This is likely due to a better matching of the refractive index of the crosslinked SU-8 and the BT nanoparticles following photoexposure. The refractive indices of barium titanate at 600 nm is about 1.54⁵ and that of SU-8 is about 1.59⁶, which suggests that the index of SU-8 was reduced during the processing.

The capacitance and frequency response test yielded some promising results. Figure 7 shows the dielectric constant for each volume loading, including the neat SU-8 capacitor. As the volume loading of BT increased, so did the dielectric constant. This shows that the dielectric constant of SU-8 can be improved with the addition of BT nanoparticles⁴. Wong et al. have reported a dielectric constant at ~18 for 20% v/v of BT in SU-8. While the dielectric constants calculated in this study are not as high, the dissipation factor measured is less. Wong et al. reported a dissipation factor of no less than .04 for any volume loading⁴. In this study the highest dissipation factor (Figure 7, bottom) was found to be no more than .03.

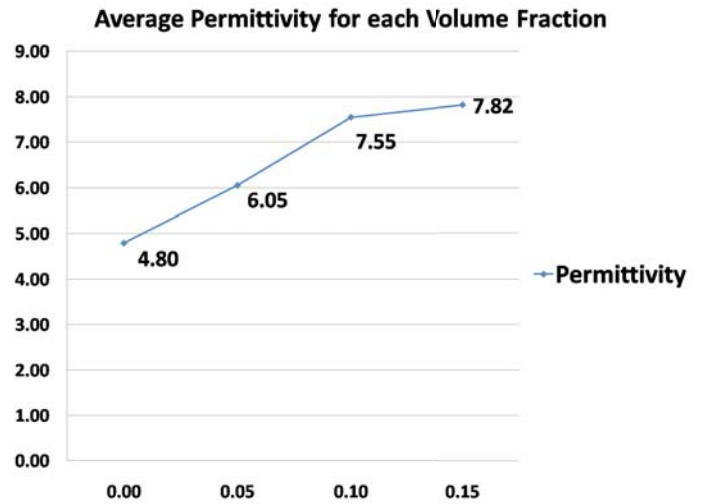


Figure 7. Dielectric constant of films as a function of particle volume fraction for BT:SU-8 nanocomposites.

Conclusion

The surface modification of BT and PBPA was successful, and the composites of SU-8 and PBPA exhibited good processability. A procedure for photopatterning the nanocomposite was developed and a light induced increase in transmission was observed in the photopatterned nanocomposites. Optimization of the photopatterning and development processes will continue to be developed in future work. Moreover, capacitors with good dielectric properties were fabricated and tested. As the volume loading of PBPA increased, so did the dielectric constant. In future work breakdown voltage will be measured, and different volume loadings will be processed.

References

1. P. Kim, S. C. Jones, P. J. Hotchkiss, J. N. Haddock, B. Kip-pelen, S. R. Marder, and J. W. Perry, *Adv. Mat.*, 19, 1001-1005 (2007).
2. Windlass, Hitesh P.; Raj, Markondeya; Barlarman, Devarajan; Bhattacharya, Swapan K.; Tummala, Rao R.; *IEEE*. 2003. Vol. 26, No.1 1521-3323.
3. Xu, Tianweu; Moon, Kyoung-Sik; Pramanik, Ranabes; Bhat-tacharya, Swapan; Wong, C. P.; *IEEE*. 2003. Vol. 26, No. 1. 1521-3323.
4. Xu, Jianwen; Wong C.P.; *Journal of Applied Polymer Science*. 2007. Vol. 103, 1523-1528.
5. Lee M.-K.; Liao, Hsin-Chih; Tung, Kuan-Wen; Shih, Chung-Min; Shih, Tsung-Hsiang; *J. Phys. D: Appl. Phys.* 2002. Vol. 35, 61-64.
6. Borreman, A.; Musa, S.; Kok, A. A. M.; Diemeer, M. B. J.; Driessen, A.; *Proceedings Symposium IEEE/LEOS*. 2002. Ben-elux Chapter Amsterdam.

Acknowledgements

This research was made possible by the help and guidance of Ajit Bhaskar as well as Joseph Perry and the Perry Research Group. Funds for this research were provided by the Office of Naval Research, the Center on Materials and Devices for Information Technology Research (CMDITR), NSF Science and Technology Center No. DMR 0120967.



AUDREY L. SLUTSKY plans on attending Georgia Tech in the fall to finish her bachelor's degree in chemical engineering. Afterwards she plans on attending graduate school to get her master's degree before she goes into the industry.

Transmission Sensor of an Advanced Intravital Microscope

COURTNEY SMITH, Norfolk State University

Dr. Jennifer Barton, Dr. Urs Utzinger, University of Arizona

Introduction

Ovarian cancer arises within one or both of the ovaries. Most commonly, it occurs on the surface of the organ, in which case it is known as ovarian epithelial carcinoma. Alternatively, the cancer can come from an egg cell in which case it is known as a malignant germ cell tumor. In 2008, there were 21,650 new cases of ovarian cancer and 15,520 deaths were caused by it.¹ The best way to prevent these deaths is to be able to detect the cancer at an early, curable stage. Also, an understanding of what causes the disease could aid in prevention and control.

The Advanced Intravital Microscope (AIM) will enable researchers to study normal and cancerous ovaries *ex vivo*, or after surgical removal from the body, and potentially could be adapted to be a new minimally invasive investigative device. The AIM has the potential to be used for intravital imaging, nonlinear fluorescence excitation, scattered light imaging and fluorescence lifetime imaging. However before we can use this tool to help detect and determine the cause of ovarian cancer, we must develop this microscope.

The objective of developing this microscope is to specify, design, build and test appropriate detectors. Although some highly sensitive detectors are commercially available the AIM lacks the ability to assess transmitted light for coherent transmission imaging. This imaging approach is particularly useful when imaging thin samples a few mm thick because it provides images similar to phase contrast imaging. In order to equip the AIM with a laser transmission sensor, a detector will need to be specified, an analog circuit will need to be designed and a detector housing will need to be manufactured. The photodetector must meet the sensitivity, rise time, dark current and size specifications necessary for eventual use in the AIM. The detector and circuit will be placed in a housing, also containing a dichroic mirror, that will reflect the fluorescence from the sample and transmit the laser light onto the detector. The housing will be inserted into the transmission.

Research Methods

The detector to be selected must fit several specifications in order to handle the amount of power being output by the light source. It was necessary to use a photodetector material that had a strong spectral response in the wavelengths emitted by the Titanium Sapphire laser of 700 to 1100nm. The other fundamental aspects needed by the detector include sensitivity, rise time, dark current, and size. Another important aspect to selecting the detector is cost.

The sensitivity (or the magnitude of response) reflects the quantity of detector current is produced based on the incident light applied

to the detector. The sensitivity desired for this project is .5 A/W. The dark current is any current detected when no light is applied to the detector. When the dark current is high it may equate to noise in the system. A response needs to be generated quickly by the detector and is measured by the rise time which is measured in seconds. Since signals are measured up to 10 MHz a rise time in the order of 100ns is desired. The detector selected will be placed in a housing that will be attached to the microscope so space is limited and the detector must have a reasonably sized sensor area so that the scanned area images onto the detector.

Selecting a Detector

Silicon photodiodes work between 190-1100 nm. Silicon is an established, inexpensive technology so was considered most appropriate for this application. This choice narrowed the type of detector to three; the Silicon Photodiode, Silicon PIN photodiode and the Avalanche Photodiode. After comparing performance and prices the PIN photodiode was the best option. A PIN photodiode has best signal to noise performance for high levels of light and its speed can be improved when using a reverse bias. The reverse bias increases the depletion region, causing the sensors internal capacitance to decrease and therefore its bandwidth to increase. The Hamamatsu Si PIN photodiode S6775 was chosen for this project as it fit all the requirements and was reasonably priced.²

An amplifier is also a necessary component to work with the detector. An operational amplifier (op amp) was selected for the project that operated with a supply voltage of $\pm 15V$ and a 50 MHz gain bandwidth product (at 1MHz operation) and $9nV/\sqrt{Hz}$ input noise voltage at 10 kHz.

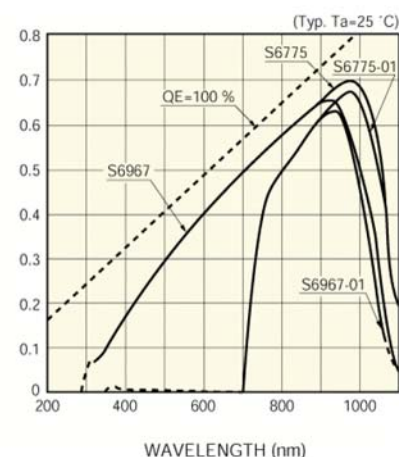


Figure 1. This diagram verifies that the S67752 is sensitive in the wavelength range of 700 and 1100nm.

Conclusion

With the addition of this photodiode into the AIM system, the power emitted by the laser will be known and controlled. With the completion of this project this will be another step closer to producing a state of the art research device for intravital imaging. The Advanced Intravital Microscope is designed to be customized for imaging of other types of complex samples as well.

References

1. "Ovarian cancer," National Cancer Institute (2008).
2. "Si PIN Photodiode S6775" Hamamatsu Photonics (2008)

Acknowledgments

I would like to thank Dr. Arlene Maclin at NSU for suggesting I take this opportunity. I would also like to thank Dr. Jennifer Barton and Dr. Urs Utzinger for exposing me to the world of Biophotonics. Funds for this research were provided by the Center on Materials and Devices for Information Technology Research (CMDITR), and the NSF Science and Technology Center No. DMR 0120967 and Norfolk State University.



COURTNEY SMITH will complete her undergraduate degree in Optical Engineering in May of 2010. She hopes to continue her education by obtaining an MD/PhD in Biomedical Engineering.

Light Polarization Changes Passing Crystals of Point Group 42

STEVEN STEININGER, Highline Community College
Werner Kaminsky, University of Washington

Introduction

The state of polarization of light passing any matter may change depending on the symmetry of the medium.¹ The known mechanisms introducing those changes include natural and induced linear refraction plus dichroism and reflection, natural and induced optical rotation, as well as the Raman, Cotton Mouton, and natural and induced Faraday Effect, nonlinear optics, and finally aspects of negative refractive indices.² Ferroic media may drastically enhance these interactions.³

It is often observed that the chiroptical properties interfere with the linear ones and special techniques are needed to determine the chiroptical strength of a medium. In the past such techniques have successfully been applied to measure for example the optical rotation of crystals where the symmetry is compatible with the existence of this property. In particular, the optical rotation strength of $\text{NH}_4\text{H}_2\text{PO}_4$ (ADP) is well understood, its linear refractive indices known to 5 digits, the tensors of second harmonic generation (SHG) is known and one should be able to predict the polarization signature of this material for all possible directions of incident light.

It was therefore quite astonishing that for the special case of a sample perfectly cut normal to its fourfold symmetry axis, which coincides with a direction of optical isotropy (optical axis, oa), an up to 80 times larger signal was detected than can be calculated from the known tensorial properties. The method to detect chiroptical responses unfolded from linear birefringence is called the 'Tilter Method'. Here, linear polarized light passing a sample is probed with a second polarizer. The incident polarization, analyzer polarization and sample orientation are modulated to derive all relevant optical properties simultaneously. With $\delta = 2\pi\Delta nL/\lambda$, phase factor, Δn birefringence (anisotropy of refraction), L optical path length, λ wavelength, an additional signal was characterized following the empirical description

$$\varphi = A \frac{\delta}{\pi^2 - \delta^2} \sin^2\left(\frac{\delta - \pi}{2}\right),$$

eq. 1

where φ denotes a rotation of the incident polarization and A is constant amplitude.

Procedure

With an ADP sample cut normal to the optic axis, the value of δ increases with the angle between the laser beam and the optic axis. As a result, the $\cos(\delta)$ signal will start to oscillate with δ . The chiroptical signal, derived from $-(a_1 + a_2)/4$, is supposed to show a $\varphi(\alpha)\sin(\delta)/\delta$ dependency. The parasitic contribution $\sin\delta(q-p)/4$, although not negligible, is still small. Taking into account the tensorial character of the optical rotation, the corresponding rotation angle $\varphi_0(\alpha)$ increases with tilt angle α . The expected signal for ADP, when cut on the oa, then follows in a good approximation for tilt angles below 20°:

$$\varphi = c' \sin(c'' \alpha^2), \quad c' = 0.05^\circ,$$

$$c'' = \text{constant value}$$

eq. 2

This expression, however, shall serve only to estimate the signal strength due to OA. The analysis of the raw intensity readings is done with an exact treatment of birefringence and the tensorial character of OR in ADP.

To complicate matters, the signal strength of this contribution varies strongly when probing different sample areas or samples. Several tests were performed to elucidate the origin of the confusing reading.

Results

The signal was found to depend on the sample preparation, but could not be modeled by inserting an absorption filter after the sample intended to block any second harmonics of the incident laser light. Covering the surfaces with cover slides and oil as immersion fluid was of no significant effect. Most strikingly, when the sample was rotated azimuthally so that the incident linear polarization would point into different directions in the a-b plane perpendicular to the optic axis, the parameter A followed that of optical rotation, i.e. vanished for polarizations along $\langle 110 \rangle$ and was largest along $[100]$ and opposite in sign along $[010]$.

The irregular dependency of amplitude A of the additional signal on sample preparation was studied in detail taking full tilt scan topographies of the samples. A single tilt scan produces the 3-dimensional orientation of the sample (offsets α and β_0) for given birefringence the sample thickness L , the optical rotatory power

$\rho_{22} = -\rho_{11}$ in ADP, the amplitude of the additional signal A , and

concomitant with offset angle μ , the offset between polarizer and analyzer. Figure 1 shows the color coded distribution of amplitude A across one of our samples.

Most importantly, the signal correlated to a small anomalous birefringence up to $\delta = 0.6$ causing a small split of the optic axis into two axes. The direction of the split was along $\langle 110 \rangle$. The sample thickness was not found to be important, however, the samples needed to be oriented well on the optic axis.

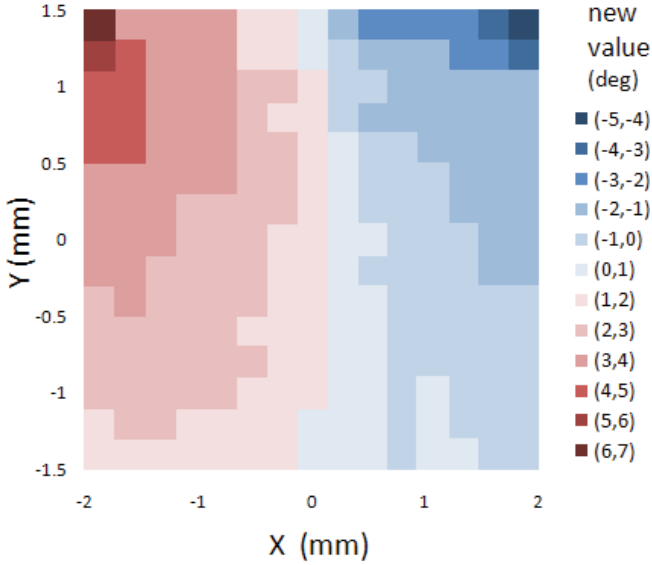


Figure 1. Variation of contribution A , eq. 1, across a rotationally twinned sample (twin boundary in the sample middle. Thickness 1.32 mm, probing wavelength 670nm.

We believe that the effective light modes are caused by multiple circular differential reflections, the effect of which is simulated by a creator/annihilator matrix.

ADP is optically active for any angle of incidence other than the optic axis. A linearly polarized wave can be thought of being composed of two circular polarized waves which will be reflected to different amounts. This causes a net circular polarization inside the crystal in addition to the transmitted linear polarized wave. The strength of the CDR effect was estimated from the theoretical treatment by Meteva and Lalov. The CDR is found to be in proportion of $\gamma_{11}\epsilon_3/(\epsilon_0^2-\epsilon_3^2)$ leading to a few percent in ADP.

Following the projection of access circular polarization along the optic axis, the cpw remains unaffected in the absence of any birefringence along the oa. The sample exit face causes CDR as well, but producing an access circular polarization of opposite hand. The circular polarized wave from both surface reflections cancel out. The resulting waves and states of polarization (neglecting secondary reflections and linear polarized reflections) are depicted in Figure 2.

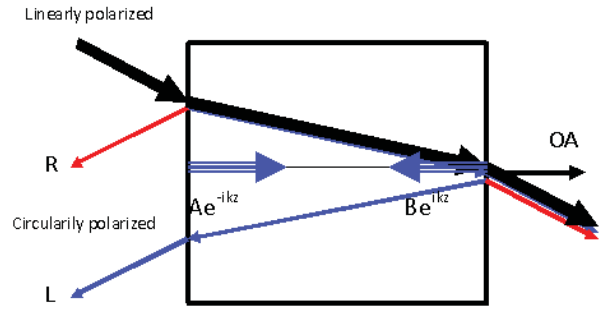


Figure 2. Circular differential reflection on a tilted ADP plate. R(L) denote right(left) circular polarized light. OA: direction of the optic axis. Fat arrows: incident linear polarized light. Striped arrows: net circular polarized light traveling along the optic axis. The reflections of linear polarized light are not shown for clarity.

A small anomalous birefringence induces a phase shift δ_0 between the components of the circularly polarized wave (cpw) inside the sample following a $\cos(\delta_0)$ dependency. This results in a reduction in the amplitude of the cpw and creates a second circularly polarized wave of opposite hand and a $\pi/2$ phase shift.

These waves interfere inside, whereas the waves outside the sample cancel out any circular polarization. The problem is symmetric to the intersection in the middle of the sample. The amplitudes and polarizations of the cpw with opposite propagation directions need to match for interference. The anomalous birefringence seems to be necessary in this context (a thorough treatment of this phenomenon has not been established). At the surfaces (a) and (-a) we have no circular polarizations as pointed out above.

at surface - a:

$$A(-a)e^{ika} + B(-a)e^{-ika} = 0$$

at surface +a:

$$B(a)e^{ika} + A(a)e^{-ika} = 0$$

The vanishing determinant of this system demands

$$A(a)A(-a) - B(a)B(-a) = 0,$$

And since e^{ika} , e^{-ika} do not vanish we need:

$$A(a) = B(a) = A(-a) = B(-a) = 0$$

The simplest non-trivial solution that satisfies the system of equations and boundary conditions for all values of z is achieved with the 'Ansatz':

$$A(z) = \text{const.}(1-z^2/a^2)$$

eq. 3.

The physical meaning is that the circular polarized waves interfere less when further away from the surfaces, whereas at shorter distances to the surfaces the amplitudes of all interfering waves need to reach smoothly the boundary condition of vanishing amplitude.

The parabolically changing amplitude of a circular polarized wave traveling from sample surface $-a$ to the one at a is the result of differential circular reflection on both surfaces of the sample which create access circular polarized Huygens elementary waves from which the mode along the optic axis forms. We will abbreviate this by SIRCPM, a surface induced reflective circular polarized mode.

The projection of SIRCPM on the linearly polarized wave running through the crystal at angle β towards the sample normal vector becomes less favorable at steeper incident angles; however, the projection to the optically active directions will increase to compensate for it, qualitatively explaining why amplitude A in eq. 3 is constant over the range of tilt angles in the experiment.

Conclusions

We showed how circular differential reflection can cause an additional signal to measurements of optical rotation employing HAUP when a sample is probed with incident light close to an optic axis. The additional signal requires anomalous birefringence of the sample, without which nothing is observed. The effect is described by a circular polarization in projection to the optic axis with decreasing amplitude in proportion to anomalous birefringence along the optic axis.

Further work is under way to test our model on crystals of different symmetry and compositions and complete and refine the theoretical treatment.

References

1. Haussühl S 1983 Kristallphysik Physik Verlag Verlag Chemie, Weinheim
2. See as an example: J. B. Pendry, Phys. Rev. Lett. 85, 3966 - 3969 (2000)
3. See for example
 - a) W. Kaminsky: Reinvestigation of electrogyration in triglycine sulphate. Phase Transitions 52 (1994) 235-259.
 - b) W. Kaminsky: Topographies of linear and chiral optical properties in FeBO₃, using a novel polarimeter, the 'tilter'. Ferroelectrics 204 (1997) 233-246

Acknowledgements

This work was made possible by the NSF sponsored Science and Technology Center on Materials and Devices for Information Technology Research, No. DMR-0120967.



STEVEN STEINGER attends Highline Community College and plans to transfer to the University of Washington in Winter 2010, where he will work toward a Bachelor of Science in Physics. He hopes to study nuclear physics and relativity in grad school.

New Phthalimide-Based Polymer Semiconductors for Efficient Photovoltaic Cells

AMANDA Y. SUN, Duke University

Pei-Tzu Wu, Samson A. Jenekhe, University of Washington

Introduction

Previous work in the field of organic polymer semiconductors has resulted in relatively poor efficiencies in photovoltaic cells. A recent study, however, revealed a new polymer incorporating an electron-rich platinum (Pt) component combined with conjugated thiophene donor and benzothiadiazole acceptor units in the backbone of the polymer that greatly improves the light-absorbing properties¹. This polymer has a low band gap of 1.85 eV and in solar cells showed a power conversion efficiency (PCE) of 4-5%, which is comparable to poly(3-hexylthiophene) used in state-of-the-art fullerene-based solar cells. This indicates that this class of polymers holds great promise for applications in photovoltaic cells and that higher efficiency can be achieved through further chemical modifications.

This project aims to address the problems of poor charge transport in this class of polymers². In addition, this project seeks to improve the light harvesting capabilities of this class of polymer semiconductors. If successful in improving the charge transport and light-harvesting properties of this class of polymers, this research could advance the efficiency of polymer solar cells.

These polymer semiconductors are significant for their ease in processing, flexibility, and cost-efficiency, and hence they possess great potential for widespread use in photovoltaic cells. This would subsequently lead to the spread of photovoltaic cells as an inexpensive, ubiquitous energy source.

The aim of this research project is to develop new polymer semiconductors based on the new electron-accepting building block, phthalic imide, that improve light harvesting of the solar spectrum and enhance charge transport properties for applications in photovoltaic cells.

Results and Discussion

Synthesis.

The synthesis of the target polymer, Ph-BTPt, follows Scheme 1 and includes seven steps starting from phthalic anhydride. These reactions are (a) bromination, (b) N-alkylation, (c) Stille coupling with 2-tributylstannylthiophene, (d) bromination, (e) terminal ethynylation, (f) deprotection, and (g) polymerization. The polymerization step was accomplished through a Sonogashira-type coupling reaction to obtain the target polymer shown in Figure 1.

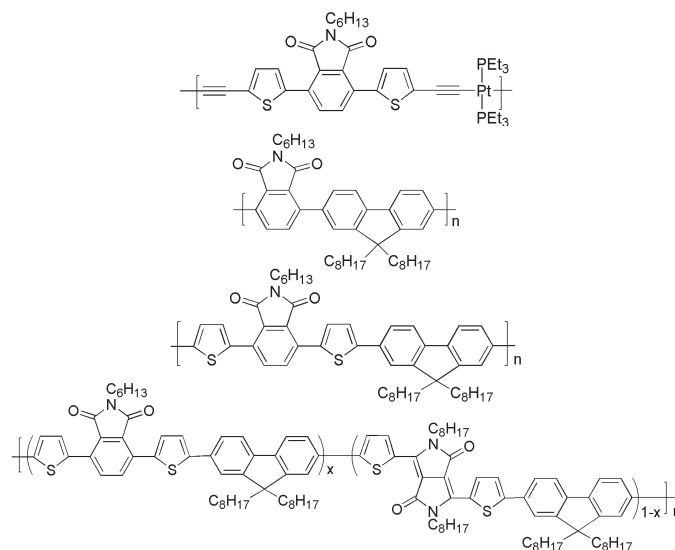


Figure 1. Target polymers (from top to bottom): Ph-BTPt, PPhF, P2TPhF, PPhDPPF

4,7-dibromo-isobenzofuran-1,3-dione (1).

The bromination of phthalic anhydride was carried out following the previous literature.³ ¹H NMR (CDCl₃, 300 MHz, ppm): δ 7.87 (s, 2H). GC-MS: m/z: 305 (C₈H₂Br₂O₃+).

4,7-dibromo-2-hexyl-isoindole-1,3-dione (2).

1 (7.0 g, 23 mmol), hexylamine (3.9 mL, 30 mmol), and glacial acetic acid (130 mL) were combined and refluxed under argon at 110°C for three hours. After removing the acetic acid from the reacted mixture, N-hexyl-3,6-dibromophthalimide was isolated through column chromatography (silica gel, dichloromethane:hexanes 1:3). White crystals were obtained (8.1 g, 91% yield). ¹H NMR (CDCl₃, 300 MHz, ppm): δ 7.67 (s, 2H), 3.66 (t, 2H), 1.67 (m, 2H), 1.33 (m, 6H), 0.90 (m, 3H). GC-MS: m/z: 388 (C₁₄H₁₅Br₂NO₂+).

2-hexyl-4,7-di-thiophen-2-yl-isoindole-1,3-dione (3).

2 (3.0 g, 7.7 mmol), 2-(tributylstannyl)thiophene (5.4 mL, 17 mmol) and tetrakis(triphenylphosphine) palladium (0) (0.445 g, 0.386 mmol) were combined, degassed, and refluxed at 100°C for 24 hours. The reacted mixture underwent extraction using dichloromethane and, after removing the solvent through rotary evaporation, was further purified through column chromatography (silica gel, ethyl acetate:hexanes 1:20). A yellow powder was obtained after filtration from methanol and hexane (2.68 g, 88% yield). ¹H NMR (CDCl₃, 300 MHz, ppm): δ 7.79 (s, 4H), 7.50 (d,

2H), 7.19 (t, 2H), 3.68 (t, 2H), 1.66 (m, 2H), 1.36 (m, 6H), 0.90 (t, 3H).

2-hexyl-4,7-di-thiophen-2-yl-isoindole-1,3-dione (3).

2 (3.0 g, 7.7 mmol), 2-(tributylstannyl)thiophene (5.4 mL, 17 mmol) and tetrakis(triphenylphosphine) palladium (0) (0.445 g, 0.386 mmol) were combined, degassed, and refluxed at 100°C for 24 hours. The reacted mixture underwent extraction using dichloromethane and, after removing the solvent through rotary evaporation, was further purified through column chromatography (silica gel, ethyl acetate:hexanes 1:20). A yellow powder was obtained after filtration from methanol and hexane (2.68 g, 88% yield). ¹H NMR (CDCl₃, 300 MHz, ppm): δ 7.79 (s, 4H), 7.50 (d, 2H), 7.19 (t, 2H), 3.68 (t, 2H), 1.66 (m, 2H), 1.36 (m, 6H), 0.90 (t, 3H). (tributylstannyl)thiophene (5.4 mL, 17 mmol) and tetrakis(triphenylphosphine) palladium (0) (0.445 g, 0.386 mmol) were combined, degassed, and refluxed at 100°C for 24 hours. The reacted mixture underwent extraction using dichloromethane and, after removing the solvent through rotary evaporation, was further purified through column chromatography (silica gel, ethyl acetate:hexanes 1:20). A yellow powder was obtained after filtration from methanol and hexane (2.68 g, 88% yield). ¹H NMR (CDCl₃, 300 MHz, ppm): δ 7.79 (s, 4H), 7.50 (d, 2H), 7.19 (t, 2H), 3.68 (t, 2H), 1.66 (m, 2H), 1.36 (m, 6H), 0.90 (t, 3H).

4,7-bis-(5-bromo-thiophen-2-yl)-hexyl-isoindole-1,3-dione (4).

3 (2.68 g, 6.78 mmol), dimethylformamide (15 mL), and dichloromethane (50 mL) were mixed and cooled to 0°C for 15 minutes while under protection from light. Next, N-bromosuccinimide (2.53 g, 14.2 mmol) was added slowly to the mixture, and the reaction was allowed to continue at 0°C for two hours and then at room temperature for 18 hours. The mixture was quenched with water to

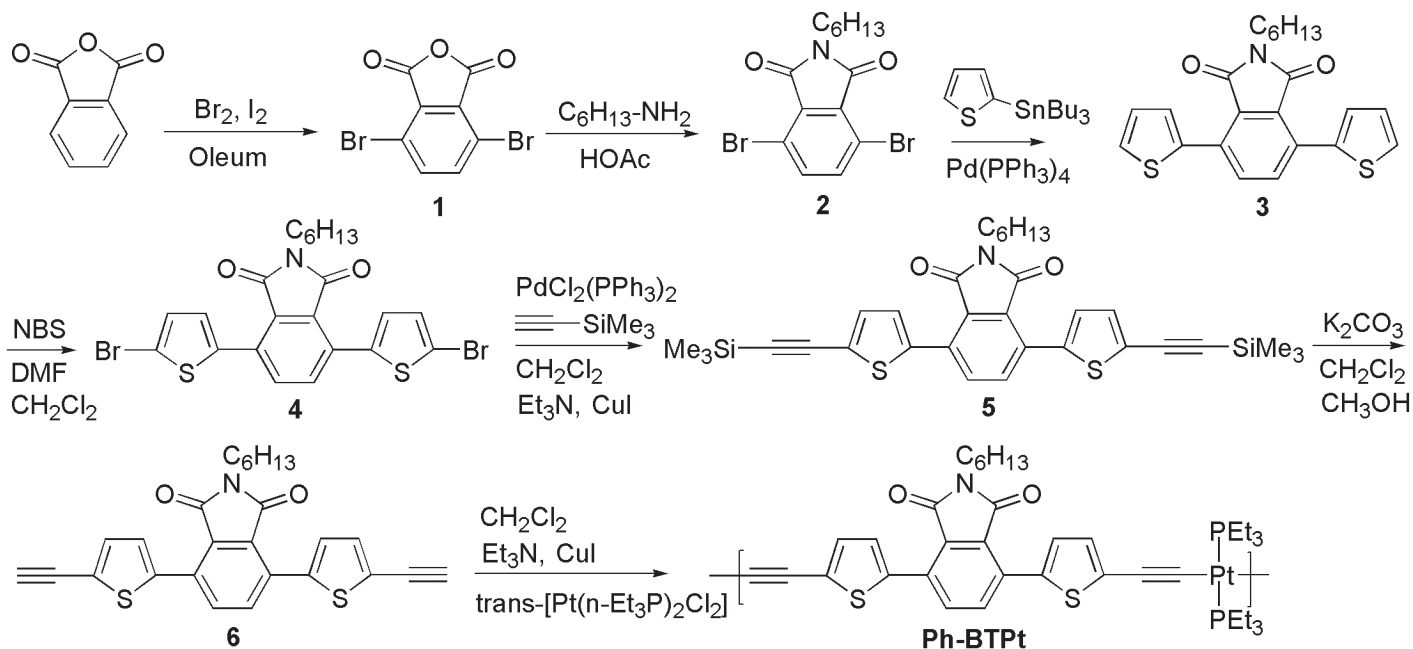
stop the reaction. Then extraction was performed and the product was purified through column chromatography (silica gel, ethyl acetate:hexanes 1:20). Yellow crystals were obtained after filtration from methanol (2.745 g, 73% yield). ¹H NMR (CDCl₃, 300 MHz, ppm): δ 7.72 (s, 2H), 7.53 (d, 2H), 7.15 (d, 2H), 3.68 (t, 2H), 1.69 (m, 2H), 1.35 (m, 6H), 0.89 (t, 3H).

2-hexyl-4,7-bis-(5-trimethylsilyl-ethynyl-thiophen-2-yl)-isoindole-1,3-dione (5).

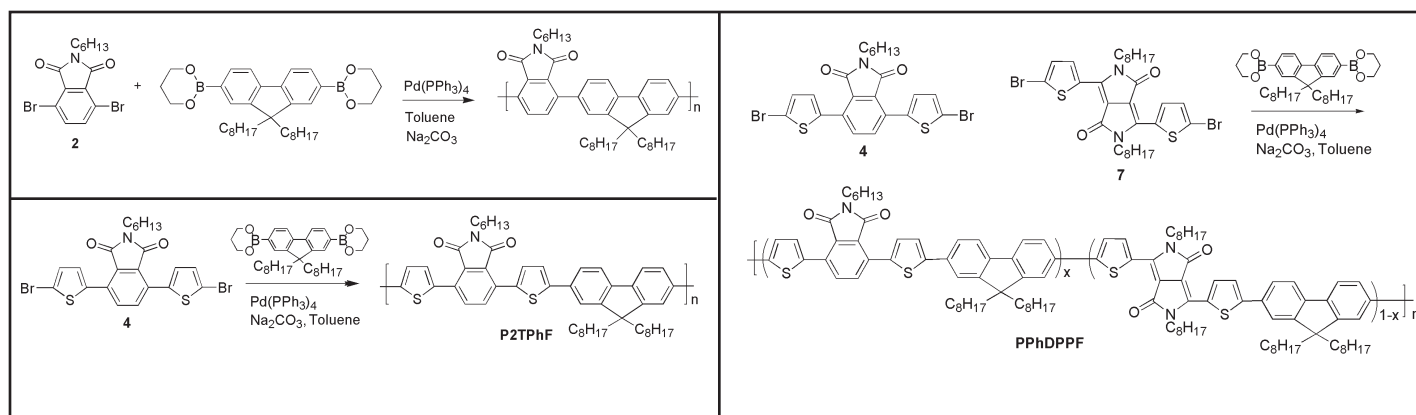
4 (2.7 g, 4.5 mmol), dichloromethane (55 mL), and triethylamine (50 mL) were combined at 0°C. Next, copper iodide (100 mg, 0.53 mmol) and dichloro-bis(triphenylphosphine)palladium (II) (0.234 g, 0.33 mmol) were added and the mixture was degassed and stirred at 0°C for 30 minutes. Trimethylsilylacetylene (2.8 mL, 20 mmol) was then added and the mixture continued to be stirred at 0°C for 30 minutes. After allowing the mixture to return to room temperature for 30 minutes, it was refluxed at 50°C for 24 hours. The mixture was then cooled to room temperature, and the solvent was evaporated through rotary evaporation. The product was dissolved in dichloromethane and ethyl acetate and column chromatography was performed (silica gel, dichloromethane:hexanes 1:4). The crude product was then recrystallized twice from ethanol to provide yellow crystals (1.23 g, 42% yield). ¹H NMR (CDCl₃, 300 MHz, ppm): δ 7.75 (s, 2H), 7.65 (d, 2H), 7.27 (d, 2H), 3.68 (t, 2H), 1.66 (m, 2H), 1.32 (m, 6H), 0.89 (t, 3H), 0.29 (s, 18H).

4,7-bis-(5-ethynyl-thiophen-2-yl)-2-hexyl-isoindole-1,3-dione (6).

5 (1.2 g, 2.0 mmol), anhydrous methanol (12.5 mL), and anhydrous dichloromethane (50 mL) were combined and stirred under argon until dissolved. Then, potassium carbonate (0.62 g, 4.5 mmol) was added, and the reaction was allowed to continue at room



Scheme 1. Reaction scheme for Ph-BTPt



Scheme 2. Reaction schemes for PPhF, P2TPhF, and PPhDPPF

temperature while shielded from light for 12 hours. The solvent was removed and the target molecule was isolated via column chromatography (silica gel, dichloromethane: hexanes 1:9) and filtration from methanol. A yellow powder was obtained as the final monomer (614 mg, 68% yield). $^1\text{H NMR}$ (CDCl_3 , 300 MHz, ppm): δ 7.76 (s, 2H), 7.65 (d, 2H), 7.33 (d, 2H), 3.68 (t, 2H), 3.47 (s, 2H), 1.68 (m, 2H), 1.32 (m, 6H), 0.89 (t, 3H).

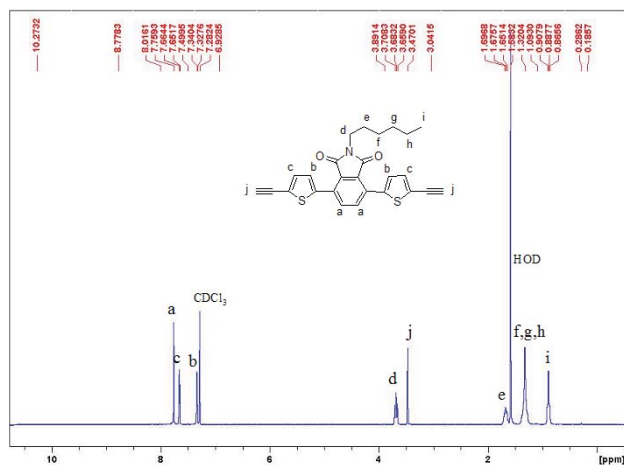


Figure 2. $^1\text{H NMR}$ graph of final monomer 6.

Ph-BTPt.

Polymerization was carried out by mixing **6** (355 mg, 0.80 mmol), trans-dichlorobis-(triethylphosphine)-platinum (II) (402 mg, 0.80 mmol), anhydrous dichloromethane (120 mL), and anhydrous triethylamine (120 mL), stirring the mixture under argon, and degassing for five minutes. Copper iodide (45 mg, 0.24 mmol) was then added, upon which the mixture turned deep red in color. The reaction continued under shielding from light and at room temperature for 18 hours. The solution was then heated at 50 °C for an hour. The solvent was removed through rotary evaporation, and the mixture was filtered through molecular sieves. After collecting the filtrate, the solvent was partially evaporated and the product was precipitated using methanol and filtered to collect the solid. Then, Soxhlet extraction was performed for three days using acetone to obtain a bright orange solid (577 mg, 83%). $^1\text{H NMR}$ (CDCl_3 , 300 MHz, ppm): δ 7.69, 6.92, 3.68, 2.19, 1.68, 1.29, 0.89.

PPhF.

Polymerization was performed by combining **2** (600 mg, 1.54 mmol), 9,9-dioctylfluorene-2,7-diboronic acid bis(1,3-propanediol) ester (861 mg, 1.54 mmol), and anhydrous toluene (45 mL) and stirring under argon. The mixture was degassed, and a 2M sodium carbonate solution (20mL) was prepared and added along with seven drops of Aliquat. Further degassing was employed for five minutes, after which $\text{Pd}(\text{PPh}_3)_4$ was added. In addition, 8 mL of tetrahydrofuran (THF) was added to improve mixing. The mixture was refluxed at 100°C for 48 hours. The aqueous layer of the reaction mixture was removed using a separatory funnel. The solvent was then evaporated until there remained a small amount (about one-third of the original amount), after which the product was precipitated out using methanol and filtered. Soxhlet extraction with acetone was performed to isolate the polymer, a dull orange powder (802 mg, 82%). $^1\text{H NMR}$ (CDCl_3 , 300 MHz, ppm): δ 7.89, 7.80, 7.64, 3.66, 2.09, 1.69, 1.33, 1.19, 0.84.

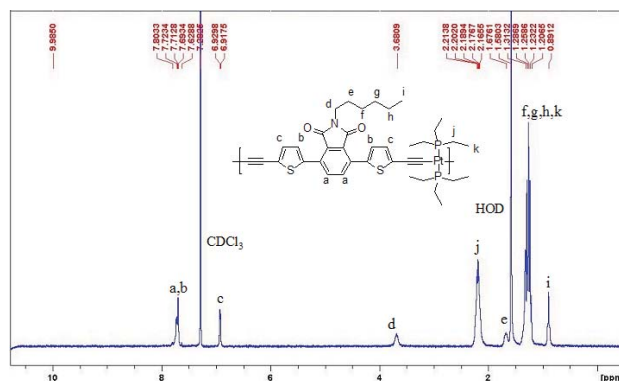


Figure 3. $^1\text{H NMR}$ graph of final polymer Ph-BTPt

P2TPhF.

Procedure for PPhF was repeated in polymerization except using **4** (500 mg, 0.90 mmol), 505 mg (0.90 mmol) of 9,9-dioctylfluorene-2,7-diboronic acid bis(1,3-propanediol) ester, 35mL of toluene, 15mL of 2M sodium carbonate and about 52mg of $\text{Pd}(\text{PPh}_3)_4$. This resulted in a dull green solid (621mg, 88%). $^1\text{H NMR}$ (CDCl_3 , 300 MHz, ppm): δ 7.90, 7.66, 7.49, 3.74, 2.08, 1.72, 1.35, 1.12, 0.80.

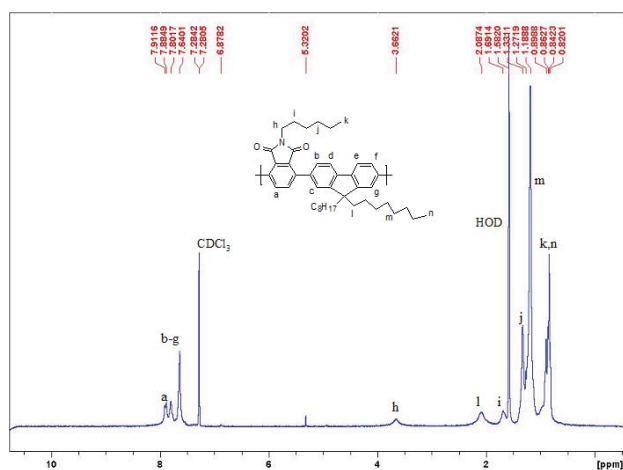


Figure 4. ^1H NMR graph of final polymer PPhF

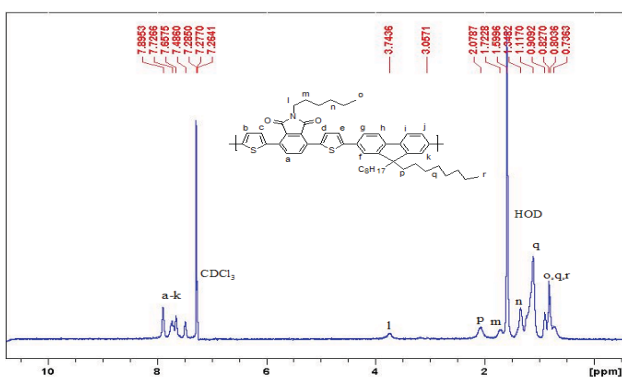


Figure 5. ^1H NMR graph of final polymer P2TPhF

PPhDPPF.

Procedure for P2TPhF was repeated in forming this random copolymer, except using **4** (203mg, 0.366mmol), **7**, a previously made monomer (250 mg, 0.366mmol), and 409mg (0.732mmol) of **8**. A dark green solid was obtained (477mg, 77%). Analysis of the NMR spectrum revealed that $x = 0.63$. ^1H NMR (CDCl_3 , 300 MHz, ppm): δ 9.03, 7.89, 7.66, 7.49, 4.20, 3.75, 2.06, 1.87, 1.70, 1.32, 1.12, 0.91, 0.82.

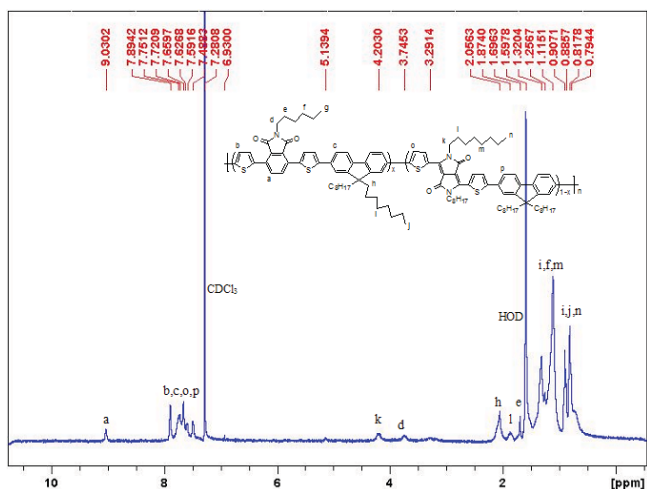


Figure 6. ^1H NMR graph of final polymer PPhDPPF

The reaction schemes for polymers PPhF, P2TPhF, and PPhDPPF are found in Scheme 2.

Characterization.

^1H NMR and GC-Mass were carried out to confirm the synthesized monomer and intermediates. Furthermore, Gel Permeation Chromatography (GPC) was performed on the polymers to obtain the molecular weight, polydispersity index (PDI) and degree of polymerization data (n).

	M_n	PDI	M_w	n
Ph-BTPt	13,900	2.78	38,600	15.9
PPhF	32,000	7.13	228,200	50.6
P2TPhF	19,400	1.08	21,000	24.8
PPhDPPF	5,000	1.06	5,300	6.0

Table 1. Gel Permeation Chromatography results: number average molecular weight (M_n), polydispersity index (PDI), weight average molecular weight (M_w), and degree of polymerization (n) for the four polymers

As shown by the data, PPhF has a high degree of polymerization but also a high PDI, indicating a broad distribution in polymer chain length. Both P2TPhF and PPhDPPF had small PDI values; however, PPhDPPF has a low molecular weight, which may be due to its low solubility in chlorobenzene and inability to pass through the filter during filtration prior to performing GPC analysis.

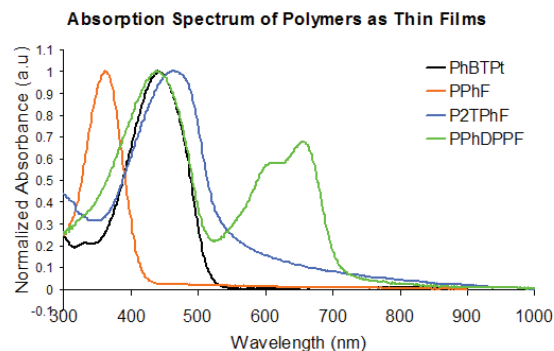
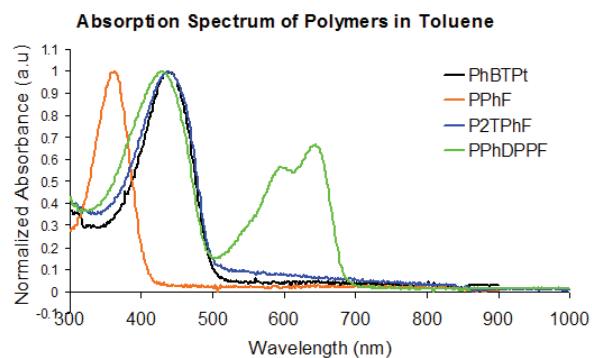


Figure 7. Absorption spectra of the four final polymers in solution (toluene) and as thin films

Optical properties.

Absorption spectra of the polymers were obtained on UV-Visible spectroscopy. Based on the absorption spectra of thin films of

polymers, the onset, optical band gap, and peak maximum were obtained. This data shows a much red-shifted absorption spectrum for the PPhDPPF random copolymer, with a maximum peak at 656 nm and a low band gap of 1.75 eV. The other polymers show high band gaps and low maximum peak and onset wavelengths. This indicates that PPhDPPF holds promise in applications such as solar cells, whereas there will likely be constraints on the potential for the three polymers, Ph-BTPt, PPhF, and P2TPhF, to hold applications in photovoltaic cells. In addition, the PPhDPPF spectrum possesses two peaks, with the low-wavelength peak likely corresponding with the absorption of the phthalimide-thiophene group and the more red-shifted low-energy peak corresponding with the DPP-thiophene group in the random copolymer. This suggests that the phthalimide-thiophene pair does not show a strong intramolecular charge transfer, and thus the absorption band is primarily in the visible

	Onset (nm)	Optical Band Gap (eV)	Wavelength of Maximum Peak (nm)
Ph-BTPt	520	2.38	442
PPhF	420	2.95	362
P2TPhF	560	2.21	465
PPhDPPF	710	1.75	(1) 439; (2) 656

wavelength region.

Table 2. Onset, optical band gap, and maximum peak wavelength(s) data obtained from absorption data for the four polymers.

Photoluminescence (PL) spectra were recorded on the photoluminescence spectroscopy. The intensity of the photoluminescence spectrum of PPhDPPF was too low to be detected. In the case of PPhF, it showed a maximum peak at about 460 nm, meaning that it is a fluorescent and blue-emitting material. The PL results suggest that PPhF may have significant implications in potential uses in organic light-emitting diodes.

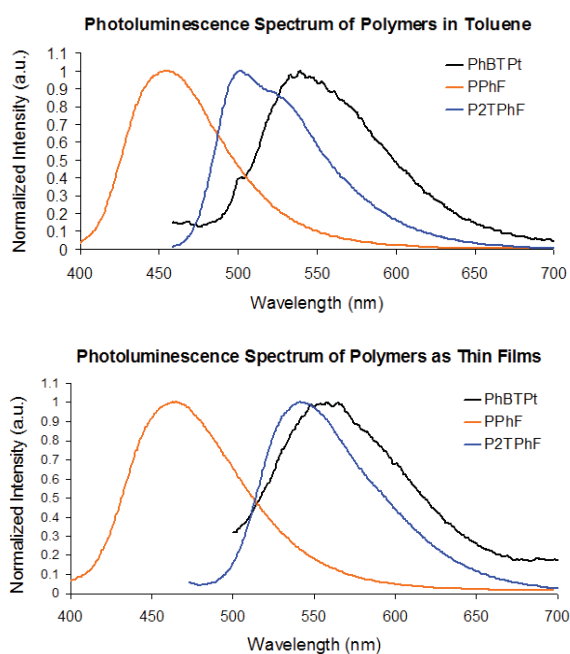


Figure 8. Photoluminescence spectra of the four polymers in solution (toluene) and as thin films.

Cyclic voltammetry was performed to probe their reduction and oxidation potentials and calculate their electron affinity, ionization potential, and HOMO/LUMO values. 2 wt% solutions of the polymers were prepared using 30 mg of polymer in 1 gram of chloroform. Subsequently, platinum wires were uniformly coated with this solution and used for cyclic voltammetry. The parameters of electronic structures in these four polymers were summarized in Table 4. The electronic structures of P2TPhF and PPhDPPF were not derived from attempted CV analysis.

	Wavelength of Maximum Peak (nm)	
	In Toluene	As Thin Films
Ph-BTPt	539	558
PPhF	454	463
P2TPhF	501	541

Table 3. Maximum peak wavelengths in solution and as thin films for three polymers, Ph-BTPt, PPhF, and P2TPhF. PPhDPPF showed no significant emissions.

	Reduction Potential (V)	Oxidation Potential (V)	Electron Affinity (eV)	Ionization Potential (eV)	LUMO (eV)	HOMO (eV)	Band Gap (eV)
Ph-BTPt	-1.37	0.96	3.03	5.36	-3.03	-5.36	2.33
PPhF	-1.58	1.64	2.82	6.04	-2.82	-6.04	3.22

Table 4. Reduction potential (E_{red}), oxidation potential (E_{ox}), electron affinity (EA), ionization potential (IP), HOMO and LUMO levels, and band gap (E_g) values for the polymers Ph-BTPt and PPhF

Conclusions

Four phthalimide-based conjugated polymers have been synthesized and characterized. Through UV-Visible spectroscopy, the random copolymer PPhDPPF was found to possess a low band gap and high maximum peak wavelength and hence may be promising as the electron donor and light-harvesting medium in solar cells, whereas photoluminescence spectroscopy indicated that PPhF is fluorescent and blue-emitting and may be useful in light emitting diodes. Further work will be required on these polymers to further assess its potential for use in organic photovoltaic cells and other optoelectronic devices. Charge transport of these polymers will need to be investigated by fabrication of thin-film transistors. Furthermore, the three polymers Ph-BTPt, PPhF, and P2TPhF shall be implemented in organic light-emitting diodes, whereas PPhDPPF shall be implemented in photovoltaic cells.

References

1. Wong, Wai-Yeung; Wang, Xing-Zhu; He, Ze; Djuricic, Aleksandra; Yip, Cho-Tung; Cheung, Kai-Yin; Wang, Hai; Mak, Chris; & Chan, Wai-Kin. *Nature Mater* 2007, 6, 521-527.
2. Wu, Pei-Tzu; Bull, Tricia; Kim, Felix; Luscombe, Christine; & Jenekhe, Samson. *Macromolecules* 2008, 42, 671-681.
3. Guo, Xugang; Kim, Felix; Jenekhe, Samson; & Watson, Mark. *J. Am. Chem. Soc.* 2009, 131, 7206-7207

Acknowledgments

Funds for this research were provided by the Center on Materials and Devices for Information Technology Research (CMDITR), NSF Science and Technology Center No. DMR 0120967. In addition, special thanks go to Pei-Tzu Wu and Dr. Samson A. Jenekhe for this research opportunity and their guidance and support.



AMANDA SUN currently attends Duke University and will complete her B.S. degree in Biology in May 2011.

Electric and Optical Properties of Organic-Inorganic Hybrid Sol-Gel Films

AMY VAN NEWKIRK, Grove City College
Hongxi Zhang and Mahmoud Fallahi, University of Arizona

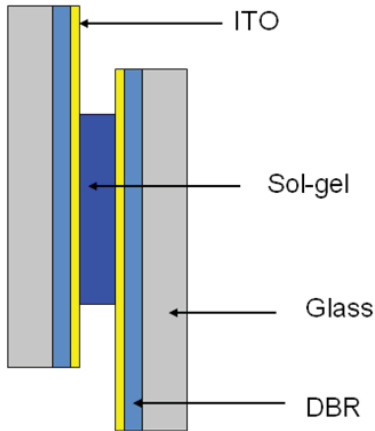


Figure 1. Fabry-Perot interferometer with sol-gel as active medium.

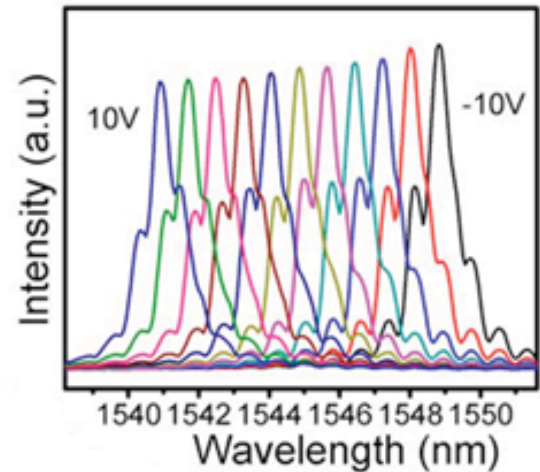


Figure 2. Transmission wavelength shift of a tunable filter with different applied voltages.²

INTRODUCTION

Recently, sol-gels have been introduced as a viable option for use in electro-optic devices. Their stability combined with their electro-optic properties make them a promising media for future devices, including tunable filters, Fabry-Perot spatial light modulators, and waveguide arrays. These devices can then be used to improve communications, sensor systems, and biomedical technologies. Sol-gels have been found to have a strong inverse piezoelectric response, the origin of which is unknown. By applying a voltage across the material, the piezoelectric effect would change the width between the reflecting surfaces of a Fabry-Perot interferometer as demonstrated in Figure 1. This change in width would produce a phase change and would shift the wavelengths that would be able to pass through the reflective surfaces, creating a tunable filter as shown in Figure 2.¹

The hybrid sol-gels combine the benefits of both organic and inorganic materials. The ease of processing, low cost, wide fabrication flexibility, low optical loss, and stability make hybrid sol-gels a promising alternative for future applications.^{1,3}

In this project, the electrical and optical properties of MAPTMS (methacryloxy propyl trimethoxysilane) sol-gel doped with zirconium are investigated.

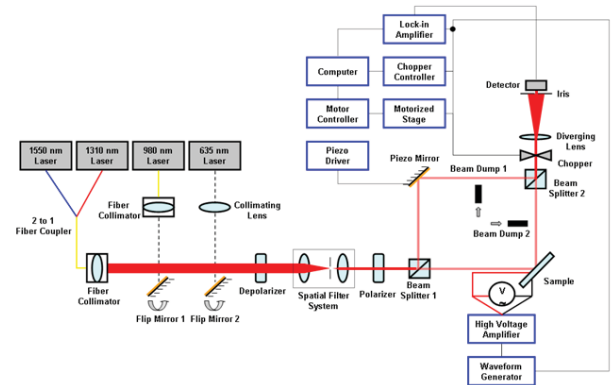


Figure 3. Schematic setup of the interferometer.

Methods

The MAPTMS-Zr sol was processed according to an earlier report.⁴ Sol-gel film samples containing Zr compositions of 0%, 5%, 10%, and 20% were spun onto titanium-coated silicon wafers at speeds of 2000, 3000 and 4500 rpm, respectively, soft baked at 100 °C for 60 min and then hard baked at 180 °C for 120 min. The thickness was measured with an optical profiler. The top gold electrode was sputtered on to the films through a shadow mask.

A section of the sol-gel was then scraped off in order for the thickness to be measured with an optical profiler.

Wires were then attached to the electrodes using silver conductive epoxy. The capacitance of each of the samples was measured using an LCR meter. In order to evaluate the thermal stability of the dielectric property of MAPTMS-Zr sol-gel films, the samples were heated from room temperature to 100 °C on a hot plate.

The samples were then poled to orient the molecules in the films in order for the inverse piezoelectric effect to be significant. They were heated up to 150 °C - 180 °C and a high voltage (~100 V/μm) was applied across the electrodes for 30 minutes. The samples were then cooled to room temperature with the electric field still applied so that the orientation remained.

The piezoelectric coefficients of the sol-gel films were tested using an interferometer as schematically shown in Figure 3. The wavelength of the laser used is 980 nm. A beam splitter separates a reference arm, which reflects off of a piezoelectric mirror, and the sample arm, which reflects off of the gold electrode of the sample to be tested. The sol-gel film changes in thickness as a voltage is applied across it. This causes a path length change for the beam of the laser hitting the gold electrode on the sol-gel film. This change is then measured by the interference pattern of the two beams in the detector and the piezoelectric coefficient of the films can be derived.

Results

The thickness of the various MAPTMS-Zr samples was compared as shown in Figure 4. As the speed of spin coating increased, the thickness of the film decreased. The thickness of the films is also dependent on the zirconium concentration of the samples as shown in the same figure.

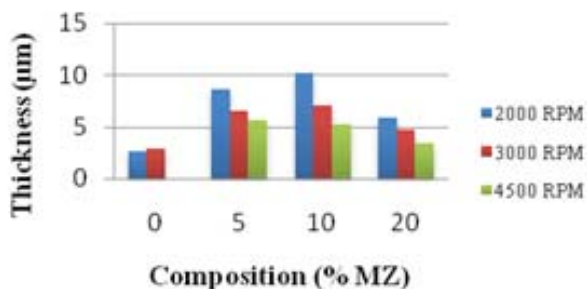


Figure 4. Graph of thickness vs. composition and spin coating speed.

The capacitance of the samples was measured using an LCR (Stanford Research SR720) meter and the dielectric constant was calculated using the following equation:

$$C = \kappa \epsilon_0 \frac{A}{d}, \quad (1)$$

where C is the capacitance, κ the dielectric constant, ϵ_0 the permittivity of vacuum, A the area of the top electrode, and d the distance between the electrodes (the thickness of the film). For applications in high speed electro-optic devices it is preferable for the dielectric constant to be low.³

As shown in Figure 5, the dielectric constant of the sol-gel films varied with both the concentration of zirconium and the frequency. Compared to inorganic materials whose dielectric constants are a few tens to a few thousands, the sol-gel materials have lower dielectric constants of 3 ~ 6, which are favorable for high speed electro-optic devices.

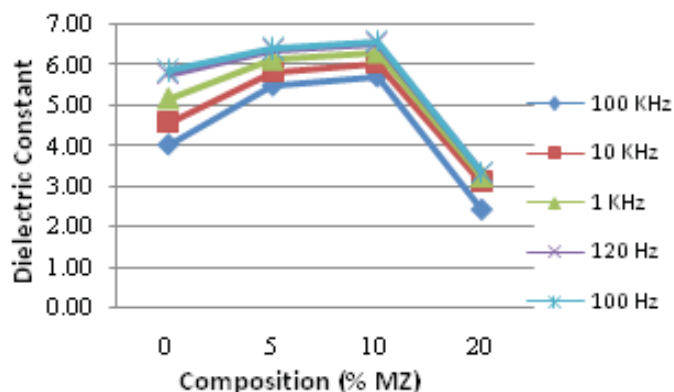


Figure 5. Graph of dielectric constant vs. composition.

Figure 6 shows the dependence of dielectric constant on frequency. The variation is ~10% in the wide frequency range from 100 Hz to 100 kHz.

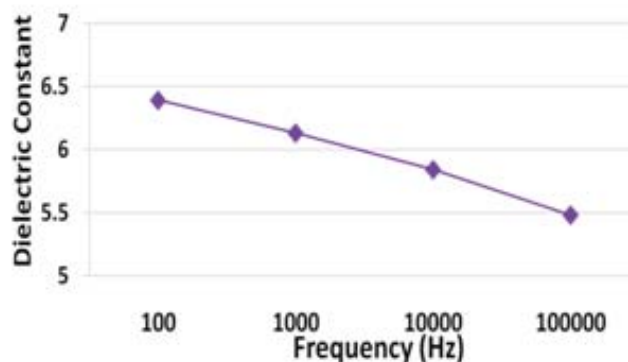


Figure 6. Graph of dielectric constant vs. frequency for the 5% Zr sample.

The thermal stability of the sol-gel with respect to dielectric constant was fairly high. The average change for the samples was 11.8% with some samples changing as little as 4.2% as the temperature increased. Figure 7 shows a graph for one of the samples measured with different frequencies at temperatures ranging from 22 °C to 100 °C.

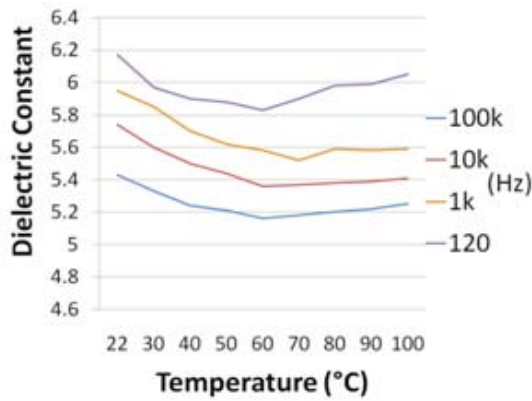


Figure 7. Graph of dielectric constant vs. temperature for the 5% Zr, 3000 rpm sample.

The piezo coefficient (d_{33}) can be calculated using a plot of the intensity of the interference pattern from the interferometer (as shown in Figure 8) using the following equation:

$$d_{33} = \frac{\lambda |I_1 + I_2| \cos \theta}{4\sqrt{2} \pi (V_{rms}) (I_r)} \quad (2)$$

Where I_1 and I_2 are the intensity values from two successive peaks of the interferometer pattern as shown in Figure 8, θ is the incident angle at which the sample is placed with respect to the beam in the interferometer as shown in Figure 3, V_{rms} is the root-mean-squared of the applied voltage, I_r is the maximum difference in intensity of the interference plot of the reference run (before a voltage is applied), and λ is the wavelength of the laser used.

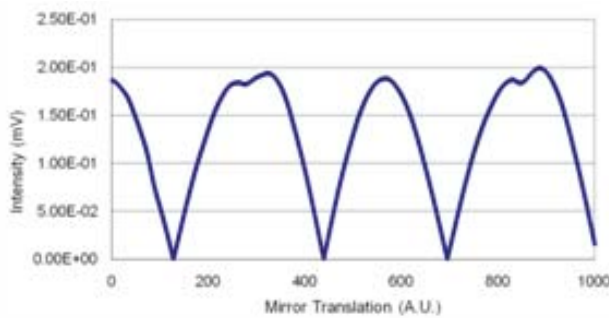


Figure 8. Intensity pattern from interferometer.

A few of the samples were tested with the interferometer and the sample containing 5% Zr showed a piezoelectric coefficient of 35 pC/N at 8.4 kHz.

Conclusions

Through this research, the basic electrical and optical properties of MAPTMS-Zr sol-gel with different compositions were revealed. The thickness of the material varies not only with the speed of the spin coating, but also with the zirconium concentration. The dielectric constants are very low compared with inorganic materials and have a dependence on the composition of the sol-gel as well as the frequency. The thermal stability of the dielectric properties of the materials was shown to be fairly high at temperatures up to 100 °C.

The piezoelectric coefficients of the sol-gel films were measured with optical interferometer. Some of the samples have a high piezoelectric response of up to 35 pC/N.

The low dielectric constant, high piezoelectric response of the hybrid sol-gel, accompanied with the ease of processing, low cost, wide fabrication flexibility, low optical loss, and stability make it a superior material for use in high speed electro-optic devices such as tunable filters and spatial light modulators.

References

1. H. Gan, H. Zhang, C.T. DeRose, R.A. Norwood, N. Peyghambarian, and M. Fallahi, Appl. Phys. Lett. 89, 041127 (2006).
2. H. Gan, H. Zhang, C.T. DeRose, R.A. Norwood, and M. Fallahi, Appl. Phys. Lett. 89, 141113 (2006).
3. H. Zhang, D. Lu, M. Fallahi, Optical Materials 28, 992-999 (2006).
4. Oleg Michelkin, Ph. D Thesis, University of Arizona, (2004).

Acknowledgements

This work was made possible by the NSF sponsored Science and Technology Center on Materials and Devices for Information Technology Research under the contract No. DMR-0120967.



AMY VAN NEWKIRK is going to be a junior at Grove City College. After getting her bachelor's degree in Applied Physics she plans to attend graduate school.

Use of Ion-Exchange Functionalized DNA as a Host Material for Enhanced Poling Induced Order and Molecular Hyperpolarizability

TERRY VILLARREAL, North Seattle Community College & University of Washington

Meghana Rawal, Professor Larry R. Dalton, University of Washington

Introduction

Current high-speed electronics are reaching the limits of their potential bandwidth. As computer processors improve, the ability to manage larger amounts of data at greater speeds will become necessary. Because of intrinsically high potential bandwidth, photonic (e.g., fiber optic) technologies present one potential solution. However, in order to encode electrical information into optical signals an electro-optic technology capable of operating at extremely high speeds must be implemented. For this purpose organic electro-optic materials present several clear potential advantages. Two of the main advantages are increased speed (potentially, bandwidths on the order of tens of terahertz) and processability. However, in order for these organic materials to become viable technologies, these organic materials must possess high electro-optic coefficients along with high transparency, and good thermal and photochemical stability.

In order to achieve a high material electro-optic coefficient (r_{33}) a high first nonlinear optical susceptibility must exist. To achieve this, molecular components (with high nonlinear polarizabilities, β) may be arranged accentrically to form an asymmetric material lattice. For r_{33} to reach an optimized value a large concentration of high- β molecular components (chromophores) must be present and a high degree of dipolar order must exist.^{1,2}

Objective

This project focuses on enhancing electric field poling-induced dipolar order through intermolecular interactions between chromophores and their environment. When attempting to align chromophores in an electric field, the dipolar order obtained is defined by the interplay among external (poling field) and internal (intermolecular electrostatic) forces. As the number density increases, the number of dipole interactions increases, thereby limiting poling-induced order (and the electro-optic coefficient).

If order was introduced, as to limit the movement of the chromophore in at least one axis, the overall electro-optic coefficient will potentially be improved.^{3,4,5}

Experimental Section

The purpose of this study is to limit the movement of chromophores along one axis and thereby limit the orientational possibilities that the chromophore may access. The overall goal will be to attach a chromophore to a surfactant with a quaternary ammonium salt that will then be intercalated with DNA (See Fig 1).

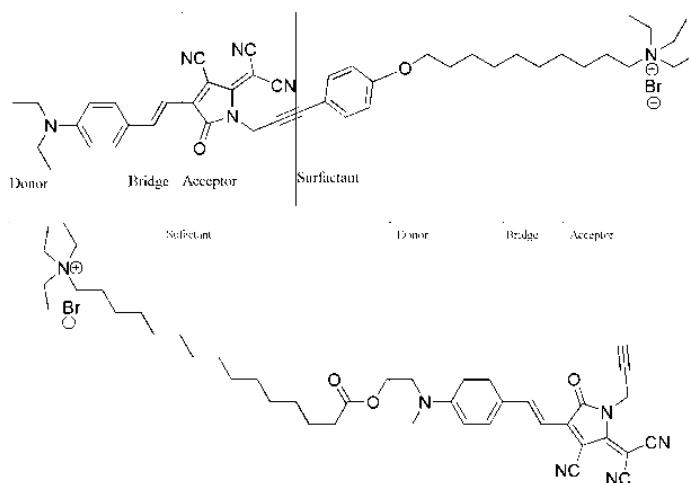
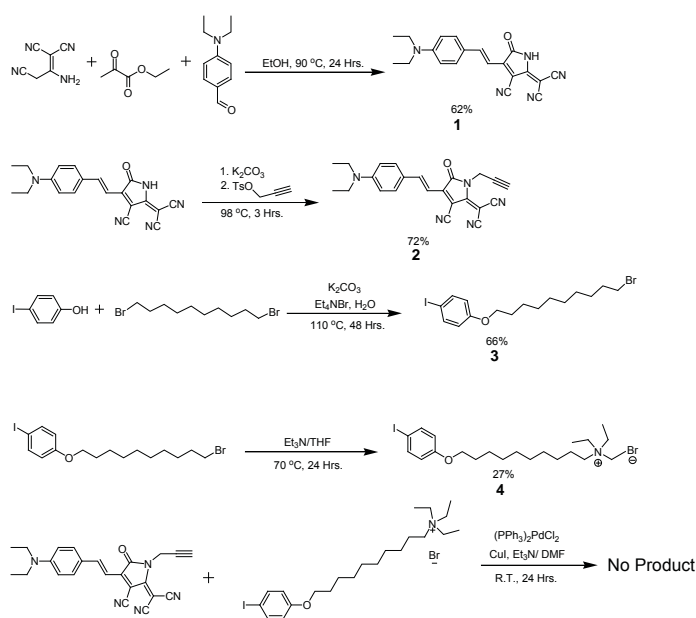


Figure 1. Surfactants attached to Chromophore



Scheme A^{6,7}

Synthesis:

1A. Ethyl Pyruvate (16 mL, 141.043 mmol), and ethanol (56 mL) were combined and stirred for 5 minutes under a nitrogen atmosphere. Malononitrile dimer (7.454 g, 56.417 mmol) was then added to the stirring solution. The solution was then refluxed for 100 minutes at 90 °C. At the end of the 100 minutes, diethylamino benzaldehyde (7 g, 39.49 mmol) was added to the solution and

refluxed at 90 °C for 24 hours. The heating was then turned off and the reaction was allowed to cool to room temperature. The reaction was filtered and the green precipitate was washed with Dichloromethane until the filtrate looked clear. The green product was then transferred to a vial and placed in a vacuum oven for 2 hours. (6.718 g, 50% yield)

2A. 1A (5 g, 14.56 mmol) and acetonitrile (100 mL) were combined and stirred for 5 minutes under nitrogen atmosphere. Potassium carbonate (6.037 g, 43.68 mmol) was then added to the stirring solution. The solution was then refluxed for 25 minutes at 98 °C. Propargyl tosylate (7.5 mL, 43.68 mmol) was then added and allowed to reflux for an additional 80 minutes. The heating was then turned off and the reaction was allowed to cool to room temperature followed by quenching with de-ionized water (100 mL.) The reaction was filtered and the precipitate washed sequentially with de-ionized water and ethyl acetate. The product was collected and dried under vacuum overnight. (3.956 g, 71% yield)

3A. p-Iodophenol (4.0 g, 18 mmol), 1-10, Dibromodecane (4.9 mL, 22 mmol), Potassium Carbonate (2.510 g, 18 mmol), Tetraethylammonium bromide (.382 g, 2 mmol), and water (40 mL, 2.220 mol) were combined and refluxed at 110 °C for 2 days under a nitrogen atmosphere. The resulting solution was quenched with water and allowed to cool, during which time a precipitate formed, which was, filtered over a frit funnel, washing with water. The product was placed in a vacuum oven for 3 days. The product was dissolved in DCM (50 mL), washed with 1M HCl (3x 20 mL), dried over Magnesium Sulfate, filtered over buchner funnel and evaporated to dryness. (5.787 g, 66% yield)

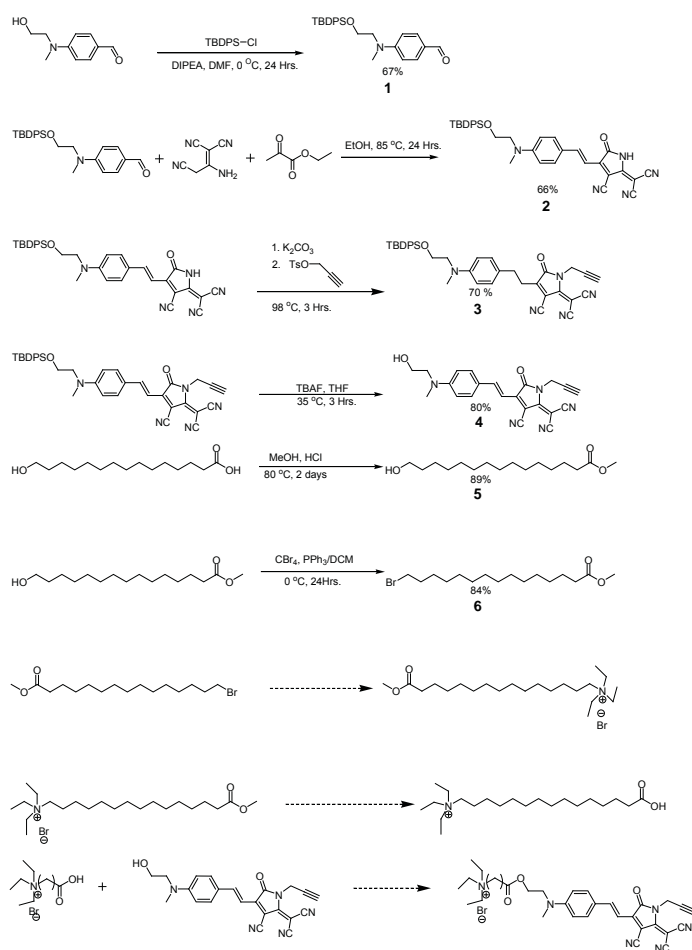
4A. 3A (5.77 g, 13 mmol) and triethylamine/THF 33% solution (36 mL) were combined and refluxed at 70 °C for 72 hours. The heating was stopped and the reaction was quenched with 5% sodium bicarbonate (50 mL.) The reaction was extracted with dichloromethane (3 x 30 mL), dried over sodium sulfate and evaporated to dryness. (1.632 g, 27% yield)

Originally the goal was to attach the surfactant to the acceptor side of the chromophore via a Sonogashira Coupling reaction. However, after numerous attempts, under varying conditions, this reaction could not be driven to completion.

Synthesis:

1B. Methyl-hydroxyethylamino benzaldehyde (10g, 56 mmol) and DIPEA (49mL, 280 mmol) was dissolved in DMF (150mL) at 0 °C. TBDPS-Cl (18mL, 70 mmol) was then added dropwise to the reaction. The reaction was allowed to run for 24 hours. The reaction was quenched with brine (200mL) and extracted with ethyl acetate (3x100mL.) The solution was dried over magnesium sulfate, filtered and then evaporated to dryness. The compound was then recrystallized in a 10% ethylacetate/hexane solution. (15.74g, 67% yield.)

2B. Ethyl Pyruvate (12 mL, 107.76 mmol), and ethanol (220 mL) were combined and stirred for 5 minutes under a nitrogen atmosphere. Malononitrile dimer (7.11g, 53.88 mmol) was then added to the stirring solution. The solution was then refluxed for 100 minutes at 90 °C. At the end of the 100 minutes, 1B (15 g, 35.92 mmol) was added to the solution and refluxed at 90 °C for 24 hours. The heating was then turned off and the reaction was



Scheme B^{8,9}

allowed to cool to room temperature. The reaction was filtered and the green precipitate was washed with hot ethanol until the filtrate looked clear. (14.743g, 67%)

3B. 2B (2.249g, 3.85 mmol) and acetonitrile (43mL) were combined and stirred for 5 minutes under nitrogen atmosphere. Potassium carbonate (1.597g, 11.56 mmol) was then added to the stirring solution. The solution was then refluxed for 15 minutes at 98 °C. Propargyl tosylate (2mL, 11.56 mmol) was then added and allowed to reflux for an additional 80 minutes. The heating was then turned off and the reaction was allowed to cool to room temperature followed by quenching with de-ionized water (50mL.) The reaction was filtered and the precipitate washed sequentially with de-ionized water and ethyl acetate. The product was collected and dried under vacuum overnight. (1.65g, 70% yield)

4B. 3B (1.420g, 2.311mmol) was dissolved in a TBAF/THF (4.7mL, 4.622mmol) 1M solution. The reaction was refluxed at 35 °C for 4 hours. The reaction was then removed from heat and quenched with 10mL of 1M HCl. The product was then extracted with DCM (2x20mL.) The product was washed with 1M HCl (3x20mL) and evaporated to dryness. A column was run in ethyl acetate/dichloromethane, 30%. The desired fractions were evaporated to dryness. $R_f = 0.24$, (.090g, 11.2%)

5B. 15-hydroxypentadecanoic acid (4.812g, 19mmol), MeOH (40mL, 190mmol) and HCl (.60mL, .569mmol) 12M were combined and refluxed at 80 °C for 72hours. The reaction was then removed from heat and quenched with de-ionized water (50mL) and then extracted with ethyl acetate (3x20mL.) The organic layer was then dried over magnesium sulfate and filtered. The solution was then evaporated to dryness. (4.599g, 89% yield)

6B. 5B (4.499g, 16.5mmol), carbon tetrabromide (6.840g, 20.6mmol) and DCM (49.5mL) were combined under nitrogen atmosphere and cooled down to 0 °C. Triphenylphosphine (5.410g, 20.6mmol) was then added drop wise over a 30 minute time frame. The reaction was allowed to stir for 3 hours and slowly return to room temperature. The reaction was then concentrated to dryness, washed with hexane and then ran through a plug. The resulting solution was evaporated to dryness. (4.651g, 84%yield)

Discussion

As this project is a proof of concept, more work and synthesis is required. The synthesis of the linker molecule is as yet incomplete. The bromide end needs to be converted into a quaternary ammonium salt, followed by hydrolyses of the methyl ester to the carboxylic acid as shown in scheme B. The carboxylic acid will be attached to the chromophore using DCC/DPTS coupling to give the target molecule.

Conclusion

Once the target molecule has been correctly synthesized, it will be titrated with low molecular weight sodium DNA. If the published theory is correct, the surfactant will undergo an ionic exchange with the phosphate backbone of DNA and then the chromophore should intercalate between the base pairs of the DNA. Further analysis of this molecule will be performed at that time to measure its optic-coefficient value, r^{33} .

References

1. Dalton, L.R. et. al. Optical Materials 2002, 21, 19-28
2. Davies, J. et. al. J. Am. Chem. Soc. 2008, 130, 10565-10575
3. Miller, D. Angew. Chem. Int. Ed. 1998, 37, 1768-1785
4. Braun, C.S.; Et.al. Biophysical Journal 2003, 84, 1114-1123
5. Kawabe, Y.; Wang, L.; Horinouchi, S.; Ogata, N. Adv. Mater. 2000, 12, No. 17
6. Jang. Et.al. Chem. Mater. 2006, 18, 2982-2988
7. Green, T.W.; Wuts, P.G.M. Protective Groups in Organic Synthesis , 3rd Ed., 1999, New York, NY. Pg 142
8. Baughman, T.W.; Sworen, J.C.; Wagener, K.B. Tetrahedron, 2004, 60, 10943-10948
9. Moss, R.A.; Chung, Y.C. J. Org. Chem. 1990, 55, 2064-2069

Acknowledgements

Funds for this research were provided by the Center on Materials and Devices for Information Technology Research (CMDITR), NSF Science and Technology Center No. 0120967. I would also like to thank the Dalton Research Group, especially my mentor Meghana Rawal, for all of the mentoring and training that was given and Jim Patterson, who let me know of this opportunity.



TERRY VILLARREAL is a junior, currently majoring in biochemistry at the University of Washington with hopes of pursuing a career in the medical, pharmaceutical or chemical research industry.

Plasmon-resonant silver nanoprisms for performance enhancement of organic photovoltaic cells

JOSIAH G. WARD, South Seattle Community College

Abhishek Kulkarni, Keiko Munechika, David Ginger, University of Washington

Introduction

Currently, many domestic photovoltaic cells are built utilizing silicon wafers which can be moderately efficient (10-15%) at converting solar energy but these cells are expensive to produce. An alternative to these are organic photovoltaics (OPVs) based on solution processable polymers. One of the common architectures is based on thin films comprising of a bulk heterojunction blend of poly(3-hexylthiophene) (P3HT) and phenyl-C₆₁-butyric acid methyl ester (PCBM).¹ One major obstacle to the advancement of these organic photovoltaics, however, is built into their geometry. Because we are using thin films, there is a tradeoff between the amount of current extractable and the amount of light absorbed in the device. In order to maximize the light absorption, a thicker polymer film (~150 nm) is necessary, however the amount of current extracted from the cell is decreased as the film gets thicker due to charge carriers and excitons recombining.¹ Previous research has shown that an extra layer of plasmon-resonant metal nanoparticles can enhance the local electric field, which leads to better absorption of incident light.² Most of these involve nanoparticle synthesis methods with no shape control or tunability of the plasmon resonance peak, typically yielding oblate and spherical particles.² We believe using silver nanoprisms is a superior method due to shape control and tunability of the localized surface plasmon resonance (LSPR) peak. The nanoprisms also exhibit a tendency to scatter ~80% of incident light, which could increase the path length of light within a device, allowing more time for the active layer to absorb the photons. In general, we would like to be able to tune the LSPR peak between 500 and 750 nm. The silver nanoparticle film should theoretically allow us to make the polymer film in the OPV thinner (20-30 nm) while still absorbing all incident light. The initial goal of our research is to analyze changes in optical properties of polymer films due to spectral overlap between the LSPR spectra of the nanoparticles and absorption spectra of the polymer. Eventually, we would like to incorporate the silver nanoparticles into organic solar cells to test the hypothesis.

Experimental Methods

Thermal synthesis of silver nanoprisms.³

Aqueous stock solutions in deionized water of silver nitrate (0.1 mM), trisodium citrate (30 mM) and polyvinylpyrrolidone (PVP) (0.7 mM) were prepared. Sodium borohydride solution (100 mM) was freshly prepared for each synthesis. All solutions were kept cold in an ice cooler. While stirring, the solutions were combined in order: 12.5 mL silver nitrate, 750 μ L PVP, 75 μ L trisodium citrate and 30 μ L hydrogen peroxide (wt. 30%). Continuing to stir, some amount of borohydride solution is injected, typically in the range

of 30-60 μ L. Immediately, the solution became pale light yellow in color. After several minutes of stirring the color changed to a very deep yellow, then quickly changed colors as the nanoprisms formed and the LSPR peak redshifted. The final color and LSPR peak depend on the amount of borohydride injected.

Photochemical synthesis of silver nanoprisms.⁴

This process is best done in the dark and is very sensitive, so all glassware should be cleaned as thoroughly as possible. An aqueous (deionized water) stock solution of silver perchlorate (10.8 mM) was prepared and stored in the dark. On ice and while stirring, 90 mL deionized water, 8.7 mg sodium citrate and 3.7 mg sodium borohydride were combined in a clean glass beaker. Then, using a sterile needle, 1 mL silver perchlorate solution was injected. The solution immediately darkened and after ~3 minutes stabilized to a yellow color characteristic of the growth of spherical nanoparticles. The solution is transferred into clean vials, sealed and capped, then exposed to high intensity LED light for 3-7 days. The LED's used are Luxeon V high output LED's from Philips Lumileds. Figure 1 displays light output characteristics of the LED's utilized in the experiment.

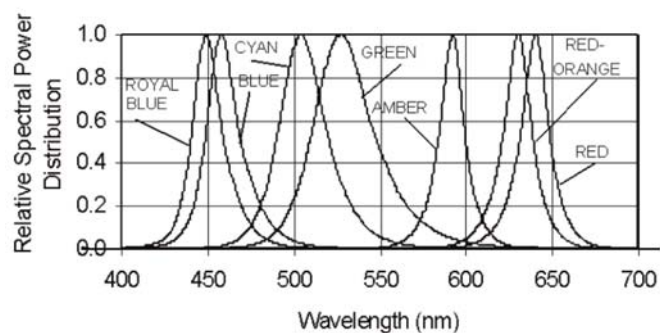


Figure 1. Light output characteristics of LED's provided by Philips Lumileds (www.lumileds.com)

Our experimental setup (figure 2) was a small closed box with an array of four LED's placed atop (for two-color experiments the second array enters through the back, which is otherwise covered), with vials of nanoparticles resting in the bottom. We also placed a small fan in the side to prevent overheating of the LED array.

Silanization of glass substrates.⁵

The silanization process is done in order to self-assemble a monolayer of nanoparticles on a glass substrate.



Figure 2. Photo of experimental setup for LED nanoparticle synthesis.

The substrates are first cleaned by sonication for 15 minutes each in detergent, deionized water, acetone and isopropanol. The substrates are then placed in a plasma cleaner for 3-5 minutes. A solution is prepared by combining 50 μL acetic acid (Glacial), 500 μL aminopropyltrimethoxysilane (Aldrich 97%) and filling to 50 mL with isopropanol. After plasma cleaning, the substrates are immersed in the APTMS solution and let sit in the dark for 5-6 hours. The substrates are then washed with isopropanol, dried with nitrogen and cured on a hot plate under nitrogen flow for 1 hour. After curing, the substrates are placed in individual vials of nanoparticle solution, covered, and left in the dark for 24 hours.

Results and Discussion

Due to the high sensitivity of the thermal nanoprism synthesis to foreign contaminants and possibly other factors, results are often inconsistent; however, the process has yielded nanoprisms with dipole resonance peaks ranging from ~ 480 -760 nm. Figure 3 displays the range of extinction spectra that were obtained. Figure 4 shows a photograph of assorted colloids in solution.

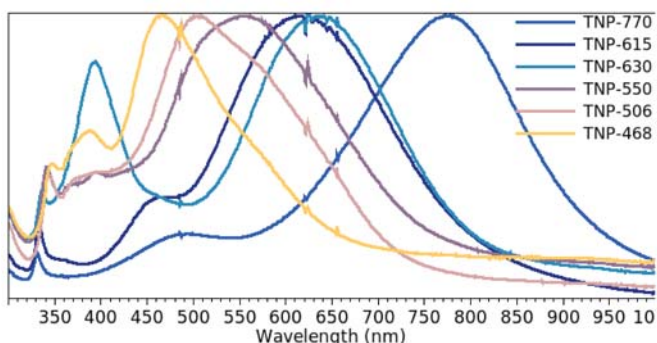


Figure 3. Normalized extinction spectra of various thermal nanoparticles.

The spectral position of the LSPR peak depends on the relative concentration of borohydride injected. At 30 μL , TNP-468 or TNP-506 is generated. At 60 μL , TNP-770 is generated, leading to a general linear relationship between the amount of borohydride and the LSPR peak position. Increasing the borohydride leads to a redshift in the peak position. The visible color of the colloid ranges,

in the same fashion, from orange and pink (30-35 μL borohydride) to purple and blue (55-60 μL). Figure 5 shows a scanning electron microscope (SEM) image of a thermal nanoprism colloid with LSPR peak at 550 nm.



Figure 4. Photo of assorted thermal nanoprism colloids arranged in order of increasing borohydride concentration.

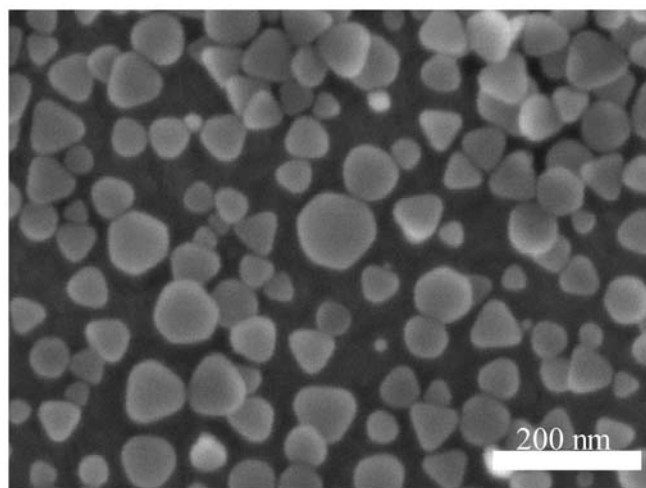


Figure 5. SEM image of a thermal nanoprism colloid made by adding 40 μL borohydride.

Photochemical experiments were performed with Fluorescent white light, Blue, Cyan and a combination of Blue and Green (colors taken from figure 1). Previously in the lab, most of our nanoparticles were synthesized by exposure to a white fluorescent light. Figure 6 shows the typical spectra obtained from these experiments. The yellow curve is a typical initial spectra of the colloid before exposure to radiation. Observing the LSPR peak positions, the trend seems to be that the LSPR peak wavelength occurs 50-60 nm redshifted from the wavelength of incident radiation. Figure 7 shows an SEM image of a photochemical nanoprism colloid with LSPR peak at 500 nm, generated from a blue 460 nm LED array.

Comparing figures 5 and 7, the most notable difference is the sharpness of the prisms. Because of the sensitivity of the thermal synthesis, it is much easier to generate nanoprisms with LSPR peaks at 500 nm using photochemical synthesis rather than thermal. Thermal nanoparticles with LSPR peaks at 500 nm tend to have very low optical density (OD), requiring additional steps such as centrifugation in order to obtain high enough OD for

such colloids to be potentially useful in a device. Unfortunately, to date our lab has not been able to use photochemical colloids in silanization. Attempts at making nanoparticle films on silanized substrates were unsuccessful. The reasons for this are under investigation.

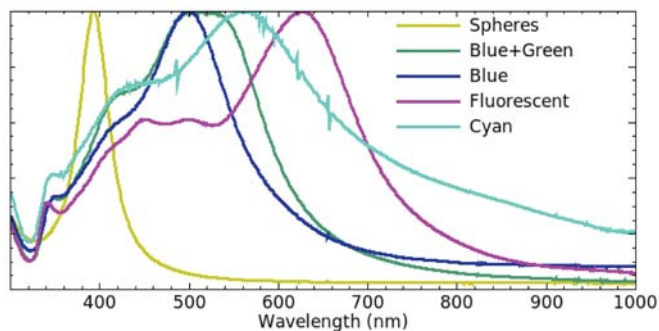


Figure 6. Normalized extinction spectra of various photochemical nanoprism colloids color-coded to the color of incident radiation in Figure 1.

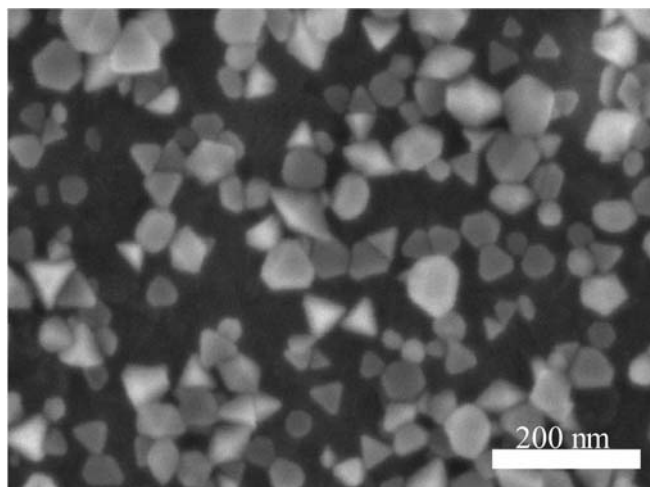


Figure 7. SEM image of a photochemical nanoprism colloid generated from 460 nm radiation.

Conclusions

Larger batches (100-150 mL) of nanoparticles were able to be created using both synthesis methods, allowing us to perform more experiments with a single set of nanoparticles. LED synthesis was also explored in detail and a nanoprisms with a range of LSPR peaks were generated. Colloids with LSPR peaks around 500 nm, corresponding to the absorption maximum of P3HT, were also generated from both thermal and photochemical synthesis methods. Dual LED irradiation will be explored in future work in an attempt to make nanoparticles with narrower LSPR spectra.

References

1. Hoppe, H., Sariciftci, N.S., J. Mater. Res. 2004, 19, 7, 1924.
2. Morfa, A.J., et al, J., Appl. Phys. Lett. 2008, 92, 013504.
3. Metraux, G.S., Mirkin, C.A., Adv. Mater. 2005, 17, 412.
4. Jin, R. et al., Science 2001, 294, 1901.
5. 5. Xue, C., Li, Z., Mirkin, C.A., Small, 2005, 1, 513.

Acknowledgments

Funds for this research were provided by the Center on Materials and Devices for Information Technology Research (CMDITR), NSF Science and Technology Center No. DMR 0120967. I would also like to thank the University of Washington department of Chemistry and my mentors, Abhishek Kulkarni and Keiko Munechika, as well as Dr. David Ginger and the rest of the Ginger lab for their guidance and allowing me to use their equipment and facilities.



JOSIAH WARD is an undergraduate at South Seattle Community College pursuing a dual-degree in Electrical Engineering and Mathematics. He plans on transferring to the University of Washington to complete his B.S. and continuing on to graduate school in the sciences.

